Numerical modelling of environmental dose rate and its application to trapped-charge dating

Roger P. Nathan

St Hugh's College, Oxford

NUMERICAL MODELLING OF ENVIRONMENTAL DOSE RATE AND ITS APPLICATION TO TRAPPED-CHARGE DATING

Roger Philip Nathan

St Hugh's College

Doctor of Philosophy

Michaelmas, 2010

Abstract

Accurate estimation of environmental dose rate is essential for high-resolution trapped-charge dating. Beta and gamma emissions from simulated sediments containing radioactive uranium, thorium and potassium are modelled in contexts that are spatially heterogeneous. Dose rate was modelled using Monte Carlo radiation transport codes MCNP and PENELOPE. A number of key issues that affect dose rate evaluation are examined and updated corrections are calculated.

Granular structures used for geometrical input into the models were simulated using randomly packed ellipsoids. The pair correlation function and chord length distributions were derived. The effects of water content on dose rate were modelled and compared with cavity theory. Apart from activity dilution, the variation of grain size or water content was shown to be significant for gamma radiations due to the transition from charged particle equilibrium. The standard correction for beta dose rate due to grain size was found to be satisfactory although sensitivity to grain shape and material should be taken into account.

Dose rate modeling was applied to three dating studies of early human fossils: Skhul V, Israel skull; Hofmeyr, South Africa skull and the Forbes' Quarry, Gibraltar skull. The spatial modelling was implemented using computerised tomographic (CT) images and dose rate found to be modified significantly by the presence of the skull in the sediment. Time evolution of the dose rate was examined for the latter two skulls and dates of 36±3ka (Hofmeyr) and 55-95ka (Forbes' Quarry) were calculated.

Acknowledgements

I am very grateful for the support of the Research Laboratory for Archaeology and the History of Art for taking me on ... and waiting for me to finish. It has been a most enjoyable time in the Oxford luminescence dating lab and I most obliged to those who have been around for the last 10 years.

I must extend my first thanks to Jean-Luc Schwenninger who has been unstintingly supportive, enthusiastic and inspirational. Many thanks to Ed Rhodes, who got me started and has supplied me with ideas throughout. In a similar way, Richard Bailey seems to always have had sensible and novel directions for my work at every meeting. Barry Brennan has always lent a kind ear to my madder ravings and I am much obliged for his support.

The trapped-charge dating community, more generally, has offered many encouragements and help over the course of my D.Phil. and I am most grateful. In particular, thanks to Andrew Murray for having me over to Risø several times and to Barbara Mauz for pushing for practical applications for the modelling.

Good luck to Guillaume Guerin who has taken up the 'fight' for environmental dose rate modelling in dating and probing the boundaries with new work.

Sincere and loving thanks to Portia and da boys for everything.

Table of contents

Abstract

Preface

List of Figures

List of Tables

List of peer reviewed papers

on environmental dose rate

2002   **Nathan, R.P.**, Thomas, P.J., Jain, M., Murray, A.S., Rhodes, E.J.: Environmental dose rate evaluation in conditions of beta heterogeneity and its implications for luminescence dating: Monte Carlo modelling and experimental validation. *Radiation Measurements*, **37**, 305-313.

     Aznar, M.C., **Nathan, R.P.**, Murray A.S., Bøtter-Jensen, L.: Differential dose rates in a mixed beta and gamma field using shielded Al_2O_3:C: results of Monte Carlo modelling. *Radiation Measurements*, **37**, 329-334.

2003   **Nathan, R.P.**, Grün R.: Gamma dosing and shielding of a human tooth by a mandible and skull cap: Monte Carlo simulations and implications for the accuracy of ESR dating of tooth enamel. *Ancient TL*, **21**, 79-84.

2005   Grün, R., Stringer, C., McDermott, F., **Nathan, R.**, Porat, N., Robertson, S., Taylor, L., Mortimer, G., Eggins, S., McCulloch, M.: U-series and ESR analyses of bones and teeth relating to the human burials from Skhul. *Journal of Human Evolution*, **49**, 316-334.

     Loughlin, M.J., **Nathan, R.P.**: Estimates of dose rates during the dismantling of JET. *Radiation Protection Dosimetry*, **115**, 486-490.

2007   Grine, F.E., Bailey, R.M., Harvati, K., **Nathan, R.P.**, Morris, A.G., Henderson, G.M., Ribot, I., Pike, AW.G.: Late Pleistocene human skull from Hofmeyr, South Africa, and modern human origins. *Science*, **315**, 226-229.

     Willerslev, E., … , **Nathan, R.**,.., et al.: Ancient biomolecules from deep ice cores reveal a forested Southern Greenland. *Science*, **317**, 111-114.

2008   Gilbert, M.T.P., … , **Nathan, R.**, et al.: Paleo-Eskimo mtDNA genome reveals matrilineal discontinuity in Greenland. *Science*, **320**, 1787-1789.

     Nathan, R.P., Mauz, B.: On the dose rate estimate of carbonate-rich sediments for trapped charge dating. *Radiation Measurements*, **43**, 14-25.

2009   Mauz, B., Elmejdoub, N., **Nathan, R.**, Jedoui, Y.: Last interglacial coastal environments in the Mediterranean–Saharan transition zone. *Palaeogeography, Palaeoclimatology, Palaeoecology*, **279**, 137-146.

List of acrynoms

MCNP	A Monte Carlo radiation transport code
ITS	A Monte Carlo radiation transport code
GEANT	A Monte Carlo radiation transport code
EGS `	A Monte Carlo radiation transport code
PENELOPE `	A Monte Carlo radiation transport code
MC `	Monte Carlo
CPE	Charged particle equilibrium
TL	Thermoluminescence
OSL	Optically stimulated luminescence
ESR	Electron spin resonance
IM(D)	Infinite-matrix (dose/dose-rate)
CSDA	Continuous slowing down approximation
ENSDF	Evaluated nuclear structure data file
FOM	Figure of merit
DPK	Dose point kernel
RMS	Root mean squared
MATLAB	Programming software
CT	Computer tomography
(MC)-ICP-MS or AES	(Multi-collector) - inductively coupled plasma – mass spectrometry or atomic emission spectrometry

Chapter 1: Introduction

1.1   Trapped charge dating

Trapped charge dating is an important radiometric method for dating the landscape up to at least several hundred thousand years before present (Murray and Olley, 2002). A date is achieved by measuring the absorbed dose (also commonly called the equivalent dose) in a suitable sample, such as quartz sediment, and the dose rate expected from ionising environmental radiation such that

$$Age = \frac{Absorbed\ dose}{Mean\ dose\ rate}$$ (1.1)

Trapped charge, a population of electrons occupying metastable sites in minerals, is accumulated with dose and this provides a suitable proxy to assess absorbed dose in the sample. The amount of trapped charge may be estimated through measuring luminescence generated by the depletion of the trapped charge. This may occur when stimulating the sample with suitable wavelengths of light (Huntley et al., 1985) (optically stimulated luminescence or OSL) or heat (Aitken, 1985a) (thermoluminescence or TL). Electron spin resonance (ESR) methods (Ikeya, 1975) measure the trapped charge intact using microwave stimulation of paramagnetic centres. For the purposes of dating, several types of mechanisms remove the trapped charge prior to burial – the so-called "zeroing" event. These include exposure to sunlight especially for sedimentary material (OSL), sufficient heat (OSL, TL) from hearths, and formation of teeth (ESR).

The dose rate arises from ionising radiation emitted during the decay of radioactive isotopes found in trace quantities in the regolith and from cosmic radiation. The key isotopes from

terrestrial sources are members of the decay chains of uranium and thorium (Figure 1.1), potassium-40 and, to a lesser extent, rubidium-87. Measurement of the dose rate can be made directly using dosimetry, decay counting or calibrated spectrometry; indirect measurements often involve the evaluation of elemental mass ratios of uranium, thorium and potassium in the sample.

The impact of trapped-charge dating on archaeological science and interpretation of archaeological sites has been profound (Wintle, 2008). Early applications of thermoluminescence dating were focussed on fired clay associated with archaeological material (Zimmerman and Huxtable, 1971), pottery (Fleming and Stoneham, 1973), burnt stones due to human activity (Goksu et al., 1974, Valladas and Valladas, 1987, Mercier et al., 2007) and authenticity applications. ESR dating of human and animal teeth as well as other suitable contextual material associated with archaeological research has been important (Ikeya, 2004), particularly over several decades of providing chronologies of Palaeolithic sites. With the advent of OSL, the ubiquity of mineral grains such as quartz and feldspar has allowed dating of archaeological-rich (and also sterile) stratigraphy to provide high-resolution and coherent sampling of sediments. Two examples are: 1) Lang and Wagner (1996) show a correlation between the human settlement and landscape erosion by dating adjacent colluviums; and 2) Sanderson et al. (2007) used OSL to date a sequence of Cambodian canals from infilled sediments. Luminescence dating is well placed to date the dispersal of modern humans since it either complements radiocarbon dating for <50ka or provides primary dates for layers >50ka (Grine et al., 2007, Jacobs et al., 2003, Thorne et al., 1999, Gillespie and Roberts, 2000), however not all dates are without controversy (cf. Lake Mungo, Australia).

Recent improvements in the accuracy and precision of OSL estimation of dose in quartz have made the dating method considerably more robust. These include a single-aliquot regenerative-dose protocol (Murray and Wintle, 2000), component-resolved luminescence (Bailey et al., 1997), the routine application of single grain methods (Jacobs et al., 2008) and

instrumental advances (Botter-Jensen et al., 2003, Greilich et al., 2005). Much less notable progress has been made for dose rate estimation. With the view towards obtaining correct and precise dates, the dose rate becomes a limiting factor. This dissertation will address two areas of the dose rate calculation:

1) implementation of numerical modelling for simulating sedimentary environments and updating commonly applied dose rate corrections

2) specific concerns in achieving dates for various types of heterogeneous sediments.

Monte Carlo modelling with robust codes provides a highly accurate means to compute dose rates in a wide range of environments.

1.2 Environmental dose rate estimation

1.2.1 Environmental radiation

Radiation is emitted during the radioactive decay of unstable nuclei to energetically more stable states (Evans, 1955). The probability of a decay event occurring for a nuclide, related to its decay constant λ, and emission characteristics of radioactive decay are governed by stochastic processes. If the daughter nuclide is unstable it will in turn decay, leading to the formation of a "decay chain". The existence of such chains (see Figure 1.1) when considering the dose rate contributions of very long lived isotopes such as uranium-238, uranium-235 and thorium-232 becomes important. In fortuitous circumstances where a closed system is preserved (that is, no net migration of nuclides through the material), the decay series will be in a state of secular equilibrium such that the activities of all members of the chain will almost be identical (i.e., $N_i \lambda_i \approx N_j \lambda_j$ where N is the population of isotopes and λ is the decay constant. Half-life can be calculated from $t_{1/2} = ln(2) / \lambda$). In this case, the dose rate can be determined solely by measurement of the concentration of the parent isotope of the chain and the dose rate can be assumed to be constant over time.
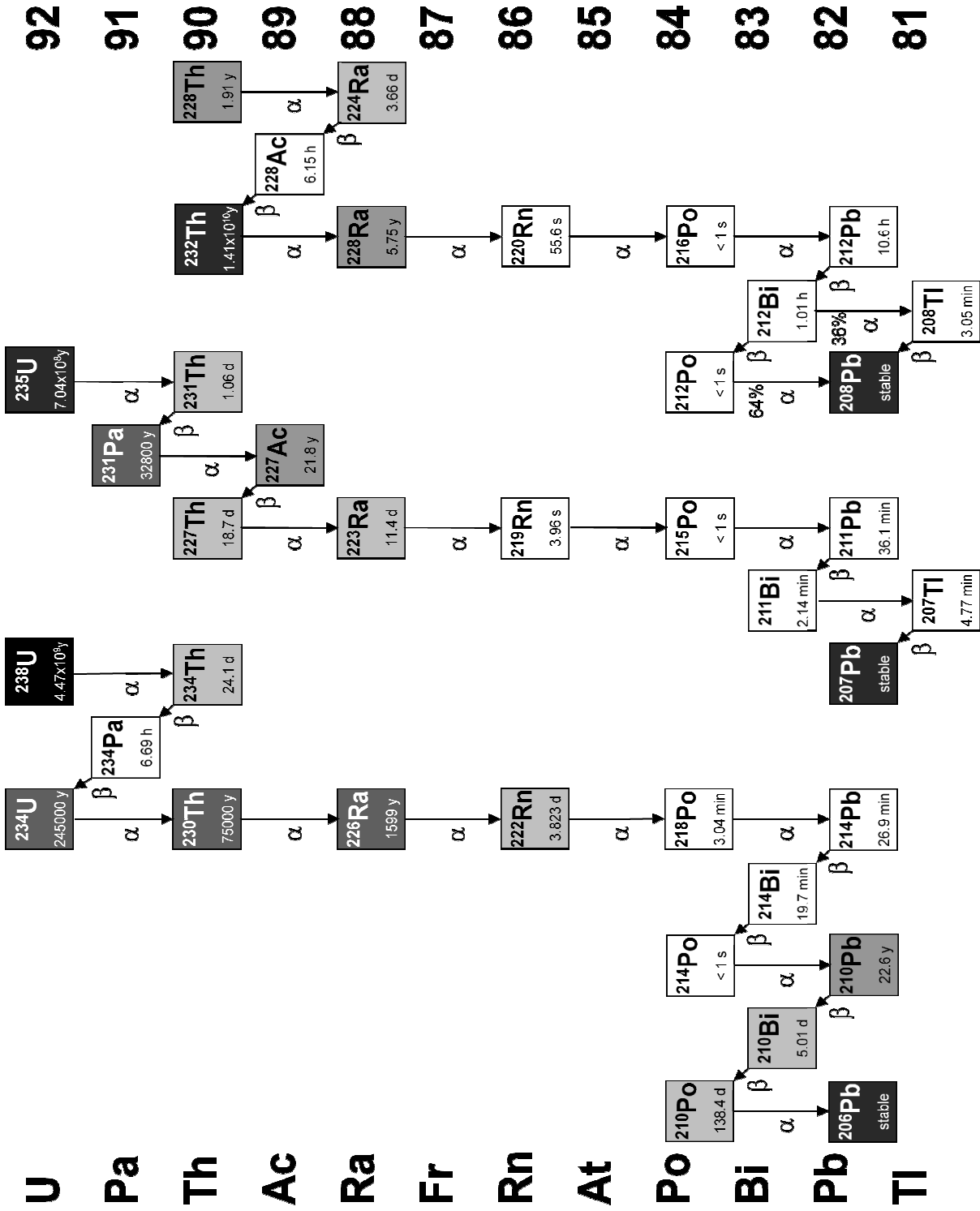
Figure 1.1 Decay series of uranium and thorium.
Darker shades denote longer half-lives. After Bourdon, et. al. (2003)

4

Several studies have identified the occurrence of secular disequilibrium in sediment (Olley et al., 1996, Olley et al., 1997) and archaeological material (Aitken, 1985a). When the environment is restored to a closed system the decay chains will return to radioactive equilibrium gradually over time (a generally stated rule-of-thumb is six half-lives of the daughter (Bourdon et al., 2003)). The dose-rate becomes variable with time and can be found from

$$D = \int_{t=0}^{Age} \dot{D}(t)dt \qquad (1.2)$$

where t is time, D is dose and $\dot{D}$ is dose rate.

The decay chains can be segregated into decay groups (a shorter chain of nuclides where secular equilibrium is present and characterised by a longer-lived nuclide decaying into a number of short-lived daughters) that reflects both the geochemical causes of secular disequilibrium (Bourdon et al., 2003) and the probability that fractionation will be significant before subsequent decay (based on the longevity of the nuclide). Alpha recoil may dislodge nuclides from the mineral matrix and this may lead to preferential mobility of the daughters of alpha decay (e.g. common increase in the activity of ^{234}U compared to ^{238}U in coastal sediments). The extent of fractionation is largely governed by the geochemical behaviour of the nuclide and the environment. A predominant cause of fractionation is due to the precipitation of the soluble uranium salts in the U^{6+} state to the immobile U^{4+} under reducing conditions (Ivanovich and Harmon, 1992). Less soluble daughter nuclides have ameliorated mobility in groundwater (eg. ^{230}Th, with strong absorption properties (Porcelli and Swarzenski, 2003), may be quickly precipitated from ground water) and may exist in secular disequilibrium with the more soluble parent. Another example is radon which exists as an inert gas and its escape by diffusion to the surface will lead to secular disequilibrium of its daughters. The relatively short half-life of radon (up to several days) and the reduced migration of the gas in dry conditions reduce the potential effects of radon loss on dose rate

for sedimentary environments. Olley *et al.* (1996) estimate that for fluvial and lacustrine environments, the dose rate is typically affected by a 5-10% variation due to secular disequilibrium of the decay chains. It is likely that presence of significant secular disequilibrium in sediments is under-reported in the trapped charge dating literature since measurements to determine secular disequilibrium are not made routinely in all cases.

The decay groups presented in this thesis (Table 1.1) are a slightly condensed version of groups discussed by Rosholt (1959) and Murray (1981). The ^{210}Pb $\rightarrow$ ^{206}Pb group has been assumed to be in equilibrium with the ^{222}Rn parent in the ^{238}U series because of relatively short half-life (22 years) of ^{210}Pb, the rapid adsorption of lead onto clay (Murray, 1981) and the relatively low contribution to dose rate from these nuclides (^{210}Pb $\rightarrow$ ^{206}Pb nuclides contribute 2.33% of the dose rate for a sediment containing U = 40Bq kg^{-1}, Th = 40Bq kg^{-1} and K = 600Bq kg^{-1}; see Table 1.2). Another two decay groups that were not included were the ^{220}Rn and ^{219}Rn subdivisions. The migration of ^{220}Rn and ^{219}Rn is largely modulated by their short half-lives (56s and 4s respectively) and only in exceptional circumstances, such as high-porosity pottery with a substantially higher dose rate compared to the sediment, will there be any call for a further investigation. Tanner (1964) suggests that the diffusion range of ^{220}Rn in soil is about 2 cm but this value may be significantly different depending on the physical characteristics of the sediment.

Decay chain parent	Decay group	Parent half-life (yr)
^{238}U	^{238}U $\rightarrow$ ^{234}Pa	(4.468 ± 0.003) x 10^9
	^{234}U	(2.455 ± 0.006) x 10^5
	^{230}Th	(7.538 ± 0.030) x 10^4
	^{226}Ra	(1.600 ± 0.007) x 10^3
	^{222}Rn $\rightarrow$ ^{206}Pb	(1.047 ± 0.000) x 10^{-2}
^{235}U	^{235}U $\rightarrow$ ^{231}Th	(7.038 ± 0.005) x 10^8
	^{231}Pa $\rightarrow$ ^{207}Pb	(3.276 ± 0.011) x 10^4
^{232}Th	^{232}Th $\rightarrow$ ^{208}Pb	(1.405 ± 0.060) x 10^{10}
^{40}K		(1.265 ± 0.013) x 10^9
^{87}Rb		(4.750 ± 0.040) x 10^{10}

Table 1.1 Nuclide decay groups with their respective half-lives.

Dose (in units gray or Gy) is the amount of absorbed energy in a material per unit mass (1Gy = 1J kg^{-1}) and dose rate is the dose absorbed per unit time (for archaeological applications mGy yr^{-1}) (ICRU, 1980). Pedantically, "absorbed energy" refers to the "energy imparted to matter" (Roesch and Attix, 1968) such that over a finite time, absorbed energy is the sum of energies entering a given mass minus the sum of energies leaving the mass and any energy increase in the rest mass. Radiation released during radioactive decay will undergo multiple interactions as it penetrates matter, producing a shower of secondary lower-energy radiations that will themselves interact with the material. Ionising radiation must carry energies higher than 4-25 eV so that valence electrons may escape the atom (Attix, 1986). Three types of radiation arising from terrestrial sources are relevant for trapped charge dating (with the scale that the radiation should be considered in parantheses): "alpha" particles or helium nuclei (tens of microns); "beta" particles or electrons (several millimetres); and "gamma" particles or photons (tens of centimetres). The behaviour of the different radiation has implications for dose rate assessment. Alpha and beta radiations are charged particles and lose their energies incrementally as they traverse a material through many small Coulomb-force interactions. In contrast, gamma radiation follows an exponential attenuation and undergoes a few, large interactions before transferring its energy to fast electrons.

Alpha decay commonly produces a daughter in the ground state, leading to particles of well-defined energy. Alpha particles are massive charged particles with some having emission kinetic energies up to 7.7 MeV. They are heavily ionising over a short distance. In the material to be dated, the core of the track is saturated with charge due to high LET (linear energy transfer) so a significant correction must be applied to relate the total trapped charge signal to dose (Aitken, 1987). For coarse grain dating of minerals such as quartz that are largely inert in alpha activity, the exterior of the grain is typically HF acid-etched prior to measurement to remove the alpha contribution of absorbed dose. This minimises any detrital

contaminants that may be enhanced near the exterior due to the alpha tracks and may reduce the complexity of the dose rate calculation with the subsequent benefit of improved accuracy. Beta particles are emitted with energies up to several MeV but unlike alpha and gamma decays, a continuous spectrum of energies is produced (see Section 2.4.3.) during decay since the energy released from the transformation of a neutron to a proton is shared with a neutrino. Beta radiations follow a convoluted path due to numerous collisions with other electrons. An additional source of electrons may be observed when an excited daughter nucleus releases energy directly to an atomic "internally converted" electron coupled with either associated Auger electron or X-ray emissions. Gamma radiation may have energies up to several MeV and it is emitted as a daughter nucleus de-excites. A number of gamma radiations may be generated according to the transition states occupied by the nucleus. Cosmic radiation that contributes to the dose rate of buried sediments is composed primarily of muons ("hard component") generated from cosmic particles interacting with the atmosphere and a secondary shower of photons/electrons ("soft component") (Hillas, 1972). The soft component penetrates up to about 60cm of typical composition rock or unconsolidated sediment while the hard component is almost completely absorbed for depths greater than about 6m (Prescott and Hutton, 1994).
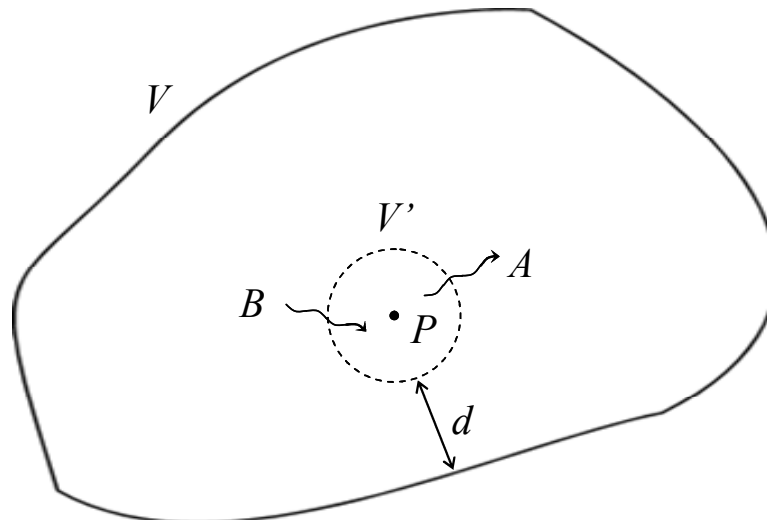
Figure 1.2 Radiation equilibrium existing at a point *P* within an infinite-matrix volume *V*. Energy carried by charged particle *A* out of a small volume *V'* surrounding *P* is equal to the energy of particle B entering *V'*. The distance *d* must be greater than the range of the particles. After Roesch and Attix (1968).

A common assumption that is made in regular dose rate calculations for trapped charge dating is the existence of an infinite-matrix in the sediment (and sample). If an infinite-matrix (IM) is present, it follows that a state of radiation equilibrium is reached where dose rate is uniform throughout the sediment and the absorbed dose at a point is the energy per unit mass emitted from the source. Figure 1.2 illustrates radiation equilibrium where the probability of a radiation *A* carrying a particular energy leaving a small volume *V'* is matched by the probability of a radiation *B* entering *V'* with the same energy. For the purposes of this discussion, there are several conditions (Roesch and Attix, 1968) for the infinite-matrix assumption that need to be satisfied:

1) The atomic composition and density of the sediment is homogeneous.

2) The distribution of radioactive sources in the sediment is homogeneous.

3) The sediment is infinite in extent or at least it continues beyond the effective range of the most penetrating radiation. For beta radiation this range would need to account for the distances associated with the generated bremsstrahlung x-rays.

9

Radiation equilibrium militates against any change in dose rate thoughout a material even if part of the medium is an evacuated cavity. The Fano theorem suggests that dose rate will remain constant across a material of uniform composition but with a density varying in proportion to activity (Fano, 1954). The Fano theorem is only approximately correct but it extends the use of radiation equilibrium into a considerably greater number of sedimentary contexts and applications. Often, the conditions of an infinite-matrix (IM; or IMD for infinite-matrix dose) do not apply for bulk sediments but simple corrections to dose rate can be made if charged particle equilibrium (CPE) is present - that is, when the secondary electron fluence spectrum is constant throughout the material. The energies of gamma emissions are largely transferred to charged particles prior to dose deposition and a localised approximation of dose, called kerma (**k**inetic **e**nergy **r**eleased per unit **ma**ss), can be made in CPE conditions. Since the range of charged particles is considerably smaller than the mean free path of gamma emissions, the photon energy flux does not need to be uniform across the entire matrix (radiation equilibrium) for CPE to exist; only within a region surrounding V' that is greater in extent than the range of the charged particles (i.e. several millimetres).

1.2.2   Evaluation of dose rate
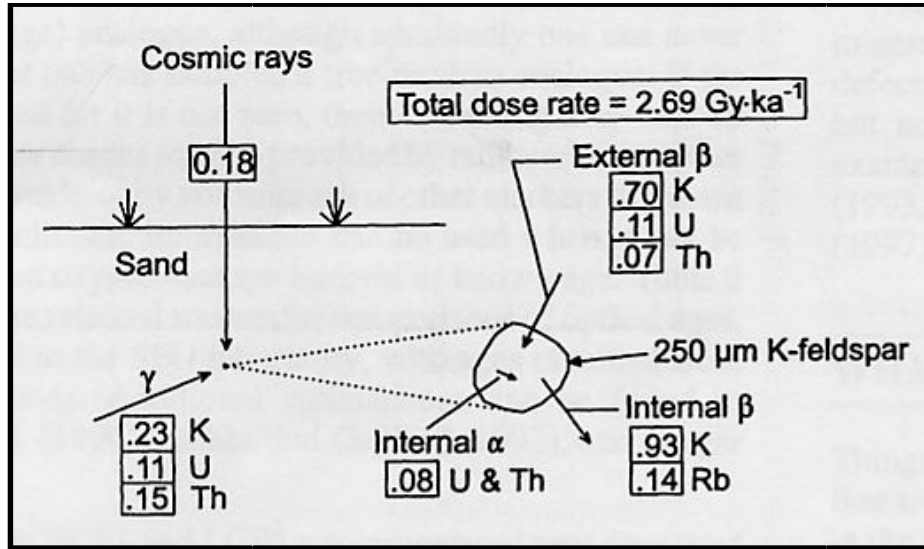
Figure 1.3 Typical sedimentary dose rates (numbers in boxes; mGy a^{-1}).
From Aitken (1985a).

The environmental dose rate

$$\dot{D} = \omega\dot{D}_\alpha + \dot{D}_\beta + \dot{D}_\gamma + \dot{D}_c \qquad (1.3)$$

is commonly expressed (Aitken, 1985a) as a linear combination of alpha, beta, gamma and cosmic dose rates respectively (some with internal and external components) where we have used here ω to represent the fraction of the alpha dose rate contribution that generates the equivalent trapped charge signal as identical beta/gamma dose rates. There are several methods available to calculate the alpha correction specific for the sample; ω may be evaluated as the k-value (Zimmerman, 1971); the a-value (Aitken and Bowman, 1975); the b-value (Bowman and Huntley, 1984); and S-value (Valladas and Valladas, 1982). The latter three methods are numerically related (Aitken, 1985b) and they are largely energy independent in contrast to the k-value system (Aitken, 1985a). The b-value (=13 multiples of the a-avalue or 10^{-6}S if b is in units Gy μm^2) is defined as

$$b = \frac{\text{trapped charge signal / unit alpha track length / unit volume}}{\text{trapped charge signal / unit absorbed beta dose}} \qquad (1.4)$$

11

Nuclide[s]		Energy release per parent disintegration (MeV)	Dose rate per unit specific activity of parent isotope (μGy a^{-1} per Bq kg^{-1})
Natural uranium			α 216.485 ± 0.862 β 11.325 ± 0.107 γ 8.721 ± 0.156
^{238}U series	^{238}U → ^{206}Pb	α 42.872 ± 0.178 β 2.283 ± 0.022 γ 1.774 ± 0.032	α 216.762 ± 0.900 β 11.544 ± 0.111 γ 8.968 ± 0.163
	^{238}U → ^{234}Pa	α 4.191 ± 0.177 β 0.886 ± 0.019 γ 0.029 ± 0.032	α 21.191 ± 0.896 β 4.480 ± 0.094 γ 0.144 ± 0.160
	^{234}U	α 4.759 ± 0.009 β 0.012 ± 0.000 γ 0.002 ± 0.000	α 24.064 ± 0.045 β 0.060 ± 0.001 γ 0.008 ± 0.001
	^{230}Th	α 4.664 ± 0.015 β 0.013 ± 0.001 γ 0.001 ± 0.000	α 23.582 ± 0.075 β 0.066 ± 0.004 γ 0.007 ± 0.001
	^{226}Ra	α 4.774 ± 0.003 β 0.004 ± 0.000 γ 0.007 ± 0.000	α 24.140 ± 0.017 β 0.019 ± 0.000 γ 0.037 ± 0.001
	^{222}Rn → ^{206}Pb	α 24.482 ± 0.001 β 0.516 ± 0.012 γ 1.735 ± 0.006	α 123.784 ± 0.003 β 6.920 ± 0.059 γ 87.504 ± 0.032
^{235}U series	^{235}U → ^{207}Pb	α 41.624 ± 0.226 β 1.295 ± 0.027 γ 0.661 ± 0.010	α 210.454 ± 1.145 β 6.5462 ± 0.1343 γ 3.3432 ± 0.0487
	^{235}U → ^{231}Th	α 4.339 ± 0.165 β 0.186 ± 0.019 γ 0.207 ± 0.005	α 21.941 ± 0.833 β 0.939 ± 0.098 γ 1.046 ± 0.027
	^{231}Pa → ^{207}Pb	α 37.284 ± 0.155 β 1.109 ± 0.018 γ 0.454 ± 0.008	α 188.513 ± 0.785 β 5.608 ± 0.092 γ 2.297 ± 0.040
Thorium series	^{232}Th → ^{208}Pb	α 35.946 ± 0.109 β 1.339 ± 0.028 γ 2.322 ± 0.007	α 181.744 ± 0.549 β 6.7680 ± 0.1414 γ 11.7395 ± 0.0371
Potassium	^{40}K	β 0.499 ± 0.001 γ 0.156 ± 0.003	β 2.526 ± 0.004 γ 0.787 ± 0.014
Rubidium	^{87}Rb	β 0.082 ± 0.001	β 0.413 ± 0.003

Table 1.2. The energy released during decay and dose rate per unit activity for each decay group. Based on ENSDF data January 2002.

Elemental concentration	Activity (Bq kg^{-1})
U (1 ppm)	12.918
Th (1 ppm)	4.0579
K (1 %)	277.79
Rb (1 ppm)	0.9058

Table 1.3. The conversion factors for parent nuclide concentrations to activity

with the assumption that the signal intensity is near constant along the track length (Lyons, 1988). A well-known example of sedimentary dose rates is presented in Figure 1.3 illustrating the relative dominance of the beta dose rate and lithogenic potassium-40 contributions.

The infinite-matrix (IM) sediment dose rate from radioactive sources is derived using

$$\dot{D}_{\alpha,\beta,\gamma} = \left(\sum_P A_P E_P \right)_{\alpha,\beta,\gamma} \tag{1.5}$$

where $\dot{D}_{\alpha,\beta,\gamma}$ is the dose rate of either alpha, beta or gamma radiations respectively, A_P is the activity of the parent of the decay group or series, and E is the total alpha/beta/gamma energy released in the decay group or series per parent decay. The most recent description of energies and intensity of particles associated with nuclide decay and their half-lives can be extracted from the Evaluated Nuclear Structure Data File (ENSDF) database published by the Brookhaven National Laboratory, USA (www.nndc.bnl.gov). All data used in this thesis were downloaded on 16 January 2002). Table 1.2 gives the relevant data required to find the dose rate using specific activity measurements while Table 1.3 allows the conversion of elemental concentrations into parent activities (For example, sediment with 1 ppm natural U would have an infinite-matrix beta dose rate of (12.918)(11.325 ± 0.107) giving 0.146 ± 0.001 mGy a^{-1}). The values presented in these tables are similar to Adamiec and Aitken (1998) with the notable exceptions of a 1.6-2.1% increase in the alpha energy release for the majority of nuclide decays, a 1.2% decrease in the average beta energy of the ^{231}Th decay and decreases of 3-4 keV in the gamma energy release of ^{214}Bi and ^{223}Ra. The cosmic dose rate can be found from an analytical expression (Prescott and Hutton, 1994) that includes average burial depth during deposition, overburden density, latitude and altitude of the site and long-term correction for changes in the geomagnetic field.

Two correction factors to the environmental dose rate, the water content and the beta absorption in coarse grains, are commonly applied (Aitken, 1985a) and these will be discussed further in Chapters 4 and 5. The water content correction accounts for the difference expected between the IM dose rate in a wet burial environment and the IM dose rate of dry sediment measured in the laboratory. The correction is employed in different weightings depending on the type of radiation such that

$$\dot{D}_{\alpha,\beta,\gamma} = \frac{\left(\dot{D}_{\alpha,\beta,\gamma}\right)_{dry}}{1 + x_{\alpha,\beta,\gamma} \dfrac{m_w}{m_s}} \tag{1.6}$$

where $\dot{D}_{\alpha,\beta,\gamma}$ and $\left(\dot{D}_{\alpha,\beta,\gamma}\right)_{dry}$ are the wet and dry dose rates respectively for alpha, beta and gamma radiation, $x_{\alpha,\beta,\gamma}$ is the ratio of the efficiency of energy absorption for water to sediment (stopping powers for alpha and beta radiation; absorption coefficients for gamma radiation), and m_w / m_s is the ratio of the mass of water to the mass of dry sediment. The commonly used values of $x_{\alpha,\beta,\gamma}$ are 1.50 for alpha, 1.25 for beta and 1.14 for gamma radiations (Zimmerman, 1971). The beta coarse grain correction (Mejdahl, 1979), c_β, accounts for the difference in dose rate delivered from sources only outside or inside the grain to the IM dose rate. The correction, where

$$\left(\dot{D}_\beta\right)_{grain} = c_{1\beta}\left(\dot{D}_\beta\right)_{IM} + c_{2\beta}\left(\dot{D}_\beta\right)_{internal} \tag{1.7}$$

varies with grain size and decay group/series and it is greater than 0.85 for the external correction in grains smaller than several hundred microns.

	Shale	Sandstones	Carbonates	Igneous Rocks
K (%)	2.66	1.07	0.27	2.59
Rb (ppm)	140	60	3	90
Th (ppm)	12	1.7	1.7	9.6
U (ppm)	3.7	0.45	2.2	2.7

Table 1.4 The abundance of key radioactive elements in typical major sedimentary
rock types and an average value for igneous rock.
From Turekian and Wedepohl (1961).

The average natural abundance of potassium, rubidium, thorium and uranium in sediments (Turekian and Wedepohl, 1961) are presented in Table 1.4. In practice, the distribution of radioactive minerals in the environment is highly variable over a number of spatial scales and considerations such as the underlying geology of the region and the mineral fractionation that may have occurred during transport and deposition should be included. Several methods are commonly employed to estimate the contributions to dose rate of uranium, thorium and potassium (and less frequently rubidium). Perhaps the most intuitive approach is the use of *in situ* dosimeters placed at representative sample locations within the sediment for a sufficient length of time, often months, for adequate beta/gamma dose rate exposure. The dosimeters – usually CaF_2 or Al_3O_2:C – are encased in a light-shielding cover that may shield beta radiation either partially or fully depending on its thickness. In both cases, some form of correction must be made to the absorbed dose in the dosimeter to determine the corresponding gamma dose rate of the environment (Aznar et al., 2003). A different method of dose rate measurement is by spectrometry where ionising radiation produces photons during passage through a scintillating material which are subsequently detected usually by a photomultiplier tube. The resulting energy spectrum after calibration gives the total activity of the sample and it can be deconvolved into separate decay group activities depending on the dynamic range (e.g. efficiency, resolution, and peak-to-Compton ratio) of the instrument (Gilmore and Hemingway, 1995). High-resolution gamma spectrometry with a germanium scintillation

crystal provides sufficient definition to determine decay group activities for secular disequilibria estimation. Sodium iodide scintillation spectrometers are more readily used in the field since they operate at room temperature. The spectrometer head can be inserted directly into the holes in the sediment where samples were extracted and a precise estimate of the gamma contributions from each of the decay series can be found. Thick-source alpha counting using zinc sulphide scintillation screens is a well-established technique for uranium and thorium activity measurements (Aitken, 1985a). However, the relative inefficiency in achieving precise estimates of thorium activities using the "slow pair" emissions of ^{220}Rn and ^{216}Po (~3% of counts) militates against a large throughput of samples for high-resolution dose rates. Beta scintillation spectrometry and counting is also used but less frequently. A different approach to dose rate determination is the measurement of nuclide concentrations. Radioisotope concentrations are commonly measured (Pollard and Heron, 1996) using instrumental neutron activation analysis or inductively coupled plasma mass spectrometry. Neutron activation analysis makes measurements of characteristic gamma emissions after a neutron capture reaction or after subsequent radioactive decay. Mass spectrometry methods estimate concentrations of nuclides directly and therefore only the long-lived isotopes are measured. Other analytical techniques include atomic absorption, X-ray fluorescence and flame photometry (potassium only). The accuracy of all the above measurement techniques is largely dependent on the equipment and protocols used and it is likely to be ±2-5% or worse.

Water content is measured either directly from the sample or from associated material. The sample is sieved prior to trapped-charge measurement and grain size bounds of the dated sub-sample are usually significantly constrained in terms of the beta dose rate attenuation correction. For the calculation of the cosmic dose rate, the depth, and position of the sample must be estimated in the field (density can be found in the laboratory).

1.2.3   Further comments

The dose rate assumption of radiation equilibrium is used for a homogeneous body. However, different forms of heterogeneities may exist in sediments which militate against the universal adoption of radiation equilibrium, for example from grain coatings to large boulders and from high activity mineral grains to coarse stratigraphic variations in radionuclide content. The nature of trapped-charge dating often means these differences often can only be inferred since the exact radiation environment of each of the dated grains in a matrix is not easily recorded and larger structures may be missed when collecting sediments for laboratory-based dose rate determination. All is not lost, as we expect the perturbations of the integrated dose rate from the measured values to be small in most cases. However, it is necessary to have a clear understanding of the sensitivity of the heterogeneities on the dose rate. Since the dose rate computation treats alpha, beta and gamma radiations independently, the validity of the dose rate estimation needs to be determined for each type of primary radiation and secondary particles.

1.3   Scope of this thesis

This thesis addresses the estimation of beta and gamma dose rates after measurements of activity or elemental U, Th, K have been made, with a particular focus on several issues that arise with trapped charge dating due to heterogeneities in the regolith. Numerical modelling is used for exploring the effect of different sedimentary conditions on dose rate. The approach has focused on numerical modelling instead of insights through experimental studies. This was for three primary reasons: 1) radiation transport models are very flexible and a wide diversity of situations can be investigated relatively quickly; 2) numerical modelling often achieves more accurate results for specific situations since the codes are well benchmarked and exact environments can be constructed; and 3) the use of

radioactive materials required specialist facilities. The experimental validation of the modelled results was not made. Although desirable, experimental corroboration was not essential since: 1) the numerical models used in this thesis fit reasonably comfortably within the design physics of the codes and therefore already is implicitly tested by a wealth of experimental evidence from other workers; and 2) most of the thesis deals with subtle differences in dose rate which would be masked by experimental uncertainty. Alpha dosimetry and the cosmic dose rate have not been included in this thesis.

Chapter 2 provides a scaffold of methodology and data which is subsequently used in numerical modelling of the beta and gamma dose rate. Chapter 3 presents various simulated granular sediments that are used as geometrical inputs into the models. Chapters 4 and 5 deal with the standard correction factors of water content and beta attenuation through coarse grains respectively. These corrections are regularly used by the trapped charge dating community and require careful calculation to reduce systematic uncertainties. Chapter 6 details work done on evaluating dose rates associated with hominid fossil skull contexts where geometric considerations become important.

Throughout this thesis, the terms dose and dose rate are used somewhat interchangeably, according to the appropriate context. Where the results are given as a ratio of the infinite-matrix dose or infinite-matrix dose rate (IMD), the ratio is a dimensionless quantity (Gy/Gy or Gy/a / Gy/a) and both forms give identical results.

Chapter 2: Monte Carlo modelling of
beta and gamma dose rates

"The generation of random numbers is too important to be left to chance."

Robert R. Coveyou

"Anyone who considers arithmetic methods for producing
random digits is, of course, in a state of sin."

John von Neumann

2.1   Introduction

Numerical modelling is well suited to the study of environmental dose rate since the physical system can be investigated in a controlled and diverse way. The wide variety of sedimentary contexts where accurate dose rate estimation is essential requires an approach that can test the sensitivity of a large number of relevant parameters where a homogeneous infinite-matrix sediment does not exist. Therefore, a general-purpose radiation transport code offers the flexibility to quickly and robustly provide dose rate solutions in many complex environments.

Radiation transport is described by the Boltzmann equation that expresses that the number of particles in a mass is dependent on: i) particles flowing through bounding surfaces; ii) collisions in the mass; and iii) sources in the mass. The validity of the modelled results is subject to the assumptions and simplifications implicit in the model and the robustness of the algorithms used to solve the transport problem. Radiation transport modelling can be split into two main groups. Firstly, deterministic methods attempt to solve the Boltzmann transport equation in the entire phase space of the model using terms that include derivatives of time and space. The most common of these is the discrete ordinates approach (Price, 2000), which evaluates the average behaviour of radiation moving through a modified geometry. Although

highly efficient for simple problems, the method may quickly become computationally very expensive for high-resolution three-dimensional models. A different type of technique to model radiation transfer is based on stochastic principles, the so-called Monte Carlo (MC) method (National Bureau of Standards, 1951). No transport equation is explicitly solved but rather the average behaviour of the system is revealed via the Central Limit Theorem by simulating the passage of a large population of individual particles through a defined environment. In effect, Monte Carlo approaches yield the same solution of the transport equation (Berger, 1963) but the problem can be deconstructed into simpler forms and they can be more generally applied. Random sampling of tabulated data determines the location and type of interactions the particles undergo as well as the outcome. Any information that the radiation transport generates must be specifically requested and logged during each particle history but the process is capable of supplying a reconstruction of a complete history of a particle. Since MC calculations are amenable to complex, three-dimensional radiation transport problems, the approach was favoured for the work presented in this thesis despite the well-known limitations of slow convergence.

This chapter will deal with the methodological issues arising from the application of Monte-Carlo methods to assess dose rate. Initially a brief explanation of the mechanics behind the MC approach is made for electron and gamma radiations. This is coupled with remarks about the suitability of the technique for the requirements of this thesis and some evidence for the validation of the transport codes used. The second half of the chapter will present the implementation details for the MCNP and PENELOPE codes.

2.2 Monte Carlo radiation transport

2.2.1 Introduction

The MC method is closely analogous to experimentation – a scenario is constructed, the experiment is allowed to run, and the results collated – since complete knowledge of the

system is not required and the precision is related to the number of trials. Three-dimensional high-resolution Monte Carlo models differ in the implementation of the transport algorithms but their general structure is reasonably consistent. A model is inputted into the code stating the geometry, associated material composition, the characteristics of the particle source, and auxiliary administrative information such as the number of particle histories and energy cutoff values. The Monte Carlo approach uses a sequential collection of random walks (see Figure 2.1) to generate a life history of a particle and all its progeny. A random walk is a Markov chain of stochastic events describing the passage of a particle through a material. Each step in the random walk can be related to behaviour of the particle in reality and, importantly, there is no dependence on any previous steps. The basis of the calculations is the database of differential cross sections that are used to generate probability distribution functions determining mean free path, type of interaction, the energy loss and angular deflection in an event as well as possible secondary particle production. The models are initialised for each primary particle with a sampled location, velocity and weight (reflects the contribution that the particle will make when scored). The model follows the history of each particle, whether primary or secondary, until they either fall below a specified energy or exit the geometry. The results are tallied across specified regions. This information may include energy loss and/or energy flux but it can be extended to virtually any behaviour found in the model, if required.
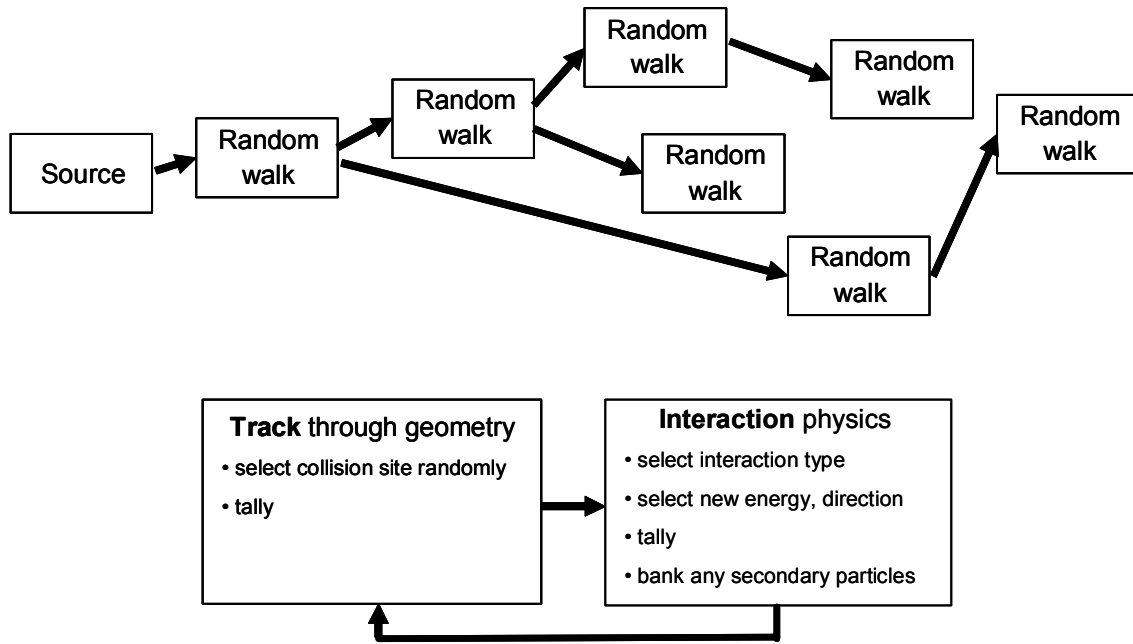
Figure 2.1. Top: Monte Carlo transport of a particle and its progeny through a material. Bottom: A step in a random walk. After Booth (2005).

The development of Monte Carlo methods in radiation transport problems has its origin with atomic weapons research in the 1940's. With the advent of electronic computers, the technique became available for routine calculations. Most "state-of-the-art" general purpose (e.g. radiotherapy, nuclear reactor) Monte Carlo modelling codes for beta and gamma radiation transport (e.g. MCNP, EGS, ITS, PENELOPE, GEANT) all share similar characteristics: the ability to model complex physical systems; the treatment of particle interactions; the scoring of particle properties; and the setting of physical constraints. Each code has specific advantages, whether ease of use, generality, and/or improved physics. It is beyond the scope of this thesis to discuss in detail the physics involved in electron/photon transport modelling – that would only be appropriate in a more theoretical study. However, all the above codes can be described as following best practice, although there remain several important differences in their approaches to solving the physical system, and these will be discussed where appropriate. MCNP4C (Briesmeister, 2000), and more recently MCNP5 (X-5

Monte Carlo Team, 2003), were the favoured codes for the study of environmental dose rate as they were found to be versatile for modelling three-dimensional structures with complex sources, well documented and widely used. Previous experience of using ITS, which is similar to MCNP, was useful. The PENELOPE suite of codes (Salvat et al., 2006) has been developed over several decades but a recent restructuring of the package has seen the software gain increasing cachet. The code boasts accurate electron/gamma shower modelling down to 100eV and the PENELOPE code (2001 to 2006 versions) is used as a benchmark in this thesis. However, this package is not as flexible as MCNP, especially having no in-built facility for three-dimensional sources, and therefore it is only used where easily implemented or after code modifications.

It should be noted that MC methods can optimise the precision of the simulation by increasing the number of particles run. The accuracy of the computation, therefore, often rests with two types of systematic uncertainties (Siebert, 2000): a) the quality of the implementation of the physics; and b) the input of the problem. Since this thesis is mainly focused on dose rate estimation in simulated environments rather than real contexts, the input terms for the geometry and materials are exact. Remaining uncertainties involve the radiosource spectra, the interaction databases and the interaction algorithms.

2.2.2   Beta radiation

In coupled electron/gamma models, electron transport computation is significantly more expensive than for gamma radiation due to the comparatively large number of interactions involved. Some 100,000 charged-particle interactions occur during the slowing down of a 0.5MeV beta particle to 0.06MeV compared to only several interactions for an equivalent gamma particle (X-5 Monte Carlo Team, 2003). An example of electron tracks is shown in Figure 2.2. The very high collisional cross-section exists due to the long-range nature of Coulomb interactions. Implementation of electron transport by analogue simulation of

individual interactions (see Figure 2.3) over macroscopic distances becomes problematical if a large number of histories is required. The formulation of a "condensed history" approach attempts to bridge this difficulty by combining many collisions using multiple scattering probability distributions. The path of the particle is divided into electron steps that contain the basic unit of condensed histories. The step size is a trade off between various assumptions (Briesmeister, 2000) used in the calculations (e.g. sufficiently large number of interactions; mean energy loss is small) and computational efficiency. In a seminal paper, Berger (1963) discusses the technique and resolves two main approaches into class-I algorithms (representing codes based on the ETRAN implementation (Seltzer, 1991) including more recent versions of MCNP) and class-II algorithms (including EGSnrc (Kawrakow and Rogers, 2001) and PENELOPE).
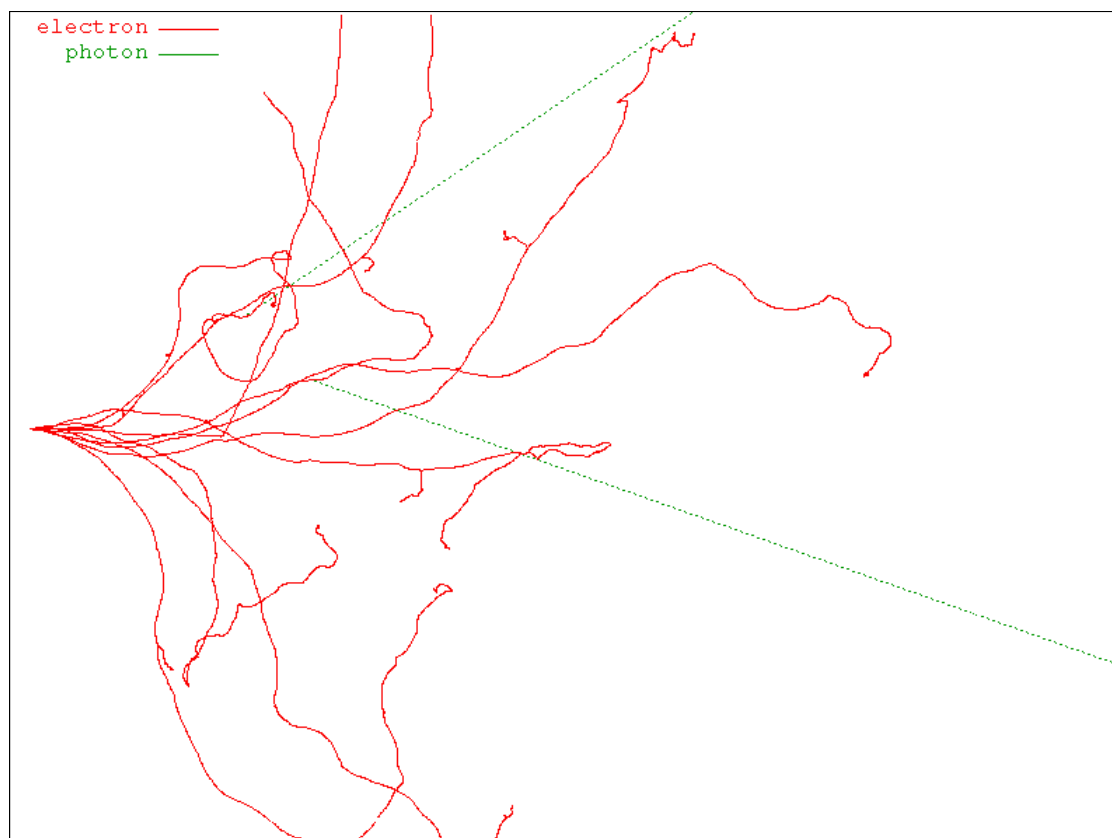
Figure 2.2. Ten 1MeV electrons incident on quartz ($\rho = 2.65g\ cm^{-3}$). The red solid tracks represent the slowing down of electrons until 100eV and the green dotted lines represent bremsstrahlung emissions. The simulation uses the SHOWER code which is based on PENELOPE Monte Carlo algorithms. The thickness of the quartz (horizontal dimension) is 2.5mm.

The MCNP system determines the energy loss, with a direct estimate of energy straggling, by the Landau distribution (Landau, 1944) using the binding effect modifications of Blunck and Leisegang (1950). Angular multiple scattering is treated exactly using the Goudsmit-Saunderson distribution (Goudsmit and Saunderson, 1940). The Goudsmit-Saunderson distribution is not amenable to rapid, accurate computation – especially for short pathlengths due to slow convergence (Berger and Wang, 1988) – and is pre-calculated using an energy grid such that 8.3% of the energy of the electron is lost during each step. A shortcoming of using the Goudsmit-Saunderson distribution is the decoupling of the primary electron and secondary particle production with knock-on electrons and bremsstrahlung photons produced at the end of the electron step. The energy step is further divided into substeps in an attempt to improve the description of the trajectory of the electron (ie. curved rather than angular). Despite improvements in efficiencies that are yielded by tabulated data, errors are introduced in situations where the energy of the particle does not conform to the energy grid and interpolation is required. This is particularly relevant during the electron step approaching interfaces in a model where the distance to be traversed is poorly matched to the pathlengths of the pre-defined energies of the substeps. Schaart *et al.* (2002) have shown marked improvement in the accuracy of dose scoring in problematic geometries if the interpolation follows the ITS method (uses the nearest energy group) as opposed to the MCNP default option (uses energy indexing to the centre of the energy group). Chibani and Li (2002) found that the performance of ITS indexing is clearly superior in high-Z media with fast electrons but 10% discrepancies between ITS style indexing and the default may occur for dose profiles in other contexts.
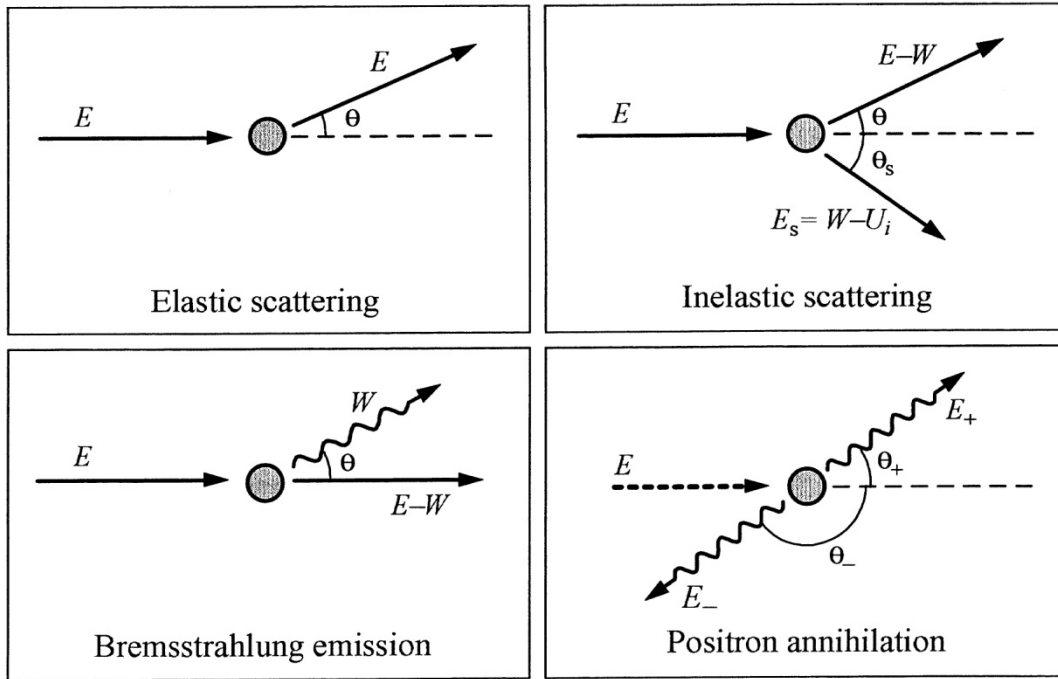
Figure 2.3. The main interactions that an electron may undergo during
passage through a material. From Salvat *et al.* (2006).

The PENELOPE code, which arguably contains the most accurate condensed history beta particle transport algorithms of the major codes (Cobut et al., 2004), maintains physical accuracy of electron transport down to around 100eV according to its authors. PENELOPE uses a class-II, mixed condensed history algorithm that partitions the treatment of hard and soft interactions. Hard interactions are infrequent catastrophic events leading to large energy loss and/or track perturbation and they are individually treated in detail. Between these events, soft interactions can be collectively simulated using condensed history algorithms. User defined energy loss or deflection cutoff parameters that separate hard and soft interactions are kept relatively small to reduce the contribution of the soft component on the transport but high enough to maintain an acceptable level of computational efficiency. The theory of multiple scattering for the soft elastic and inelastic collisions is a transformed and simplified version of the Goudsmit-Saunderson distribution where the computation is relatively straightforward and dependent on slowly varying differential cross-sections. The

"random-hinge" mechanism (Fernández-Varea et al., 1993) is used to link angular deflection and translation so that a particle travels a random distance before a soft scattering event is sampled before it continues along the new trajectory for the remainder of the step. Any step crossing an interface is stopped and resumed in the new material. Salvat *et al.* (2006) argue that a mixed simulation should be favoured over purely condensed history schemes due to improved track behaviour and simulation of particle transport near interfaces.

2.2.3   Gamma radiation

Since photons have no electric charge, far fewer interactions occur along the path of the particle compared with electrons. An example of photon tracks is shown in Figure 2.4. During the passage of gamma and x-ray radiations through matter (see Figure 2.5.), photons are either absorbed with subsequent charged particle emissions and/or scattered but the extent is dependent on large statistical fluctuations. This makes the numerical simulation of photon transport amenable to a detailed analogue treatment of each interaction using Markov processes. The three main competing mechanisms are the photoelectric effect, Compton scattering and pair production. Coherent (Rayleigh) scattering is less important but it is also included in most high-resolution MC codes. Figure 2.6 show the dominant interaction for different energies and media. The photoelectric effect is the process of the ejection of a bound electron from an atom due to the complete absorption of an incident photon with most of the photon energy transferred to the electron and most of photon momentum given to the positive ion. Eviction of electrons from the innermost shell is common since the binding energies are often less but closest to the photon energy. The probability of a photoelectric interaction occurring is heavily weighted to the atomic number of the absorbing material (approximately Z^4) and to low-energy photons of less than around 100keV. The Compton process is a photon interacting with a "free" electron that has an insignificant binding energy compared to the energy of the photon. During the interaction, part of the energy and momentum of the photon is transferred to the electron, with the photon exiting with a lower energy and deflected

direction. The photon scattering is biased to a forward direction with increasing incident photon energy and relatively less energy is imparted to the recoil electron. The probability of a Compton interaction occurring is proportional to the atomic number of the absorbing material. Pair production is the process of the substitution of a photon incident on the Coulomb field of the nucleus with a positively and negatively charged electron pair. Although the minimum energy requirement of the photon is 1.02MeV, which corresponds to twice the rest mass of an electron, the process only dominates above photon energies available from typical lithogenic radiosources. The probability of a pair production interaction occurring is proportional to the square of the atomic number of the absorbing material.
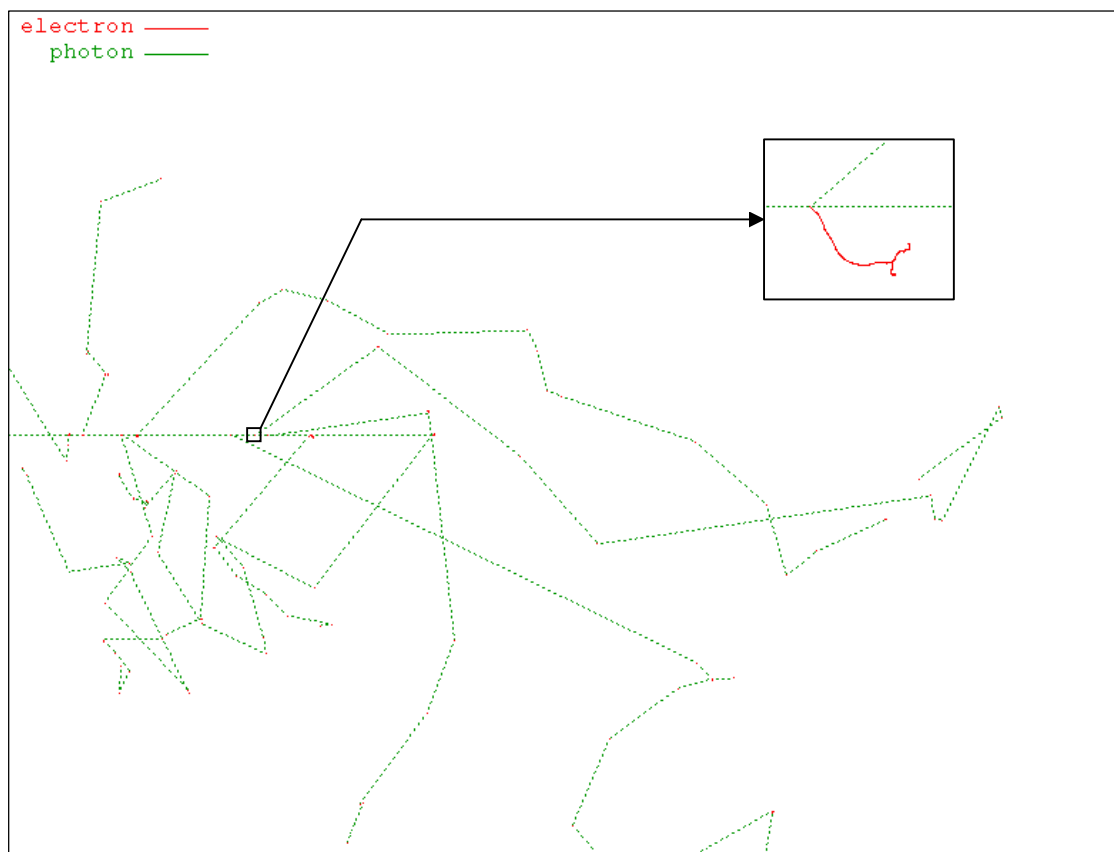
Figure 2.4. As for Figure 2.2. but for incident photons modelled down to 100eV. The thickness of the quartz is 40cm. The inset picture is for an initial (beamline) collision showing the generation of a primary (and secondary) electron.
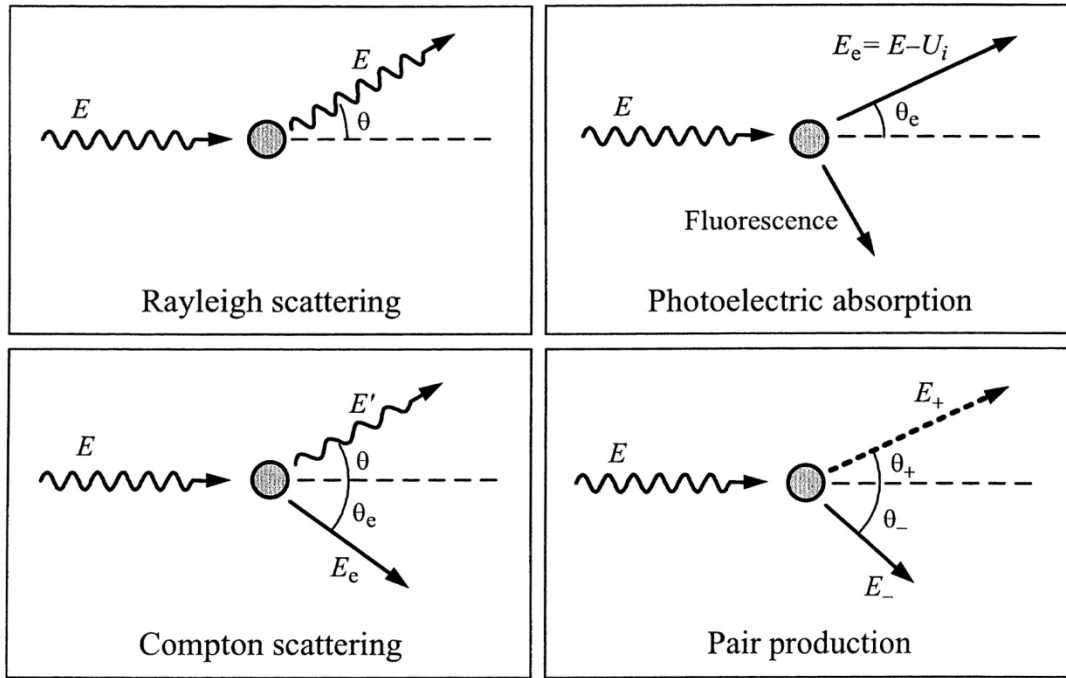
Figure 2.5. The main interactions that a photon may undergo during passage
through a material. From Salvat *et al.* (2006).
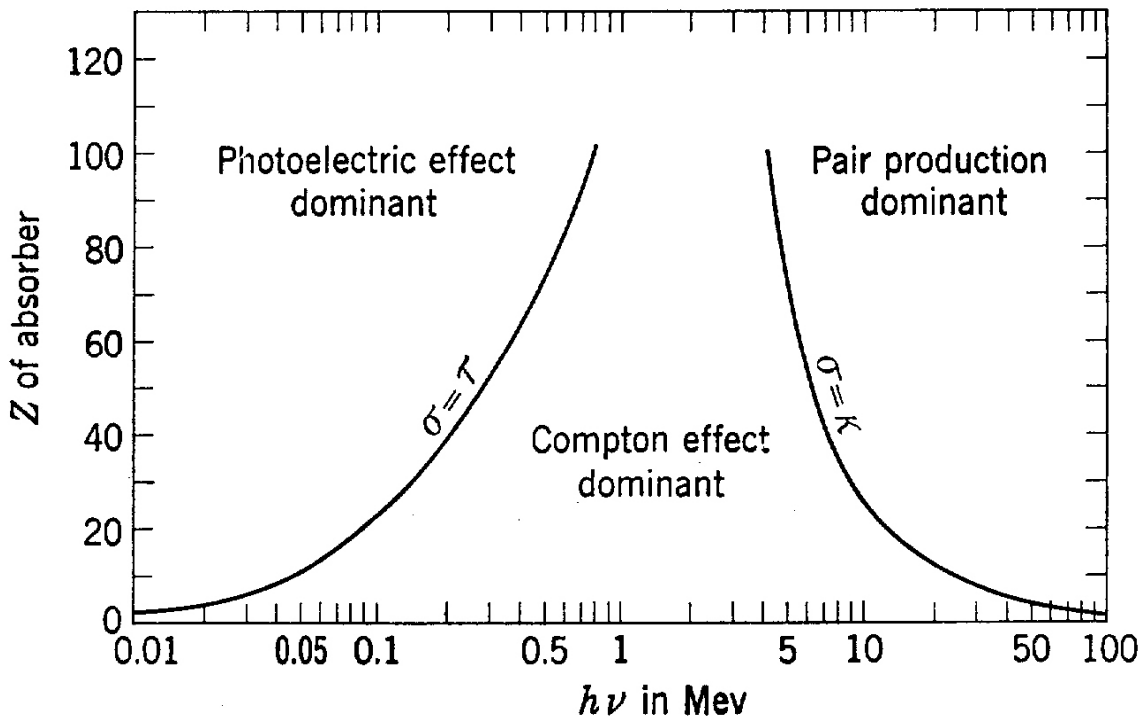
Figure 2.6. The relative contributions of different interactions. From Evans (1955).

Versions of MCNP and PENELOPE used in this thesis both implement a detailed treatment of photon transport using similar algorithms. The Klein-Nishina formula (see Evans (1955)) for Compton energy loss is modified to include Doppler broadening where the atomic electrons have a momentum distribution. Emissions of fluorescent photons and Auger electrons are included in the simulation. PENELOPE uses the EPDL97 database (Cullen et al., 1997) for photoelectric absorption and XCOM (Berger and Hubbell, 1987) is used for pair production cross sections. Compton and Rayleigh mean free paths are computed using revised differential cross-sections that account for Doppler broadening. The data are significantly different from XCOM for energies less than 50keV (Zaidi, 2000). MCNP can be paired with photon databases derived from EPDL97 after 2002 (0.04p ACE identifier) or updated libraries that are based on the 1982 standard ENDF/B-IV.

2.3. Validity of Monte Carlo codes

2.3.1. Introduction

The validation of a radiation transport code is invariably a trade off between comparing simulations with other codes and experimental data. Since all experimental results have some form of systematic bias and codes share many similar algorithms, it becomes a difficult to ensure that some circularity of argument does not exist.

However, in this section, a broad array of studies using a significant number of different experimental measurements from different laboratories is presented to assess the validity of MCNP and PENELOPE. Any conclusions rely on the interpretations of each author since the investigation and quantitative analysis of each experimental result is beyond the scope of this thesis.

It should also be noted that some validation tests are more sensitive than others. For example, depth-dose profiles, the key information that is required in this thesis, represent relatively

robust markers compared to electron backscattering, which subtly examines the interplay between angular deflections and energy loss.

2.3.2.   Recent case studies

Sempau *et al.* (2003), some of whom are authors of the code, comprehensively reviewed experimental benchmarks for PENELOPE. A series of comparisons of electron backscattering and transmission simulations with fourteen measurement datasets all convincing agreed to within experimental error. Similarly, depth-dose and radial dose distributions show close agreement with several experimental results apart from higher energy electrons (1MeV), which had discrepancies of several percent near the peak dose against one set of measurements. Thick-target bremsstrahlung spectra were studied in several different contexts and any significant differences to experimental data was explained as either subtraction of parts of the spectra by the experimentalists or high measurement uncertainty.

Chibani and Li (2002) investigated the validity of electron and photon simulations using the GEPTS, EGSnrc and MCNP codes. Experimental results (Lockwood et al., 1980, Wall and Burke, 1974) of depth-dose profiles in homogeneous and heterogeneously layered media are used as a benchmark standard. Electron beams of 0.5MeV and 1MeV were modelled in uniform beryllium, molybdenum and uranium and the dose profiles were obtained with approximately 60 slabs. The GEPTS, EGSnrc and measurements were in very close agreement, while MCNP showed some variation with a higher peak and reduced deposition for greater depths. Chibani and Li find that the ITS-style energy indexing is slightly inferior to the default setting for beryllium but preferred for transport in heavier elements. For the multilayer media, MCNP with ITS indexing, GEPTS and EGSnrc each accurately predicted the measured dose profiles but MCNP using the default energy indexing underestimated the dose in high-Z material in the middle of the slab. Photon dose simulations were benchmarked using parallel plate ionization chambers where the ends could be fitted with different foils and

dose measured through the instrument. All the codes modelled the depth-dose profiles within several percent for aluminium at depths greater than 0.05g cm^{-2} but they significantly underestimated dose near the interface by some 5%.

Das *et al.* (2002) reported the consistency between EGS4 and PENELOPE simulations and measured values for both backscatter and forward dose perturbation factors near the interfaces of thin high-Z materials embedded in water. The agreement between modelled results and the experimental measurements from ^{137}Cs photon with 0.1mm thick lead was close for backscatter but unreliable for the forward dose perturbation profile, particularly for EGS4. Significant differences were found for the modelled dose perturbation factors and PENELOPE for 100-300kV photon beams, although less so for the higher energy beams, which the authors explain in terms of experimental inaccuracies and/or unattributable reasons.

Cobut *et al.* (2004) simulated electron tracks of 1keV and 4MeV particles through thin slabs for a) a detailed purpose-built code that assesses individual interactions; b) PENELOPE; and c) experimental observations of electrons incident on silicon (Singh, 1969) and aluminium (Rester and Derrickson, 1971, Nakai, 1963). The angular distributions and energy spectra were in good agreement although PENELOPE was found to overestimate transmission by several percent for particles that travel at an angular deflection of <40° relative to the incident direction in silicon. The depth-dose profiles within aluminium were well matched (to within ±5%) with PENELOPE slightly underestimating dose up to the peak energy deposition and overestimating dose at greater depths.

Benedito *et al.* (2001) compared angular distributions of high-energy electrons backscattered by aluminium or gold generated by PENELOPE to experimental findings of Tabata (1967). They reported excellent agreement in the aluminium model for all incident energies and an overestimation of several percent for large angular backscatter in the gold model.

Jun (2003) derived energy deposition profiles of 0.5-2MeV monoenergetic electrons incident on thick elemental slabs using MCNP4C and ITS3 and compares the results with experimental data of Lockwood *et al.* (1980), Nakai (1963) and Trump *et al.* (1950), the former having uncertainties of ±1-2%. The agreement between the simulations and experimental results appears to be within several percent.

Joneja *et al.* (2003) investigated the applicability of MCNP4C and PSI-GEANT for microscale applications and achieved consistent results for range calculations over cells of sub-micron dimensions for electron energies of up to 50keV.

DeMarco *et al.* (2002) studied the application of MCNP cross-sections and tallies on 10-1000MeV photon sources. For low energies, the MCNP cross-section DLC-200 overestimated dose in water compared to EGS4 using XCOM cross-sections by about 25% and underestimated dose between 20-40keV by around 7%. Using the kerma approximation of dose the overestimation of dose was far more pronounced probably due to inconsistent use of the flux-to-dose conversion factors. This study would suggest that these shortcomings have since been corrected with updated cross-sections used by MCNP. Ye *et al.* (2004) replicated these findings when comparing radial dose distributions between PENELOPE2001, MCNP4C and EGS4 codes for low energy photon transport (10-150keV) and found good agreement to within ±5% for most of the data when the updated MCNP cross-sections were used. Above 100keV, the differences in dose scores between codes are insignificant.

Hendriks *et al.* (2002) used MCNP to simulate the pulse-height count in a HPGe scintillation spectrometer placed within vessels filled with either K, U and Th rich minerals. The experimental spectra proved to be contaminated by background/cross-talk radiations and radon escape. Since the modelled spectra could not be compared easily, the authors do not reach a conclusion for benchmarking. This case study underlines the difficulties associated with using sedimentary-like contexts to validate simulations.

2.3.3. Additional comments

Both MCNP and PENELOPE perform favourably when compared with experimental findings – the latter consistently providing near indistinguishable results from measurements. With the advent of more recent databases for MCNP, it has greatly improved the veracity of its output and it can now be considered reliable to within several percent for depth-dose profiles in most situations.

As mentioned previously, in this thesis, MCNP was used as the primary tool. Although the algorithms may not match PENELOPE for accuracy, results are sufficient since uncertainties in measuring water content and radioisotope concentrations and computing decay data and the cosmic dose rate will swamp any systematic variability of the MCNP output. MCNP is a very flexible code that allows the user to easily implement a wide variety of geometrical and source definitions largely unmatched by other packages. Throughout this thesis, since PENELOPE has considerably higher computational overheads in speed and versatility, it was only used to check MCNP output where possible, on a regular basis.

2.4. Implementation of Monte Carlo modelling

2.4.1. Input files

The input of the MC model includes: a) geometry; b) sources; c) tallies; d) materials; e) particle restrictions and variance reduction components and f) simulation parameters. MCNP requires one input file with cards describing firstly the properties of each cell, then secondly a card for each surface, and lastly cards for all other parameters which are each initiated with an identifying word tag. PENELOPE requires three input files for the geometry, the material cross-sections, and the remaining user-defined parameters. The material file is generated using software supplied with the PENELOPE package.

It was recognised early in this project that errors were likely to arise from manual coding of a large number of input files required for this thesis. As a consequence, almost all input files for MCNP and PENELOPE were generated using bespoke software written in MATLAB. Different modules were designed for specific types of geometry, sources, tallies, most routine forms of variance reduction and other standard parameters. Software was also written to read the text files of the model output into matrices to facilitate any further analysis.

2.4.2. Geometry

Both MCNP and PENELOPE use intersecting quadric surfaces (the set includes plane, sphere, cylinder, ellipse, cone, and torus) to define a collection of cells forming the geometry of the model. A key requirement of this type of combinatorial geometry is that no ambiguous regions (whether from overlapping cells or undefined volumes) exist. All geometries were carefully checked by both visually using native graphics software packages (as well as VisEd) and simulating a large number of particles through a void geometry to evaluate whether any particles were "lost". When modelling beta radiations in MCNP, the number of cells containing the same material was reduced where possible to minimise boundary effects generated by an incomplete condensed history step; this was not needed for PENELOPE as the algorithm completes the step within the new cell. There was little need to simplify gamma-only radiation environments since there are no adverse effects as photons move from one cell to another despite possible differences in fabric.

Decay chain parent	Decay group	Beta radiation ranges (g cm^{-2})						Gamma radiation ranges (g cm^{-2})			
		Sediment			Water			Sediment		Water	
		CSDA	99% dose	50% dose	CSDA	99% dose	50% dose	99% dose	50% dose	99% dose	50% dose
Elemental U		1.90	**0.89**	0.12	1.64	0.81	0.16	**113**	21	101	19
^{232}Th	^{232}Th → ^{208}Pb	1.29	**0.70**	0.10	1.10	0.64	0.10	**128**	22	114	20
^{40}K		0.72	**0.44**	0.12	0.60	0.40	0.12	**121**	24	107	21
^{87}Rb		0.09	**0.05**	0.01	0.07	0.05	0.01	**N/A**	N/A	N/A	N/A
^{238}U	^{238}U → ^{234}Pa	1.32	**0.81**	0.20	1.13	0.73	0.19	**92**	12	86	15
	^{234}U	0.02	**0.01**	ε	0.02	0.01	ε	**16**	0.1	26	0.4
	^{230}Th	0.03	**0.02**	ε	0.03	0.01	ε	**31**	0.1	38	0.4
	^{226}Ra	0.08	**0.04**	0.01	0.07	0.04	0.01	**57**	13	58	15
	^{222}Rn → ^{206}Pb	1.90	**0.97**	0.09	1.64	0.87	0.09	**114**	21	102	19
^{235}U	^{235}U → ^{231}Th	0.11	**0.04**	ε	0.09	0.04	ε	**53**	9	57	11
	^{231}Pa → ^{207}Pb	0.79	**0.44**	0.09	0.67	0.40	0.09	**70**	14	68	15

Table 2.1. The distance limits that an infinite matrix assumption can be made as a function of source group, material and the definition of the range in typical sediment. CSDA is the continuous slowing-down approximation of range of the maximum end-point energy from Berger *et al.* (2000). ε represents distances of less than 0.005 g cm^{-2}. All values are accurate to the last significant figure and calculated using MCNP5.

The distance that the geometry must extend to provide an infinite-matrix environment is dependent on the limits of the penetrating strength of the beta and gamma radiations. They can be treated in different ways since they have different pathways of energy loss. Electron depths can be assessed in terms of the range of the particle (see Table 2.1.), typically the continuous slowing-down approximation (CSDA) which is the average distance that an electron of a given energy will travel until it stops (i.e. deposits all of its kinetic energy). CSDA ranges were most recently downloaded from the ESTAR database (Berger et al., 2000) on 30 October 2006 at http://physics.nist.gov/PhysRefData/ Star/Text/contents.html. The sensitivity of the CSDA to fluctuations due to the amount of energy loss in the traverse direction along the path (range straggling) can be substantial (Fitzgerald et al., 1967). However, significantly more than 99% of the dose rate contributions are accounted for at a point surrounded by material extending to the CSDA range for energies up to several MeV, assuming that bremsstrahlung radiation is in equilibrium throughout the sediment (MCNP predicts that the dose deposited within the CSDA range of a 1 MeV electron in water is >99.8% and a 100 keV electron in water is >99.6%). The maximum distance for the consideration of gamma radiation at first appears to be an appropriate

multiple of the mean free path. The relationship between a distance where an arbitrary fraction of dose is deposited and the mean free path is not straightforward since the latter represents the attenuation of radiation rather than energy loss. A possible candidate would be the inverse of the mass absorption coefficients but there is no easy way to calculate a representative energy for the degraded photon spectrum in the calculation. The most intuitive method of calculating the effective range of the gamma radiations (and beta radiations) is to use the Monte Carlo transport codes to compute this distance. MCNP was used to model a point source and estimate the radial distance that accounts for 99% of beta and gamma dose deposition up to its boundary. The results were achieved using linear interpolation between predetermined distances. The dose-dependent range estimation of electron and photon sources using MC codes reduces the necessity for integrating range data across the primary emission spectra.

2.4.3. Radiation source

The version of *penmain* that was distributed with PENELOPE-2006 only permits a point source directed along a solid angle. By contrast, MCNP offers a multipurpose source package which can construct three-dimensional sources as well as degenerative surface or point sources. This is particularly useful for environmental modelling since no manipulation of the results is needed to represent solid body sources.

The primary beta emissions in ENSDF are given as average energies and end-point energies (i.e. all the kinetic energy available from the decay is retained by the beta particle). Due to the lack of a complete atlas of beta particle energy spectra for the uranium and thorium decay chains at the outset of this thesis, spectra were computed as a function of end-point energies of beta decay and transition states (Evans, 1955). Fermi's theory of beta decay (Fermi, 1934) results in a description of the normalised beta-ray spectrum for a particular transition, $N(E)$ evaluated between E and $E+\mathrm{d}E$, as

$$N(E) = \tau_0 f(Z',E)(E^2 + 2m_e c^2 E)^{1/2}(E_{max} - E)^2(E + m_e c^2)S(E) \qquad (2.1)$$

where τ_0 is a constant, $m_e c^2$ is the rest energy of an electron, E is the total energy of the beta particle, E_{max} is the value at the maximum electron energy, $f(Z',E)$ is the Fermi function, Z' is the atomic number of the daughter nucleus, $S(E)$ is the shape factor that corresponds to the forbiddenness of the transition and all other terms together represent the statistical factor that electron emission energy will be between E and $E+dE$. The Fermi function, $f(Z',E)$, which evaluates the effect of the nuclear coulomb potential and therefore is most influential in the low-energy region of the beta spectrum, can be treated as a perturbation on the electron wave function. A relativistic approximation is used, where $f(Z',E) = f(Z',\eta)$ (see Evans (1955)) and η is the momentum of the particle following the relationship $\eta^2 = E^2 - 1$, such that

$$f(Z',\eta) = \eta^{2+2Q}e^{\pm\pi\delta}\left|\Gamma(1+Q+i\delta)\right| \qquad (2.2)$$

where $Q = \sqrt{1 - \left(\dfrac{Z'}{137.0}\right)^2} - 1$ and $\delta = \dfrac{Z'\sqrt{1+\eta^2}}{137.0\eta}$. The spectral shape factor, $S(E)$, accounts for the effect of centrifugal force acting on particles that are ejected tangentially from the nucleus. For any particles that have orbital angular momentum, the centrifugal potential barrier is sufficiently high at the edge of the nucleus that the outgoing particle must "leak through" it (Fano, 1952). The correction to the energy spectrum shape for the most common type of transition (the 'allowed' transitions where the electron and neutrino carry away a total of either zero or one unit of angular momentum) is independent of energy. In this case, the electron-neutrino system is either in a spin triplet state (Gamov-Teller transitions) or in a spin singlet state (Fermi transitions). Other changes in nuclear spin or parity from parent to daughter are denoted 'forbidden' transitions. For ease of calculation, shape factor corrections suggested by Behrens and Szybisz (1976) are used where S_N corresponds to the N-th order of forbiddenness such that

$$S_1 = E(1 + 2m_e c^2) + (E_{max} - E)^2$$

$$S_2 = E^2(1 + 2m_e c^2)^2 + (E_{max}E)^4 + 3.33E(1 + 2m_e c^2)(E_{max} - E)^2 \qquad (2.3)$$

$$S_3 = E^3(1 + 2m_e c^2)^3 + (E_{max} - E)^6 + 7E(1 + 2m_e c^2)(E_{max} - E)^2[E(1 + 2m_e c^2) + (E_{max} - E)^2]$$

Here the shape factors emphasise the high-energy region of the beta-ray spectra compared to the allowed spectra. The calculation of the spectral shape factors for non-unique forbidden transitions is formidable since they depend on complex functions representing coupling constants and nuclear matrix elements. Therefore, non-unique forbidden transitions are assumed to have an allowed spectral shape, which introduces small, but relatively insignificant, distortions into the calculated beta spectra. The beta spectra for all environmental beta-decaying radioisotopes are calculated for transitions that contribute more than 1% to the total beta energy of a beta emitter. Summed beta spectra for each series are obtained by normalising each transition in terms of its probability of occurrence. Internal conversion and Auger electron energies are included for all relevant radioisotopes. All beta decay is assumed to be β- decay and the radioisotopes residing in decay groups are in secular equilibrium within that group. Figure 2.7(a)-(c) shows the integrated beta spectra for expected for elemental U, Th and K respectively. The average β-particle energy of ^{40}K in the published ENSDF database was found to be anomalously large (~10%) and it has since been corrected after consultation with its author. The spectra are entered as a histogram distribution for MCNP and PENELOPE with 1keV bin widths. The beta spectra compare favourably (mostly to within 1-2% for shape and average energy, with the notable exceptions of ^{40}K and ^{87}Rb which are significantly in error presumably due to their shape factors representing third-order forbidden unique and non-unique transitions respectively) with recent spectra distributed by the RADAR website www.doseinfo-radar.com (Stabin and da Luz, 2002) although no comment is made regarding how the beta spectra were generated in this publication. A similar agreement was found with spectra computed using polynomial methods by Murthy (1971).

Gamma spectra were generated from ENSDF and included all isomeric transitions. The emissions were retained as discrete gamma energies for MCNP and the spectra were converted to a histogram distribution for PENELOPE using 10keV bin widths. Figure 2.8(a)-(c) illustrates the primary gamma spectra for elemental U, Th and K respectively.
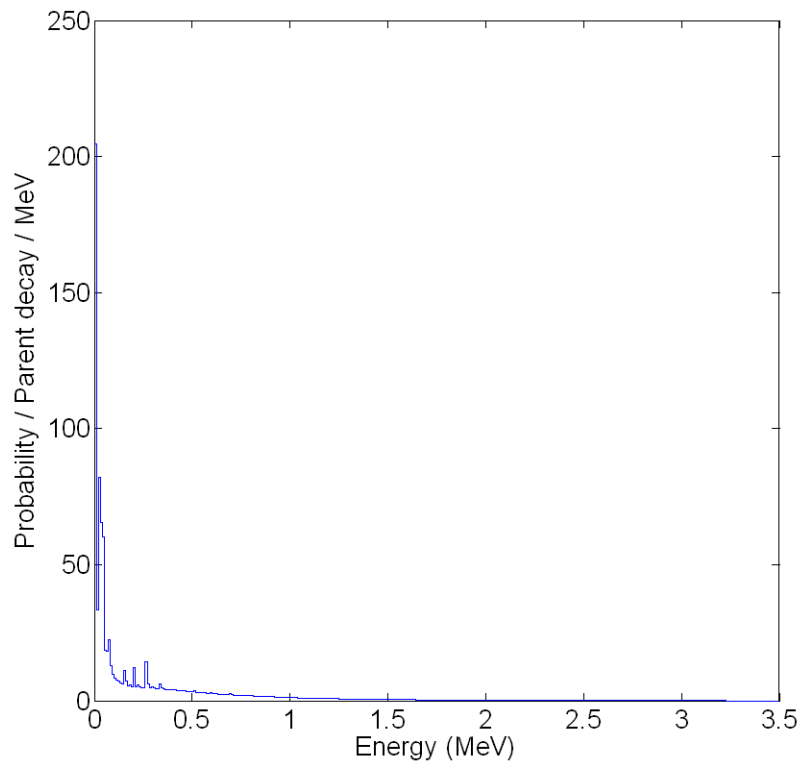
Figure 2.7(a) Primary beta emission spectra for natural U decay chain. Bin widths are 10keV.
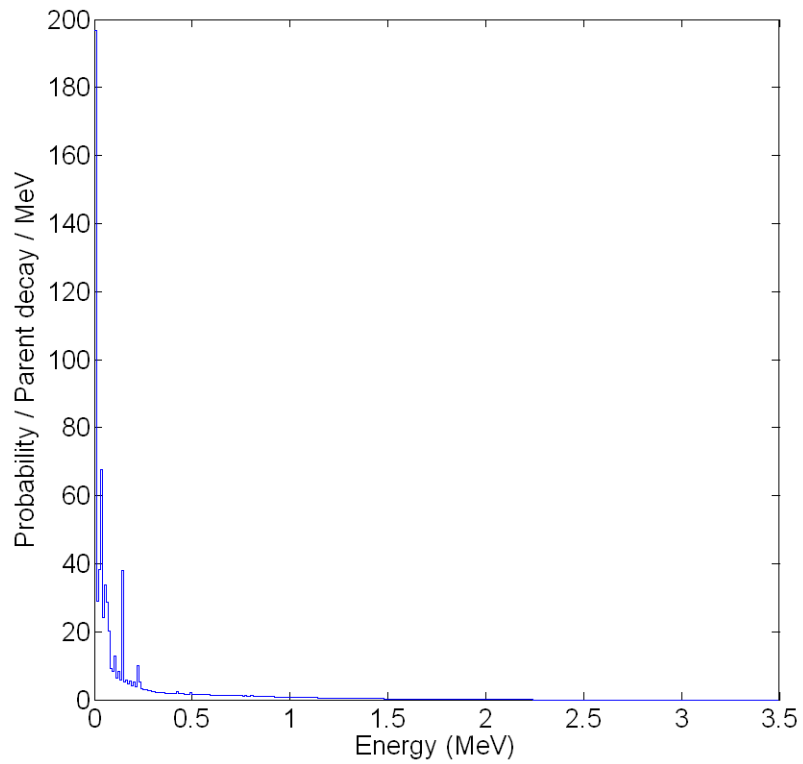
Figure 2.7(b) Primary beta emission spectra for [232]Th decay chain. Bin widths are 10keV.
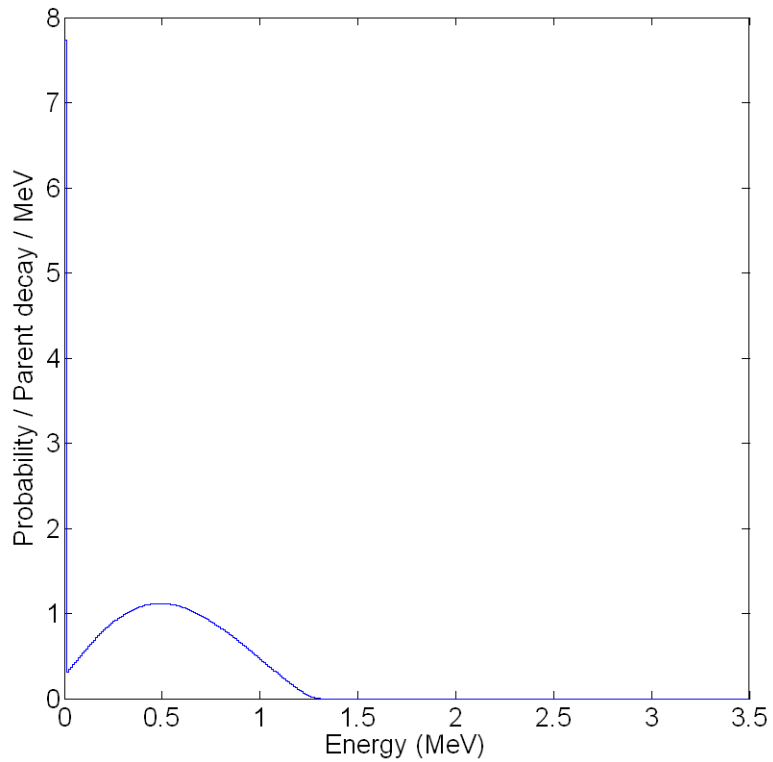
Figure 2.7(c) Primary beta emission spectra for[40]K. Bin widths are 10keV.
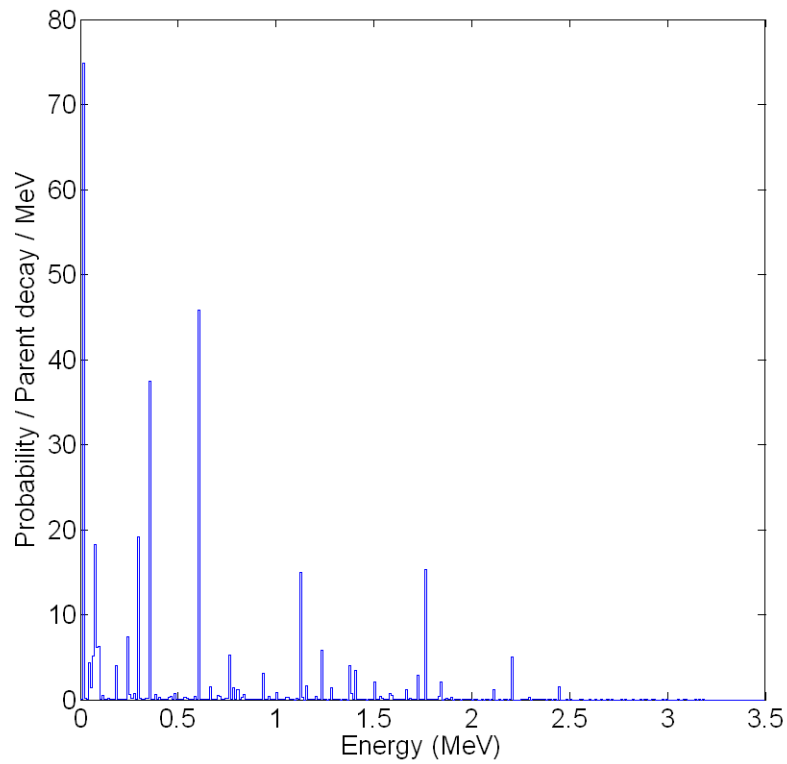
Figure 2.8(a) Primary gamma emission spectra for natural U decay chains. Bin widths are 10keV.
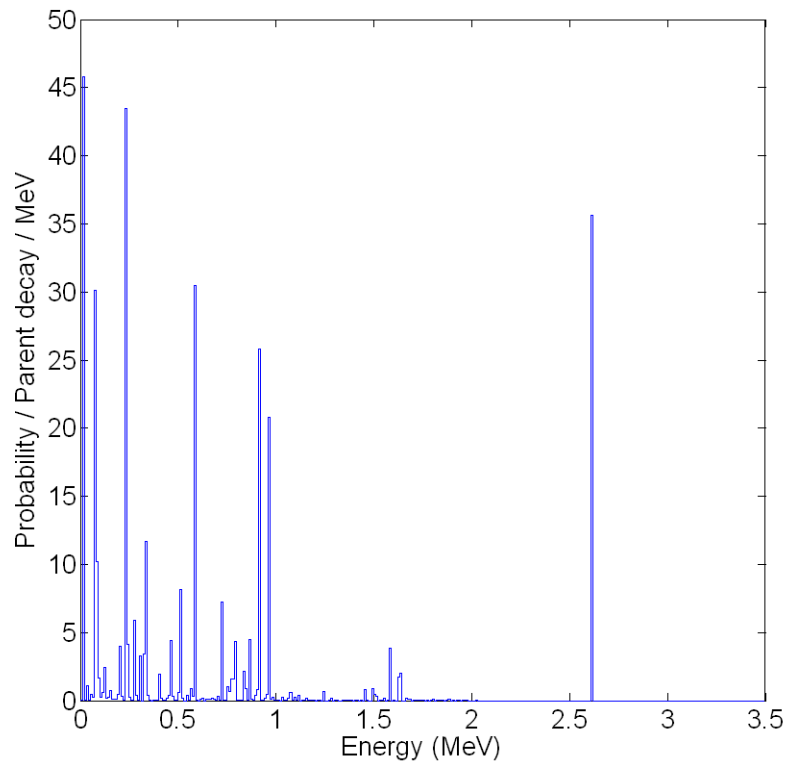
Figure 2.8(b) Primary gamma emission spectra for ^{232}Th decay chain. Bin widths are 10keV.
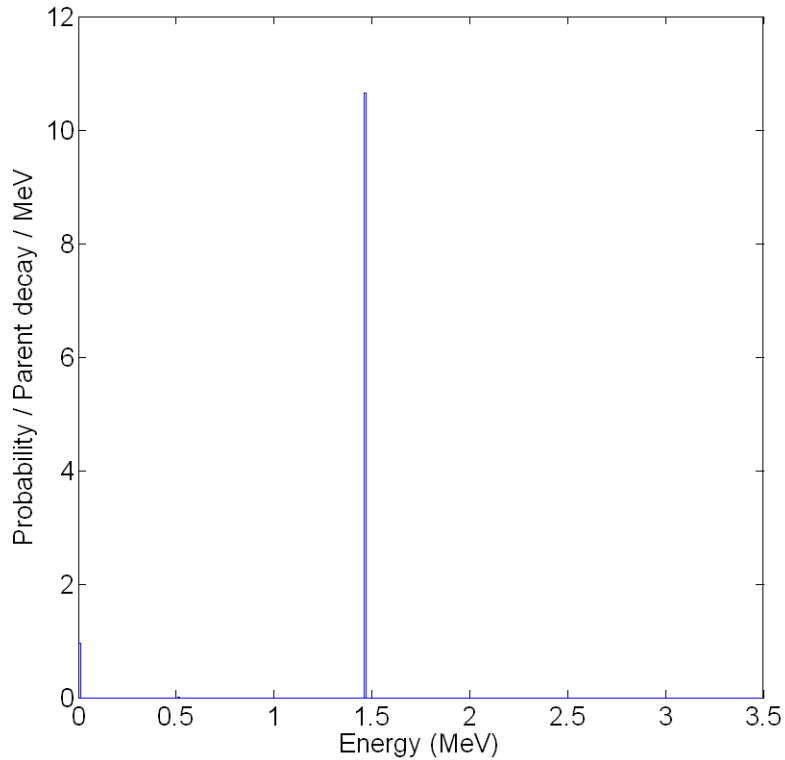
Figure 2.8(c) Primary gamma emission spectra for ^{40}K. Bin widths are 10keV.

For illustrative purposes, a "typical" environmental radiosource is applied with concentrations 1ppm uranium, 3ppm thorium, 1% potassium and 50ppm rubidium throughout this thesis. By constrast, an alternative "average" source suggested in the literature (Olley et al., 1996) has activities in the ratio 40Bq kg^{-1} uranium, 40Bq kg^{-1} thorium and 400Bq kg^{-1} potassium which corresponds to concentrations of 3.1ppm uranium, 9.9ppm thorium and 1.5% potassium - a slight increase in thorium and suppression of potassium compared to the source used in this thesis. In addition, Mejdahl (1979) suggests average concentrations of 3ppm U, 12ppm Th and 1% (or 2%) K$_2$O.

2.4.4. Tallies

MCNP allows a wealth of information to be retrieved from the modelled environment. Tallies are the scoring cards for particle interactions within specified regions of the model. Following the nomenclature of MCNP, a tally is denoted if the card begins with 'f' and the proceeding number defines which quantity is scored. Several standard types of tallies are available from MCNP but this study required the use of three: 1) the f4 tally which records the flux averaged over a cell (particles cm^{-2}); 2) the f6 tally which records the dose deposition averaged over a cell from gamma radiosources (MeV g^{-1}); and the *f8 tally which records the energy deposition averaged over a cell (MeV). The first two tallies are macroscopic track length estimations and are related by energy-dependent multipliers. Track length estimations are well-suited to gamma radiations since scoring is dependent only on a particle traversing a cell rather than a collision taking place. The advantage of gains in efficiency is offset by the requirements of the scoring kerma where dependence on the energy and distribution of radiosources may violate CPE conditions and result in overestimates of absorbed dose. The *f8 tally is conceptually different since it explicitly records energy loss within each cell and it is the most robust score for charged particle energy deposition. However, it is significantly less efficient than track length tallies for gamma radiation, increasingly so as cell size decreases.

The use of the flux tallies to estimate dose deposition under conditions of CPE (charged-particle equilibrium) has been tested by sampling the flux within a 10m radius sphere that forms the interior of a 12m radius spherical mass of quartz ($\rho = 2$g cm^{-3}) containing uniformly distributed potassium gamma sources. The absorbed dose tally *f8 for photons and electrons was used to provide a microdosimetric evaluation of dose. A kerma estimation of dose is

$$\int_0^{E_{max}} \frac{\mu_a(E)}{\rho} E \Phi_p(E) dE$$ where μ_a / ρ is the mass energy absorption coefficients for quartz, E

is the photon energy and Φ_p is the photon flux (number of particles per cm^2 per energy bin). The kerma can be computed using *f4:p with a flux-to-dose response function (de4 and df4 containing the energy and mass absorption data from Hubbell and Seltzer (2004). The results need to be normalised by multiplying by mass. The absorbed dose calculated using the charged particle fluence can be found in a similar manner as $\int_0^{E_{max}} \left(\dfrac{dE}{\rho dx}\right)_c \Phi_e(E)dE$ where

$(dE/\rho dx)_c$ is the mass collisional stopping power for quartz and Φ_e is the electron flux (number of particles per cm^2 per energy bin). This expression for absorbed dose is valid for thin bodies where CPE is conserved but, importantly, the fluence relates only to the incident spectrum. Therefore, Φ_e must be calculated for the electron flux arising from energy imparted by photons only (or the degraded beta emission spectra if required). The relevant MCNP cards used are f4:e with a flux-to-dose response using mass stopping powers (here we use Berger *et al.* (2000) but just as easily we could extract similar values from a MCNP output file). Additionally, knock-on electron generation were prevented from contaminating the particle fluence by inserting an explicit "phys:e 1.4608 6j 0" card to set RNOK = 0. The results for about 100,000 source particle histories in terms of energy deposition are 0.774±0.002 MeV, 0.774±0.003 MeV and 0.771±0.002 MeV for each respective method and these results are identical within uncertainty limits. We can conclude the particle fluence calculated using MCNP for both electrons and photons can be adequately used to calculate dose at a point and the microdosimetric calculations corroborate these findings.

The absolute dose is limited in value for the purposes of this thesis and it is more appropriate to present the tallies as a fraction of the dose expected in an infinite-matrix. This is achieved using

$$\Omega = \frac{D_d}{D_{IM}} = \frac{m_s}{E_{mean}}\frac{*F8}{m_d} \tag{2.4}$$

where D_d / D_{IM} is the ratio of the dose in the detector to the infinite-matrix dose, m_s and m_d are the mass of the source and detector respectively, and E_{mean} is the average energy emitted by the source. The choice of φ to denote D_d / D_{IM} has been circulated in the trapped charge literature (notably by Mejdahl (1979)). This may become confusing since in radiation dosimetry nonmenclature φ also describes the flux density or $d\Phi / dt$ (cf. Attix (1986)).

Apart from exceptional circumstances, coarse mineral grains from archaeological contexts of typical activity are expected to be exposed to a large number of radiations during the burial duration. However, the results from MC simulations are expected to fluctuate as a function of the number of tracks passing through scoring cells and the precision of the tallied estimate of dose may be significant for interpreting the results. In most situations, a smooth and continuous dose gradient is likely to be present in homogeneous sediments up to an interface and it is valid to improve the accuracy of the modelled results by removing these fluctuations. Tabata (1997) recommended a moving-window least squares polynomial fit for electron depth-dose profiles and this is implemented in this thesis where appropriate for both gamma and electron dose gradients. Cubic polynomials were found to work well over the main part of the distribution but quadratic polynomials were used over the final 10% of the profile to avoid evidence of oscillatory behaviour for increasing distances from the interface also found by Das *et al.*(2002). Cubic spline interpolation was used where smoothing was not required; in cases of abrupt changes in slope, cubic Hermite interpolation was used to prevent anomalous and/or oscillatory behaviour.

2.4.5. Variance reduction

Monte Carlo modelling is rather inefficient for most of the types of problems associated with sedimentary contexts. Consider a model finding the effective beta dose rate in a quartz grain embedded within a uniform sediment with a homogeneous distribution of radioactive sources. Very few of the simulated particles would travel close to the grain. A large number of

histories would be required to achieve a high precision score and subtle variations in dose rate due to compositional or geometrical factors would likely be masked by unfavourable counting statistics. The models need to be biased to improve the number of particles interacting in the region of interest to give the same expected tally scores but reduced variance for a given number of primary particles. Two main strategies were used in this study.

For homogeneous fabrics that are infinite or semi-infinite in extent (Fitzgerald et al., 1967), analytical solutions can be found using dose point kernels (see Section 2.5). The uncertainty of the two-step solution is dependent solely on the variance of the depth-dose transport results. Although the dose point kernel approach is widely used for symmetrical geometries and homogeneous materials, the inaccuracies of applying dose point kernels in heterogeneous environments and the advent of fast Monte Carlo codes meant they were largely redundant and there was no need for their widespread adoption in this thesis.

A more dynamic method, applied directly within the Monte Carlo transport calculations, is importance mapping with tailored energy cutoffs (source biasing was also attempted but it resulted in only modest speed gains). Importance mapping is a robust biasing technique where particles are split as they enter cells closer to the tallied region and particles have a probability of being eliminated (so-called Russian Roulette) as they travel further from the tallied region. The tallies are corrected by adjusting the weights of any particle undergoing an importance game so that split particles have proportionately less weight and Russian roulette survivors have proportionately greater weight (see Figure 2.9). This allows more sampling over the tallied region with little deleterious effects on the solution of the model. In order to optimise the precision of the model, beta particles that have energies whose continuous-slowing-down approximation (CSDA) range is <85% the minimum distance from the tallied region are removed from further consideration (the value of 85% was conservatively included to account for range straggling of particles). Gamma energies are cutoff for distances greater than 3

mean free paths since the contribution of these photons to dose rate would be neglibible (<0.01%).
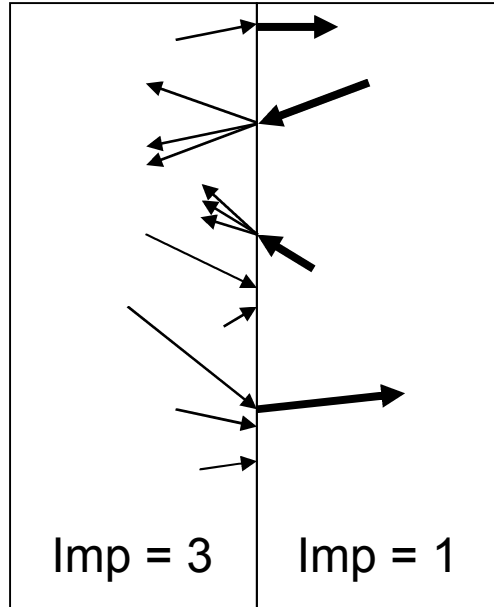
Figure 2.9. An illustration of importance mapping across an interface. The region on the left has an importance three times the region on the right. Particles travelling left to right across the interface suffer Russian roulette but the survivors increase their weight whereas particles travelling right to left split but carry less weight. Sampling is biased towards regions of highest importance and overall weight of particles is conserved.

Importance mapping and energy cutoff often produces a speedup of some two orders of magnitude or more. A demonstration of the benefits of variance reduction are presented in a case study that details different variance reduction schemes for the dose absorbed in an inert 300μm quartz grain embedded in a infinite-matrix of quartz (3mm radius) with a uniformly distributed 1MeV beta source. Initially the IM consisting of a single cell was compared to an IM built from concentric spherical shells of 0.5mm thickness. Importance mapping and energy cutoffs were applied to the structured IM cells both as individual variance reduction trials and combined. Table 2.2. presents the results of the case study. Little difference in efficiency is seen between a simple cell and a stratified cell with the figure of merit,

$$FOM = \frac{1}{(precision)^2.time}$$, slightly smaller for the more complex geometry as expected

(FOM is expected to be independent of the number of histories run, N, since precision is proportional to $1/\sqrt{N}$ and time is proportional to N). The importance mapping decreases the rate of histories since additional particles are generated in regions of high importance, however, the FOM has increased by a factor of three. The energy cutoff approach is significantly more effective. Although the method has a high number of starting histories per scoring particles, electrons unable to traverse a sufficient distance to reach the grain are discarded and no further computations are expended on these electrons. The FOM is more than an order of magnitude greater than the importance mapping. Combining both importance mapping and energy cutoffs yields the greatest efficiency with the FOM some 50 times larger than the unbiased geometry at over 1100. By way of reference, the track length tally of dose for gamma radiation produces a typical FOM of several 100,000.

Variance reduction method	Histories (10^3)	Histories per minute (10^3)	Dose in grain (per IMD)	Precision (fractional 1σ)	Figure of merit
None (plain)	1,124	19	0.955	0.029	20
None (structured)	1,000	19	0.959	0.032	19
Importance mapping	1,000	17	0.944	0.016	63
Energy cutoff	1,000	800	0.954	0.031	829
Importance + cutoff	1,000	307	0.970	0.016	1144

Table 2.2. A case study of the efficiency of variance reduction methods for dose deposited in a 300μm grain from an infinite-matrix of quartz with a uniform 1MeV beta source. The rate of computing histories and the figure of merit is machine dependent and these values we computed using a Pentium M; 1.6 GHz CPU; 2 Gb RAM system running Windows XP Pro. See the text for further details.

2.4.6. Materials

The choice of sedimentary materials to model in this thesis was broadly based on a) the most common minerals used as dosimeters, namely quartz and feldspar; b) common regolith

fabrics, namely an "average" minerogenic sediment and peat; and c) common intrusive materials, namely water, carbonates and silicates. Both quartz (SiO_2; $\rho = 2.65$g cm^{-3}) and feldspar (orthoclase $KAlSi_3O_8$; $\rho = 2.55$g cm^{-3}) were assumed to be pure homogeneous minerals. The "average" sediment used in this study follows the specification of Garrels and Mackenzie (1971) and it almost certainly will not reflect the composition of site specific sediments in detail. Essentially, the composition is a mixture of typical values of shale (~81%), sandstone (~11%) and limestone (~8%). Mason and Moore (1982) suggest that there may be an underestimation of the limestone contribution when comparing these data with the compendium approach of Ronov and Yaroshevsky (1969). Peat is assumed to be entirely organic in order to maximise the differences in Z_{eff} although the ash content may range from several percent to the majority of the mass (Wüst et al., 2002). The peat value used in this study was the average of a sawgrass peat sample from The Everglades, Forida sited below the zone of biodegradation (Chefetz et al., 2000) and a core taken from a tropical peaty marsh in Tritrivakely, Madagascar (Bourdon et al., 2000). For simplicity, carbonate is assumed to be calcium carbonate ($CaCO_3$; $\rho = 2.71$g cm^{-3}) and silicates to be silicon dioxide (SiO_2; $\rho = 2.65$g cm^{-3}). Table 2.3 presents the relevant compositional data used in the modelling of materials.

		Quartz	K-feldspars	Average (dry) sediment	Average (organic) peat	Water	Carbonate	Silicate
Element (%wt)	H	-	-	0.38	6.06	11.19	-	-
	C	-	-	1.28	50.29	-	12.00	-
	N	-	-	-	3.54	-	-	-
	O	53.26	45.99	49.91	40.16	88.81	47.96	53.26
	Na	-	-	0.67	-	-	-	-
	Mg	-	-	1.57	-	-	-	-
	Al	-	9.69	7.73	-	-	-	-
	Si	46.74	30.27	27.91	-	-	-	46.74
	K	-	14.05	2.66	-	-	-	-
	Ca	-	-	3.43	-	-	40.04	-
	Fe	-	-	4.47	-	-	-	-
Density (g cm^{-3})		2.65	2.55	1.9	1.0	1.0	2.71	2.65

Table 2.3. Average elemental composition (%wt) and average density of some materials referred to in this thesis. See main text for references.

Recent cross-section datasets have been used for the simulations. That is, for MCNP, the MCPLIB04 and EL03 libraries and the default cross-sections attached to PENELOPE. The data for the differential cross-sections are provided by atomic number and it is assumed that isotopic variability is negligible. The materials implemented in the MC codes have associated parameters that need to be defined. The energy cutoffs for MCNP are always set to 1keV for both electron and photon transport. In MCNP, the step size itself cannot be directly changed and it is set as a function of the fractional energy loss of the particle. The division of the step into substeps, at which level the angular deflection and secondary particle production is sampled, reduces the significance of any interruption in the step during transit through the geometry. The number of substeps, m, per condensed history energy step may be specified (using the "estep" card) as a constant for a particular material. The MCNP authors recommend (2003) that "*an electron should make at least ten substeps in any material of importance to the transport problem*". Conversely, numerous substeps across a small volume may lead to an unsatisfactory assessment of collisions to satisfy Goudsmit-Saunderson multiple scattering theory (Berger and Wang, 1988) in addition to a proportionate decrease in efficiency. In finely grained sedimentary environments where a large number of interfaces over small scales are expected, it is necessary to determine the range of m required for accurate modeling. A study of the sensitivity of depth-dose distributions generated by MCNP4C to different layer thicknesses and values of m was presented by Schaart *et al.* (2002). For electron energies less than about 0.2 MeV (range of 450μm in water), the dose is deposited nearer the end of the track as more boundaries are crossed per electron and the electron scattering is reduced. For higher energies, the effects are ameliorated although still significant for thicknesses smaller than 10% of the electron range. An improvement in the dose-depth distributions is made if m is scaled proportionately with layer thickness however some deterioration in the quality of the results is found for models with around 50 boundaries per range of the electron. The influence of changes to m on the depth-dose profiles is

considerably weaker, even for simulations where several thousand substeps were produced over the range of the electron.

Further investigations were performed for planar environments, namely the dose response of a) the high energy region of the beta spectra to thin materials where m may be inadequate, b) the low energy region of the beta spectra where m may be excessive and c) a complete spectrum. The radiation transport is simulated in an average dry sediment ($\rho = 2g\ cm^{-3}$) from a "typical" beta unidirectional source spectra partitioned at 200keV. The simulation divided the material into thin layers orthogonal to the source direction. The layer thickness was varied from 5-80μm for different values of m ranging from the default to 500. Figure 2.10 (a)-(c) and Figure 2.11 (a)-(c) shows the depth-dose profiles for the different energy spectra for different m values and layer thicknesses respectively. The results show that MCNP is reasonably robust with the default m values when considering a spectrum of emission energies with only small perturbations along the profile from higher m values. The depth-dose profiles for thinner layers slightly overestimate dose near the peak absorption and underestimate dose at greater depths. The magnitude of the perturbations is in the order of several percent. The different beta source spectra preserved the small systematic effect on the dose-depth profiles for different m values and thicknesses but the magnitude of perturbation was slightly higher for the low energy spectrum.

PENELOPE was originally designed to provide a high-resolution simulation of electron transport:- the parameters required to specify the material treatment are more flexible to allow the user to tune the physical treatment of the system. For each material the following need specifying:

- *EABS*, the absorption energy cutoffs for electrons and photons.

- The average angular deflection of an electron along a track, *C1*. Larger *C1* will speed the calculation since there are less hard elastic events.

- The maximum energy fractional energy loss between hard elastic events, *C2*.

- *WCC* and *WCR*, the cutoff energy loss for hard inelastic collisions and hard bremsstrahlung emissions respectively.

- *DSMAX*, a geometrical limitation that may be used for each thin body and specifies the maximum step length.

All of the above parameters were defined using the same criteria as Sempau *et al.* (2003) for their benchmark studies. *EABS(e⁻)* was 1% of the lowest kinetic energy of the beta source and *EABS(γ)* a tenth of this value. The minimum value of *EABS* was set at 1keV. *WCC* and *WCR* was set to *EABS(e⁻)* and *EABS(γ)* respectively. *C1* and *C2* each taken as 0.05. Where thin layers were needed, *DSMAX* was set as a tenth of the layer thickness.
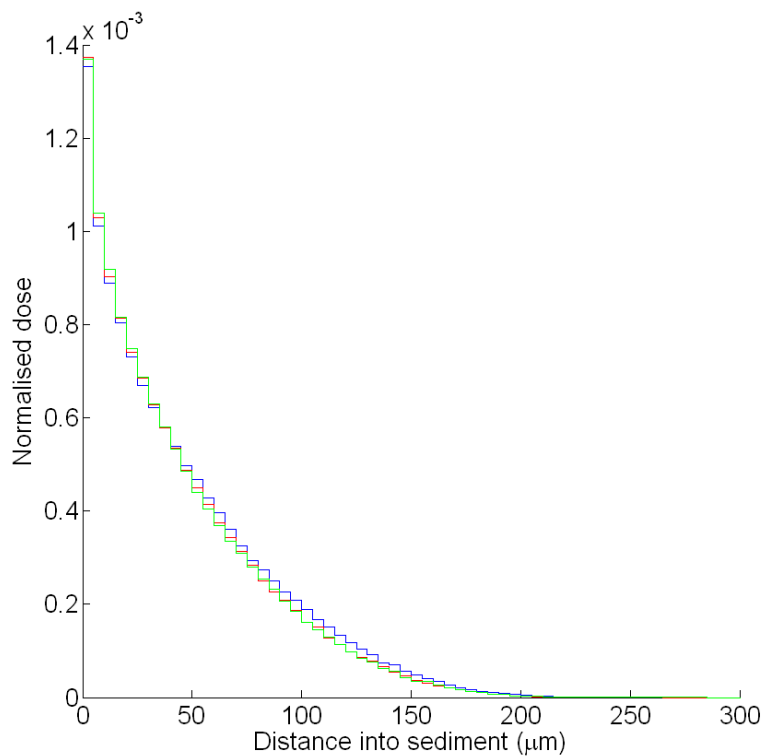
Figure 2.10(a) Depth-dose profiles in an average sediment for layers of 5µm from a "typical" beta source with a spectra of energy less than 200keV. Blue is the default value of *m*; red is for *m* = 50; and green is for *m* = 500.
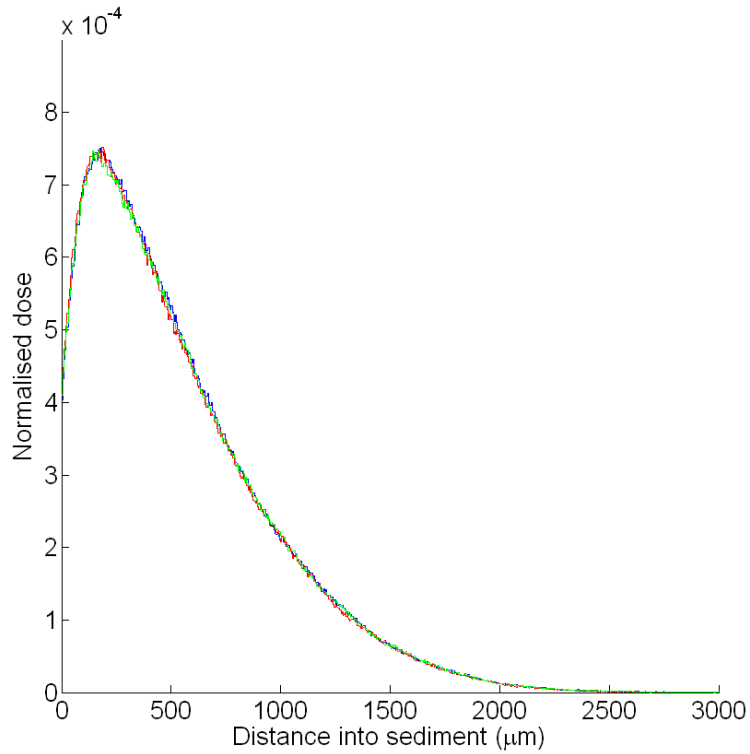
Figure 2.10(b) Depth-dose profiles in an average sediment for layers of 5μm from a "typical" beta source with a spectra of energy greater than 200keV. Blue is the default value of *m*; red is for *m* = 50; and green is for *m* = 500.
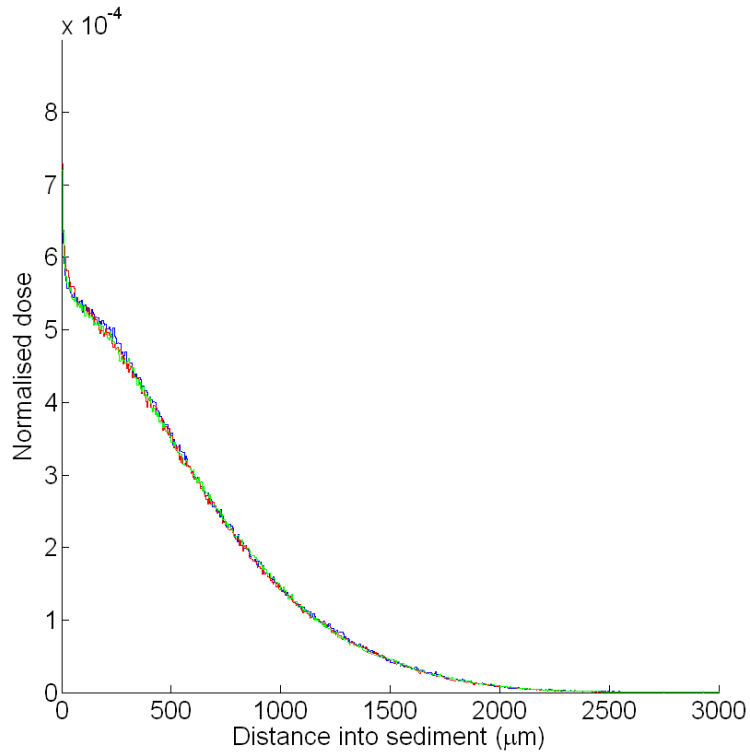
Figure 2.10(c) Depth-dose profiles in an average sediment for layers of 5μm from a "typical" beta source with a complete spectrum. Blue is the default value of *m*; red is for *m* = 50; and green is for *m* = 500.
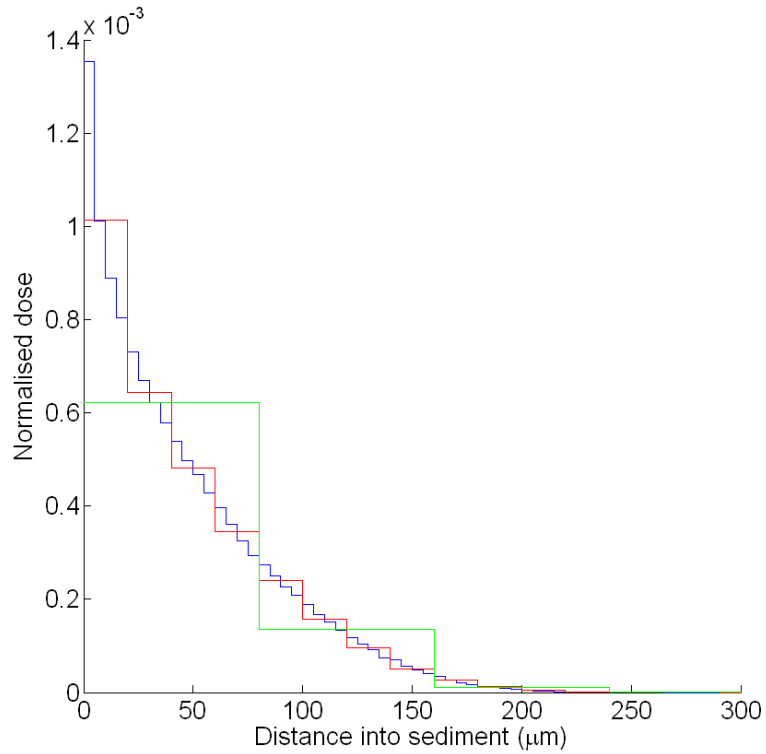
Figure 2.11(a) Depth-dose profiles in an average sediment for layers of 5μm (blue), 20μm (red) and 80μm (green) thickness from a "typical" beta source with a spectrum of energy less than 200keV. The default value of *m* was used.
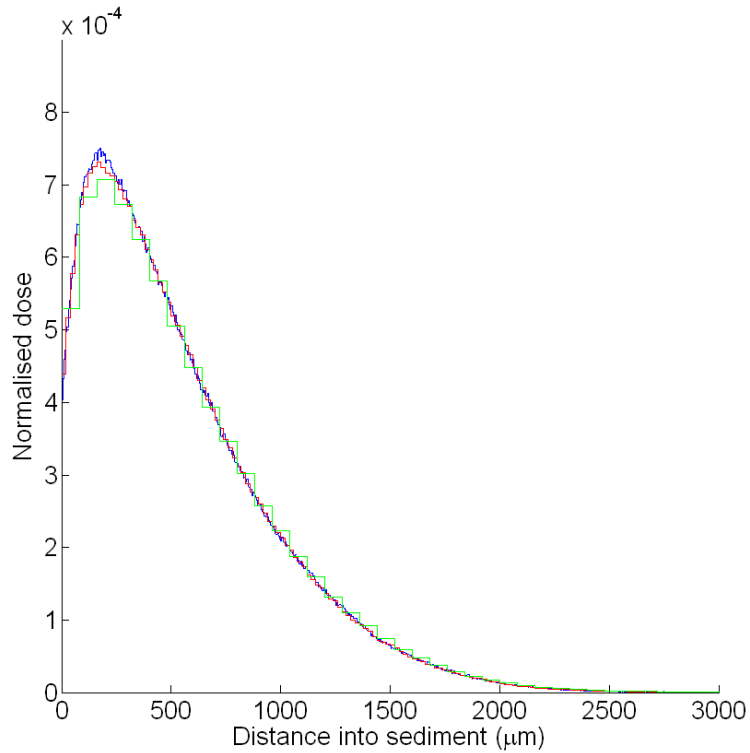
Figure 2.11(b) Depth-dose profiles in an average sediment for layers of 5μm (blue), 20μm (red) and 80μm (green) thickness from a "typical" beta source with a spectrum of energy greater than 200keV. The default value of *m* was used.
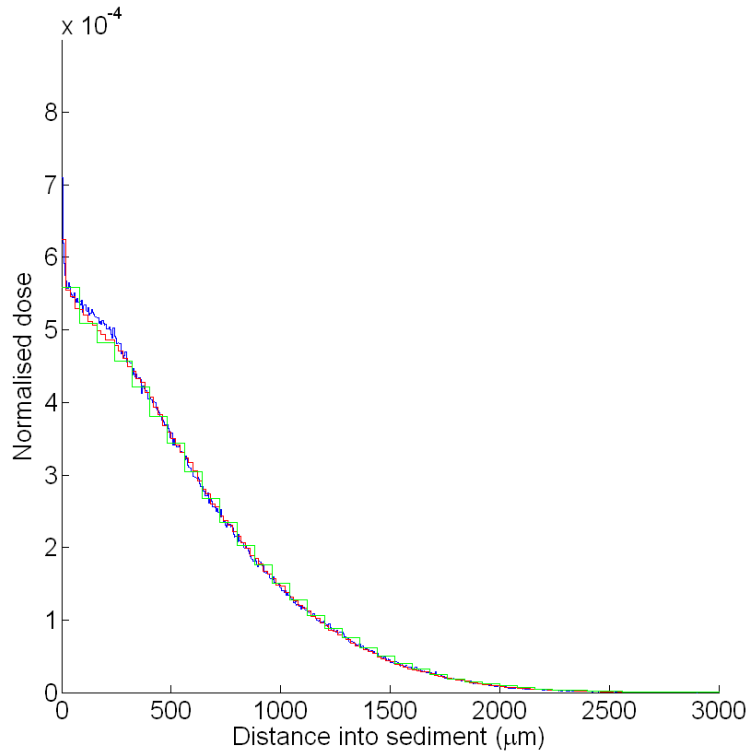
Figure 2.11(c) Depth-dose profiles in an average sediment for layers of 5μm (blue), 20μm (red) and 80μm (green) thickness from a "typical" beta source with a complete spectrum. The default value of *m* was used.

2.4.7. Other parameters

Several additional input parameters should be considered for MCNP and PENELOPE. Both codes require the specification of the problem cutoff. The "mode" card for MCNP restricts the transport to either only photons, electrons or coupled photon/electron showers – if other types of particles are produced, they are deposited locally. The former case assumes that a condition of charged particle equilibrium is maintained throughout the geometry.

In all cases, the "ITS" algorithm is used for energy indexing the electron transport cross-sections in MCNP following the recommendations of Schaart *et al.* (2002). This is implemented by a "dbcn 17j 1" card.

2.5. Dose point kernels

Dose point kernels (DPK) are radial distributions of dose from a point source within a uniform material. DPKs provide the most common numerical basis for calculating integrated dose through an infinite homogeneous body with an extended source (Fitzgerald et al., 1967)) or the average dose over a finite mass. The relationship between dose, $D(s,E)$, at distance s and the dose point kernel, $F(s)$, in a homogeneous medium of density ρ with a source of energy E_0 is

$$D(s,E) = \frac{E_0 F(s,E)}{4\pi\rho s^2} \text{ and } \int_0^\infty F(s)ds = 1 \tag{2.5}$$

The dose point kernel is a function for weighting dose with distance. A common measure of distance is in terms of range or 90% dose (Berger, 1971, Cross et al., 1992). Analytical methods have been suggested to approximate the DPK in different media (Loevinger, 1956) based on empirical evaluation of experimental results and Cross (1968) provided a procedure to scale DPK as a function of effective Z. The convolution of dose point kernels to estimation dose within heterogeneous region has been comprehensively researched (Goldstein, 1959) but the underlying theory does not support such an approach unless in suitably restrictive situations. However, once generated, DPKs are amenable to very rapid computation and this approach avoids the potential problems of slow solution convergence when Monte Carlo modelling simulates the whole system. The immediate benefit of DPKs is to provide reciprocal relationships for symmetrical bodies centred at the origin. For example, in an IM environment, the dose absorbed in a spherical shell surrounding a point source at origin is equivalent to the dose at a point at origin from the spherical shell as the source. For Monte Carlo computation, this has important implications; for the above example, a MC transport solution of a large source surrounding an infinitesimally small detector is near intractable whereas the solution becomes highly efficient for a point source surrounded by a large detector.

2.5.1. Computation

Dose point kernels were generated using both MCNP5 and PENELOPE2006 for isotropic beta and gamma sources for all decay groups. Thin spherical shells were used to approximate the radial distribution of dose across spherical surfaces. The gamma source DPKs were constructed with 50 shells of 5mm thickness near the source to near 10cm thickness at 1.5 times the 99% dose range (thicknesses spaced logarithmically). A higher spatial resolution near the source was selected since in this region most of dose is deposited and the gradient is steeper. PENELOPE was used in a similar way for beta sources with shells of 5μm thickness continued for 1.2 times the CSDA range of the maximum energy. To ensure that no deleterious effects of the numerous interfaces on the transport calculations, some models were repeated for 20μm thick shells. No significant variation was observed. As discussed in Section 2.4.6, MCNP is expected to be sensitive to the number of interfaces active in the model and the computation of DPKs was made in a two stage procedure. Firstly, DPKs from monoenergetic electron point sources were produced for twenty different energies ranging from 10keV to 3.5MeV. It was found that approximately 20-25 equally spaced shells were required to characterise the DPK such that the root mean square error (achieved by considering a DPK of several hundred shells and finding the RMS distance between the DPK and the dataset resampled at a lower resolution) of the calculated locus was less than 0.001% of the smoothed curve. Models were designed with shells of 5% CSDA thickness up to distances of 1.2 times the CSDA range. Additional shells were added close to the source, with the smallest of 0.2% of CSDA range, to accurately gauge dose build up with delta particle production for higher energy sources. Following the treatment of Cross (1992), the radial distance is transformed into units of the CSDA range and the DPK becomes a dimensionless variable which is slowly changing with energy and distance (see Figure 2.12). Using the beta emission spectra, it is straightforward to linearly interpolate intermediate distance values and log interpolate intermediate energy values in order to construct the dose point kernel arising from a beta source such that

$$D(s) = n\int_0^{E_{max}} N(E)D(s,E)dE$$

$$= \frac{n}{4\pi\rho s^2}\int_0^{E_{max}} N(E)F(s/s_{CSDA},E)\left(\frac{E}{s_{CSDA}}\right)dE$$

(2.6)

The DPK are resampled to achieve a spatial resolution of 1μm. Bremsstrahlung radiation losses beyond the range of the electrons are retained explicitly in the rescaling procedure so that the kernels do not strictly sum to unity. Dose point kernels in quartz of U, Th and K sources calculated by MCNP are presented in Figure 2.13 and they were identical to within 1% with the kernels calculated by PENELOPE (except at distances close to the source where the PENELOPE models lacked comparable resolution).
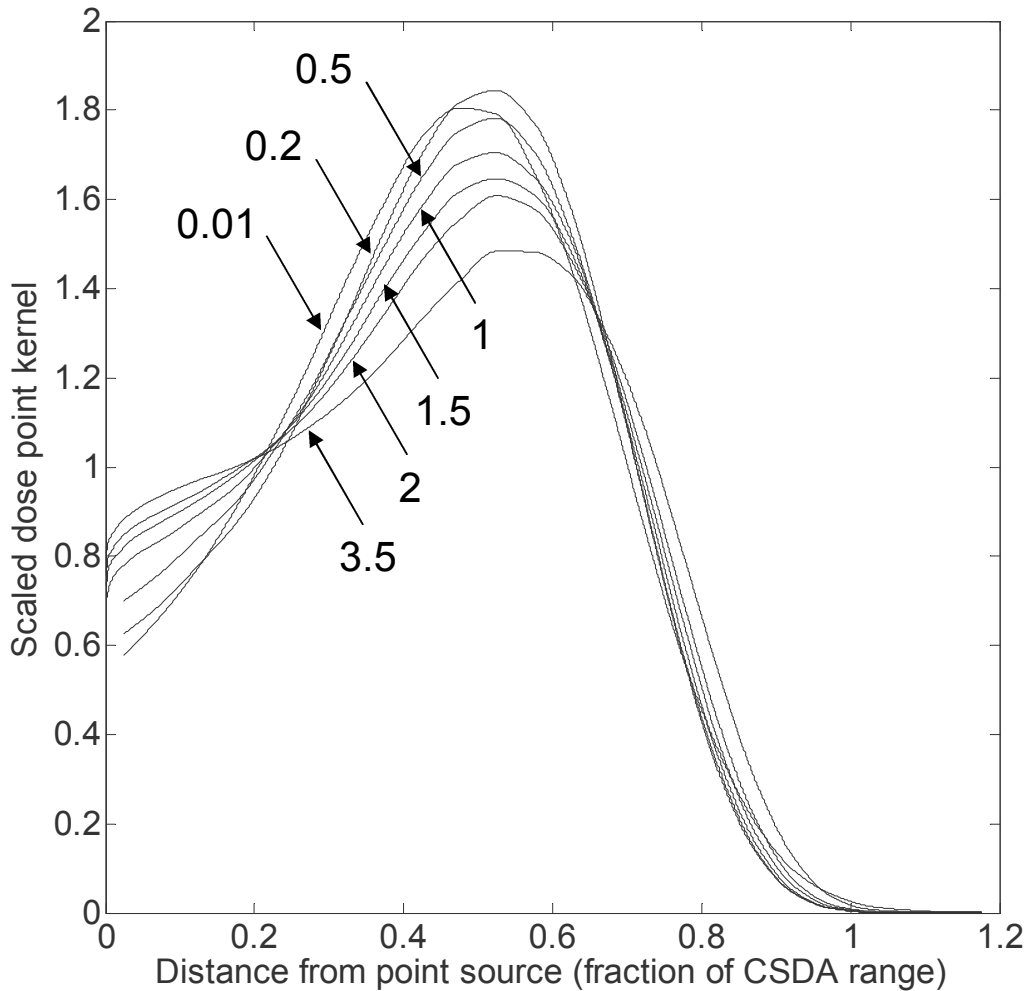
Figure 2.12. The scaled dose point kernels as a function of the continuous slowing down approximation (CSDA) range in quartz. The energies of the electron source are labelled (in units of MeV) and calculated using MCNP5.
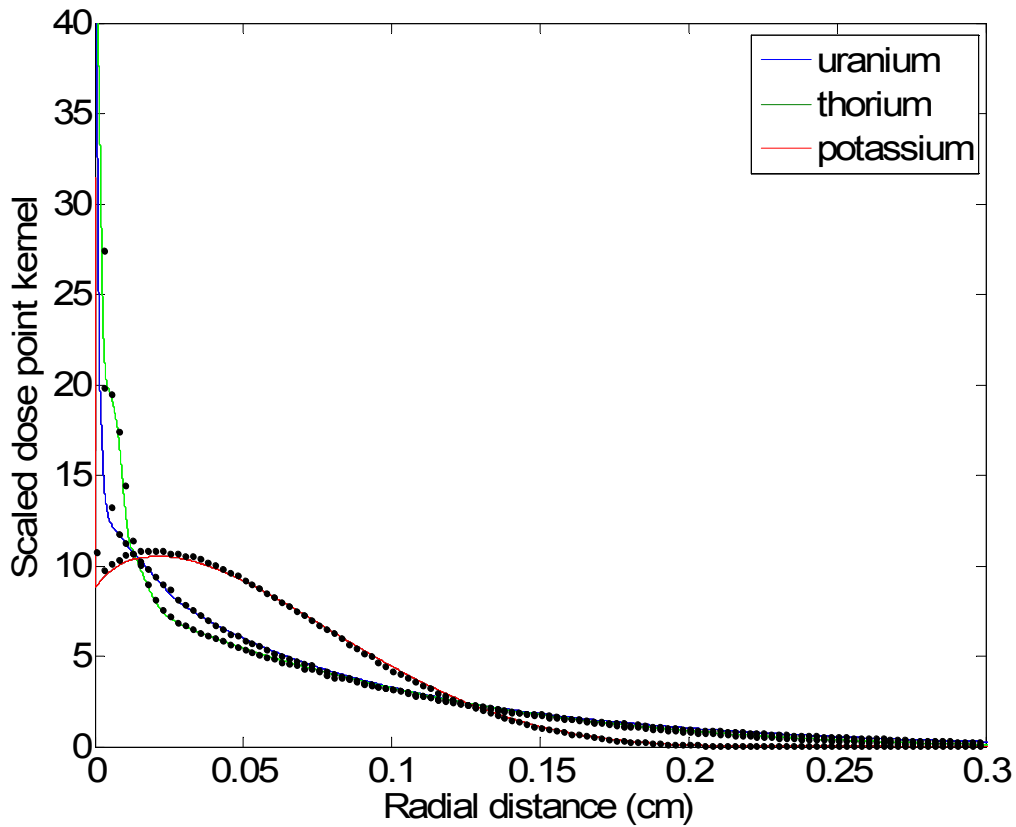
Figure 2.13. The scaled dose point kernels for beta emissions of elemental U, Th and K in quartz computed from monoenergetic dose point kernels generated by MCNP5. The heavy dots represent direct calculation of the dose point kernels by PENELOPE2006 (not all points shown). The three loci extend past the x-y scale shown here.

Comparisons of the DPK results achieved here can be made between a reference suite of measurements presented by Berger (1971, Berger, 1973) and more recent calculations. Differences between the estimates of the DPKs are most likely to reflect the different assumptions and algorithms used in the computation but may reflect also changes in the energy spectral data. The earlier paper integrated beta spectra DPKs from analytically derived monoenergetic point kernels based on the CSDA (Spencer, 1955, Spencer, 1959). Berger used the ETRAN Monte Carlo code to incorporate energy loss straggling, which weighted the point kernel towards the end of the CSDA. However, prior to 1986 the sampling of the energy loss straggling through Landau distributions by ETRAN was inaccurate (Rogers and Bielajew, 1986) and later corrected. Notable recent work have used Monte Carlo codes such

as EGS4 ((Simpkin and Mackie, 1990), ACCEPT from the ITS suite (Cross et al., 1992), and EGSnrc (Minegra-Hing, et al. 2004). Figure 2.14 gives direct comparisons between the dose distribution in water from monoenergetic point sources from these publications and values computed using MCNP5 and PENELOPE2006. At low energies, MCNP5 was found to emphasise the dose near the peak of deposition and restrict the dose deposition away from the peak; PENELOPE calculated results consistent with EGS/EGSnrc codes. The bias of MCNP, compared to other codes, towards the peak is much reduced at higher energies and distributions arising from 1MeV point sources generated by the various codes (with the exception of ETRAN) agree with to within several percent along the radial distance. It should be noted that Cross (1992) assumed that the dose at the source can be approximated by the restricted stopping power. However, the effect of delta particle build up becomes an important component of the composite kernel generated from the beta spectrum near the source.

2.5.2. Ancillary calculations

When using dose point kernels, the geometrical construction for calculating the dose is based on the spherical shell (i.e. the volume between two concentric spheres of different radii). In order to retain as much information as possible, the radial distribution is retained in distances matching the radii of the tallied cells. If a finer shell width is required, the dose point kernel distribution is sampled using cubic spline interpolation. The mass of a spherical shell centred on point P and bounded by a spherical grain is found to be

$$\frac{\pi\rho}{12x}\left[6\left(R^2 - x^2\right)\left((r + \Delta r)^2 - r^2\right) + 8x\left((r + \Delta r)^3 - r^3\right) - 3\left((r + \Delta r)^4 - r^4\right)\right] \quad (2.7)$$
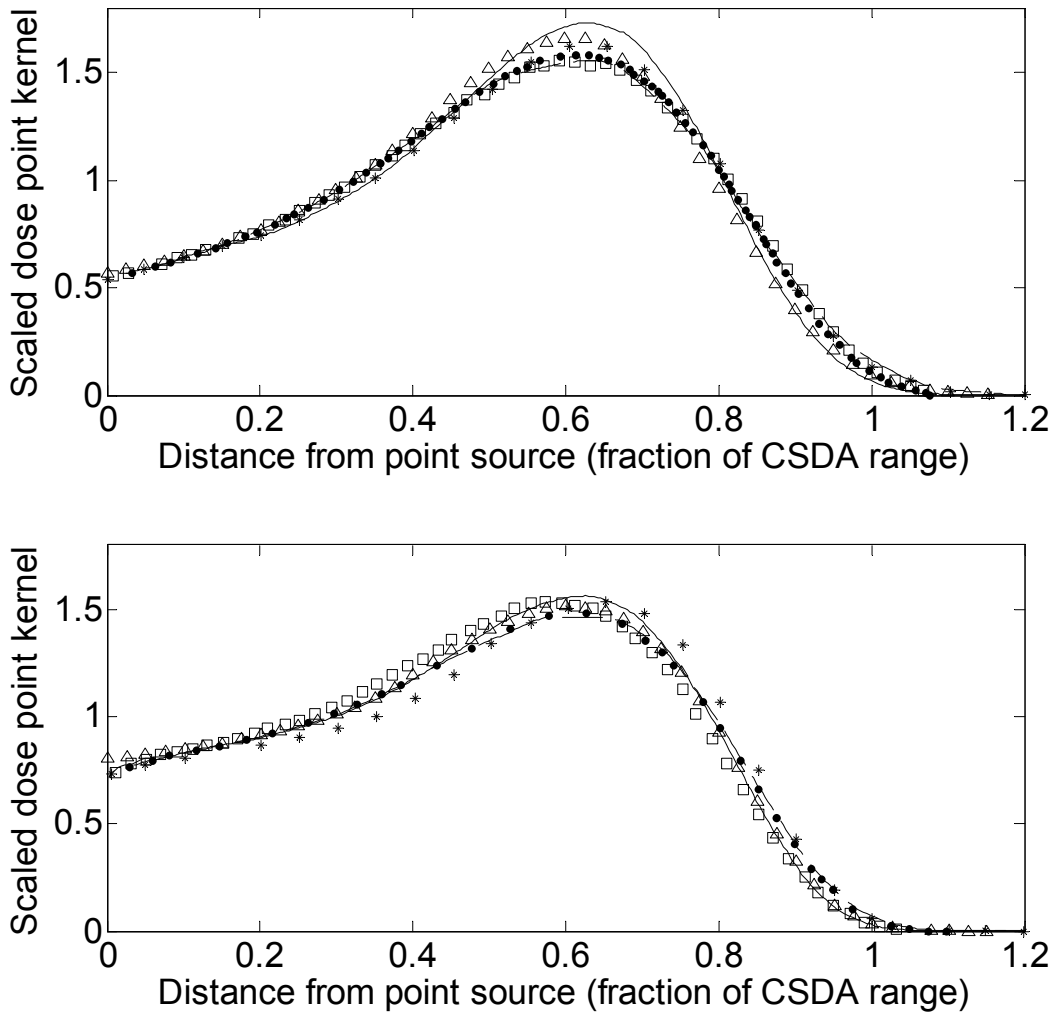
Figure 2.14. A comparison between monoenergetic dose point kernels (50keV upper panel; 1MeV lower panel) in water computed by different codes: MCNP5 (solid lines); PENELOPE2006 (dashed lines); EGSnrc (Mainegra-Hing, et al. 2004) (dots); EGS4 (Simpkin and Mackie 1990) (squares); ACCEPT (Cross, Freedman et al. 1992) (triangles); ETRAN (Berger 1973) (asterisks). Following Mainegra-Hing, et al. (2004).

where ρ is the density of the grain, r is the radius of the inner surface of the spherical shell of thickness Δr and x is the distance between point P and the centre of the grain of radius, R. This equation is derived by considering the volumes of a combination of spherical caps and then collecting terms. As $r \rightarrow x - R$ and $\Delta r \rightarrow 2R$ we get the familiar volume equation for a sphere namely $(4/3)\pi R^3$.

Using spherical shells, we can account for dose deposited at a point P from a region within a source grain, such that

$$D(x) = E_0 \int\limits_{r=x-R}^{x+R} \frac{H(r)}{m_s(r)} dr \qquad (2.8)$$

where E_0 is the average energy of the beta source, $H(r)$ is the dose point kernel evaluated between r and $r+dr$ and $m_s(r)$ is the mass of the spherical shell source region inside the grain between r and $r+dr$. In effect, the source grain is divided into a series of bounded spherical shells which are weighted according to mass. $D(x)$ now gives the radially isotropic distribution of dose surrounding the source grain. Conceptually, it is convenient to treat the source grain as a point source and $H'(x) = 4\pi x^2 D(x)$ as its dose point kernel distribution with the added condition that $x \geq R$.

The contribution of dose to a point P from the grain coating of thickness R_c is the difference between the dose delivered from a grain of radius $R+R_c$ and the dose from a grain of radius R (assuming the coating and grain are composed from identical materials).

2.6. Concluding remarks

This chapter has introduced the basic concepts of Monte Carlo modelling of beta and gamma radiation transport. The science behind its implementation is a mature area of research having heralded from the 1940's. The most challenging part of the calculation is determining an accurate condensed history approach for electron transport. The numerical algorithms of MCNP and PENELOPE are well validated although each code takes different paths: MCNP uses a Type-I method that samples exact solutions over a predetermined energy grid and decouples secondary particles; while PENELOPE uses a Type-II method that mixes the simulation of hard and soft events. Comparisons between experimental measurements and the

results from simulated analogies suggested that PENELOPE was very robust and MCNP, with recent databases, was accurate to within several percent.

Recent work in trapped-charge dating have made use of the alternative Monte Carlo code GEANT (Guerin and Mercier, 2011). A more diverse collection of transport codes will provide the dating community with an increased appreciation of the robustness of the modelling results.

Chapter 3: Granular structures

3.1   Introduction

Significant dose rate fluctuations over the alpha/beta particle range can be directly related to the granular nature of sediments; therefore, it is important to understand the geometry of packed grains for accurate modelling. Two principle reasons are: a) beta dose rate closer to a discreet source increases approximately exponentially. The expected spatial distribution of grains in the immediate vicinity of the source emissions, therefore becomes important for dosimetry; and b) it would be highly advantageous to directly relate the behaviour of radiation penetrating the sediment to the macroscopic properties of sandy sediment, such as density, packing, the grain size/shape distribution, orientation and the effective nuclear number (Z_{eff}), and in some situations parameterise these properties to account for heterogeneous dose rates.

A first approximation for calculating dose rate in granular sediments is to treat individual grains as homogeneously distributed in a matrix with $1/4\pi z^2$ probability of occurring at a distance, z, from a source. As we shall find, there is spatial structure for grains packed close to a source that precludes this approach for calculating dose rate in well-sorted sediments. For our purposes, it is unfortunate that natural sediments take an almost limitless variety of forms. As well as bulk grain size analysis and density measurements, sedimentological observations of natural sands often include stratigraphic features such as bedding structures. The dose rate modelling for these characteristics are not investigated in this study. In the first instance, one of the simplest materials to investigate is the packing of spherical sand grains, where the

inherent symmetry of each particle reduces the degrees of freedom of the system due to isotropic grain orientation. When spherical balls are randomly close packed, they have been found experimentally (by mechanical disassembly or remote sensing) to form disordered arrangements (Jaeger and Nagel, 1992, Seidler et al., 2000) with a maximum density (in this chapter, density refers to relative density *i.e.* unity minus porosity) in monodisperse (well-sorted) materials of between 0.60 to 0.64 depending on the conditions involved (Torquato, 2002). In addition, polydisperse (poorly-sorted) spherical packings are investigated. The packing models have been extended to ellipsoidal shapes, but characterisation of the geometry becomes less clear, especially for polydisperse grain size distributions and/or with mixtures of different grain shapes. Spherical packings are distorted to provide some insight into the structure of packing with anisotropic grain orientation. This chapter will be used to explore chord length distributions though pores with a view to how they may inform on the effects of dose deposition throughout the matrix.

The term "random close packing" has been traditionally used to describe the maximal non-crystalline packing of bodies and this sense is used here. However, recent investigations into the mathematical description of "random close packing" would encourage the use of "maximal random jamming" to avoid ambiguities associated with so-called "rattler" components and algorithm/experimental dependencies (Torquato et al., 2000).

3.2 Sediment variation

3.2.1 Packing density

Figure 3.1 illustrates the variety of packing densities found over a wide range of different sedimentary environments. Within each site shown, there may be different sedimentary units sampled. However, it is the typical range of packing densities is between 0.5 and 0.7.

3.2.2 Grain size distributions

To achieve more realistic granular structures, it is necessary to extend the packing for different grain size distributions. Two different regimes (see Figure 3.2) are investigated for polydisperse packings: a) well-sorted sediment (referred to as Size A) comprising spheres which span nominal grain sizes from 50µm to 200µm (the grain sizes may be scaled linearly if required) with the mean value at 100µm following a log-normal grain size distribution with 1777 smaller grains per single 200µm grain. According to the grading scale of Folk and Ward (1957) the distribution would be catagorised as "well-sorted" with a sorting score of 0.39; b) a relatively poorly sorted sediment (referred to as Size B) with approximately twice the dispersion with nominal grain sizes from 30µm to 330µm with 2935 smaller grains per single 330µm grain. This sand would be considered "moderately sorted" by Folk and Ward with a score of 0.97 using graphical methods but achieves a score of 1.03 ("poorly sorted") if logarithmic methods are used. The tails of the distributions were not sampled to prevent the number of particles required to cover all grain sizes in the packing to be prohibitively large for dose rate modelling.
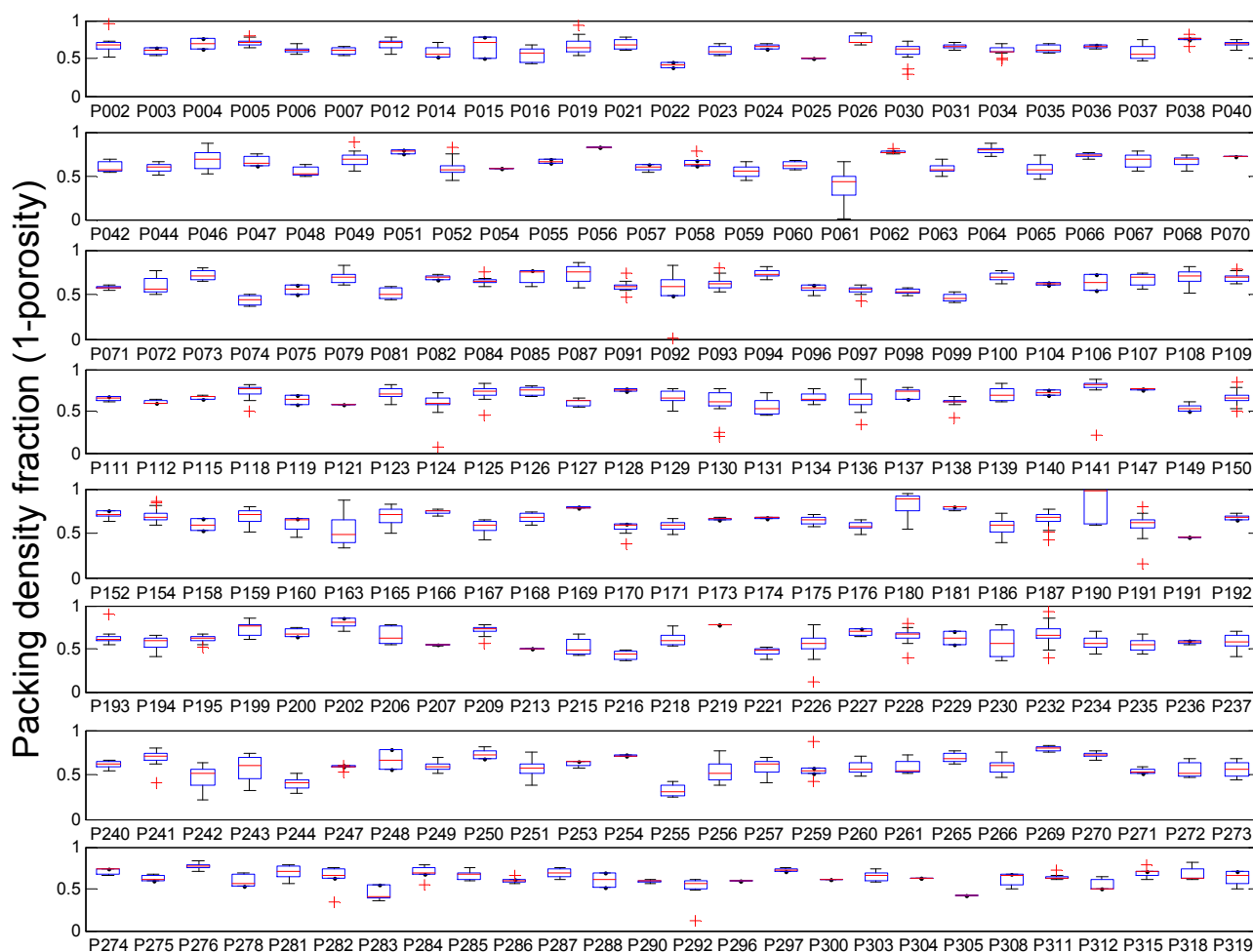
Figure 3.1. The packing density of ~3000 samples in sampling tubes extracted from sites (each project is attributed a "P" number) over several years for luminescence dating at Research Laboratory of Archaeology and History of Art, Oxford shown as box and whisker diagrams (mean, upper/lower quartiles, range and outliers are shown). Mass density of the mineral fraction is assumed as 2.65g cm^{-3}. Data from Dr J-L Schwenninger and D. Peat (pers. comm.).
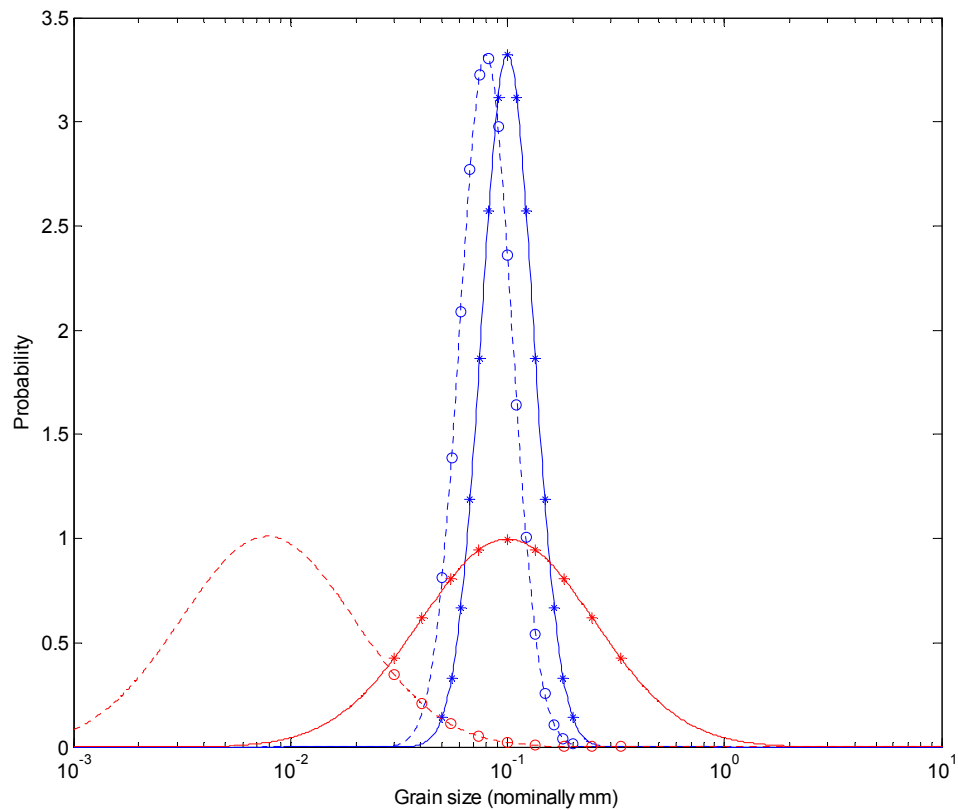
Figure 3.2. Two grain size distributions investigated by mass (solid lines) and by number (dotted lines) of well-sorted sand (Size A; blue) and poorly-sorted sand (Size B; red). The circles and asterisks refer to the sampled points in the distribution used for packing models.

3.2.3   Grain shape distributions

Grain shapes can be separated into three scales of characteristics (Barrett, 1980): 1) form or sphericity which describes the macroscopic shape; 2) roundness or angularity which summarizes the nature of the corners of the grain; and 3) the microscopic texture of the surface of the grain. The latter two have important interpretive value for sedimentologists as they may indicate the environment that the grain was exposed to prior to deposition. For the purposes of estimating the beta dose rate corrections or pore space modelling, the principle attribute

remains the overall shape since dose is primarily dependent on the compactness of the grain. Sphericity is largely unaltered during transport (Diepenbroek et al., 1992) since sphericity is inherited from the crystalline nature of the parent rock and strongly determined by the mineral type. Wadell (1935) provides an index of sphericity which is defined as the surface area of a sphere that has an equivalent volume to the grain divided by the surface area of the grain. A sphere has a sphericity value of unity and a cube has a value of slightly over 0.8. Grains are often divided into four groups which provide a basis for further analysis, according to the relationships between three orthogonal axes: spheroids (compact), rods (elongated), discs (platy) and blades. Figure 3.3 is a Zingg diagram (Zingg, 1935) of the various ellipsoidal grains with the sphericity overlain. In this case, the sphericity is calculated using $\sqrt[3]{36V^2\pi}\,/\,A$ where V is the volume of the ellipsoid (4/3πabc where a, b and c are the half length of the axes and a ≤ b ≤ c) and A is the surface area of the ellipsoid approximated using adaptive Simpson quadrature is

$$A = 2\pi\left((c^2 + b\sqrt{a^2 - c^2})\int_0^\alpha \sqrt{1 - k^2\sin^2(x)}\,dx + (bc^2/\sqrt{a^2 - c^2})\int_0^\alpha 1/\sqrt{1 - k^2\sin^2(x)}\,dx\right) \quad (3.1)$$

where $\alpha = \sin^{-1}(\sqrt{1 - c^2/a^2})$ and $k^2 = (1 - c^2/b^2)/(1 - c^2/a^2)$.

A survey of sphericity in quartz grains by Curray and Griffiths (1955) suggests a mean value of 0.75±0.08. For this study, we model the packing of three alternative shape distributions: a) a group of spheroids (referred to as Shape A) with a/b and b/c ratios fixed at 0.67 with a sphericity of 0.92; b) a group of ellipsoids (referred to as Shape B) with largely spheriodal shapes and sphericity of 0.92. The a/b and b/c ratios are restricted to within 0.5 and 1 and sampling is uniform along the isosphericity contour; and c) a group of blades, rods and discs (referred to as Shape C) with sphericity of 0.75. The a/b and b/c ratios are restricted to a

70

minimum of 0.3 and sampling is uniform along the isosphericity contour. The distributions were chosen to compare how the chord length distribution changes with either subtle or more severe aberrations of the grains from spheroids and the effects of either uniform or varied grain shapes. All grains in the distributions were normalised in size to uniform mass.
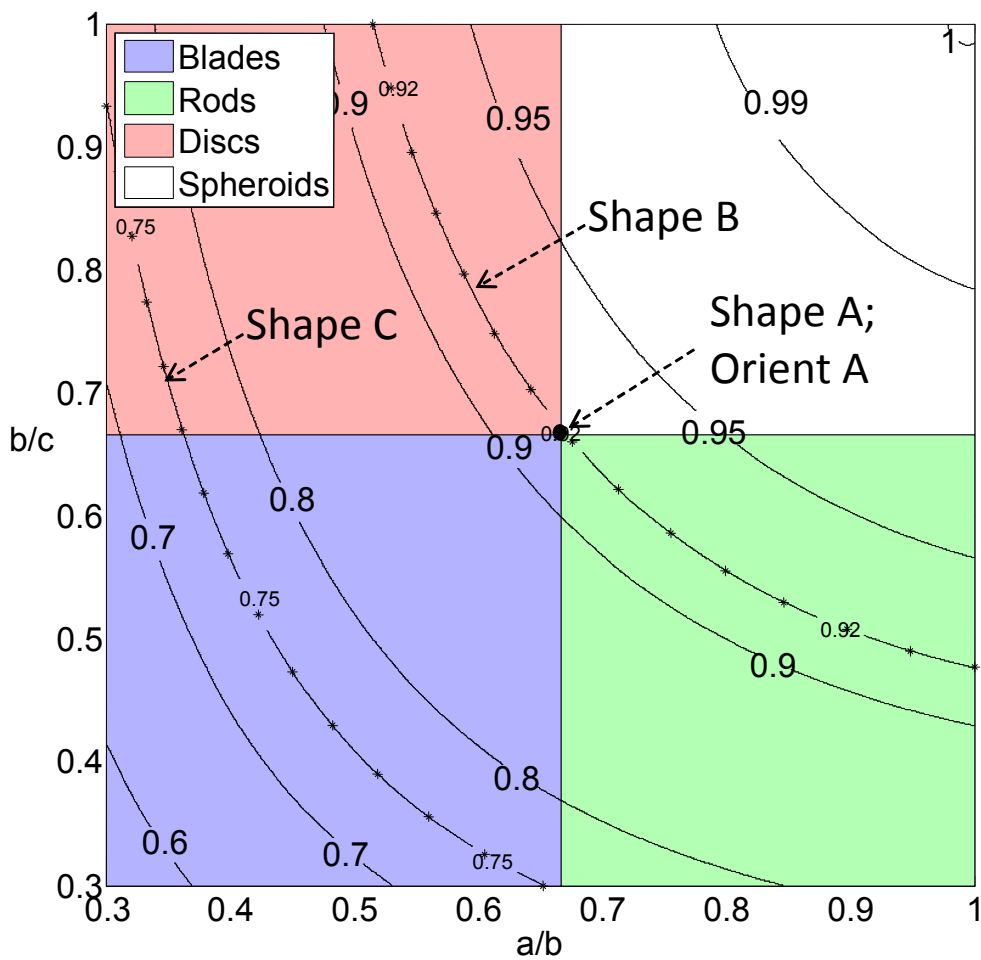
Figure 3.3. A Zingg diagram of different types of ellipsoids with a, b and c representing the short, intermediate and long axis respectively. Wadell sphericity is mapped using contour lines. Asterisks mark sampled points for grain shape distributions Shape B and Shape C (see text).

71

3.2.4   Grain orientation

Sediments are generally composed of irregularly shaped grains that commonly lead to anisotropic fabrics (Blatt et al., 1972). The orientation of sedimentary grains is usually along the long axis in hydraulic environments and it would be preferable to use this as a starting point. Although it is trivial to construct models with a bias for orientated grains, here we use a fortuitous linear distortion of the spherical packings along one dimension to form prolate ellipsoids that mimic the grains of Shape A sediment. In this case, all grains are uniform with identical orientation and this distribution is referred to as Orient A.

3.3   Packing methodology

A wide variety of mathematical approaches can be used to generate random colloidal materials. Generally, closely-packed matrices are numerically more intensive to produce and require a systematic basis for their computation.

Sparse packings may involve a simple rejection scheme where additional grains are placed into a material and are rejected if overlapping with prior grains; although reasonable for small numbers of grains, the method becomes pathological for large numbers of grains. Quasi-random closely-packed geometrical constructions have been proposed by Norman and Skolnick (1968) and Matheson (1974), where a nucleus of spheres are placed near the origin of the matrix and spheres are sequentially placed closest to the origin where they touch three spheres already packed.

Although, various other schemes have gained currency, two are particularly well-suited for the purposes of sediment reconstruction. These have been explicitly coded using MATLAB and are described below. The key consideration that must be maintained if the packings are to be used in radiation transport codes is that the spheres are strictly "hard" (i.e. there is no overlap between spheres) so that throughout the geometry, no position is shared by more than one body.

3.3.1   Drop and roll model

The "drop and roll" algorithm (Torquato et al., 2000) was initially implemented for work presented in Nathan et al. (2003) and it has the advantage of mimicking, to a first approximation, how grains are deposited in sediments. The motion of the spheres is consistent with the force of gravity (i.e. unidirectional force), with the path modified by the grains that are already packed. Balls are sequentially dropped into a volume from random starting points and may roll across surfaces of previously packed balls until either a stable position is reached when in contact with three lower balls or they land at the bottom of the volume. The sides of the volume are periodic. Once a final position is attained, the ball is considered to be randomly packed. In practice, it is necessary to play the 'game' with several starting locations and only retain for the packing the one closest to the bottom of the volume.

The "drop and roll" method has several problems. Firstly, the porosity cannot be defined as a model parameter since the algorithm automatically reduces the distribution of grains into a random close pack. Increased porosities were generated *post hoc* by stretching the dimensions of the enclosed volume causing the balls to be drawn further apart; subsequently, the balls were randomly perturbed to allow some pairs to be close together. This approach proved to be unsatisfactory as significant changes to the distribution of the balls were observed for

73

relatively small variations in the perturbation parameters. More importantly, there is no longer a basis for arguing that the arrangement of balls is physically or mathematically coherent. A second problem with the "rain" models is the anisotropic nature of the packing, especially in poorly sorted contexts where large differences in grain sizes were present through the bedding. The grains are denser along the path of gravity and it is not obvious how to remedy the situation when modelling isotropic environments. An associated issue with the algorithm was that small grains did not effectively fill voids underneath large grains. The tightest packing generated was 0.56 for 500 balls but some workers have reported densities approaching 0.58-0.60 (Visscher and Bolsterli, 1972).

3.3.2 Lubachevsky-Stillinger algorithm

The shortcomings of "drop and roll" packing were addressed with an alternative approach. The Lubachevsky-Stillinger algorithm (Lubachevsky and Stillinger, 1990) follows the dynamics and interactions of a collection of balls simultaneously in a volume with periodic boundaries on all sides. Close packing is achieved by increasing the radii of the spheres linearly with time until the required density is reached. At some stage, the velocities of the balls diverge and they become jammed. The Lubachevsky-Stillinger method is event driven (in contrast to time driven) and the algorithm progresses when either there is an elastic collision between two balls or a boundary is crossed. Overheads are reduced by maintaining only two lists that provide a schedule of events - the state of each ball (time, diameter, position and velocity) immediately after their last interaction and the predicted next interaction. Each collision is essentially a standard two-body kinematic problem with added velocity terms to account for the expanding ball radii (see Lubachevsky-Stillinger paper for details). The efficiency of the algorithm is significantly improved by using "near neighbour" filters where only spheres close to the ball undergoing an interaction are considered as candidate interaction partners. The near neighbour

74

routines were implemented by dividing the volume into rectilinear "cells" and keeping track of the balls in each cell to identify near neighbours. Figure 3.4 provides a schematic diagram of the Lubachevsky-Stillinger algorithm.

Parameters
. Cutoff density = ρ_{cut}
• Number of balls = N
• Grain size distribution = D
• Location of cell boundaries
• Dimensions of model

Initialise for i^{th} ball
• Current time, t_c = 0
• Position, $\underline{r}$ = (x,y,z) = random
• Velocity, $\underline{v}$ = (v_x,v_y,v_z) = 0
• New state, $S_{new}(i)$ = [D_i,$\underline{r}$,$\underline{v}$]
• Old state, $S_{old}(i)$ = $S_{new}(i)$
• Partner, P(i) = empty
• Next scheduled time, $T_{new}(i)$ = 0
• Last scheduled time, $T_{old}(i)$ = 0
• Place in cell(s)

Is density less than ρ_{cut}?

No

STOP

Yes

• Update current time, t_c = min(T_{new})
• i* = index which supplies t_c
• C = time of first collision of ball i* with nearest neighbours (index j*)
• B = time of first crossing of ball i* with cell boundary
• Time of next event, R = min(C,B)
• $T_{new}(i*)$ = R
• $S_{old}(i*)$ = $S_{new}(i*)$
• S_{i*} = state of ball i* at beginning of next event

B < C?

Yes

No

. $S_{new}(i*)$ = S_{i*}
• P(i*) = 0
• Assign to new cell(s)

• $T_{new}(j*)$ = R
• S_{j*} = state of ball j* at beginning of collision
• $S_{new}(i*)$ = state of ball i* after collision
• $S_{new}(j*)$ = state of ball j* after collision
• m* = P(j*); P(i*) = j*; P(j*) = i*
• If m* > 0 and m* ≠ i*
    • $S_{new}(m*)$ = advance state of ball m* to time R
    • P(m*) = 0

Figure 3.4. A schematic diagram of the Luchavesky-Stillinger algorithm for randomly close packing of spheres.

The various parameters required from the user apart from defining the problem (i.e. number of balls, grain size distribution and density) are: a) The number of cells, optimally one cell for each ball (Donev et al., 2005), is constrained by the condition that the cell dimensions must not be smaller than the diameter of the largest grain when the desired density is reached. Fortunately we can use the relationship between the set of the radii of the balls, $\underline{R}$ and (volumetric) density, ρ, so that $V\rho = (4/3)\pi \sum \underline{R}^3$ where V is the volume of the bounded model to determine the maximum diameter expected at a given density; b) Since the growth of the balls is ongoing, energy is not conserved in the algorithm, but rather increases over time. The system must be regularly restarted (ie. reinitialise the translational (and rotational) velocity of the balls) to maintain efficiency. A suitable energy threshold for resetting the model was found empirically and varied for different situations. For example, a model of 200 identical balls was restarted when any ball reached a translational velocity of 200cm/s (approximately every 1000 interactions) in a volume constructed from a cube of sides 10cm, and diameter growth of $0.1t$, where t is time in seconds; c) MCNP and PENELOPE codes require that the entire model geometry is specified without ambiguities. One of the strengths of the Lubachevsky-Stillinger algorithm is that it guarantees no overlapping of spheres. In practice, it was found that round-off errors may cause balls to overlap. At every 5000th event, all balls were advanced to the current time and the distance between them was checked. The run was discarded if ball overlapping occurred within 8 significant digits; d) The Lubachevsky-Stillinger algorithm did not reliably achieve packing of the spheres of densities greater than 0.62 in monodisperse materials and several attempts usually were needed if this was required. The packing models record to output files the state of the system whenever density changes by 0.001.

Random loose packing and random close packings are illustrated in Figures 3.5 and 3.6 respectively for a monodisperse material. There is little evidence for polycrystallinity and the

density appears to be uniform throughout the structure with the number of balls being constant to within several percent within 1000 voxel cells distributed throughout the volume. A planar horizontal slice across the middle of a random close packing is shown in Figure 3.7. The periodic boundaries, shown as black borders, reduce any spurious influences of walls. "Rattler" (locally unconstrained) balls were widespread throughout the packing. The close packings of the simulated sediments are presented in Figure 3.8. The arrangement of the balls in sediments such as Size B is consistent with a loose packing of the large spheres and a random close packing of the small balls within the interstitial spaces. Although clearer for bidisperse packings, the different sizes of balls can be considered phase separated. It should be noted that there is currently no clear understanding of the behaviour of packed polydisperse hard spheres (Torquato, 2002) and determining structural characteristics of polydisperse systems is a very active research area.
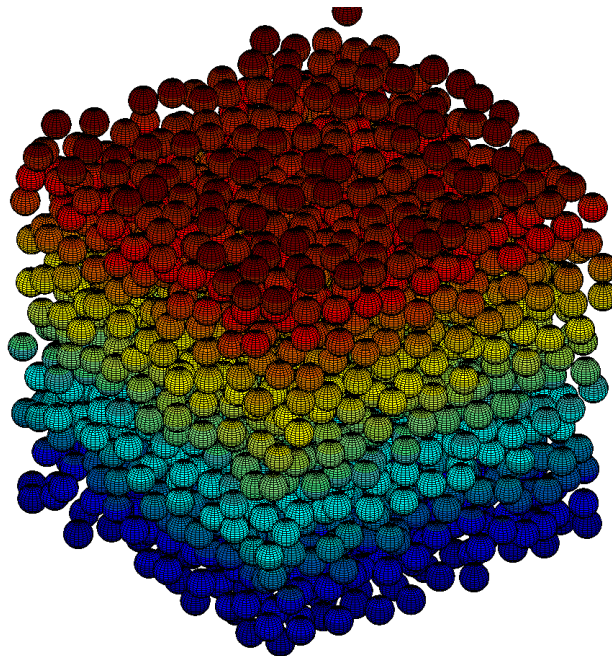
Figure 3.5. A random packing of 2000 identical spheres (density = 0.36) using the Lubachevsky-Stillinger method.
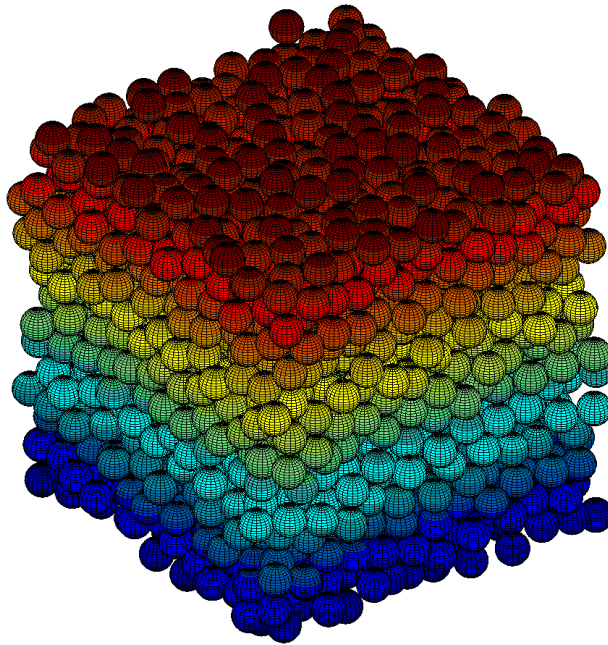
Figure 3.6. A random close packing of 2000 identical spheres (density = 0.62) using the Lubachevsky-Stillinger method. This is achieved after further iteration of the packing in Figure 3.5.
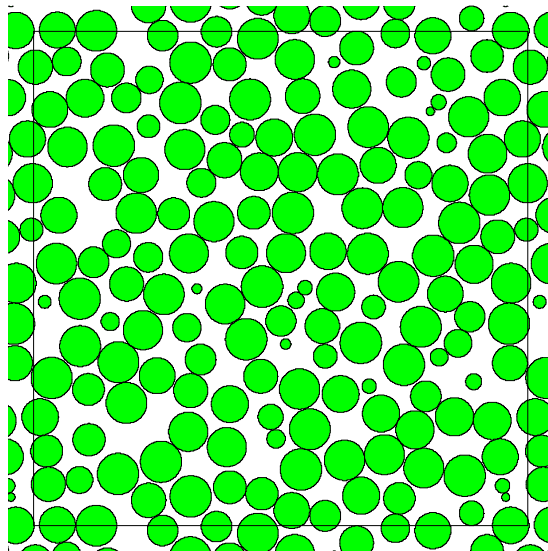
Figure 3.7. A horizontal slice through the packing in Figure 3.6. The black horizontal and vertical lines near the border of the image describe the position of the periodic surfaces.

Size A

Size B

Shape A

Shape B

Shape C

Orient A
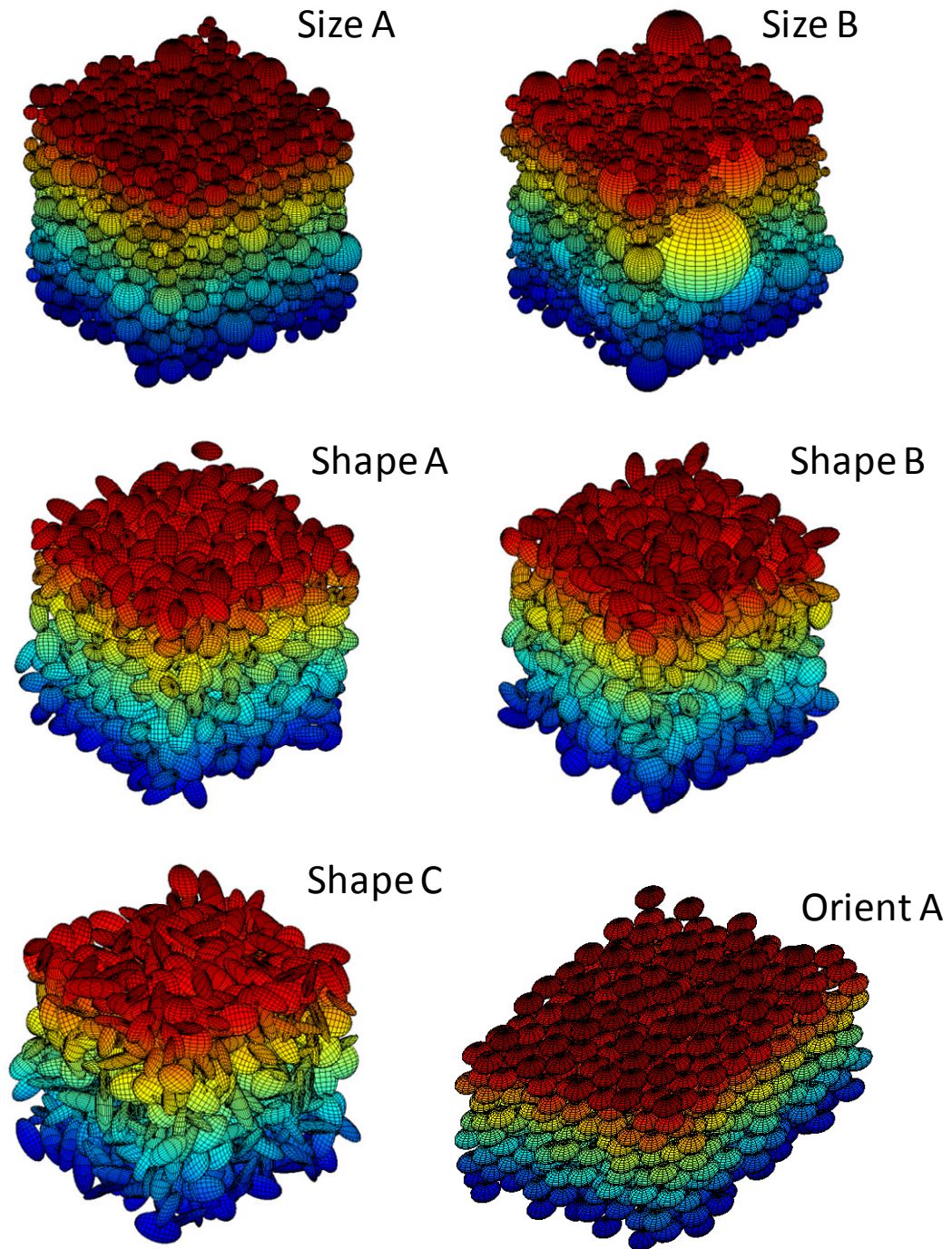
Figure 3.8. Random close packing of selected simulated sediments using the Lubachevsky-Stillinger method.

79

3.3.3   Ellipsoidal grain packing

The Lubachevsky-Stillinger algorithm was extended for the packing of ellipsoids by (Donev et al., 2005) with several additional considerations. Primarily, the rotational dynamics of the ellipsoids must be included via quaternion algebra and the nearest-neighbour algorithms take account of the non-symmetrical shape of the grains. It is expected that the maximal random packing density of ellipsoids extends significantly beyond those found with sphere and is often greater than 0.7. Donev et al. (2004) experimentally found packing densities approaching 0.70 and optimal packings of 0.74. This can be explained by the increase in contacting neighbours due to greater rotational degrees of freedom allowing unjamming to occur.

Recent research has involved packing other geometrical forms based on Platonic and Archimedean solids (Torquato and Jiao, 2009, Haji-Akbari et al., 2009) which underscores the complexity of randomly packed systems. Disordered, quasi-crystalline and crystalline phases may be found for these shapes; however, the work in this thesis is limited to ellipsoidal forms only.

3.4   Structural properties

3.4.1   Pair correlation distribution

For the purposes of dose rate estimation, a useful statistic for the packing of spheres is the pair-correlation function (McQuarrie, 1975) of the arrangement of the balls (also commonly known as the radial distribution function), $g(r)$ such that $4\pi r^2 N\rho(r) = \rho\ g(r)$ where $\rho(r)$ is the average density of particles at a radial distance between $r\text{-}dr/2$ and $r\text{+}dr/2$ from a typical particle and ρ is the average density of particles in the material. This function can be considered a weighting modifier with radial distance when applying dose point kernels. The

calculation of $g(r)$ is achieved by taking each particle in turn and counting the number of spheres that fall within each radial bin. The statistic is normalised by dividing $g(r)$ by the number of balls in the population N and by the volume of each spherical shell, $4\pi r^2 dr$. Various dose rate studies (e.g. Brennan et al. (1997)) have considered a homogeneous distribution of solids through a volume, which assumes $g(r) = 1$ for all r.

The pair correlation function of a monodisperse random close packing generated using the Lubachevsky-Stillinger algorithm is presented in Figure 3.8. Since there is no overlap of the spheres, $g(r)$ is zero for less than one radial distance. The pair correlation peaks at about one radius due to the comparatively high probability that balls are in very close proximity to each other when densely packed. Due to the concentration of near touching balls, there is a paucity of balls approximately 1.5 radially distant and $g(r) < 1$. The split second peak, which appears to be characteristic in random close packings, has maxima at $r\sim1.7$ and 2. Finney (1970) suggests the first of these peaks may correspond to a distance $r = \sqrt{3} = 1.73$ which would result from the positioning of pairs at opposite apices of two coplanar tetrahedra. The peak at $r = 2$ reflects the appearance of collineations of three balls (Bernal, 1964) and the leading spread is consistent with small perturbations of the collineation angle from π. Donev et. al. (2005) found a pronounced discontinuity at this distance reflecting strong local order. As the radial distance increases, $g(r)$ follows a dampened oscillation about unity with $g(r) \rightarrow 1$ as $r \rightarrow \infty$ since random packing is by definition a disordered structure on a macroscopic scale. A comparison of a pair correlation function calculated by the Lubachevsky-Stillinger algorithm is made against the models constructed using purely geometrical methods (Finney 1970) and the data collected from CT scans of a sandpile (Seidler et al., 2000). The results are shown in Figure 3.9 and there is a broad similarity between the different approaches. It should be noted that each dataset needed to be scaled and/or shifted vertically so that a direct

comparison could be made. It remains unclear why *g(r)* was not immediately compatible across datasets.
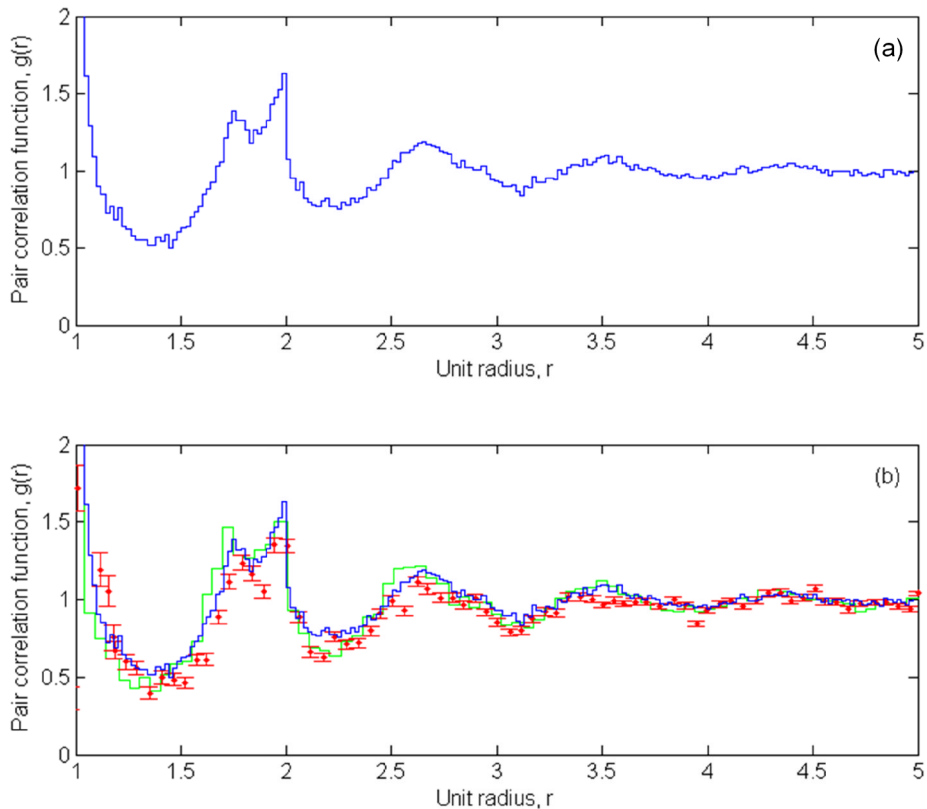
Figure 3.9. The pair correlation function of random close packing of spheres. (a) Results from the packing illustrated in Figure 3.6. (b) Comparison with modelled packing (blue) to results from Finney (1970) (green) and Seidler (2000) (red).

The behaviour of the pair correlation function as the density of the packing increases is demonstrated in Figure 3.10. One aspect of interest is the location and breadth of peaks as density changes since this has direct bearing on the modification of dose point kernels to the packing structure. In very loose packing with densities less than about 0.3, the only significant feature is the first peak at one radius distance and an associated tail from this peak up to *r ~ 2*.

As the density increases from 0.3 to 0.5, further peaks in $g(r)$ become evident. The development of the split second peak is found for close packings with densities greater than 0.5 and the oscillations become more pronounced.

The pair correlation function can be applied to poorer sorted materials such as distributions Size A (well-sorted spheres) and Size B (poorly-sorted spheres). In bidisperse cases, $g(r)$ commonly retains little structure apart from peaks with significant tails associated with r equal to the small and big ball diameters. A third significant peak is present for the average ball diameter. As the number of grain sizes becomes more disperse, the collection of pair correlation peaks increases (see Figure 3.11) which can be regarded as the undersampling of $g(r)$ for the true continuous grain size distribution. For the Size A sediment, the oscillatory and continuous nature of the underlying behaviour is apparent after smoothing. As the grain size distribution becomes broader, pair correlation is damped due to the increased number of possible packing configurations. In addition, the predominance of the small grain sizes tends to skew the pair correlation behaviour to these grain sizes. The pair correlation function is naturally smoothed for ellipsoid packings since the orientation of the grains additionally perturb the distance between solids.
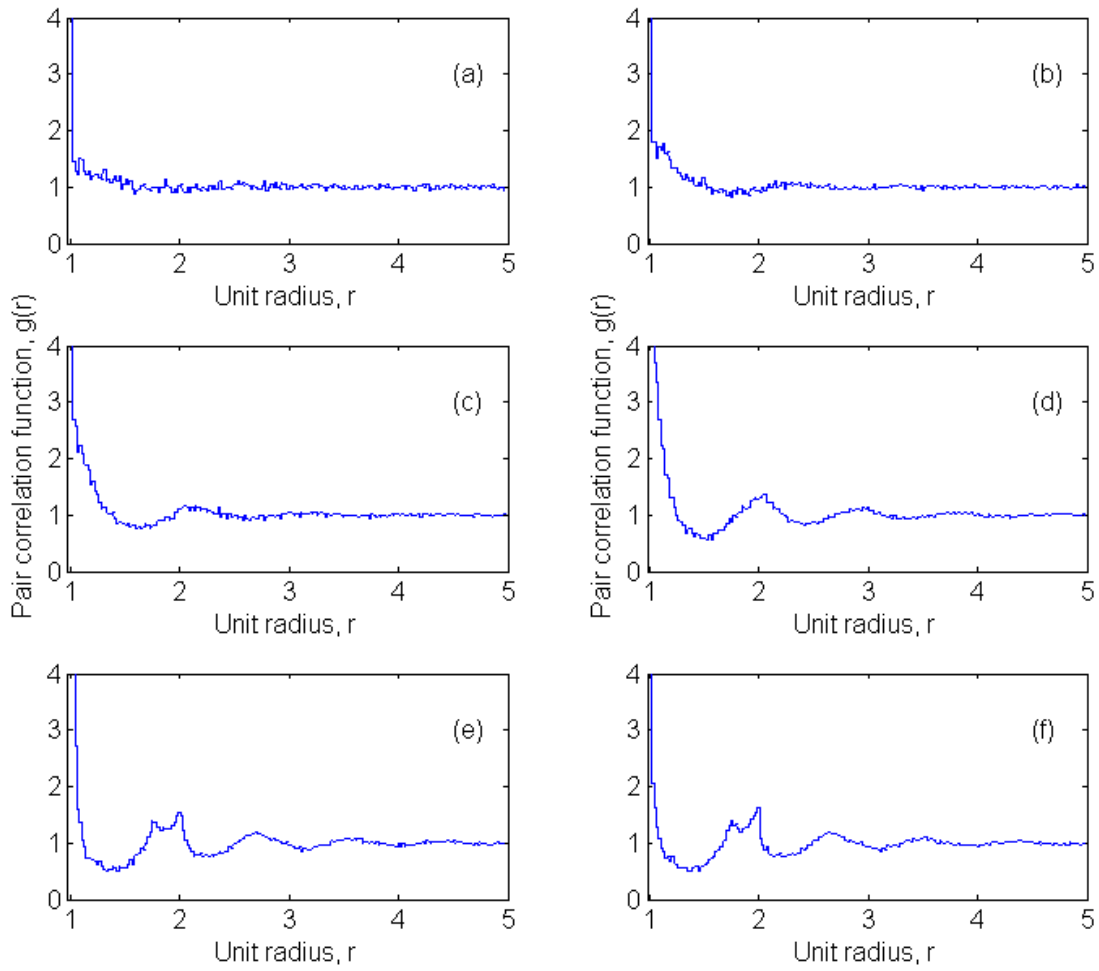
Figure 3.10. The development of the pair correlation function for random close packing of spheres at densities: (a) 0.15; (b) 0.24; (c) 0.36 [refer to Figure 3.5]; (d) 0.48; (e) 0.60; (f) 0.62 [refer to Figure 3.6].
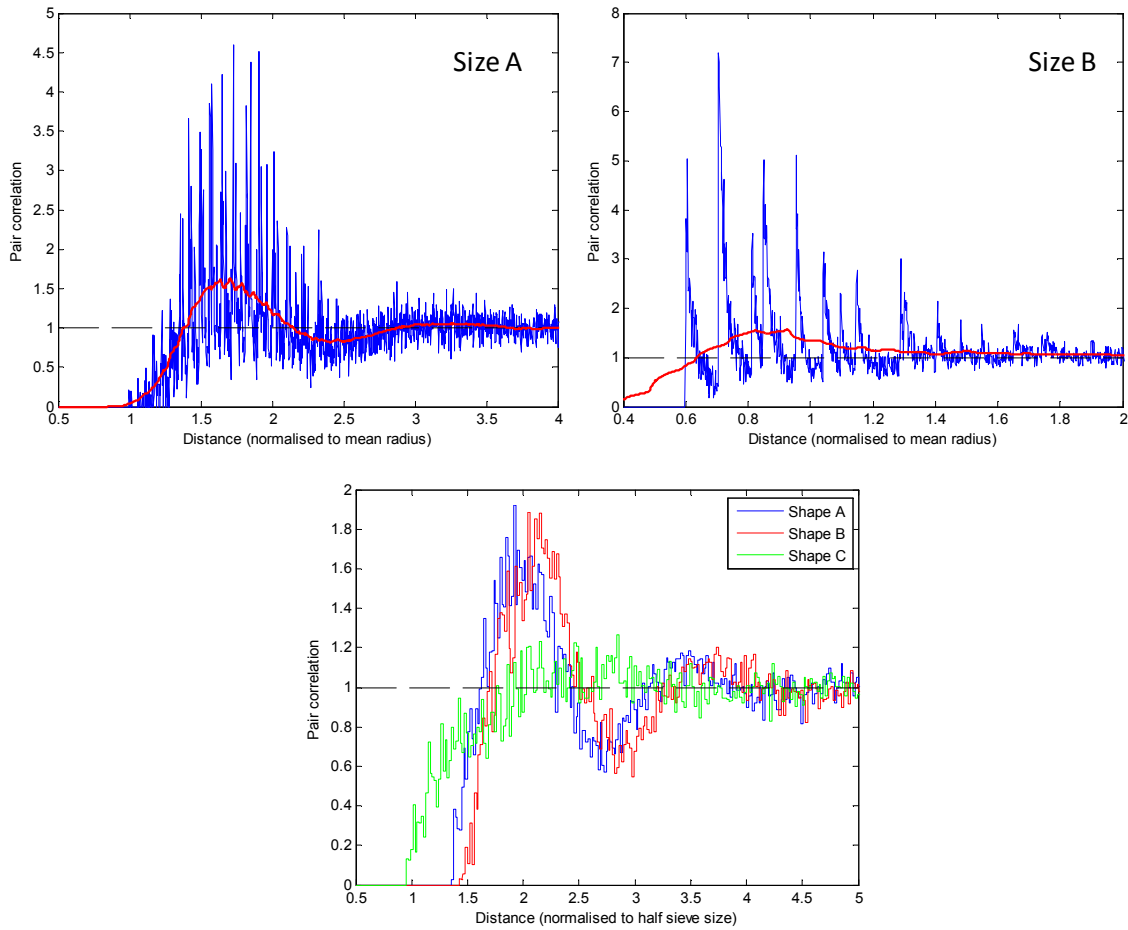
Figure 3.11. Pair correlation functions of different simulated sediments in random close packing. Distance is normalised to either mean radius by mass (sphere packing) or half the mean sieve size (ellipsoid packing). The red line in Size A and Size B plots is the smoothed function.

3.4.2 Chord length distribution

It is of considerable interest to assess the distribution of track lengths across the grains and pore spaces since this is directly correlated with changes in the secondary electron flux within the sediment. In Chapter 4, these distributions will be used to inform of appropriate corrections to the infinite-matrix dose rate if interstitial material, such as water, enters the system.

The chord lengths were computed using Monte Carlo sampling methods for various densities of the simulated sediments. For a large number of draws, a starting location and three-dimensional direction of a straight-line ray was randomly selected and the track lengths were measured for every sphere/ellipsoid boundary intercepted. The periodic nature of the packing allowed a relatively large volume to be generated from a small number of grains (around 1000) and thereby significantly increasing the efficiency of the calculation. Figure 3.12 illustrates the sampling of a draw history.
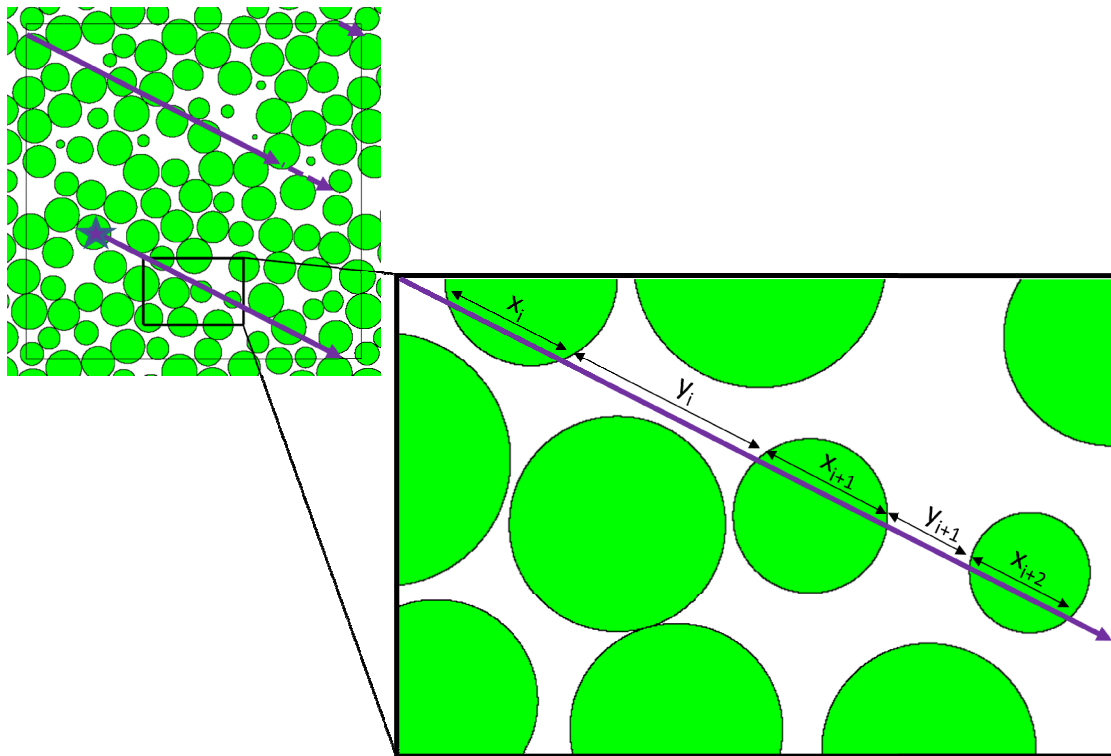
Figure 3.12. An illustration of the computation to find the grain and pore space track length distributions in a random packing of grains (here 1000 grains of unit radius with density 0.64 and periodic boundaries). A random source location and direction is sampled isotropically and continues across a large number of grains. Each time a grain boundary is crossed, the track distance is calculated (here x for grains and y for pores).
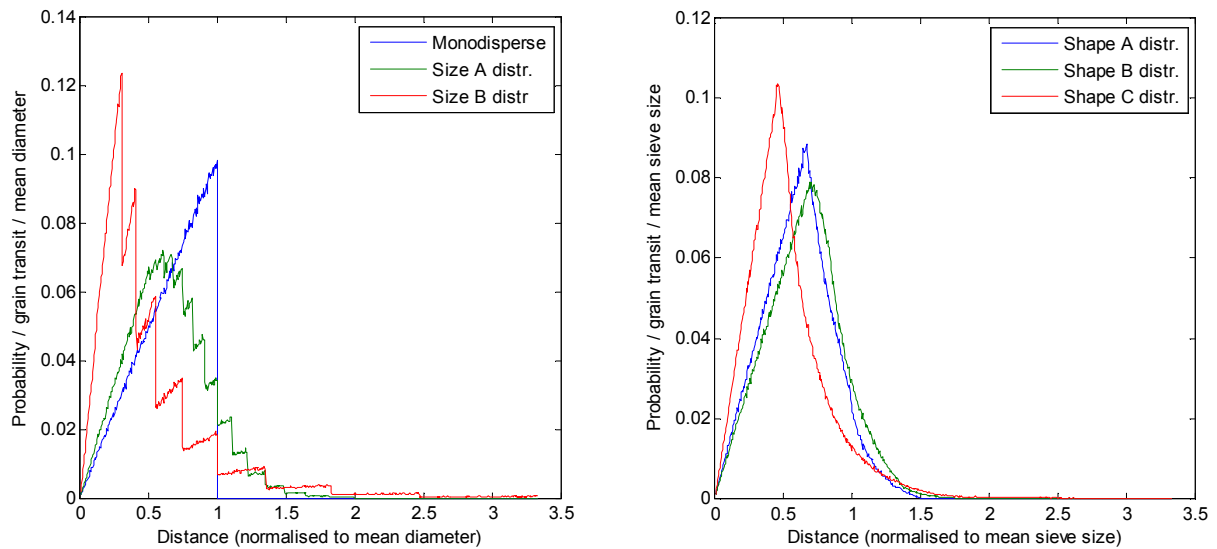
Figure 3.13. The chord length distribution within grains from the different simulated sediments. Left graph is for packed spheres and right graph is for packed ellipsoids (see text for details).

The chord length probabilities within the grains are shown in Figure 3.13 and provide a check for numerical modelling as they match to theoretical distributions within precisional uncertainty. The stepping features of the Size A and Size B sediments arise from the integrated chord length distributions for the different grain sizes; however, since Size B is a broader grain size distribution, the chord lengths are sampled predominately for the smaller grains and the distribution becomes biased to shorter chords.

The chord length distribution in pores for various packing densities of monodisperse spheres is presented in Figure 3.14. Several features of these distributions are evident: 1) the chord length distribution is a little greater than the modal value, and is approximately exponential with slope dependent on the density of packing. Lu and Torquato (1993) show that the result has a theoretical basis and it is supported in numerous experiments (Pavlovitch et al., 1991, Cousin et al., 1996); 2) the nature of the L-S packing algorithms tend to minimise the number of close

neighbours since the frequency of modelled events for near jammed bodies rises dramatically. It is evident in Figure 3.14 that the probability for shorter chord length follows non-exponential behaviour and this can be considered an unfortunate artefact of the packing (i.e. fewer touching grains than expected). By contrast, for other algorithms this effect is insignificant, such as geometrical placement models; 3) a subtle change in slope of the probability occurs for chords around 0.7 mean diameter length. This has not been investigated but it is presumably an artefact of a specific entropy state. Lu and Torquato (1993) argue that the exponential slope of the chord length distribution after distance is normalised by grain size is proportional to density/(1-density). We have applied this density correction to the chord length distribution and it is clearly successful (see Figure 3.15). Slope constants ranging from -0.75 (for random close packing) to -0.80 were found which compares well with a theoretical value of -0.75.

The change of the chord length distributions for different sediment types (see Figure 3.16) is most pronounced for the more heterogeneous sediments (Size B and Shape C). At high packing densities, the Size B grain size distribution exhibits a pronounced excursion from exponential behaviour for longer chord lengths, while both Size B and Shape C display significantly different slopes from the other sediments. In addition, for these two sediments the likelihood for short chords across the voids is significantly elevated. This may be explained by the increased partition of the pore spaces by interrupting bodies; for Size B by small grains and for case C by part of the elongated ellipsoids. In summary, if we state that the chord length distribution, $p(z/R)$, demonstrates exponential behaviour after chord length $z/R = z_0$ where z_0 has been found to occur after approximately one normalised distance unit then $p(z/R > 1) = xe^y$ and Table 3.1 presents results for selected densities.
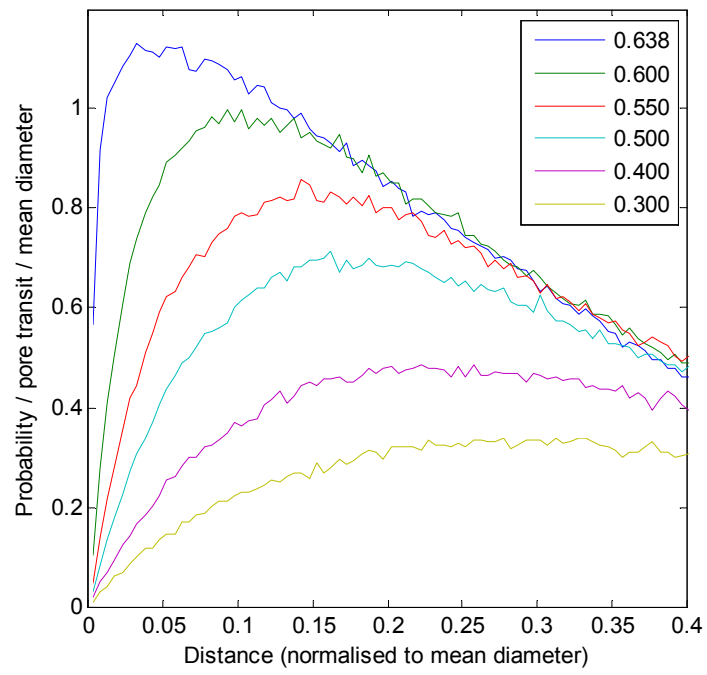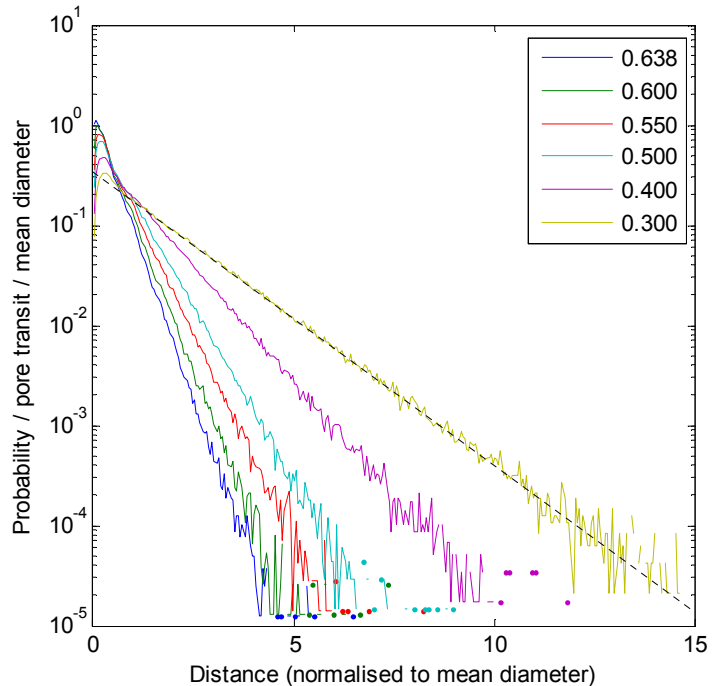
Figure 3.14. The chord length distributions across pore spaces for random monodisperse packing of spheres with different densities (top) and an enhanced view of shorter chord lengths (bottom). The dotted line (top) illustrates the exponential behaviour of the distribution.
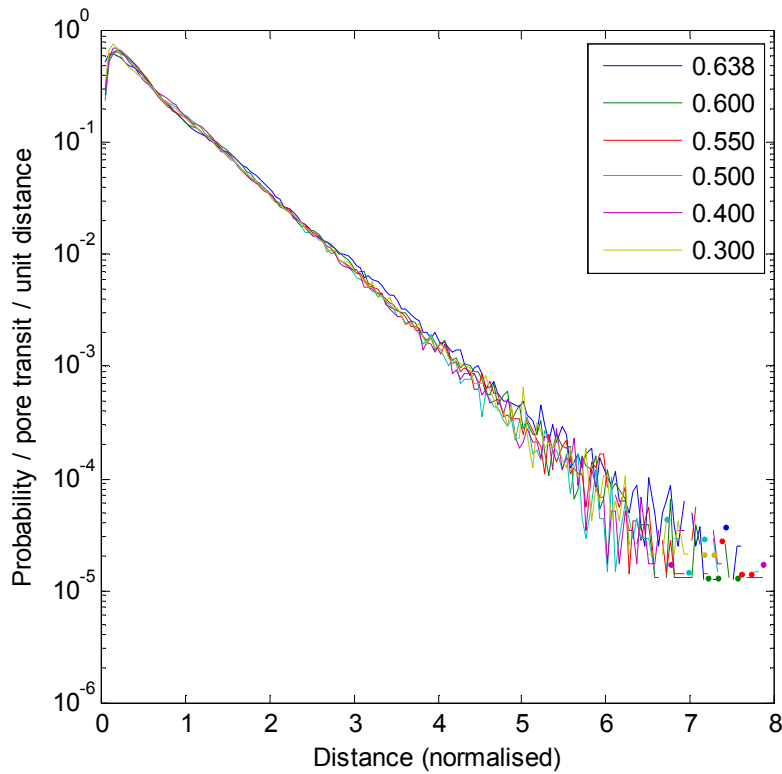
Figure 3.15. Chord length distributions for density and size normalised distances for monodisperse packings of spheres at different densities.

Sediment	Density	*x*	*y*
Monodisperse	0.638 (max)	-0.29	-0.75
	0.500	-0.17	-0.80
	0.300	-0.23	-0.78
Size A	0.656 (max)	-0.28	-0.77
	0.500	-0.13	-0.83
	0.300	-0.24	-0.80
Size B	0.719 (max)	-0.41	-0.84
	0.500	-0.06	-0.97
	0.300	-0.06	-0.96
Shape A	0.721 (max)	-0.31	-0.78
	0.500	-0.13	-0.86
	0.300	-0.17	-0.85
Shape B	0.712 (max)	-0.36	-0.73
	0.500	-0.19	-0.80
	0.300	-0.25	-0.78
Shape C	0.666 (max)	-0.46	-0.82
	0.500	-0.15	-0.94
	0.300	0.08	-1.03

Table 3.1. Intercepts and slopes of lines of best fit for the exponential relationship between density-corrected chord length in a pore space and probability for various simulated sediments.
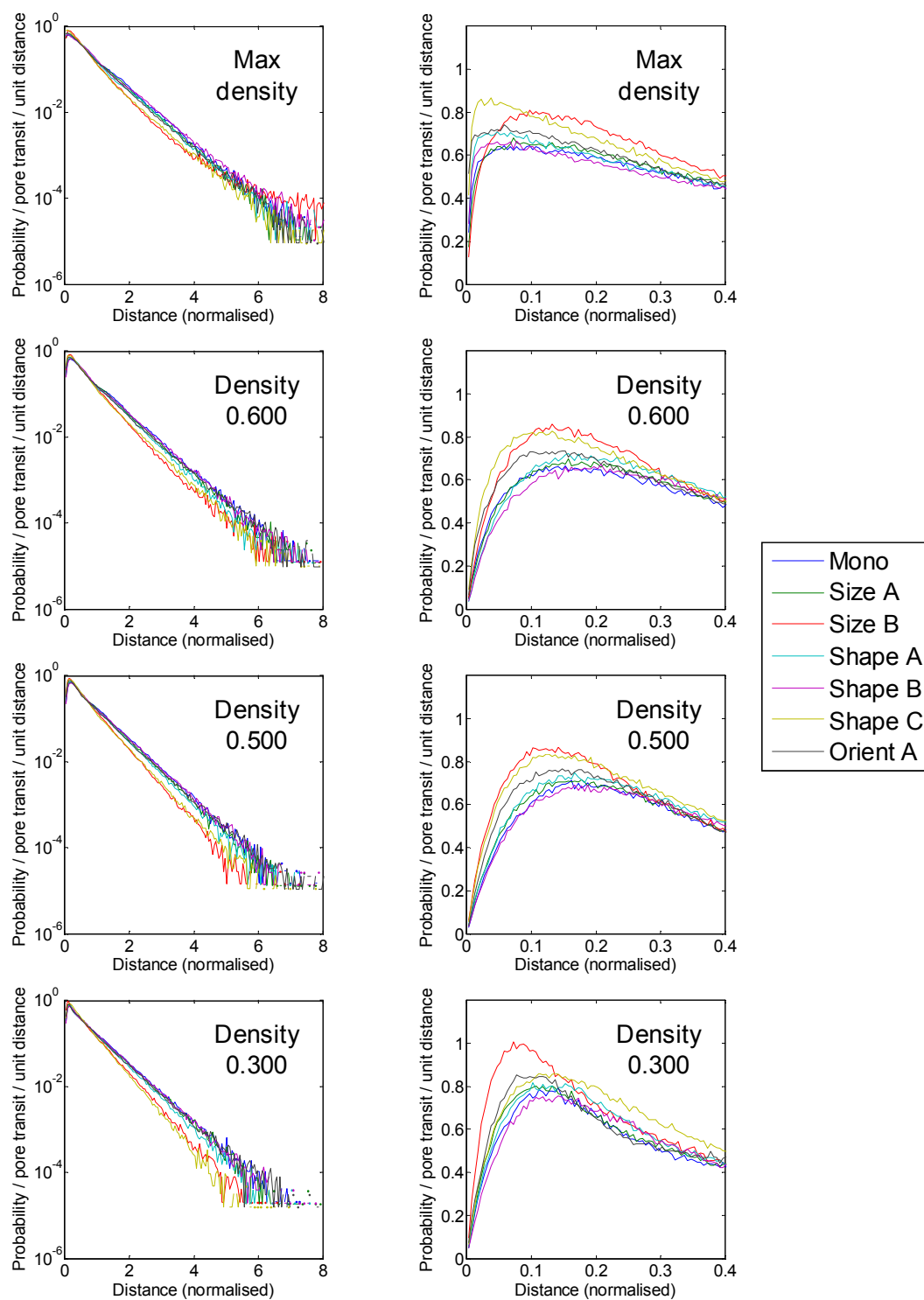
Figure 3.16. Density normalised chord length distributions for the different simulated sediment types with varying packing densities after density and grain size normalisation of distance.

3.5   Concluding remarks

The Stillinger-Lubachevsky algorithm has enabled a variety of simulated, randomly-packed sediments to be used for modelling dose rate issues. These are 1) a monodisperse collection of spheres; 2) a well-sorted collection of spheres called Size A; 3) A poorly-sorted collection of spheres called Size B; 3) a monodisperse randomly-orientated ellipsoid called Shape A; 4) a collection of near-spheroidal grains called Shape B; 5) a collection of ellipsoids with poor sphericity called Shape C; and 6) a monodisperse ellipsoid with uniform orientation called Orient A. All packs were shown to have structure in the packing over the scale of several radii. The chord length distribution was exponential for lengths greater than one radius. The sediments Size B and Shape C were the most anomalous in their structure since they consisted of the most diverse sizes or shapes. The other sediments were surprisingly similar in structure.

Implementation of the grain packing in the geometry inputs for radiation transport models was performed automatically using MATLAB script. Unfortunately, MCNP did not allow periodic surfaces on all six boundaries of a cube while PENELOPE had no card options to select periodic surfaces whatsoever. Both codes were modified to allow for any coupled planes to become periodic surfaces with simple input file flagging. Due to the high number of grain surfaces, PENELOPE was favoured over MCNP (see Chapter 2) and only PENELOPE was used in subsequent analysis.

Chapter 4: Water content correction

4.1 Introduction

The water content correction was implemented relatively early in the development of luminescence dating, but it has been a somewhat neglected subject for improvement, despite its potential importance for dating accuracy. Since the correction implicitly uses the assumption that radioactive isotopes are uniformly distributed throughout the sediment, a good first-order approximation of the correction can be made through kerma approximations.

The water content correction (see Equation 1.6; $\dot{D}_{\alpha,\beta,\gamma} = \left(\dot{D}_{\alpha,\beta,\gamma}\right)_{dry} / \left(1 + x_{\alpha,\beta,\gamma}\left(m_w / m_s\right)\right)$) was first proposed by (Zimmerman, 1971) with a brief statement of the formula to be applied and with the associated ratio of mass stopping power or mass absorption coefficients (here called x_β and x_γ respectively after the nomenclature of (Aitken and Xie, 1990)). The calculation is based on correcting for both a) the dilution of the activity in the wet sediment compared to the dry sediment which is proportional to the ratio of mass of water to dry sediment and b) the different energy absorption characteristics of dry sediment and water which is summarised by the parameter x. Zimmerman treats beta and gamma radiations in a similar way, with corresponding correction equations and aluminium as a proxy for soil in both cases. According to his D. Phil. thesis, the mass absorption coefficients are calculated for 1MeV photons ($x_\gamma \cong 1.14$) from data of Berger and Seltzer (1964) and the mass stopping powers are averaged over 0.1-3 MeV electron energies ($x_\beta \cong 1.25$) from data of Evans (1955). No arguments or calculation details are supplied

to support the water content correction and it remains unknown the assumptions that Zimmerman used. A first-order sensitivity test of the correction to different values of x is illustrated in Figure 4.1. For small quantities of water in the sediment (<10%), the correction is insensitive to the exact value of x. As the water content increases, the correction diverges for different values of x and an accurate evaluation of x becomes increasingly important.
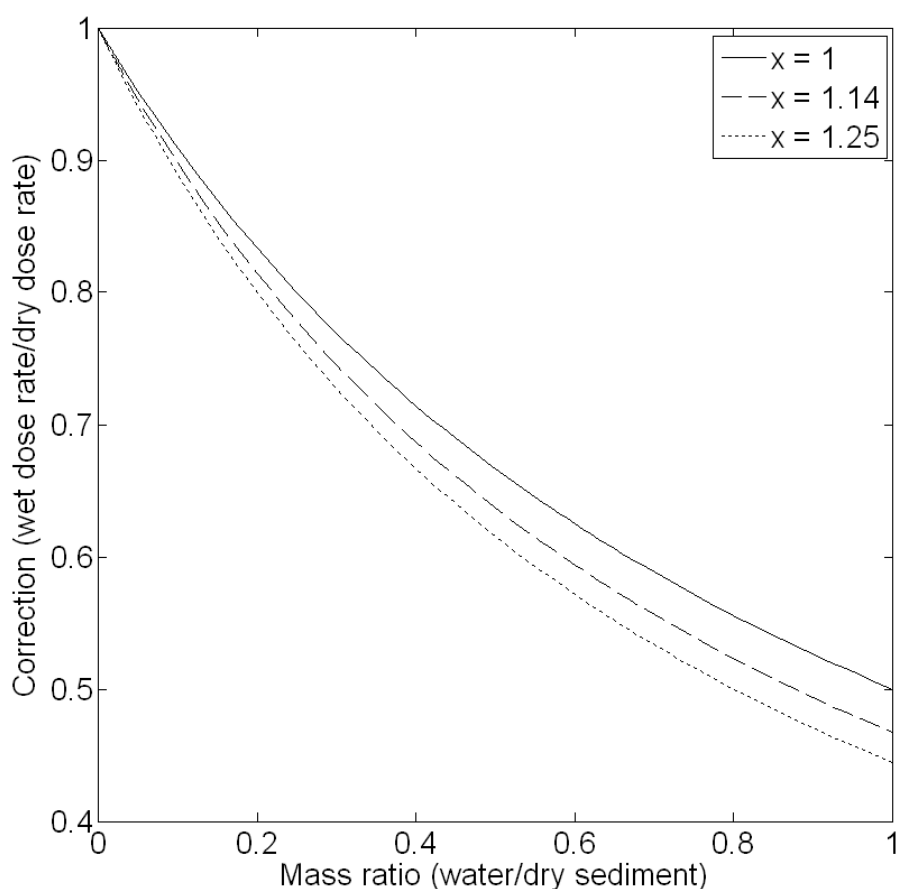
Figure 4.1 Graph showing the sensitivity of the water content correction (Zimmerman, 1971) to different estimations of x. The three x values correspond to a scenario where water has the same energy absorption properties as sediment ($x = 1$), the Zimmerman value for the gamma correction ($x = 1.14$), and the Zimmerman value for the beta correction ($x = 1.25$).

Readhead (1987) revisited Zimmerman's approach and weights the stopping powers (and absorption coefficients using the energy fluence) in a more comprehensive treatment using

$$\bar{S}_s^w = \frac{\int_0^{E_{max}} \Phi_e(E) \frac{\left(\frac{dE}{\rho dx}\right)_{water}}{\left(\frac{dE}{\rho dx}\right)_{quartz}} dE}{\int_0^{E_{max}} \Phi_e(E) dE} \qquad (4.1)$$

A range-energy approximation accounts for the probability density of the degraded electron energy spectrum, Φ_e. The photon degraded spectrum (primary + secondary) Φ_p was derived using methods of Fano *et al.* (1959). Readhead calculates the values of $x_{\alpha,\beta,\gamma}$ for the decay groups of uranium and thorium and ^{40}K and ^{87}Rb and gives associated uncertainties without explanation. The paper reports x_β for coarse grains as 1.205 ± 0.022 uranium, 1.207 ± 0.022 thorium, and 1.207 ± 0.052 potassium and x_γ as 1.094 ± 0.032 uranium, 1.094 ± 0.051 thorium, and 1.113 ± 0.121 potassium. Readhead suggests that the m_w / m_s term is the mass of water "as a fraction of the total mass". This leads to a severe underestimation of the water content correction compared to Zimmerman by approximately 45-90% depending on the water content if "total mass" refers to the wet sediment. It remains unclear that this was the intention of Readhead.

A third paper by (Aitken and Xie, 1990) attempts to reformulate the calculation of x_γ using the published U, Th and K infinite-matrix spectra of (Jain et al., 1979) for the kerma dose. Their approach used

$$\frac{D_w}{D_d} = \frac{\sum (\mu_a)_q E(\Phi_p)_w}{\sum (\mu_a)_q E(\Phi_p)_d} \qquad (4.2)$$

and it follows from Eq. 1.6 that

$$x_\gamma = \left((D_d / D_w) - 1\right) \frac{m_s}{m_w} \qquad (4.3)$$

95

The sedimentary environment is assumed to be either sandstone or shale and x_γ was found to be approximately 1.065 in shale with $m_w / m_s = 0.26$ (uranium and thorium values are several percent lower than for potassium). The key differences between this approach and Zimmerman's are that the kerma is for quartz only and the photon energy fluence is different between dry sediment and wet sediment. The implications of the Aitken and Xie paper is that x_γ is no longer independent of water content and must be determined for different values of m_w / m_s. The authors do not explore in any detail the variation and the sensitivity of x_γ to water content levels since they were limited to the published infinite-matrix spectra. A number of difficulties are readily acknowledged in the article regarding the appropriateness of using the value of x_γ to compute the water content correction in sedimentary environments for two types of situations, namely a) for compact samples, such as flint, calcite and teeth, the fluence will be perturbed near the material and the estimation of kerma should be modelled and b) no accounting is made of the ionisation partition of water and sediment over the charged particle range. A portion of their discussion addresses the issue of which fraction of the secondary charged particle flux is in equilibrium and therefore can be treated as a correction with x_β. The conclusions from the analysis would suggest that x_γ should be taken as a mid-point between 1.065 and the Zimmerman x_β value of 1.25 which is approximately 1.14 (the original Zimmerman value of x_γ) for a ubiquitous application of the gamma correction, 1.065 for compact samples and 1.19 (an updated value suggested by Aitken and Xie) for silts.

With the use of numerical radiation modelling, it is possible to directly assess the water content corrections and test whether the theoretical approach is sound for beta and gamma dose rates. In particular, the reduction of the mathematical complexity of the system by invoking CPE to one degree of freedom (ie. only a dependence on energy) can be examined. It is important to note that the water content correction has made use of more advanced types of cavity theory, particularly

the Spencer-Attix (Spencer and Attix, 1955) incorporation of secondary electron effects and the more comprehensive treatment of Burlin (1968) that includes the corrections for larger cavities.

This chapter provides a more sophisticated water content correction to that proposed by Zimmerman and extend the correction to include other interstitial material. Some discussion is made of the behaviour of secondary electrons and their influence on the differences in dose deposition between water and sediment. Numerical modelling is applied to revise and check the correction within simulated sediments.

4.2   Dose deposition behaviour

4.2.1   Introduction

Dose arising from beta and gamma sources is absorbed primarily from the interaction of charged particles with matter. The mass collisional stopping power of electrons and associated CSDA (continuous slowing down approximation) range of various sedimentary materials is presented in Figure 4.2. The charged particle fluence is comprised of beta electrons with associated degraded energy spectrum, the secondary electrons generated by gamma interactions with associated degraded spectrum and the delta (knock-on) electron spectrum. If the medium is homogeneous and the sources are uniformly distributed, the charged particle fluence can be assumed to exist in equilibrium. In this case, the dose estimation is the product of the mass collisional stopping power (of the form derived by Bethe (Segrè, 1953) and modified by later workers to include a number of atomic and statistical corrections) and charged particle fluence, which is integrated over the delta-free energy spectrum. For sedimentary contexts, the presence of delta particle equilibrium is a convenient fiction but may lead to significant inaccurate estimation in various circumstances – some of these will be addressed in this chapter.
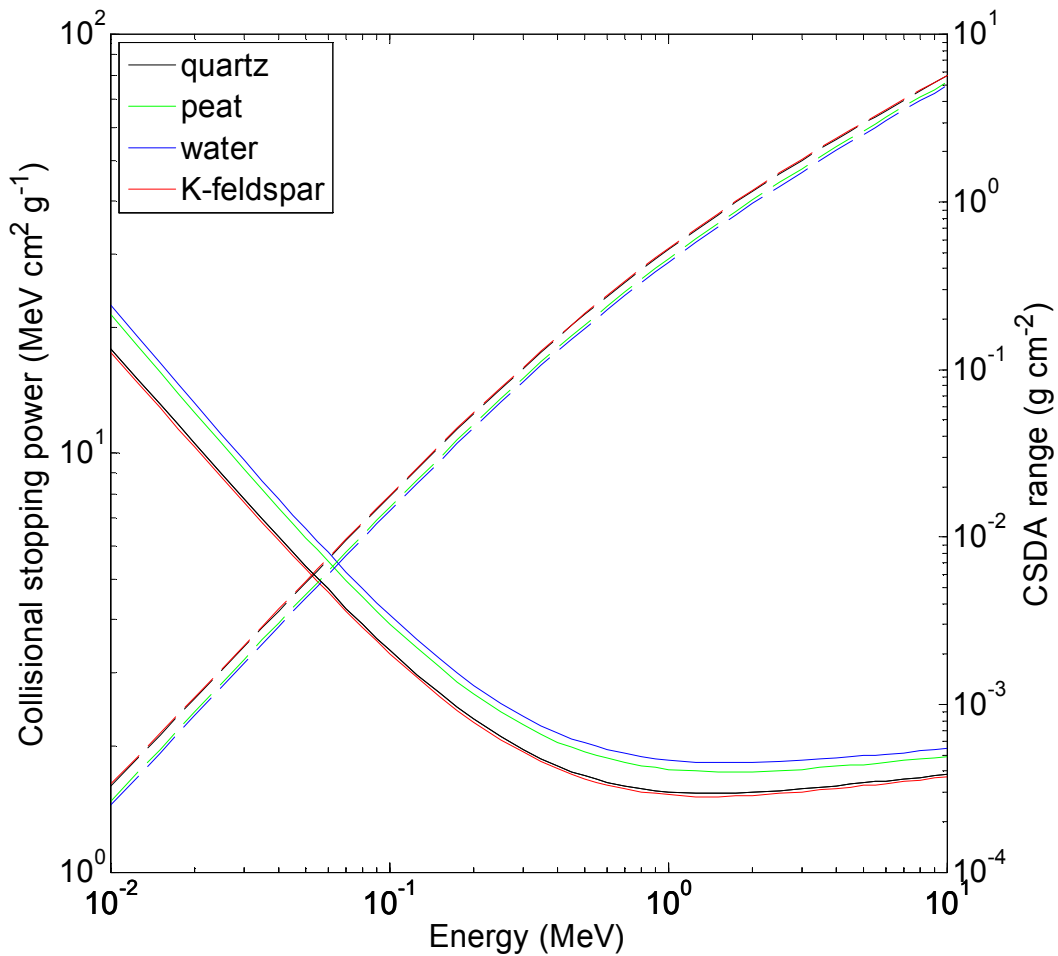
Figure 4.2. Stopping power (solid lines) and CSDA range (dashed lines) data for electrons traversing different madia. From Berger *et al.* (2000) (±2-3% for 10-100keV and ±1-2% for >100keV).

4.2.2 Infinite-matrix particle fluence

MCNP5 was used to generate the particle fluence in a uniform medium with homogeneously distributed sources. This was accomplished most efficiently by scoring, using the f4 tally, the particle flux inside a large (IM) body with a point source at origin. The charged particle fluence in an "average" sediment arising from typical radionuclide sources is presented in Figure 4.3. The

gamma fluence is substantially higher than for beta sources due to the greater average kinetic energy of the particle released during nuclide decay. The characteristic shape of the charged particle fluence is modulated by the primary source energy spectrum and the stopping power values. Since interactions of electrons of energy E_0 traversing a material will produce delta particles with energies of up to half E_0, the higher energy region of the fluence is composed solely of the degraded primary electrons. The charged particle fluence is biased toward the lower energies due to the preponderance of low energy beta emissions and photon-generated electrons. If delta particles are not considered, the degraded energy spectrum deteriorates for energies lower than around 50-100keV as the stopping power of the medium rises substantially. However, if delta particles are included, the low energy fluence remains relatively intact due to the collisional nature of energy loss where secondary particles gain kinetic energy. The size of the uniform region over which the delta particle equilibrium is assumed to remain intact can be judged from the range at the top axis of Figure 4.3. Clearly, the delta-ray population only becomes significant compared to the fluence of primary charged particles across distances of less than 1-2mm. Over distances less than 100 microns (~100keV) in media with densities (the range values can be scaled inversely with density) of 1g cm^{-3}, the delta particle fluence becomes an increasingly important contributor to the total fluence. Additionally, the graph is overlain with the weight that should be attached to the delta particles below a given energy in terms of absorbed dose. Over half of the dose is delivered by charged-particles above 100keV, while across scales of coarse sand grains (80-300μm) the lack of delta particle equilibrium would affect 20-50% of the total absorbed dose. The extent of the variation in dose due to the perturbation of delta particle equilibrium requires an examination of the contributing factors of charged particles traversing through non-uniform media. In particular, as the effective Z of the material increases, the peak of the fluence will tend to occur at higher energies for gamma sources and the relative decline of primary charged particles at lower energies will be more rapid for both beta and gamma sources.
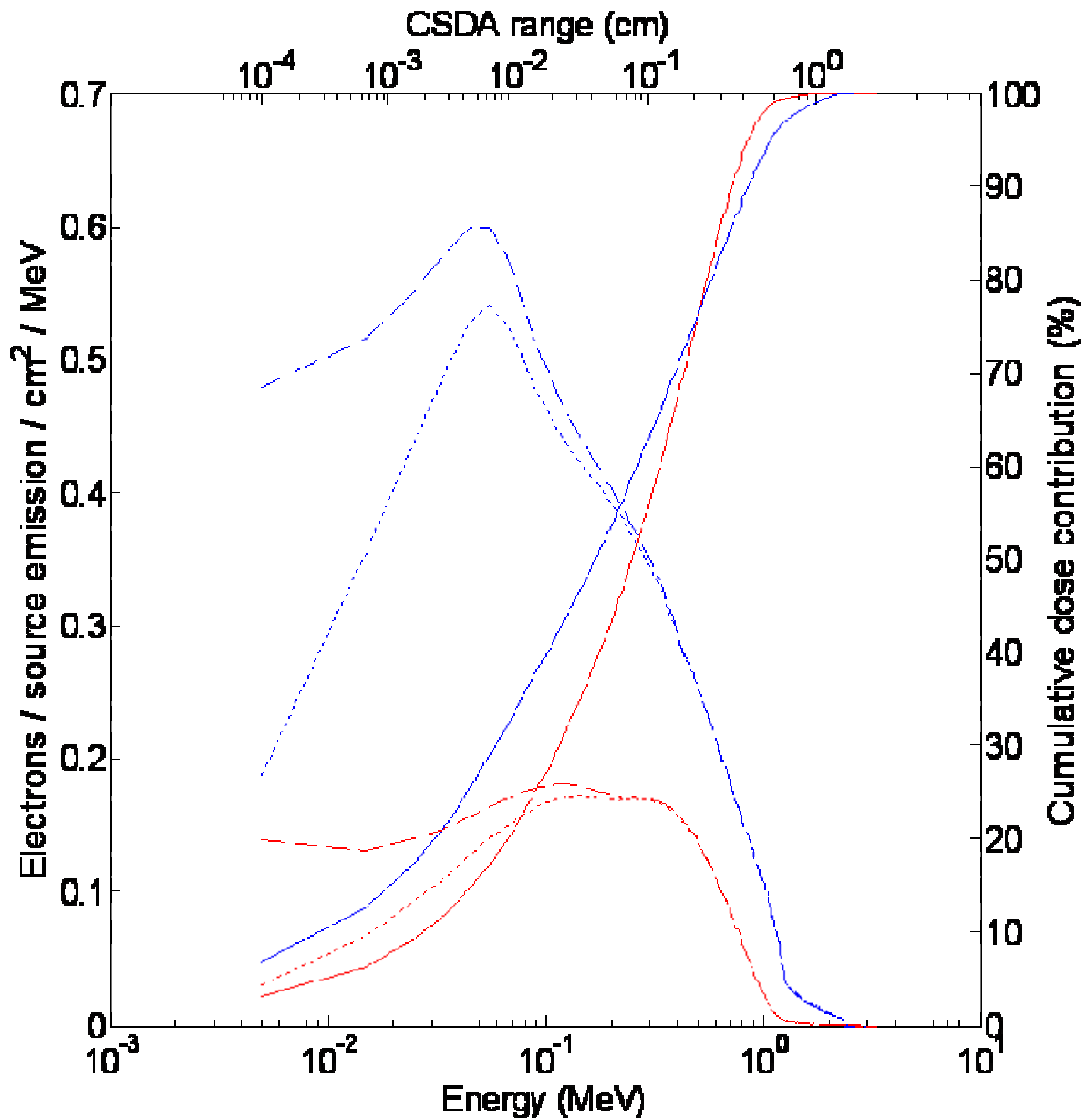
Figure 4.3. Charged-particle equilibrium spectrum in a sedimentary environment ("typical" radionuclide concentrations and average sediment of bulk density 1g cm^{-3}) for gamma radiations (blue) and beta radiations (red). The short dotted lines represent the fluence without delta rays (knock-on electrons) and the long dotted lines represent the combined (primary + delta) fluence. The flux spectrum was computed using MCNP5 across 10keV energy bins in a uniform material. The solid lines represent the cumulative dose contribution of the fluence (delta particles assumed to be in equilibrium) with increasing energy. The upper axis gives the CSDA range for electrons traversing a typical sedimentary environment with a bulk density 1g cm^{-3} (Note: non-uniform scale). Stopping power and range data are from Berger *et al.* (2000) (±2-3% for 10-100keV and ±1-2% for >100keV) and MCNP5 for energies below 10keV (±5-10%).

4.3   Theoretical background

4.3.1   Introduction

In this section, the theoretical basis for the correction of Zimmerman, as well as more advanced treatments, is explicitly described (Zimmerman did not show the derivation for his correction). Cavity theory is an analytical method for explaining the different dose deposition found in different materials. Of particular interest here, is the contrasting energy absorption characteristics of water and sediment. Cavity theory is designed to be relatively easy to implement and simplifying assumptions are introduced. The suitability of the cavity theory for the water content correction can be evaluated by comparing predictions established in this section of Bragg-Gray and Spencer-Attix theories with the Monte Carlo work in Section 4.4. Cavity theory will have limitations in sedimentary environments since there is often no charged-particle equilibrium.

4.3.2   Bragg-Gray cavities

Early dosimetry work by Bragg (1912) and Gray (1929, 1936) attempted to relate the dose in a detector to the dose in the surrounding medium from monoenergetic radiation. The detector is generalised as a cavity, or discontinuity, in an otherwise homogeneous body. The Bragg-Gray cavity theory makes two assumptions: a) the thickness of the water-to-mineral space is sufficiently small compared to the range of the charged particles that the fluence of charged particles is uniform (Attix, 1986); and b) no interactions from the primary radiation source deposit dose other than through the generated charged particle fluence and hence all secondary electrons (delta particles) are deposited locally. Laurence (1937) provided a mathematical method for computing the dose in the medium and detector for an ideal Bragg-Gray cavity. The theory was advanced by Spencer and Attix (1955) and Burch (1955) who accounted for the transport of delta particles in the medium and cavity.

101

We can infer from Equation 1.6 that the basis for the Zimmerman calculation is Bragg-Gray cavity theory. Consider first the average mass collisional stopping power for a charged particle energy distribution, $\Phi_e(E)$, crossing water

$$\bar{S}_{water} = \frac{\int_0^{E_{max}} \Phi_e(E)\left(\frac{dE}{\rho dx}\right)_{water} dE}{\int_0^{E_{max}} \Phi_e(E)dE} = \frac{D_{water}}{\Phi_e} \tag{4.4}$$

and the non-aqueous part of the sediment

$$\bar{S}_{sed} = \frac{\int_0^{E_{max}} \Phi_e(E)\left(\frac{dE}{\rho dx}\right)_{sed} dE}{\int_0^{E_{max}} \Phi_e(E)dE} = \frac{D_{sed}}{\Phi_e} \tag{4.5}$$

so we have

$$\frac{D_{water}}{D_{sed}} = \frac{\bar{S}_{water}}{\bar{S}_{sed}} = \bar{S}_s^w \tag{4.6}$$

The energy deposited in the wet sediment can be described as

$$\begin{aligned}(m_w + m_s)D_{wet} &= m_w D_{water} + m_s D_{sed} \\ &= D_{sed}\left(m_w \bar{S}_s^w + m_s\right)\end{aligned} \tag{4.7}$$

which can be used to describe of the dilution of the activity of the wet sediment compared with the dry sediment, such that

$$\frac{D_{sed}(m_w \bar{S}_s^w + m_s)}{m_w + m_s} = \frac{D_{dry}}{1 + m_w / m_s} \tag{4.8}$$

giving the Zimmerman equation after some algebraic manipulation and with $\bar{S}_s^w = x$. A symmetrical argument was made for the photon correction by replacing stopping powers with absorption coefficients (and energy fluence, $E\Phi$) but, at the least, this must restrict its application

to compact samples containing no water and sufficiently thick for CPE to exist since it is a kerma approximation of dose. Spencer and Fano (1954) reformulated the expression of $\bar{S}_s^w$ as

$$\bar{S}_s^w = \frac{D_w}{D_s} = \frac{1}{E_{max}} \int_0^{E_{max}} \frac{(dE/\rho dx)_w}{(dE/\rho dx)_s} dE \qquad (4.9)$$

since the weighting of the stopping powers with the electron fluence is implicit (Attix, 1986). It should be noted that Equation 4.1 used by Readhead is subtly different from both the Laurence and the Spencer derivation of $\bar{S}_s^w$, with the results fortuitously being similar because of the continuous, slowly varying nature of stopping powers (and to a lesser extent, absorption coefficients). Readhead gives no arguments to support his approach to determine x.

4.3.3   Spencer-Attix cavities

The Spencer-Attix cavity theory can be applied to account for the production of secondary fast electrons from primary electron (produced directly from gamma interactions or the degraded beta spectra without knock-on electrons) collisions. Since these energetic electrons may travel significant distances compared with the dimensions of the cavity, the assumptions of Bragg-Gray theory are violated (see Figure 4.4). Spencer and Attix partitioned the charged particle spectrum into energies less than Δ where all delta particles can be assumed to be dissipated locally and energies greater than Δ where the delta particles are treated as members of the charged particle fluence. The electron spectrum therefore becomes effectively zero at all energies below Δ and the stopping power is limited to all soft collisions and hard collisions resulting in secondary electrons below Δ, the so-called "restricted" stopping power. Restricted stopping power data can be calculated from the unrestricted collisional stopping power (Attix, 1986) through the relationship

$$\left(\frac{dE}{\rho dx}\right)_c - \left(\frac{dE}{\rho dx}\right)_\Delta = k\left(F^-(\tau) - G^-(\tau,\eta)\right) \qquad (4.10)$$

103

where

$$k = 0.1535 \frac{Z}{A} \frac{z^2}{\beta^2}$$

$$F^-(\tau) = 1 - \beta^2 + \frac{\tau^2/8 - (2\tau+1)\ln 2}{(\tau+1)^2}$$

$$G^-(\tau,\eta) = -1 - \beta^2 + \ln[4(1-\eta)\eta] + (1-\eta)^{-1} + (1-\beta^2)[\tau^2\eta^2/2 + (2\tau+1)\ln(1-\eta)]$$

in which Z/A is the ratio of atomic number and atomic mass (averaged by weight), z is the unit charge, β is the velocity of the electron (units of c), $\tau = E/0.511$ MeV, and $\eta = \Delta/E$. The restricted stopping power is equivalent to the unrestricted stopping power when $\Delta = E/2$. Figure 4.5 gives an illustration of the change in the collisional stopping power with different Δ in quartz. Equation 4.9 can now be reformulated as
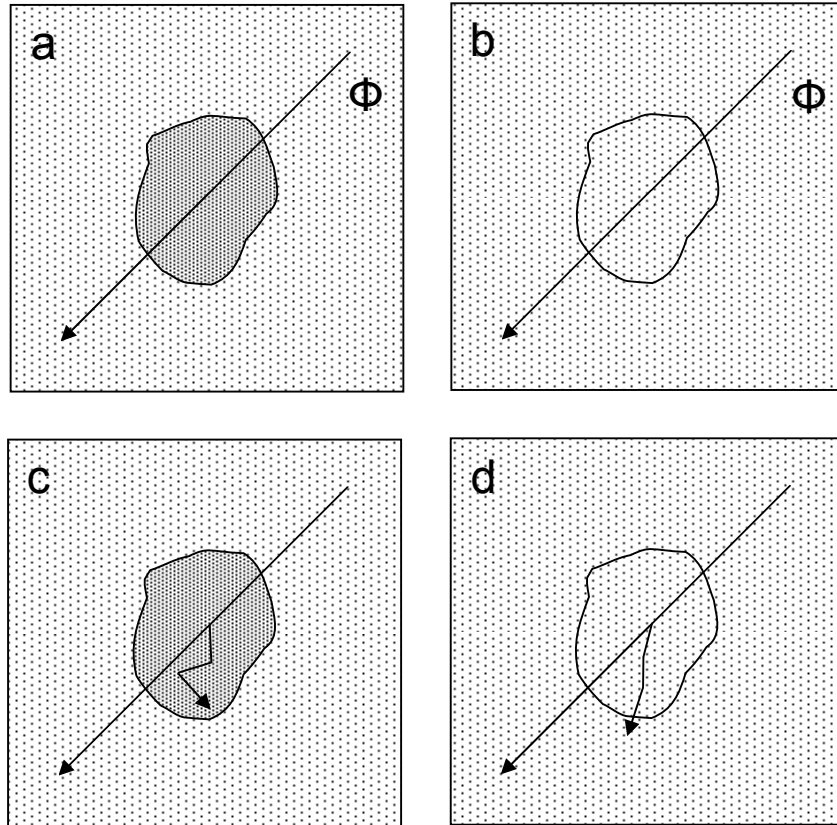
Figure 4.4. (a) A Bragg-Gray cavity is introduced (dark grey) into a medium (light grey) that is sufficiently small that the particle fluence, Φ, traversing the cavity is unchanged compared to (b) the fluence traversing an equivalent mass in the medium. (c,d) A delta particle, or secondary electron, is produced from the interaction of the charged-particle fluence with the medium. If the scattering in the cavity is greater than in the surrounding material, the delta particle will be absorbed within the cavity that would have otherwise escaped. In this case, the delta particle fluence is not in equilibrium and the Spencer-Attix cavity theory must be applied. From G. A. Carlsson.
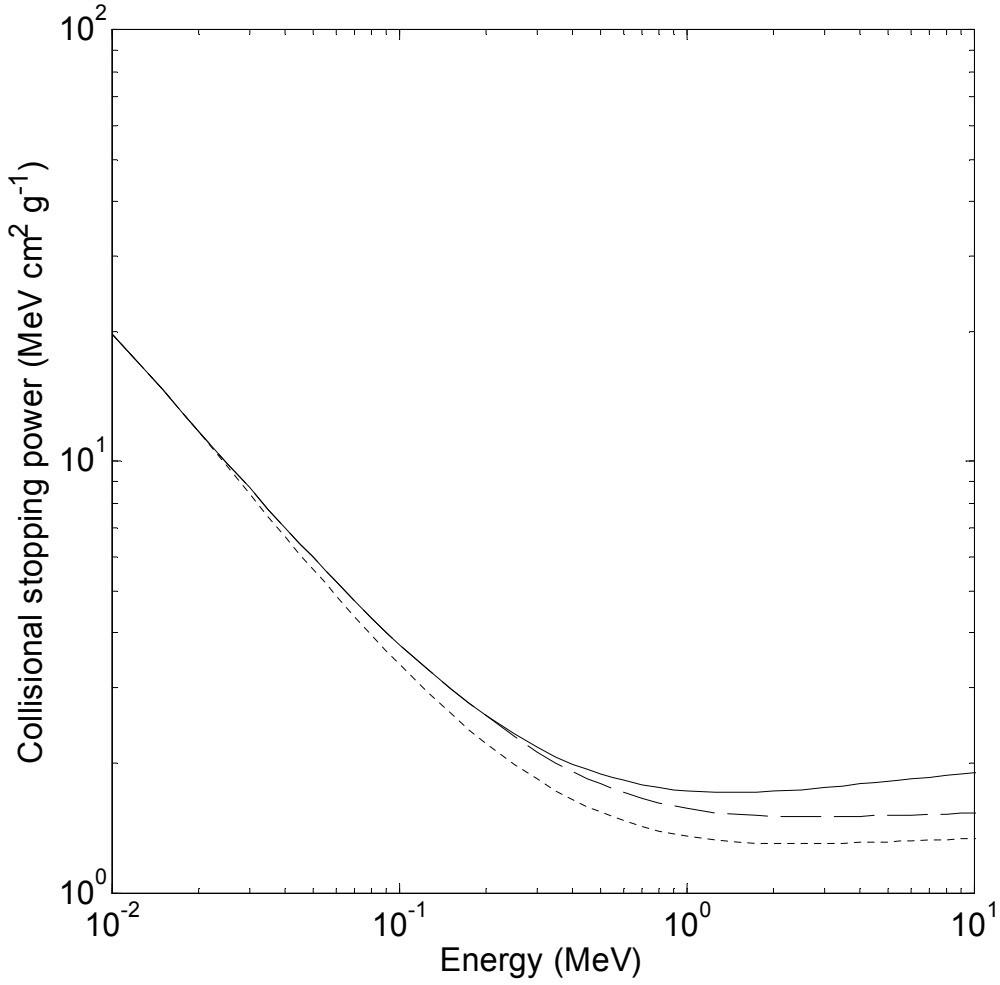
Figure 4.5. The unrestricted collisional stopping power (Berger et al., 2000) (solid lines) compared with restricted stopping powers ($\Delta = 0.1$MeV dashed lines; $\Delta = 0.01$MeV dotted lines) in quartz.

$$\overline{S}_s^w = \frac{D_w}{D_s} = \frac{\int_\Delta^{E_{\max}} \frac{R(E_{\max},E)}{\left(dE/\rho dx\right)_{sw}}.S_w(E,\Delta)dE}{\int_\Delta^{E_{\max}} \frac{R(E_{\max},E)}{\left(dE/\rho dx\right)_{sw}}.S_s(E,\Delta)dE} \tag{4.11}$$

where $R(E_{\max},E)$ is ratio of the electron flux including delta particles to the electron flux excluding delta particles, $(dE/\rho dx)_{sw}$ is the collisional stopping power of the sediment and water

mix and $S(E, \Delta)$ is the restricted stopping power calculated from Equation 4.11. Although the Spencer-Attix theory is relatively insensitive to the selection of an appropriate value for Δ, it is necessary to evaluate Δ using the following set of criteria (Burlin, 1968):

1) To a first-order approximation, the projected range (assumed to be approximately 0.8 CSDA range (Burlin, 1968)) of the charged particles is related to the average straight-line distance across a cavity and Δ should be optimised towards this value;

2) The assumptions used in the Bragg-Gray theory still apply, so Δ must be considerably smaller than the energies of the gamma sources (Burlin suggests <0.1) so that secondary electrons are not produced inside the cavity by the primary particles. Since this is not feasible for environmental gamma sources given the significant contribution of low-energy emissions in the Th and U decay chains, the uncertainty of Δ should be selected to reflect this shortcoming (although this is not addressed in this study);

3) Δ should be large compared to the binding energies of the electrons and remain above 1keV.

The first criterion is examined briefly here. In Chapter 3, considerable effort was expended to find accurate chord length distributions through pore spaces. If we assume that the interstitial material is uniformly distributed through the pore space, the projected range of the particles can be calculated as 0.8 the mean chord length. Admittedly, the shortcoming of this approach is that the high surface tension of water makes homogeneous distribution through the pore unfeasible except at complete saturation and materials such as carbonate exhibit highly localised formation. However, the mean chord length of a granular structure certainly can be regarded as a maximal value for the ensuing calculations. Mean chord lengths for the various packings from Chapter 3 are presented in Table 4.1 and may be used to look up the characteristic projected range of a packing (scaled by the fraction of water (by volume) in the pore). Evaluation of the water content correction for Spencer-Attix cavities are presented in Table 4.2 for selected projected ranges.

Charged particle (and photon) flux was calculated using MCNP from a point source in an infinite medium using a f4 tally consisting of 200 logorithmically-spaced energy bins (as well as a null bin). Knock-on electron production was switched off. The unrestricted collisional stopping power data was (mostly) downloaded on 20 January 2006 (Berger et al., 2000) from the ESTAR package (http://physics.nist.gov/PhysRefData/ Star/Text/ESTAR.html) with energies down to 1keV. All data were log-interpolated to match the energy bins of the electron flux.

It is immediately obvious that the slow varying nature of the effective stopping power ratio for different projected ranges reduces the effect of secondary particle issues in sediments. The Bragg-Gray correction typically matches pore spaces of the order of sandy sediments. Although there appears to be significant variation between the stopping power ratios and some decay groups, invariably the groups with the largest deviation from elemental ratios are associated with very low energy emissions (e.g. ^{234}U).

Packing type	Packing density	Mean grain or mesh size					
		20µm	50µm	100µm	200µm	300µm	600µm
		Mean chord length across <u>grains</u> (µm)					
Mono	Any	13	33	66	133	199	398
Size A		13	32	64	128	192	383
Size B		10	26	52	104	155	311
Shape A		12	31	61	122	183	366
Shape B		13	33	66	131	197	393
Shape C		10	26	52	104	156	312
Orient A		12	30	61	122	183	365
		Mean chord length across <u>pores</u> (µm)					
Mono	0.638	8	19	38	76	114	227
Size A	0.656	7	17	34	68	102	203
Size B	0.719	4	11	21	42	63	127
Shape A	0.721	5	12	24	48	72	144
Shape B	0.712	5	13	27	54	81	162
Shape C	0.666	5	13	27	53	80	160
Orient A	0.634	7	18	35	70	106	211
Mono	0.600	9	22	44	89	133	267
Size A		9	21	43	86	129	258
Size B		7	18	35	71	106	212
Shape A		8	20	41	82	123	245
Shape B		9	22	44	88	132	264
Shape C		7	18	35	70	106	211
Orient A		8	20	41	82	122	245
Mono	0.500	13	33	66	133	199	398
Size A		13	32	64	127	191	382
Size B		11	26	53	105	158	315
Shape A		12	31	61	122	183	366
Shape B		13	33	66	131	197	394
Shape C		10	26	52	105	157	314
Orient A		12	31	61	122	183	366
Mono	0.300	30	76	152	304	457	913
Size A		29	73	147	293	440	880
Size B		24	60	120	240	360	720
Shape A		28	70	140	279	419	838
Shape B		30	75	151	301	452	903
Shape C		24	60	120	240	360	721
Orient A		28	71	142	283	425	849

Table 4.1. Mean chord length in grains and pores of different granular packings modelled in Chapter 3. Mono refers to packing of monodisperse spheres, Size A and B refer to well and poorly sorted randomly packed spheres. Shape A, B and C refer to different ellipsoid random packings and Orient A is uniformly oriented random packings.

	Bragg-Gray	Spencer-Attix								
Projected range (μm)		5	10	20	50	100	200	300	600	∞
Δ (kev) in water		13.0	19.2	28.5	47.9	71.2	106.9	136.2	208.7	$E_{max}/2$
Beta										
Nat. U	1.19	1.21	1.20	1.20	1.20	1.19	1.19	1.19	1.19	1.18
$^{238}U \rightarrow {}^{234}Pa$	1.19	1.21	1.21	1.20	1.20	1.20	1.20	1.20	1.19	1.18
^{234}U	1.24	1.23	1.23	1.22	1.22	1.22	1.21	-	-	1.22
^{230}Th	1.24	1.23	1.23	1.22	1.22	1.21	1.21	1.21	-	1.21
^{226}Ra	1.22	1.23	1.22	1.22	1.21	1.21	1.21	1.21	1.20	1.21
$^{222}Rn \rightarrow {}^{206}Pb$	1.20	1.20	1.20	1.20	1.20	1.19	1.19	1.19	1.19	1.18
$^{235}U \rightarrow {}^{231}Th$	1.22	1.22	1.22	1.22	1.21	1.21	1.21	1.21	1.20	1.21
$^{231}Pa \rightarrow {}^{207}Pb$	1.20	1.22	1.21	1.21	1.21	1.20	1.20	1.20	1.20	1.19
$^{232}Th \rightarrow {}^{208}Pb$	1.20	1.21	1.21	1.20	1.20	1.20	1.20	1.20	1.19	1.18
^{40}K	1.20	1.22	1.21	1.21	1.21	1.20	1.20	1.20	1.20	1.19
^{87}Rb	1.22	1.22	1.22	1.22	1.21	1.21	1.21	1.21	1.20	1.21
Gamma										
Nat. U	1.20	1.21	1.20	1.20	1.20	1.20	1.19	1.19	1.19	1.18
$^{238}U \rightarrow {}^{234}Pa$	1.20	1.21	1.21	1.21	1.20	1.20	1.20	1.20	1.20	1.19
^{234}U	1.27	1.23	1.23	1.22	1.22	1.22	1.21	-	-	1.22
^{230}Th	1.25	1.23	1.22	1.22	1.21	1.21	1.21	1.21	1.20	1.21
^{226}Ra	1.23	1.22	1.22	1.21	1.21	1.21	1.21	1.20	1.20	1.20
$^{222}Rn \rightarrow {}^{206}Pb$	1.20	1.21	1.20	1.20	1.20	1.20	1.19	1.19	1.19	1.18
$^{235}U \rightarrow {}^{231}Th$	1.24	1.23	1.22	1.22	1.21	1.21	1.21	1.21	1.20	1.21
$^{231}Pa \rightarrow {}^{207}Pb$	1.22	1.22	1.21	1.21	1.21	1.21	1.20	1.20	1.20	1.20
$^{232}Th \rightarrow {}^{208}Pb$	1.19	1.21	1.20	1.20	1.20	1.20	1.19	1.19	1.19	1.18
^{40}K	1.20	1.22	1.21	1.21	1.21	1.20	1.20	1.20	1.20	1.19
^{87}Rb	1.20	1.21	1.20	1.20	1.20	1.20	1.19	1.19	1.19	1.18

Table 4.2. Effective stopping power ratios of water to quartz for different decay group emissions using either Bragg-Gray or Spencer-Attix cavity theories.

4.3.4   Charged particle equilibrium cavities

In large cavities, such as non-porous pottery deposited in porous sediment, there exists a charged

particle equilibrium, so that it is the absorption of the photon fluence that becomes relevant (see

Figure 4.6). This is achieved through the use of mass energy-absorption coefficients.
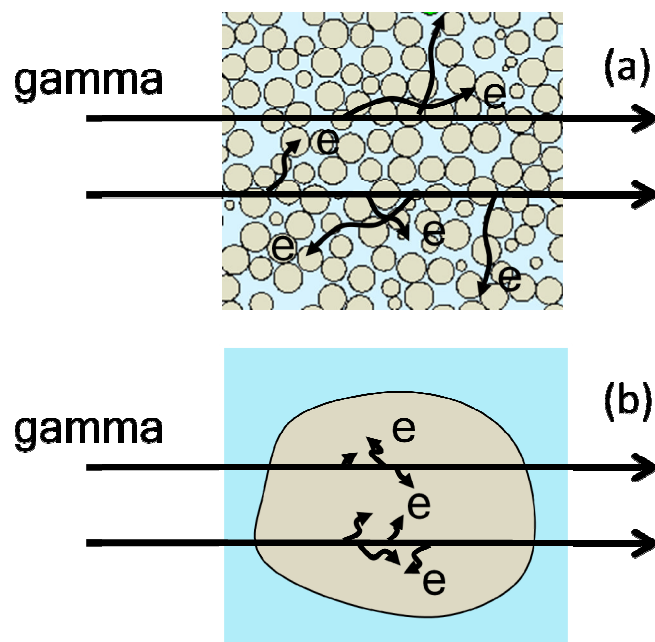
Figure 4.6. Alternative regimes for cavity theory: (a) Bragg-Gray where gamma fluence
is unaltered during transport through grains and water and the charged particle fluence
can be used to calculate the water content correction; and (b) charged particle equilibrium
exists due to sufficiently large non-aqueous bodies and the photon fluence through water
and sediment is used for the correction.
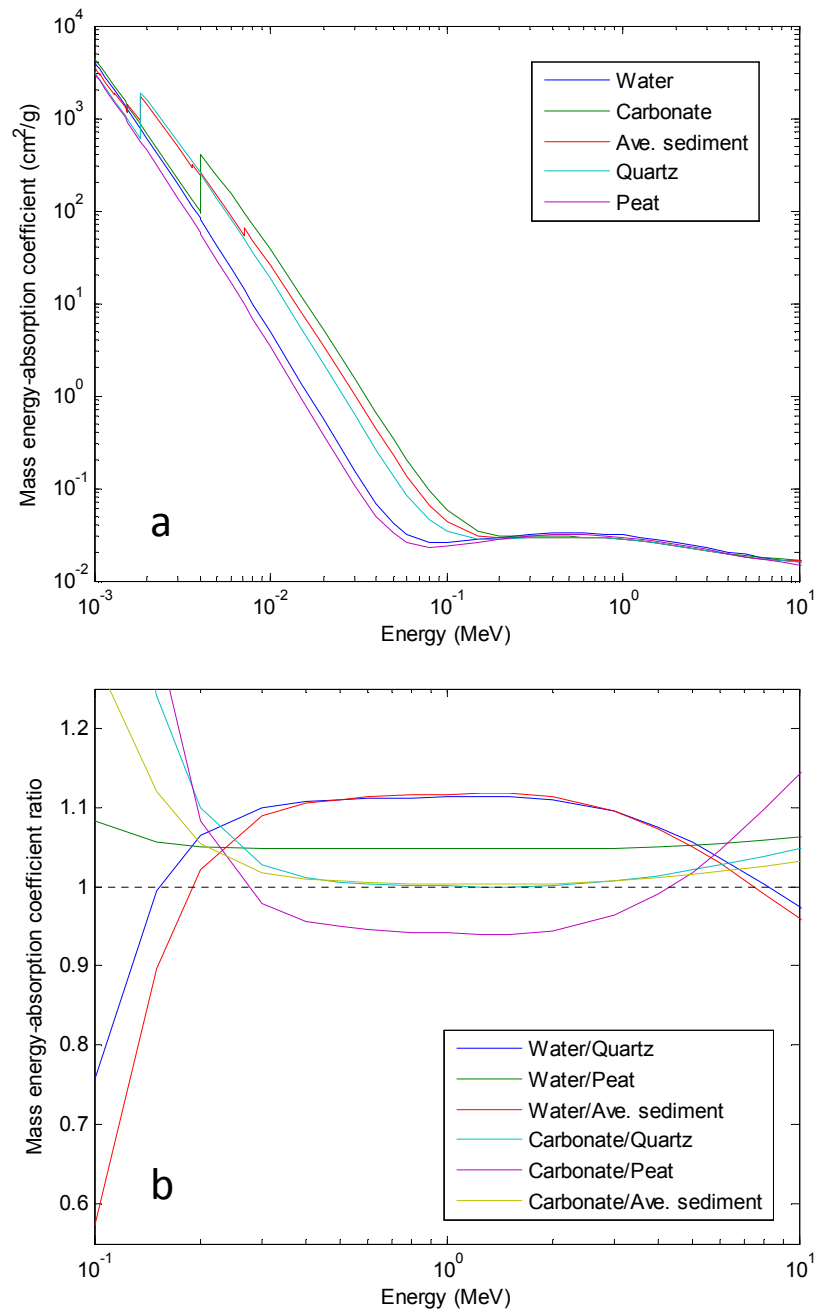
Figure 4.7. (a) Mass energy-absorption coefficients for different materials using data calculated from Hubbell and Seltzer (2004); and (b) the ratio of energy-absorption coefficients for different materials. Note: the two graphs have different energy scales.

The mass energy-absorption coefficients at different energies in water and quartz mixtures have been obtained from tabulated data (Hubbell and Seltzer, 2004) and are illustrated with other materials in Figure 4.7. Two approaches are taken: 1) find effective energy-absorption coefficient ratios using Equations 4.4-4.6 except that stopping powers are replaced by μ_a and the *energy* fluence of the photons in quartz (calculated using MCNP); or b) following Aitken and Xie (1990), the energy fluence of the photons in either a water or water/quartz mixture is calculated (MCNP) and x is found (Equations 4.2-4.3) through kerma dose. Table 4.3 presents the effective ratio of mass-absorption coefficients, $(\overline{\mu}_a / \rho)_s^w$, in an infinite-matrix of water and quartz. There is a general agreement between the two calculation methods which lends support for the robustness of the results. The evaluation matches Readhead (1987) to within uncertainties but it is somewhat different from the values found by Aitken and Xie. If we model the same material in Aitken and Xie we estimate x as 1.07, 1.06, 1.02 and 1.01 for K in sandstone and K, Th and U in shale respectively compared to 1.11, 1.08, 1.06 and 1.06 respectively found by Aitken and Xie. Since the correction is very sensitive to the ratio of dose in dry sediment to dose in water, the results would match if this ratio was perturbed by only 1% due to variation in either the energy-absorption coefficients or the degraded gamma spectra. Aitken and Xie used spectra presented in Jain et al. (1979) which is presumably identical to the data discussed by Evans et al. (1982). Evans et al. generate infinite-matrix spectra using a purpose written discrete-ordinates one-dimensional code. They list both primary gamma emissions for U, Th and K and material compositions for shale and sandstone (with densities) as input parameters and tally the degraded spectra over 10keV intervals up to the maximum emission energy. The flux spectra they produce are replicated closely by MCNP by comparing values in their published histograms. The second set of data used by Aitken and Xie is the energy-absorption cross-sections derived by Storm and Israel (1970). These values have an average difference of around 1.6% to the latest Hubbell and

113

Seltzer data and a corresponding potential disparity in kerma is expected which may explain the

differences found here.

	Bragg-Gray	Water content (m_w / m_q)						
		0.001	0.02	0.04	0.10	0.2	1.0	100
Nat. U	1.02	1.04	1.02	1.02	1.01	1.01	0.98	0.87
$^{238}U \rightarrow {}^{234}Pa$	1.02	0.97	1.03	1.02	1.02	1.02	0.99	0.89
^{234}U	1.07	1.07	1.07	1.07	1.06	1.06	1.05	0.98
^{230}Th	0.32	0.32	0.33	0.32	0.33	0.32	0.30	0.28
^{226}Ra	0.74	0.69	0.74	0.74	0.73	0.72	0.67	0.52
$^{222}Rn \rightarrow {}^{206}Pb$	1.02	0.97	1.02	1.03	1.02	1.02	0.99	0.88
$^{235}U \rightarrow {}^{231}Th$	0.64	0.65	0.64	0.64	0.63	0.62	0.57	0.44
$^{231}Pa \rightarrow {}^{207}Pb$	0.82	0.85	0.82	0.82	0.81	0.80	0.74	0.59
$^{232}Th \rightarrow {}^{208}Pb$	1.02	0.97	1.03	1.02	1.02	1.02	0.99	0.89
^{40}K	1.07	1.07	1.07	1.07	1.06	1.06	1.05	0.98

Table 4.3. Effective energy-absorption coefficient ratios of water to quartz for different decay group emissions using either Bragg-Gray cavity theory or the approach of Aitken and Xie (1990). m_w refers to mass of water and m_s refers to mass of dry quartz.

4.3.5   Burlin cavities

A more general cavity theory that includes the transition from large cavities, such as compact samples where water content does not locally affect the charged-particle fluence but it may have altered the photon fluence, to small cavities where Spencer-Attix theory holds, is provided by Burlin (1968). A weighting factor, d, is a function of the cavity size (0 for large cavities and unity for small cavities) and it can be applied (Attix, 1986) such that

$$\frac{\overline{D}_w}{D_s} = d\ \left(\overline{S}_s^w\right)_\gamma + (1-d)\left(\frac{\overline{\mu}_a}{\rho}\right)_s^w \quad \text{for gamma sources}$$

$$\frac{\overline{D}_w}{D_s} = d\ \left(\overline{S}_s^w\right)_\beta \qquad\qquad \text{for beta sources}$$

(4.12)

where $\overline{D}_w$ is the average dose absorbed in the cavity, D_s is the kerma approximation of dose in the dry sediment (i.e. in conditions of CPE), $\overline{S}_s^w$ is the mean ratio of stopping powers for water and dry sediment, and $(\overline{\mu}_a/\rho)_s^w$ is the effective ratio of mass-absorption coefficients for water and dry sediment. The parameter d is calculated from the empirical assumption of exponential attenuation of radiation fluence through the media (with no spectral changes) and a similar exponential build up of secondary electrons (Attix, 1986), where

$$d \equiv \frac{\overline{\Phi}_s}{\Phi_s^e} = \frac{\int_0^L \Phi_s^e e^{-\beta l}\,dl}{\int_0^L \Phi_s^e\,dl} = \frac{1-e^{-\beta L}}{\beta L}$$

(4.13)

such that d is the average ratio of the electron fluence through the material to the equilibrium electron fluence, l is distance of a point in the cavity from the surrounding medium along a mean chord L, and β is the attenuation coefficient which Janssens (1974) suggests should satisfy the condition $exp(-\beta t_{max}) = 0.04$ where t_{max} is the maximum depth of penetration (for our purposes let us assume t_{max} is twice L). Burlin theory uses the assumption that the cavity and surrounding matter are identical materials with the same β so that d is independent of the medium where the

fluence is estimated. Since this assumption is not sustainable for the sediment/water computation, some inaccuracies will result. With the advent of Monte Carlo modelling, Burlin cavity theory has been almost completely surpassed in dosimetry applications since the 1980's and the following section will address the variation expected due to cavity size using Monte Carlo modelling.

4.4   Radiation transport modelling

4.4.1   Modelling methodology

Cavity theories remain approximate due to the difficulties in providing a generalised account of electron energy loss in different volumes where fundamental assumptions no longer hold. Monte Carlo modelling provides a method to accurately investigate a wide range of environments, particularly for the water content corrections for coarse grained sediments. Numerical radiation transport models to investigate directly the water content correction require various attributes, mainly: 1) geometries that extend to the limits of the range of the environmental radiation; and 2) fine scale accounting of energy loss in the sediment and water as separate entities. The most direct way of satisfying the above criteria is to model the sediment and water *in situ*. The limitations in computation, primarily memory, would tend to preclude this approach. Consider sediment of 100μm quartz grains exposed to gamma radiation with an effective range of tens of centimetres. This would require the model to represent billions of grains to accurately assess the dose deposition near the centre. However, silty contexts would involve orders of magnitude more bodies and this would be unachievable using current personal computers (as well as restrictions within the codes themselves).

 The PENELOPE code (as well as MCNP but not used here) has been modified to allow periodic plane surfaces to bound the geometry to form a cube. The modifications were written before the

algorithm that updates location after a boundary crossing. If the position is in a specific material outside the periodic cube, the particle is moved to the opposite side of the cube. This design makes immediate use of the periodic granular packings presented in Chapter 3. These structures contain 150 grains (except Size A and Size B packs which require the full complement of grains – see Chapter 3) and the matrix is divided internally into 8, 64 or 512 smaller voxels (see Figure 4.8) to optimise the geometry algorithms of the code. The grains are composed of quartz while the water fills the remaining geometry uniformly. The density of the water is adjusted from 0-1g cm^{-3} depending on the required water content. This introduces a small and largely negligible systematic error in the calculations arising from dependence of the stopping power on density (<1%) through the polarisation of the incident electron travelling through the medium. More importantly, the default mean ionisation energy calculated during the construction of the material using PENELOPE software is usually several percent lower than selecting water as a preset material. All aqueous material in the pore spaces had the mean excitation potential set manually to 75eV. Energies below 1keV were deposited locally. Different grain sizes were achieved by scaling the dimensions of the periodic packing.
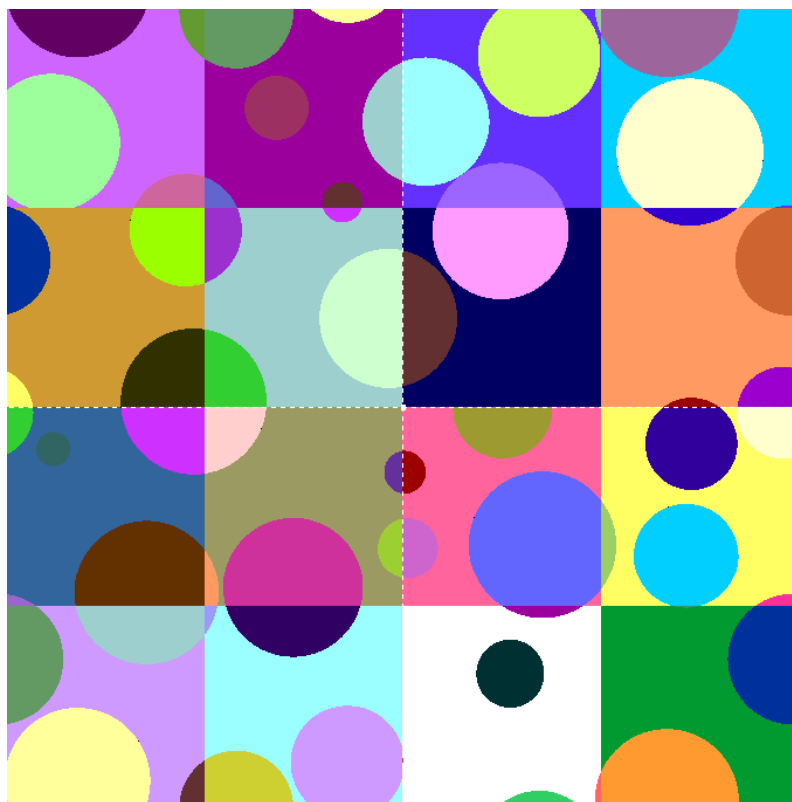
Figure 4.8. A slice through a modelled geometry using PENELOPE (produced using PENELOPE gview2d) where the four sides shown are periodic surfaces. Each contiguous region is filled with a colour and represents different entities (although some share the same colour). A packing of 150 quartz spheres to a packing density of 0.5 is shown with water with density of 0.53g cm^{-3} filling the rest of the geometry to achieve a water content of 20%.

In order to compare the Monte Carlo modelling to infinite-matrix calculations from above, the grains and water must have uniform activity. The easiest way to implement this for PENELOPE was to run two models with either grain or water as the source of emissions. These models are coupled *post hoc* with the water content fraction (mass of water to mass of dry sediment) as a weighting ratio. The evaluation of x (in Equation 1.6) is $\frac{\sum E_{water}}{Water\ content}/\sum E_{grains}$ where $\sum E$ are the total energy deposited in either water or grains. Evaluation of $\sum E$ for approximately 100,000 histories results in approximately ±1% precisional uncertainty for x (the systematic uncertainty arising from the large number of boundary crossings is unknown but unlikely to be greater than ±1%).

PENELOPE allows the user to extract cross-sections used in the simulations. Figure 4.9 shows the ratio of water to quartz for mass collisional stopping powers and a clear trend for increasing an increasing ratio as electron energy falls. The ratio is expected to fall within 1.16 and 1.32 only. However, the estimation of x is made by evaluating Zimmerman water content correction which is limited in its assumptions. Therefore, the Monte Carlo results may span beyond the expected ratios (which clearly indicates where Bragg-Gray theory is not appropriate). In the simulations, the cut-off energy was 1keV and no sampling is made from the elevated ratio energies since this has an associated sub-micron range.
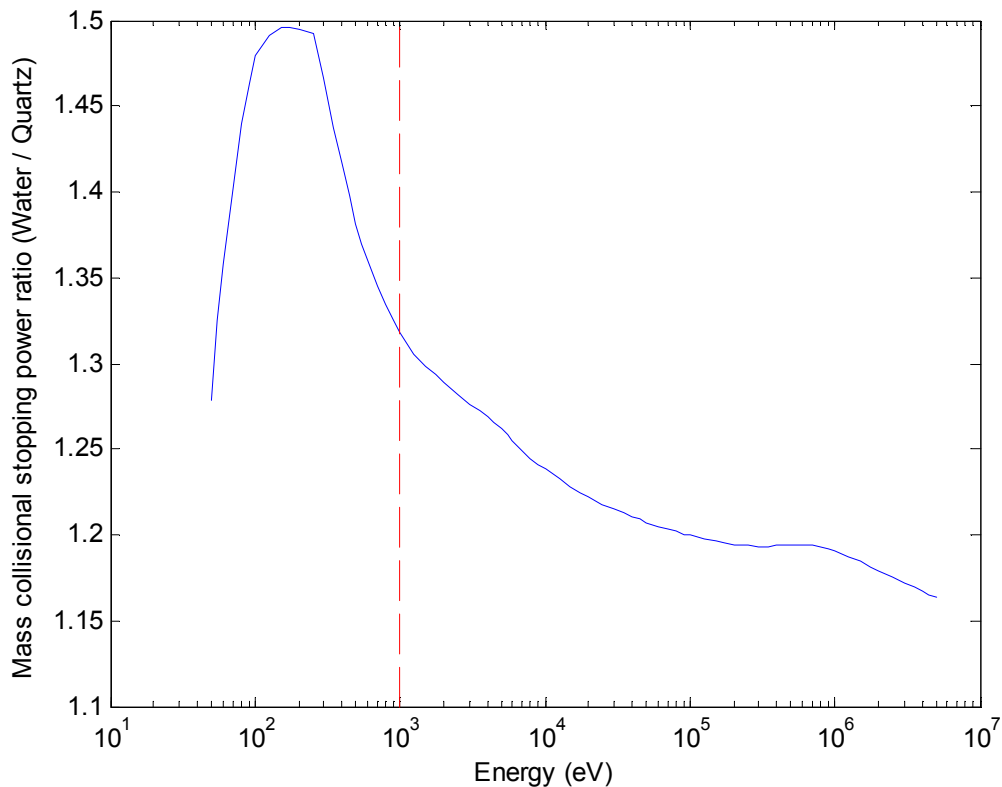
Figure 4.9. Mass collisional stopping power ratio of water to quartz from PENELOPE database. The red dashed line is the energy cut-off used in all simulations.
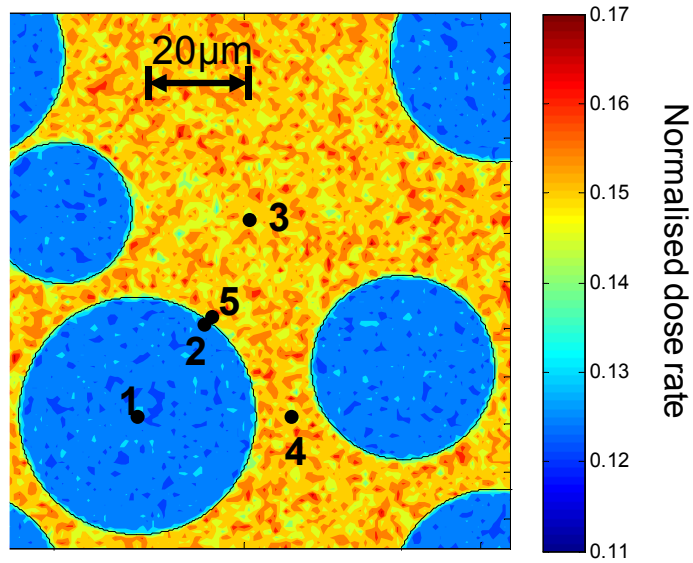
Figure 4.10. The spatially-resolved normalised dose rate for monodisperse spherical 50μm quartz grains with 10% water content and 50% porosity for K beta sources. The five points refer to locations of fluence measurements (see Fig 4.11).
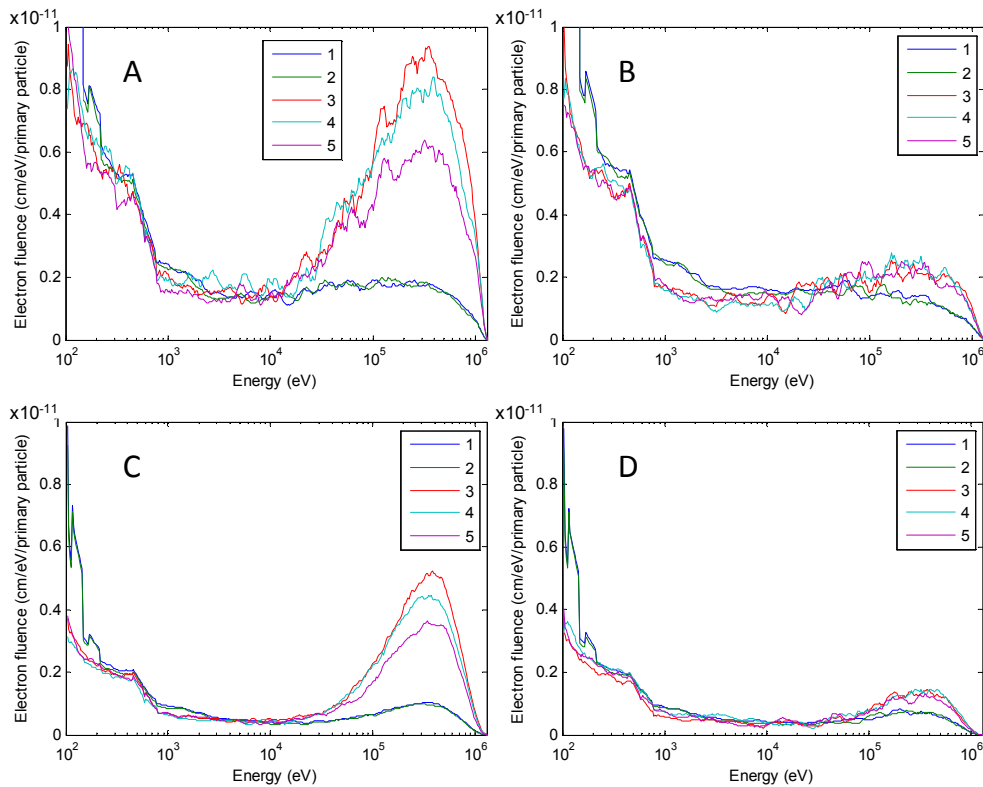
Figure 4.11. Fluence scoring at positions indicated in Fig 4.10. In all cases, K emissions with water content 10% and porosity 50% and monodisperse spherical quartz grains with: A) gamma emission and 50μm grain size; B) gamma emission with 500μm grains; C) beta emission with 50μm grains; and D) beta emission with 500μm grain size.

It is informative to evaluate the spatial-resolved dose rate (see Figure 4.10) and fluence (see Figure 4.11) distribution for specific case studies. The dose rate appears to change rather sharply for 50µm grains at transition between pore water and quartz whereas the dose rate is relatively uniform within a material. As the grain size becomes larger, this uniformity strengthens since the radiation source has homogeneous activity across both pore space and grains and therefore, the grain/water interface has less influence. The fluence spectra (Figure 4.11) clearly demonstrate the larger spatial variability for smaller grain sizes. If the sources were more localised (eg. on grain boundaries) the opposite would obtain. Account should be taken that although the absolute fluence is higher in water, the mass normalised fluence (calculated by multiplying by density – here 0.1 relative to quartz) is significantly lower in water than quartz. This is expected since water acting is a more effective absorber of energy per unit mass.

4.4.2   Dependence on water content and grain size

Initial consideration is given to the effects of the water content correction for a simple sedimentary environment where monodisperse quartz spheres are embedded in an aqueous environment. Water content and grain size are varied over a wide range (one model for each situation) with water content restricted to a maximum of 0.378 which corresponds to a density of 1g cm^{-3}. The results are presented in Table 4.4. For beta dose rate, the trend in x follows Spencer-Attix predictions within 1-2% and there is closest agreement for water content of 0.1 for different grain sizes. However, there is a clear variability of x with water content. Figure 4.12 shows the changes of x using interpolated data. It is expected that the effect of water content and grain size is correlated since the distance travelled in unit mass of water per pore transit increases in both cases leading to secondary electron perturbation. A very large grain size (6mm) was included in the analysis, perhaps skewing the perception of the changes to x, to illustrate an issue which has

not been explicitly discussed yet. For very solid large bodies, a large proportion of the primary emissions will be absorbed locally thereby not traversing both mineral and water. In this case, the effective x will tend towards unity except for emissions near the surface - certainty fundamental assumptions of unaffected primary fluence in cavity theory no longer apply.   For gamma emissions, (see Figure 4.13) as similar pattern emerges except the transition from Bragg-Gray theory to large cavity theory (relevant to energy-absorption coefficients) is clear and matches to within several percent to Burlin's theory.

	Water content	Source	Grain size (μm)					
			50	100	200	300	600	6000
Beta	**0.010** (ρ=0.027g cm^{-3})	K	1.22	1.22	1.21	1.22	1.21	1.19
		Th	1.23	1.23	1.23	1.21	1.21	1.19
		U	1.23	1.24	1.23	1.23	1.20	1.16
	0.100 (ρ=0.265g cm^{-3})	K	1.21	1.21	1.20	1.20	1.19	1.12
		Th	1.21	1.20	1.19	1.18	1.18	1.12
		U	1.21	1.20	1.20	1.19	1.18	1.14
	0.200 (ρ=0.530g cm^{-3})	K	1.21	1.20	1.20	1.20	1.18	1.10
		Th	1.20	1.19	1.19	1.18	1.15	1.08
		U	1.21	1.20	1.19	1.19	1.17	1.11
	0.378 (ρ=1g cm^{-3})	K	1.20	1.20	1.19	1.19	1.17	1.07
		Th	1.20	1.18	1.18	1.17	1.15	1.08
		U	1.19	1.19	1.18	1.18	1.16	1.08
Gamma	**0.010** (ρ=0.027g cm^{-3})	K	1.22	1.23	1.22	1.21	1.18	1.17
		Th	1.22	1.22	1.21	1.21	1.19	1.12
		U	1.22	1.23	1.20	1.19	1.18	1.11
	0.100 (ρ=0.265g cm^{-3})	K	1.21	1.19	1.18	1.17	1.16	1.11
		Th	1.20	1.18	1.16	1.15	1.13	1.08
		U	1.19	1.18	1.16	1.14	1.11	1.06
	0.200 (ρ=0.530g cm^{-3})	K	1.19	1.18	1.17	1.16	1.14	1.11
		Th	1.19	1.17	1.14	1.12	1.10	1.05
		U	1.18	1.16	1.13	1.11	1.10	1.03
	0.378 (ρ=1g cm^{-3})	K	1.18	1.17	1.15	1.14	1.12	1.09
		Th	1.16	1.14	1.11	1.10	1.08	1.07
		U	1.16	1.13	1.10	1.09	1.07	1.03

Table 4.4. The water content correction parameter, x, for monodisperse quartz spheres packed randomly to a density of 0.5 and water of different densities filling the pore spaces. Results from PENELOPE with uncertainty of ±0.01 except for 6mm grains where uncertainty is ±0.02.
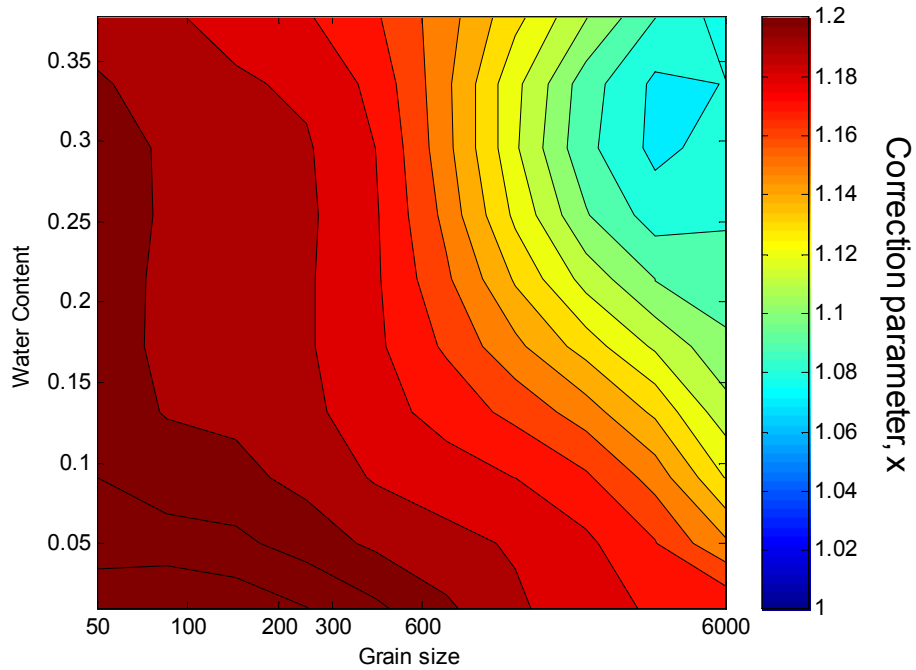
Figure 4.12. An interpolation of the water content correction parameter, x, evalued as an average from individual beta emissions of U, Th and K using PENELOPE to model radiation in monodisperse, randomly-packed spheres of quartz with water in the pore spaces.
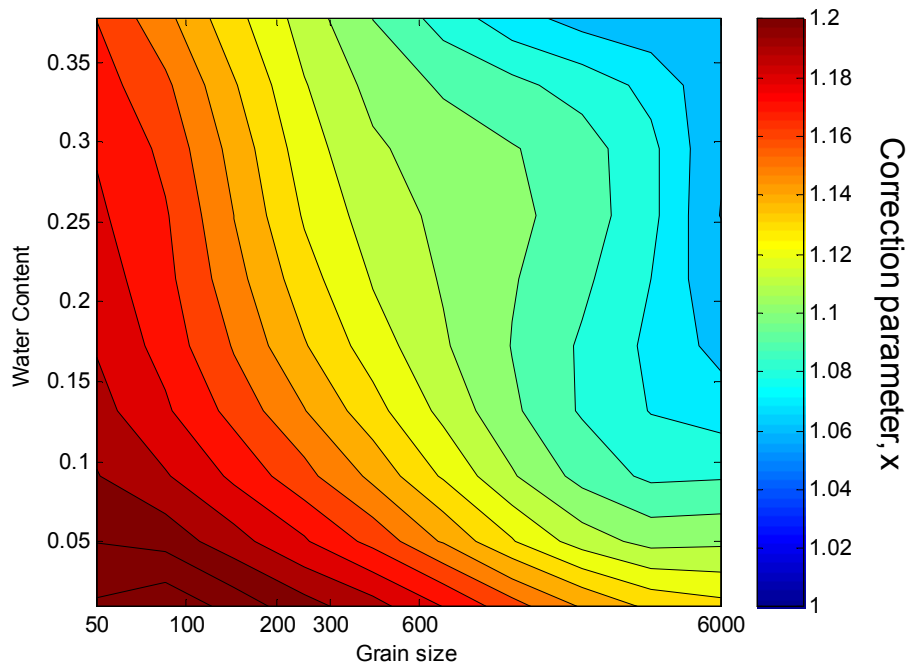
Figure 4.13. As Fig 4.12 but as an average from U, Th and K gamma emissions.

123

4.4.3   Sediment types

	Sediment type	Source	Packing density (1 – porosity)		
			Max	500	300
Beta	**Mono-disperse**	K	1.20	1.20	1.20
		Th	1.18	1.19	1.19
		U	1.20	1.20	1.19
	Size A (well-sorted)	K	1.20	1.20	1.21
		Th	1.19	1.19	1.19
		U	1.20	1.20	1.20
	Size B (poorly-sorted)	K	1.19	1.20	1.19
		Th	1.18	1.18	1.18
		U	1.18	1.19	1.18
Gamma	**Mono-disperse**	K	1.18	1.18	1.18
		Th	1.16	1.16	1.16
		U	1.15	1.16	1.15
	Size A (well-sorted)	K	1.18	1.17	1.17
		Th	1.15	1.16	1.16
		U	1.14	1.16	1.14
	Size B (poorly-sorted)	K	1.16	1.16	1.17
		Th	1.13	1.13	1.14
		U	1.14	1.13	1.12

Table 4.5. The water content correction parameter, x, for different grain size distributions (see Section 3) for quartz spheres randomly arranged to three different packing densities with median grain size 200µm and a water content of 10% filling the pore spaces. Results are from PENELOPE with uncertainty of ±0.01 except for Size B distribution (poorly-sorted) where uncertainty is ±0.02.

In contrast to immediately preceding section, grain size and water content is not varied (median grain size is 200µm and water content is 0.1) but rather the pore shape is examined. Three different randomly-packed simulated quartz sediments discussed in Chapter 3 are used: 1) monodisperse; 2) Size A distribution which is well-sorted; and 3) Size B which is moderately to poorly sorted. The packing density is also varied since this changes pore shape and has the effect of restricting the number of touching bodies for low densities. Table 4.5 presents the modelling

results for x and it is apparent that packing density only very weakly modulates changes in x. The sediment type has a somewhat more dominant effect for poorly-sorted sediments but presumably that is due to anomalously large bodies intersperse into the finer matrix which alter the secondary electron flux.

4.4.4 Heterogeneous activity

Evaluation of the water correction parameter x has assumed that the matrix has uniform activity (or that the grains were sufficiently small to mimic this) that so that buildup issues are minimised. However, sediments are typically heterogeneous over the granular scale and variability in activity in the coarse grain mineral fraction, detrital material (including grain coatings) and the interstitial material is typical. The benefit of using radiation transport modelling is that these effects can be investigated.

Additional modifications of the PENELOPE code were made to allow sources to reside on the surface of the grains. This was achieved by allowing an array of point sources to be inputted into the simulation as required. No changes in response of x to repositioning the source location for gamma radiation are identified. This is a trivial result since most of the energy fluence will travel through many grains and pores before interacting thereby making the source position irrelevant. An enormous variation in x is observed for beta emissions and it is difficult to reconcile its dominance to the change in secondary electron flux for the sources arising within the pore. It is possible a normalisation factor was not applied correctly. However it remains an open question whether this modelling is accurate although it does appear to illustrate a trend that values for x are lower for sources within the grain compared to uniform activity and higher for sources in pore spaces which is to be expected since delta particles will have a greater probability of being

deposited local to the source. Clearly this work requires more attention and the formulation of Zimmerman is not appropriate in these cases.

	Water content	Grain size	Source	Location of activity			
				Within grain	Uniform	Grain surface	Within pore
Beta	0.01 (ρ=0.026g cm⁻³)	100μm	K	1.22	1.22	1.28	1.33
			Th	1.22	1.23	1.86	2.17
			U	1.23	1.24	1.62	1.79
		300μm	K	1.21	1.22	1.36	1.45
			Th	1.19	1.21	2.82	3.52
			U	1.21	1.23	2.27	2.72
	0.378 (ρ=1g cm⁻³)	100μm	K	1.18	1.20	1.21	1.25
			Th	1.07	1.18	1.33	1.52
			U	1.10	1.19	1.29	1.43
		300μm	K	1.14	1.19	1.24	1.34
			Th	0.96	1.17	1.43	1.87
			U	1.02	1.18	1.35	1.66
Gamma	0.01 (ρ=0.026g cm⁻³)	100μm	K	1.23	1.23	1.22	1.22
			Th	1.22	1.22	1.22	1.22
			U	1.23	1.23	1.22	1.22
		300μm	K	1.21	1.21	1.21	1.21
			Th	1.21	1.21	1.21	1.20
			U	1.19	1.19	1.21	1.21
	0.378 (ρ=1g cm⁻³)	100μm	K	1.17	1.17	1.17	1.17
			Th	1.14	1.14	1.14	1.14
			U	1.13	1.13	1.13	1.14
		300μm	K	1.14	1.14	1.14	1.14
			Th	1.10	1.10	1.10	1.11
			U	1.09	1.09	1.09	1.09

Table 4.6. The water content correction parameter, *x*, for different emission locations in a monodisperse packing of quartz spheres with porosity 50%. Results were generated using PENELOPE and uncertainty is ±0.01.

4.4.5 Non-aqueous corrections

A similar application of dose rate correction for water content may be also necessary for other interstitial material which enters the sedimentary matrix after deposition. Typically this is the

result of precipitation of minerals from groundwater. The coupled effects of water and carbonate are presented in Table 4.7. The stopping power ratio of carbonate to quartz is very similar so it is expected that low water content and high carbonate content would not be much different from a simple dilution of activity. The results support this with x falling close to unity. Similarly with low carbonate and high water content, the values of x follow closely to that expected of water. The intermediate case where there are equal amounts of carbonate and water, the correction is close to the average of x_{water} and $x_{carbonate}$. This also holds for the gamma emissions correction parameter (see Figure 4.14).
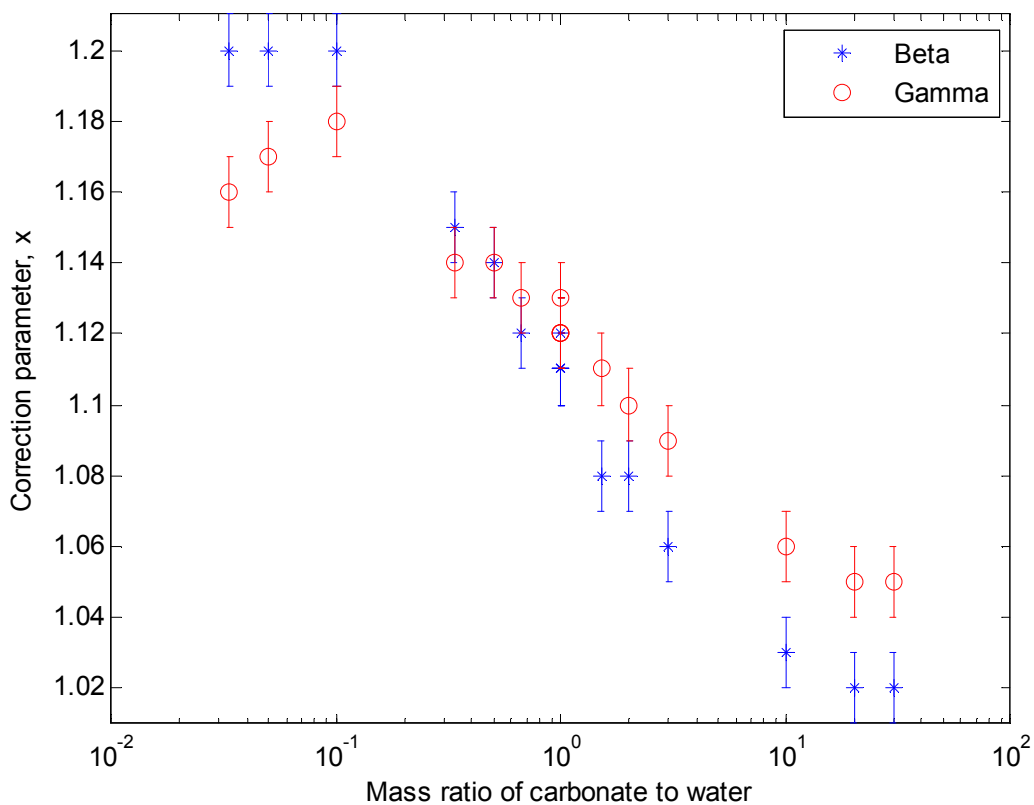
Figure 4.14. The linear scaling of the correction parameter, x, between proportions of water and carbonate. The correlation coefficient of the linear fit is given as R.

	Carbonate content	Source	Water content			
			0.01	0.1	0.2	0.3
Beta	0.01	K	1.12	1.20	1.21	1.21
		Th	1.12	1.19	1.20	1.19
		U	1.12	1.20	1.20	1.20
	0.1	K	1.03	1.11	1.15	1.16
		Th	1.03	1.11	1.14	1.15
		U	1.03	1.11	1.14	1.15
	0.2	K	1.02	1.08	1.11	1.13
		Th	1.02	1.08	1.10	1.12
		U	1.02	1.08	1.11	1.12
	0.3	K	1.02	1.06	1.09	1.11
		Th	1.02	1.06	1.08	1.10
		U	1.02	1.06	1.08	1.11
Gamma	0.01	K	1.12	1.19	1.19	1.18
		Th	1.13	1.18	1.17	1.15
		U	1.13	1.18	1.16	1.15
	0.1	K	1.05	1.12	1.14	1.15
		Th	1.06	1.12	1.14	1.14
		U	1.06	1.12	1.13	1.14
	0.2	K	1.04	1.09	1.12	1.13
		Th	1.05	1.10	1.12	1.13
		U	1.06	1.11	1.12	1.13
	0.3	K	1.04	1.08	1.10	1.11
		Th	1.06	1.09	1.11	1.12
		U	1.06	1.09	1.11	1.12

Table 4.7. The correction parameter, *x*, for water and carbonate residing in pores of a monodisperse packing (50% porosity) of 100μm quartz spheres. (Note: data missing – to be recalculated).

4.5   Concluding remarks

In this chapter, the theory of the standard treatment of the water content correction (Aitken, 1985a) has been revisited and expanded with specific attention placed on the assumptions that are used. Sedimentary environments are not particularly well-suited to cavity theory due to the repeated interactions between heterogeneous mineral and water regions and the assumption that the primary particle fluence is unaltered by the matrix is questionable in many situations.

Monte Carlo modelling was used to achieve a novel high-resolution evaluation of dose deposition in granular sediments for trapped-charge dating. The benefits of this approach are: 1) the secondary electron dose deposition is explicitly modelled; 2) complex pore spaces were simulated which would otherwise be problematical; and 3) periodic boundaries allowed the modelling of small *in situ* grains to become tractable over gamma radiation scales.

The correction was modelled for different grain sizes and water contents, with minor changes to x for beta emissions except for large grain sizes where the secondary electron flux becomes increasingly perturbed. The correction parameter for gamma radiation changes from the correction associated with stopping powers (charged particle fluence) to situations of charged particle equilibrium and the correction is obtained from the photon energy fluence. Other variables that should be considered are sediment type (e.g. Well sorted vs. Poorly-sorted), and possibly location of activity (but there may be errors in this analysis). More than one type of interstitial material can be addressed by scaling between end-point corrections (e.g. between only water and only carbonate).

Chapter 5: Grain size correction for beta dose rate

5.1 Introduction

The grain size correction for the dose rate is based on the observation that mineral dosimeters used for trapped charge dating generally contain different radionuclide activities to the surrounding medium and some scaling of dose rate must be applied to relate the dose rate of the medium to the dosimeter. The correction (see Equation 1.7) takes two parts: a) the dose rate absorbed in the dosimeter from internal activity having an infinite-matrix (IM) dose rate, $\dot{D}_{int}$ and b) the dose rate absorbed in the dosimeter from the sediment having an IM dose rate, $\dot{D}_{sed}$. The most common approach, used in a seminal paper by Mejdahl (1979), assumes that the sediment is infinite and uniform (ie. IM) and therefore radiation equilibrium exists (see Section 1.2.1). If the dosimeter is identical in composition to the sediment, the dose rate in the dosimeter can be described as

$$\dot{D}_d = \Omega \dot{D}_{int} + (1 - \Omega)\dot{D}_{sed} \tag{5.1}$$

where Ω is the fraction of dose absorbed in the dosimeter from internal sources compared to an infinite-matrix source (it should be noted that φ often is used as standard nomenclature instead of Ω in dosimetry applications). This chapter will update the evaluation of Ω for beta dose rates and address the appropriate treatment of Ω for more general types of grains.

Consider a typical sedimentary environment with activities consistent with U 1ppm, Th 3ppm and K 1% (ignore cosmic dose rate) where dates are determined using coarse grain quartz (no external alpha dose rate contribution and no internal dose rate are included). The sensitivity of the dose rate to the correction

130

can be estimated for different grain sizes using the beta correction factors of Mejdahl (1979) with the results presented in Figure 5.1. For grains less than 20μm, the dose rate is expected to be largely unaffected by the beta correction of grain size. The effects become increasingly important with the size of the grains and, for coarse grains greater than 100μm, the correction becomes a significant consideration in the dating equation. Figure 5.2 illustrates the changes of the dose rate estimation that occur if the grain size correction for beta dose rate is perturbed due to uncertainty or error. A ±10% uncertainty of the correction for a 300μm coarse grain would result in a ±1% uncertainty in the dose rate. Small percentage changes in the correction for grain sizes below 100μm are unlikely to significantly alter the dates achieved in contrast to grains greater than 1mm diameter where variation of the correction may lead to considerable changes in dose rate. A substantial internal activity would ameliorate the effects of the grain size correction (from Equation 5.1).
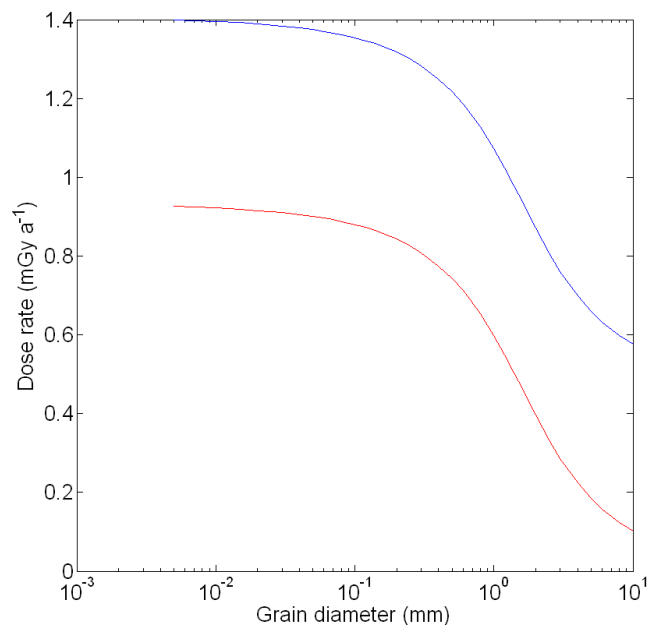
Figure 5.1. The expected variation of the (blue) total dose rate and (red) beta dose rate from a typical sedimentary infinite-matrix source in an inert spherical quartz grain of different sizes. The beta dose rate correction factors are from Mejdahl (1979).
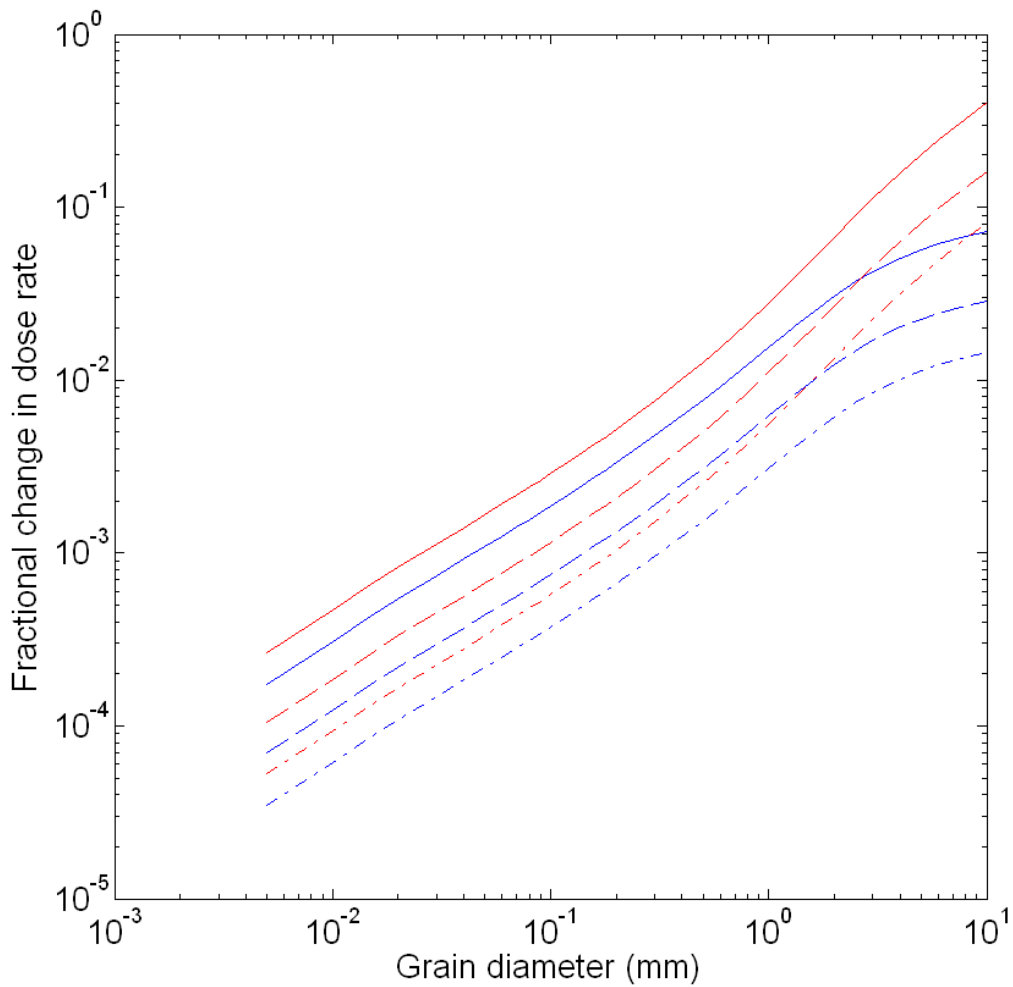
Figure 5.2. As for Fig. 5.1 but showing the change in dose rate if the grain size correction factor is altered by (dash-dot line) ±1%, (dash-dash line) ±3%, and (solid) ±10%. Blue lines are for total dose rates, red lines are for beta dose rates, as in Fig. 5.1.

Mejdahl (1979) investigated the beta dose rate correction for inert spherical quartz grains embedded in a radioactive quartz IM medium. The basis for his calculation is the integration of the dose point kernels of beta emissions, *F(s)*, over a sphere of radius, *r*, such that

$$\Omega(r) = \int_0^{2r} \left(1 - \frac{3s}{4r} + \frac{s^3}{16r^3}\right) F(s)ds \qquad (5.2)$$

132

where s is the distance through the material and $F(s)$ is the dose point kernel (DPK). The calculation of the DPK used data from Berger (1971, 1973) that was required to be scaled from a water medium to quartz by a process introduced by Cross (1968). Brennan (2003) updated the values obtained by Mejdahl by directly generating DPKs in quartz using the ITS ACCEPTP code and incorporating more recent nuclear data. The values are generally slightly lower than those found by Mejdahl (<1% for grains up to 400μm; <2% for grains up to 1mm). Fain *et al.*(1999) proposed a Monte Carlo method to assess the dose contributions from one part of the grain to another using the same DPK data as Mejdahl. The advantage of this approach is the extension of the correction to arbitrary grain shapes. The authors found higher values than Mejdahl (<1% for grains up to 200μm; <1-7% for grains up to 500μm; and around 5% for larger grains) with the exception of the smaller grain sizes from uranium series emissions. The span of Ω was found to be significant for large ellipsoid grains (of the order of mm sieve sizes).

The beta dose rate correction for coarse grains that have been acid-etched during sample pre-treatment was initially presented by Bell (1979). Brennan (2003) provided a more comprehensive method to examine the dose attenuation in grains following etching by considering the dose delivered to the etched grain from the pre-etched mass. In this case,

$$
\begin{aligned}
\Omega(r,r_e) = &\int_0^{r-r_e} F(s)ds \\
&+\int_{r-r_e}^{r+r_e} \left[\frac{1}{16}\left(\frac{s}{r_e}\right)^3 - \frac{3s}{8r_e}\left\{\left(\frac{r}{r_e}\right)^2+1\right\} + \frac{1}{2}\left\{\left(\frac{r}{r_e}\right)^3+1\right\} - \frac{3r_e}{16s}\left\{\left(\frac{r}{r_e}\right)^2-1\right\}^2 \right] F(s)ds
\end{aligned}
\tag{5.3}
$$

where r_e is the radius of the etched grain.

5.2 Estimation of the grain size correction

Previously, the beta grain size correction has been applied to quartz which is commonly assumed to be an inert mineral and we can write $\dot{D}_d = (1-\Omega)\dot{D}_{sed}$. In this section, only quartz will be considered and the

appropriate techniques used in further sections will be introduced. The grain size correction is examined in two ways:

1) directly using three dimensional Monte Carlo simulations. Quartz grains are embedded in a quartz matrix and treated first as the emission source (i.e. self-dosing). In this case, the simulation is efficient and the self-absorbed energy divided by the total energy emitted will give Ω. A second model was developed, which explicitly simulates environmental emission sources, where particles are generated outside the grain and energy absorption tallied within the grain. This requires variance reduction techniques to be implemented (predominately energy cutoff methods using about 10 equally-spaced radial regions) for around 100 million histories (although the majority of histories are not followed fully due to the cutoffs). Called "Direct".

2) analytically using dose point kernel integrations with Equations 5.2 and 5.3. Called "DPK"

Table 5.1 presents a comparison between values obtained in this study by dose point kernels with data from Mejdahl (1979) and Brennan (2003) (data digitised from graphs) as well as direct calculation of the correction for potassium sources. The estimates of the corrections agree to within 0.03 between methods with the updated values generally following the trend of Brennan compared to Mejdahl. Figure 5.3 illustrates the absolute variability of the different correction factors (using the new DPK value as a reference) as a function of grain size. The correction for DPK and direct computation has a maximum offset of about 1% of the IM beta dose rate with the greatest disparity at 1-2mm grain diameters where Ω is near the median value of 0.5. Of less interest for dose rate calculation is the percent variability of the correction factors since this is not only modulated by the grain size but also whether the sources are exterior or interior to the grain. It remains unknown why the direct measurements of the correction do not follow the DPK results within precisional uncertainties and differences are seen for potassium and thorium while the uranium results seem to agree. Several reasons were explored:

a) *Different source energy spectra were used*. The DPK construction converted linearly-spaced nuclide energy spectra into 200 binned, logarithmically-spaced energy spectra to accurately

account for variability at low energies whilst reducing the overall computational requirements of the algorithm. A direct calculation of Ω in MCNP using identical logarithmically-spaced energy spectra gave the same correction factor as the simulations with the original spectra within uncertainties.

b) *Direct computation of the correction was dependent on whether the sources were interior or exterior to the grain.* The two methods produced equivalent results (within uncertainties) for all grains greater than ~100μm diameter (for smaller grains, the tally within the grain from external sources suffers from pathologically increasing imprecision).

c) *Grain size was problematical for the condensed history algorithms.* The larger grain sizes (>1mm) should be insensitive to potential energy indexing/interface issues but discrepancies to the DPK values remain.

Grain size (mm)	Potassium				Thorium			Uranium		
	Direct	DPK	Mejdahl	Brennan	DPK	Mejdahl	Brennan	DPK	Mejdahl	Brennan
0.01		0.005	0.004	0.007	0.035	0.037	0.038	0.026	0.021	0.029
0.02		0.008	0.007	0.007	0.055	0.058	0.047	0.040	0.037	0.040
0.04		0.015	0.014	0.015	0.083	0.088	0.074	0.059	0.056	0.056
0.06		0.022	0.021	0.022	0.104	0.109	0.097	0.073	0.071	0.071
0.08		0.029	0.028	0.030	0.122	0.127	0.117	0.085	0.084	0.083
0.10	0.038 ± 0.009	0.036	0.035	0.037	0.139	0.143	0.134	0.096	0.096	0.096
0.14	0.053 ± 0.007	0.051	0.049	0.053	0.168	0.171	0.164	0.116	0.117	0.119
0.18	0.071 ± 0.005	0.066	0.063	0.068	0.192	0.195	0.190	0.134	0.137	0.140
0.20	0.080 ± 0.005	0.074	0.070	0.076	0.203	0.206	0.202	0.143	0.146	0.150
0.25	0.101 ± 0.004	0.093	0.088	0.096	0.228	0.229	0.229	0.164	0.169	0.175
0.30	0.116 ± 0.003	0.112	0.105	0.115	0.250	0.251	0.252	0.184	0.189	0.197
0.50	0.196 ± 0.002	0.189	0.175	0.193	0.321	0.320	0.329	0.255	0.263	0.275
1.00	0.379 ± 0.001	0.368	0.337	0.371	0.449	0.443	0.466	0.392	0.400	0.417
1.40	0.495 ± 0.001	0.482	0.447	0.487	0.527	0.518	0.547	0.474	0.479	0.502
2.00	0.617 ± 0.001	0.606	0.571	0.610	0.616	0.604	0.636	0.568	0.568	0.595
3.00	0.734 ± 0.000	0.726	0.696	0.728	0.716	0.701	0.734	0.674	0.667	0.698
4.00	0.797 ± 0.000	0.791	0.765	0.794	0.779	0.760	0.794	0.742	0.731	0.763
6.00	0.863 ± 0.000	0.859	0.837	0.861	0.849	0.825	0.859	0.821	0.803	0.836

Table 5.1. Updated correction values of Ω, fractional absorbed internal beta dose, for K, Th and U of spherical quartz grains using a direct MCNP calculation of external sources and dose point kernel methods are compared to values given by Mejdahl (1979) and Brennan (2003). Grain size measurement is the diameter of the grain.
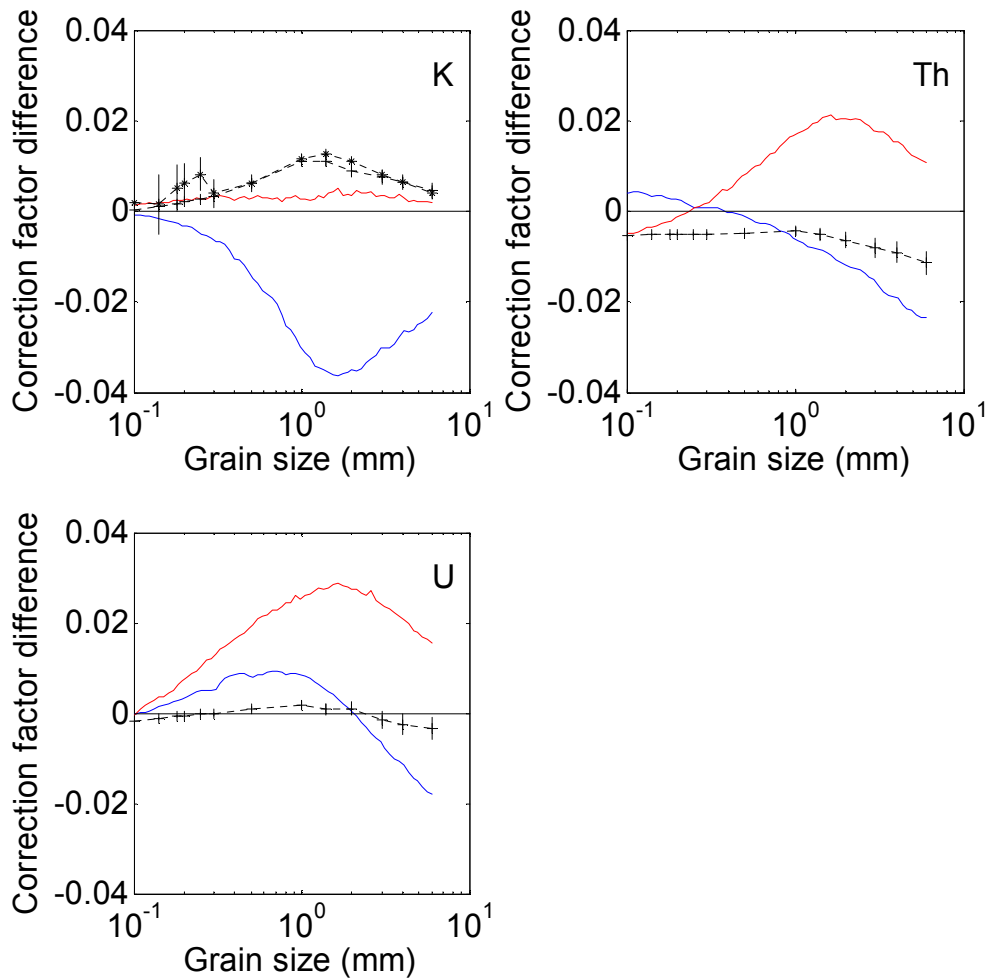
Figure 5.3. Illustration of the data presented in Table 5.1. Using the updated Ω calculated by dose point kernels for reference values, the absolute difference from this reference value is plotted for direct measurements of external sources (black asterisk) and internal sources (black crosses), Mejdahl (1979) (solid blue line) and Brennan (2003) (solid red line).

d) *Smoothing and interpolation of the monoenergetic DPK to form composite DPK introduced systematic uncertainties.* During the construction of the DPK for nuclide sources the suite of monoenergetic PDK are firstly smoothed and interpolated using cubic Hermite splines (MATLAB) so that the same distance points are sampled between DPKs, energy values between the computed monoenergetic DPK are sampled similarly, and the DPKs are resampled using

137

cubic Hermite interpolation to achieve a high resolution with distance. Unfortunately, direct computation of the composite DPK is problematical in MCNP due to the effects of repeated boundary crossings required to provide sufficient spatial resolution. However, the cubic Hermite schemes were accurate to within 0.01% across sampled data points and the differences in the correction factor is negligible for a large variety of smoothing/interpolation schemes tested (such as cubic splines, linear interpolation, etc.).

e) *Integration of DPK to provide estimate of self-dose.* No work has been done to justify Equation 5.2. However, the numerical resolution of the data used to solve the integral was sufficient to reject the possibility of rounding issues being significant.

In the absence of evidence to accept either method as correct, values derived from the DPK procedure will be used unless inappropriate (ie. heterogeneous environments) with an underlying uncertainty of ±0.01 to account for this ambiguity. The difference in values generated by Mejdahl (1979) and, more recently, Brennan (2003) can be ascribed to changes in nuclide emission data, assumptions in the beta energy spectra, and details of dose point kernel calculations. Brennan discusses these issues in some detail and gives an absolute uncertainty to his correction factors of less than ±0.01. Since his data were retrieved through the digitisation of illustrated results, it is likely that up to an extra ±0.01 uncertainty would be reasonable for the purposes of comparison. During this study, a similar procedure to Brennan was followed to generating results and it is likely that the various components of the calculation would not contribute more than ±0.01 absolute uncertainty to the results. A conservative estimate of the total absolute uncertainty for large grains (>0.1mm) is around ±0.02. For smaller grains, the correction is considerably smaller and the absolute uncertainty is probably no larger than ±0.01. It remains surprising that the updated DPK correction factors do not more closely agree with the values of Brennan. The revised DPK Ω values for Rb agree within ±0.005 from the correction factors given by Readhead (2002).
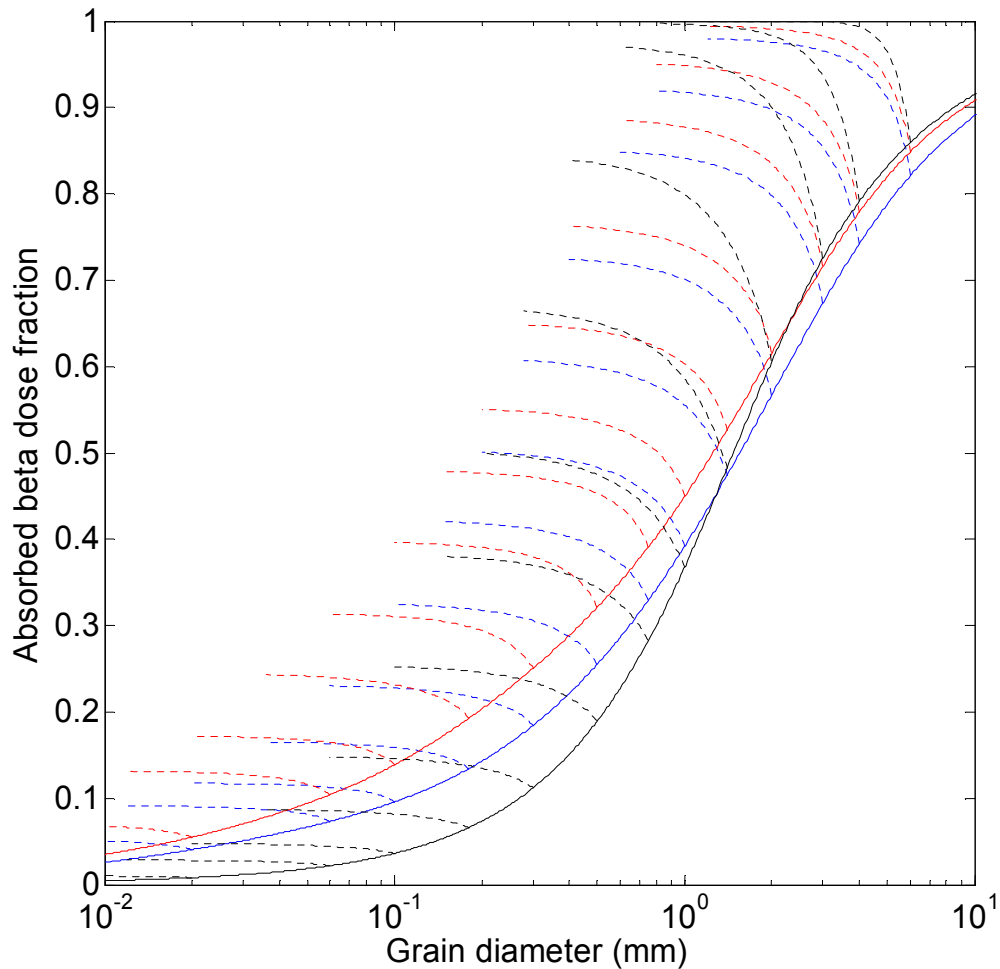
Figure 5.4. Estimation of the internal beta dose fraction Ω for K (black), U (blue) and Th (red) beta emissions from spherical quartz grains using the dose point kernel approach. The dotted lines represent the correction for grains etched to a spherical grain diameter (see text for full details).

Figure 5.4 illustrates Ω for unetched quartz grains for uranium, thorium and potassium sources with examples of the modification to the correction due to isotropic etching of the grain. The behaviour of Ω with grain size shows several general traits: 1) For smaller grains, the correction is dominated by the relative fluence of the low energy beta particles since the range of the radiation is of primary importance. For example, the comparative paucity of low-energy electrons as well as the comparatively higher

weighting of emissions between 0.5-1MeV from potassium emissions leads to a reduced estimation of Ω for grains sizes up to around 1mm; 2) As the grains become larger, the proportion and magnitude of the more energetic particles becomes significant and Ω is decreased for thorium and uranium relative to potassium; and 3) The principal effect of etching on Ω is dominated by the removal of the outer rind of the grain since the dose rate in this part of the grain has the least similarity to the self-dosing infinite-matrix dose rate. Parameterisation of the correction is a useful advance for workers in the calculation of beta dose rate. For each decay group source, the correction for a given percentage of etching of the diameter of a grain can be approximated by fitting polynomials with the dependent variable as the base-10 logarithm of the unetched grain size. It was found that Ω for each etching level was best parameterised by two sixth-order polynomials, one for smaller grain sizes and one for larger grain sizes. The partition grain size to delineate between polynomials was found optimally lie to around the region of maximum slope. A second parameter that states the maximum grain size is required to constrain the polynomial at unity. This accounts for etched grains where the remaining mass was exposed to IMD due to the range of the beta emissions. An application of the parameterisation is presented for potassium sources in Figure 5.5 with Table 5.2 presenting the best-fitted polynomials in the least-squares sense for each decay group between 0.01-10mm spherical quartz grains. The greatest uncertainty lies near the boundaries of the polynomial, namely the small and large grain sizes and near the partition between the two polynomials. An logorithmic (base-10) interpolation of the required grain size and the different corrections for etchings should be sufficient to accurately resolve the correction factor for each pre-treated quartz grain. This is especially the case for smaller grains where the changes in the correction factor due to etching is near linear. However, if the grains are particularly large, there is a significant curvature of the locus of Ω with etching and some more sophisticated methods (such as cubic spline) may be required. The parameterisations add negligible additional error to the correction factors, except around $\pm 10\%$ of the value of the partition grain size where the absolute uncertainty of the correction may be as high as ± 0.003.
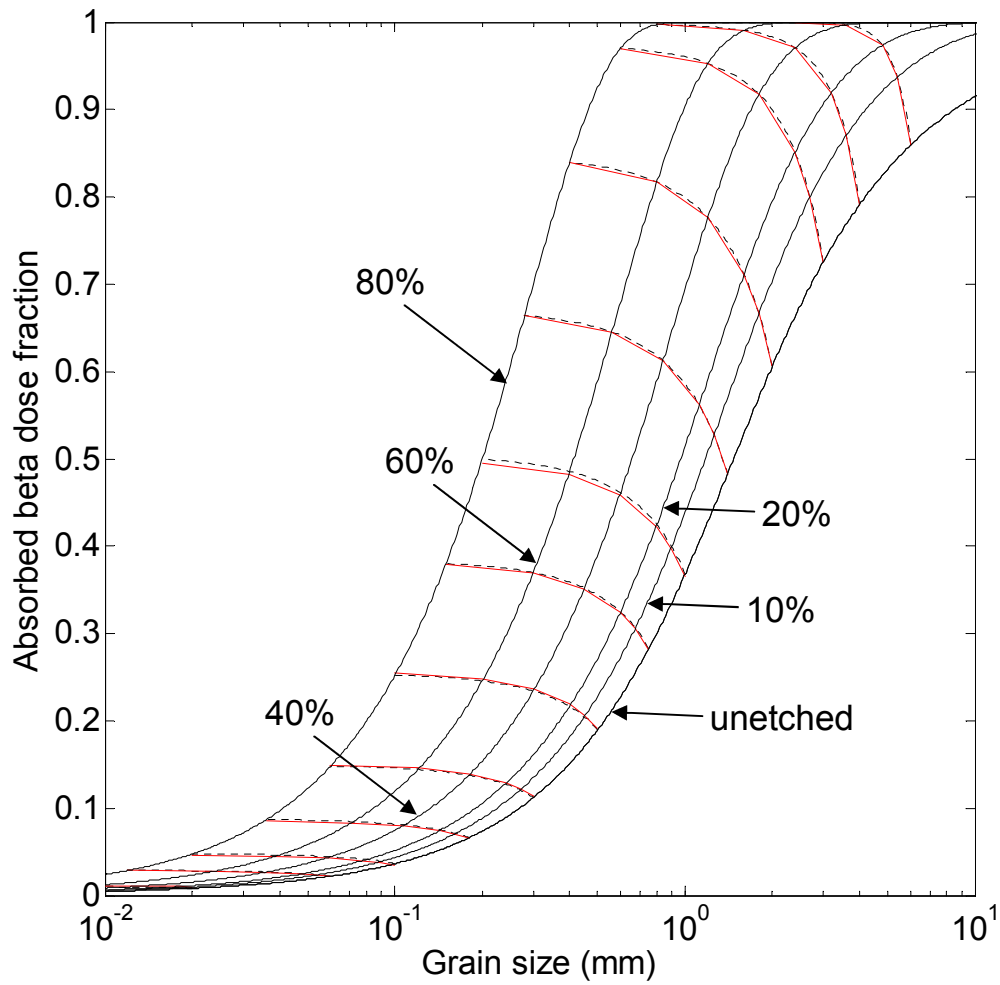
Figure 5.5. The change of Ω with grain size for K beta emissions for the etching of a specified fraction of the grain radius (solid black). The change of the correction for a particular grain size due to etching (dotted black) with the parameterized approximation (red) is illustrated.

Table 5.2. Polynomial coefficients for the parameterization of Ω for spherical quartz grains embedded in quartz for different decay groups such that $\Omega = ax^6 + bx^5 + cx^4 + dx^3 + ex^2 + fx + g$ where $a,b,....g$ are presented from top to bottom respectively and x is the base-10 logarithm of grain diameter (between 0.01-10mm). Different parameterizations are used for small and large grains with the partition grain size given as the cut size. The bracketed values denote the largest unetched grain size the parameterisation applies to (else $\Omega \approx 1$) when lower than 10mm.

	Unetched			10% etched			20% etched			40% etched			60% etched			80% etched		
	Smaller grains	Cut size	Larger grains	Smaller grains	Cut size	Larger grains	Smaller grains	Cut size	Larger grains	Smaller grains	Cut size	Larger grains	Smaller grains	Cut size	Larger grains	Smaller grains	Cut size	Larger grains
Nat U	-4.697-3	2.01	5.629-2	-5.335-3	1.99	5.116-2	-6.024-3	1.92	-7.972-2	-6.921-3	1.79	-7.276-1	-7.404-3	1.73	1.338+0	-7.631-3	1.69	-1.338+0
	-3.980-2		-4.567-1	-4.490-2		-4.572-1	-5.075-2		1.810-1	-5.880-2		3.064+0	-6.338-2		5.566+0	-6.563-2		5.671+0
	-1.121-1		1.470+0	-1.252-1		1.591+0	-1.425-1		4.347-1	-1.682-1		-4.491+0	-1.838-1		-8.408+0	-1.918-1		-8.623+0
	-7.033-2		-2.285+0	-7.630-2		-2.611+0	-9.345-2		1.618-1	-1.239-1		2.521-1	-1.447-1		5.511+0	-1.561-1		5.648+0
	2.359-1		1.490+0	2.623-1		1.747+0	2.725-1		1.259+0	2.781-1		-6.450-1	2.777-1		-1.880+0	2.767-1		-1.936+0
	5.252-1		1.897-1	5.726-1		1.639-1	6.050-1		3.246-1	6.464-1		8.097-1	6.701-1		1.085+0	6.826-1		1.107+0
	3.915-1		4.266-1	4.222-1		4.658-1	4.436-1		4.737-1	4.731-1		4.625-1	4.913-1		4.608-1	5.013-1		4.706-1
^{238}U $\rightarrow$ ^{234}Pa	-1.935-3	2.65	1.092-1	-1.972-3	2.71	2.167-1	-2.132-3	2.71	2.424-1	-2.488-3	2.68	-2.220-1	-2.601-3	2.62	-1.056-1	-2.826-3	2.62	-1.629+1
	-8.790-3		-8.648-1	-7.946-3		-1.602+0	-8.264-3		1.953+0	-9.894-3		9.004-0	-1.007-2		4.457+1	-1.156-2		6.855+1
	1.712-2		2.731+0	2.576-2		4.821+0	3.029-2		6.255+0	3.307-2		-1.269-1	3.715-2		-7.339+1	3.508-2		-1.133+2
	1.659-1		-4.238-1	1.940-1		-7.300+0	2.156-1		9.834+0	2.423-1		6.322-0	2.621-1		5.935+1	2.674-1		9.322+1
	3.781-1		2.988+0	4.200-1		5.284+0	4.561-1		7.323+0	5.087-1		-4.455-3	5.442-1		-2.521+1	5.615-1		-4.079+1
	4.382-1		-1.982-1	4.725-1		-9.431-1	5.008-1		1.630+0	5.446-1		1.658-1	5.736-1		6.437+0	5.904-1		1.018+1
	2.763-1		3.336-1	2.953-1		4.561-1	3.082-1		5.653-1	3.268-1		4.141-1	3.388-1		-2.020-1	3.458-1		-5.558-1
^{234}U	-3.123-1	0.014	2.831-4	-5.822-1	0.014 (0.75)	8.597-2	-1.243+0	0.013 (0.43)	3.053-1	-1.949+0	0.012 (0.25)	5.943-1	-1.394+0	0.012 (0.19)	-3.383-1	-9.063-1	0.012 (0.15)	-2.918+0
	-5.377-1		3.471-3	-9.385+0		4.052-1	-1.913+1		1.752+0	-2.976+1		3.791+0	-2.154+1		-3.680+1	-1.415+1		-2.514+1
	-3.769+1		-1.664-2	-6.228+1		6.489+1	-1.218+2		3.806+0	-1.879+2		9.309+0	-1.374+2		-1.540+1	-9.094+1		-8.869+1
	-1.378+2		2.356-2	-2.176+2		5.528-1	-4.102+2		4.175+0	-6.274+2		1.138+1	-4.622+2		-3.167+1	-3.070+2		-1.632+2
	-2.771+2		-1.870-2	-4.213+2		2.543-1	-7.691+2		2.457+0	-1.167+3		7.288+0	-8.634+2		-3.421+1	-5.726+2		-1.648+2
	-2.899+2		1.737-2	-4.273+2		5.859-2	-7.593+2		7.391+1	-1.144+3		2.295+0	-8.464+2		-1.859+1	-5.564+2		-8.649+1
	-1.225+2		9.906-1	-1.762+2		1.005+0	-3.071+2		1.089+0	-4.601+2		1.271+0	-3.384+2		-3.005+0	-2.181+2		-1.745+1
^{230}Th	-6.460-1	0.024	3.237-4	-7.006-1	0.024 (0.90)	8.497-2	-7.586-1	0.025 (0.52)	2.970-1	-6.302-1	0.024 (0.31)	2.471-1	-4.252-1	0.024 (0.23)	5.512+0	-3.310-1	0.023 (0.20)	6.119+0
	-9.172+0		4.587-3	-9.895+0		2.954+1	-1.068+1		1.183+0	-8.838+0		1.429+1	-5.826+0		3.524+1	-4.368+0		4.048+1
	-1.651+1		-2.395-2	-5.753+1		2.967+1	-6.189+1		1.464+0	-5.088+1		3.270+1	-3.258+1		9.071+1	-2.331+1		1.079+2
	-5.365+1		4.010-2	-1.758+2		2.538+1	-1.884+2		6.760-1	-1.533+2		3.835+1	-9.448+1		1.211+2	-6.338+1		1.493+2
	-2.809+2		-3.742-2	-2.968+2		1.267+1	-3.163+2		2.158-2	-2.536+2		2.446+1	-1.478+2		8.868+1	-8.979+1		1.134+2
	-2.492+2		3.077-2	-2.609+2		2.756+2	-2.762+2		-6.188-2	-2.161+2		8.073+0	-1.153+2		3.389+1	-5.808+1		4.499+1
	-8.909+1		9.847-1	-9.221+1		1.002+0	-9.680+1		9.884-1	-7.268+1		2.081+0	-3.281+1		6.289+0	-9.486+0		8.293+0
^{226}Ra	-7.620-3	0.16	5.369-3	-8.148-3	0.16 (2.50)	4.383-1	-5.928-3	0.17 (1.32)	1.310+0	-5.398-3	0.18 (0.72)	-2.206+0	1.073-2	0.19 (0.51)	-5.180+1	3.329-2	0.19 (0.42)	-3.931+2
	-8.023-2		-1.322-2	-8.603-2		2.893-1	-5.981-2		2.020+0	-5.192-2		-1.036+1	1.350-1		-1.920+2	3.961-1		-1.436+3
	-2.815-1		-3.495-2	-3.007-1		-1.031-1	-1.726-1		1.331+0	-1.256-1		-1.286+1	7.490-1		-2.729+2	1.970+0		-2.119+3
	-1.763-1		1.674-1	-1.721-1		2.165-1	1.687-1		9.827-1	3.258-1		-4.851+0	2.440+0		-1.899+2	5.384+0		-1.615+3
	1.163+0		-2.624-1	1.313+0		-3.430-1	1.857+0		-2.542-1	2.186+0		-7.610+1	4.984+0		-6.979+1	8.841+0		-6.730+2
	2.764+0		2.224-1	3.063+0		1.514-1	3.572+0		2.798+2	3.983+0		-4.258-2	5.934+0		-1.305+1	8.548+0		-1.459+2
	1.932+0		9.057-1	2.122+0		9.787-1	2.343+0		9.985-1	2.569+0		1.000+0	3.150+0		1.873-2	3.876+0		-1.189+1

	Unetched			10% etched			20% etched			40% etched			60% etched			80% etched		
	Smaller grains	Cut size	Larger grains	Smaller grains	Cut size	Larger grains	Smaller grains	Cut size	Larger grains	Smaller grains	Cut size	Larger grains	Smaller grains	Cut size	Larger grains	Smaller grains	Cut size	Larger grains
^{222}Rn → ^{206}Pb	-7.056-3	1.28	5.459-3	-8.130-3	1.27	-1.187-2	-9.362-3	1.22	-2.328-2	-1.124-2	1.17	1.979-1	-1.233-2	1.12	5.205-1	-1.287-2	1.09	5.470-1
	-6.551-2		-7.682-2	-7.501-2		9.388-4	-8.638-2		2.051-2	-1.044-1		-9.727-1	-1.153-1		-2.235+0	-1.208-1		-2.454+0
	-2.167-1		3.345-1	-2.463-1		2.346-1	-2.849-1		2.826-1	-3.495-1		1.974+0	-3.907-1		3.802+0	-4.124-1		4.212+0
	-2.555-1		-5.774-1	-2.882-1		-5.529-1	-3.430-1		-6.504-1	-4.451-1		-1.935+0	-5.151-1		-3.081+0	-5.538-1		-3.332+0
	1.338-1		1.888-1	1.484-1		1.508-1	1.321-1		1.456-1	8.037-2		4.910-1	3.698-2		7.291-1	1.106-2		7.373-1
	5.923-1		5.782-1	6.507-1		6.481-1	6.845-1		6.844-1	7.183-1		6.792-1	7.324-1		6.814-1	7.384-1		6.969-1
	4.535-1		4.546-1	4.924-1		4.926-1	5.199-1		5.198-1	5.571-1		5.580-1	5.793-1		5.801-1	5.913-1		5.917-1
^{235}U → ^{231}Th	3.236-2	0.039	4.829-3	2.449-2	0.038 (3.12)	-5.614-2	1.790-2	0.036 (1.75)	-6.301-2	5.383-2	0.031 (0.99)	1.944-1	1.203-1	0.034 (0.73)	5.730-1	1.413-1	0.033 (0.60)	9.076-1
	3.450-1		-1.593-2	2.244-1		-1.747-1	9.340-2		-1.830-1	4.949-1		1.067+0	1.372+0		3.143+0	1.657+0		5.063+0
	1.376+0		-4.330-3	6.357-1		-7.826-2	-3.258-1		-5.438-2	1.397+0		2.253+0	6.118+0		6.671+0	7.667+0		1.101+1
	2.426+0		7.436-2	8.859-2		1.569-1	-3.382+0		2.115-1	7.374+0		2.212+0	1.332-1		6.803-1	1.766-1		1.167+1
	1.567+0		-1.180-1	-2.417+0		-9.155-2	-9.033+0		-6.726-2	-6.077+0		7.263-1	1.434+1		3.110+0	2.093+1		5.932+0
	1.372-1		9.360-2	-3.304+0		4.173-2	-9.660+0		1.481-2	-9.379+0		9.543-2	7.062+0		6.394-1	1.219-1		1.413+0
	6.014-1		9.613-1	-5.250-1		9.922-1	-2.917+0		9.982-1	-3.531+0		1.003+0	1.901+0		1.047+0	3.506+0		1.126+0
^{231}Pa → ^{207}Pb	-4.114-3	1.41	5.718-2	-4.494-3	1.439	1.824-1	-5.063-3	1.44	1.395-1	-5.906-3	1.44	-1.961+0	-6.227-3	1.42	-8.040+0	-6.312-3	1.41 (5.41)	-1.147+1
	-3.509-2		-4.017-1	-3.815-2		-1.075+0	-4.288-2		1.062+0	-5.001-2		5.120+0	-5.271-2		2.165+1	-5.341-2		3.072+1
	-9.651-2		1.078+0	-1.038-1		2.533+0	-1.175-1		2.917+0	-1.387-1		-3.495+0	-1.465-1		-2.029+1	-1.483-1		-2.897+1
	-3.294-2		-1.278+0	-3.081-2		-2.824+0	-4.248-2		-3.512+0	-6.402-2		-7.202-1	-6.987-2		7.271+0	-6.947-2		1.102+1
	3.156-1		3.368-1	3.517-1		1.064+0	3.677-1		1.399+0	3.838-1		7.731-1	3.977-1		-1.220+0	4.077-1		-2.057+0
	6.339-1		6.714-1	6.920-1		5.937-1	7.312-1		5.764-1	7.827-1		7.123-1	8.150-1		1.001+0	8.332-1		1.115+0
	4.674-1		4.644-1	5.038-1		5.103-1	5.293-1		5.393-1	5.645-1		5.699-1	5.862-1		5.791-1	5.983-1		5.870-1
^{232}Th → ^{208}Pb	-4.072-4	1.96	6.632-2	-3.524-4	2.01	1.032-1	-2.128-4	2.01	-1.288-2	3.659-4	1.92	-1.360+0	7.370-4	1.88	-2.991+0	9.377-4	1.85	-2.326+0
	-2.482-3		-5.108-1	-1.803-3		-7.667-1	-2.503-4		-2.881-1	5.424-3		5.279+0	9.105-3		1.154+1	1.110-2		9.613+0
	1.350-4		1.553+0	3.132-3		2.287+0	9.428-3		1.645+0	3.044-2		-7.231+0	4.442-2		-1.651+1	5.208-2		-1.415+1
	4.791-2		-2.265+0	5.528-2		-3.324+0	6.738-2		-3.065+0	1.041-1		3.900+0	1.295-1		1.067+1	1.437-1		9.066+0
	2.209-1		1.355+0	2.376-1		2.073+0	2.525-1		2.085+0	2.868-1		-8.710-1	3.113-1		-3.525+0	3.255-1		-2.934+0
	4.850-1		2.383-1	5.187-1		6.455-2	5.392-1		7.132-2	5.685-1		7.648-1	5.877-1		1.322+0	5.987-1		1.227+0
	4.494-1		4.715-1	4.824-1		5.274-1	5.024-1		5.494-1	5.278-1		5.166-1	5.431-1		4.897-1	5.514-1		5.063-1
^{40}K	-3.606-3	1.46	6.731-2	-3.885-3	1.51	2.439-1	-3.863-3	1.51	3.082-1	-3.600-3	1.47	-2.510+0	-3.532-3	1.46	-1.287+1	-3.418-3	1.44 (5.11)	-1.935+1
	-2.616-2		-4.723-1	-2.773-2		1.416+0	-2.676-2		-1.913+0	-2.326-2		6.166+0	-2.193-2		3.403+1	-2.050-2		5.112+1
	-4.108-2		1.265+0	-4.031-2		3.296+0	-3.212-2		4.669+0	-1.297-2		-3.398+0	-3.840-3		-3.161+1	3.639-3		-4.816+1
	1.288-1		-1.490+0	1.519-1		-3.655+0	1.820-1		-5.284+0	2.376-1		-2.004+0	2.684-1		1.153+1	2.895-1		1.893+1
	5.429-1		3.713-1	6.053-1		1.413+0	6.627-1		2.154+0	7.553-1		1.470+0	8.116-1		-1.947+0	8.463-1		-3.659+0
	7.252-1		8.146-1	7.959-1		6.939-1	8.531-1		6.244-1	9.395-1		8.015-1	9.948-1		1.295+0	1.027+0		1.525+0
	3.644-1		3.590-1	3.964-1		4.054-1	4.211-1		4.389-1	4.577-1		4.712-1	4.817-1		4.739-1	4.953-1		4.791-1
^{87}Rb	-2.074-2	0.12	7.039-3	-2.285-2	0.12 (3.12)	1.189-1	-2.339-2	0.12 (1.71)	-2.921-2	-2.571-2	0.12 (0.95)	-1.477+0	-2.853-2	0.11 (0.69)	-3.373+0	-3.058-2	0.11 (0.57)	-3.237+0
	-2.674-2		-2.220-2	-2.943-1		2.671-2	-3.025-1		-4.637-1	-3.313-1		-4.984+0	-3.649-1		-1.149+1	-3.891-1		-1.067+1
	-1.394+0		-1.202-2	-1.531+0		-1.017-1	-1.580+0		-4.433-1	-1.727+0		-5.529+0	-1.891+0		-1.400+1	-2.009+0		-1.194+1
	-3.676+0		1.228-1	-4.026+0		2.109-1	-4.169+0		2.733-1	-4.558+0		-2.022+0	-4.974+0		-7.072+0	-5.271+0		-4.474+0
	-4.869+0		-1.948-1	-5.309+0		-2.029-1	-5.507+0		-1.247-1	-6.040+0		-4.341-1	-6.604+0		-1.777+0	-7.006+0		-1.297-1
	-2.399+0		1.587-1	-2.590+0		8.700-2	-2.672+0		3.140-2	-2.976+0		-3.531-2	-3.328+0		-2.175-1	-3.587+0		2.367-1
	4.258-1		9.335-1	4.797-1		9.862-1	5.238-1		9.973-1	5.261-1		9.990-1	4.797-1		9.897-1	4.353-1		1.034+0

Table 5.2. Cont…

143

5.3 Non-quartz grains

An identical treatment of the beta correction from the preceding section can be made for grains composed of different materials; however, the fundamental assumption that the surrounding sediment be composed of identical material as the grain still remains. Correction factors have been generated using dose point kernels for several typical mineral dosimeters (and polyminerallic soils) and the results for unetched grains are presented in Table 5.3. A polyminerallic soil from Mars (Reidler et al., 1997) has a composition of O 44.1%, Na 1.7%, Mg 4.7%, Al 4.6%, Si 23.6%, S 2.2%, Cl 0.6%, K 0.3%, Ca 4.7%, Ti 0.7%, Fe 12.7% and was introduced into this study for comparative purposes.

Various characteristics of the material can account for changes in the beta correction. The principal attribute is the density of the mineral where the unit distance that beta radiation penetrates can be scaled almost linearly with density. It follows that the beta correction for a particular material that occurs with different densities can be established by adjusting (linearly) the grain sizes. A secondary effect is the modification of the dose point kernels due to the behaviour of energy loss in materials of different composition. Table 5.3 ranks the mineral dosimeters according to density and a general trend is that the correction increases for a given grain size with density. The exception is aluminium oxide where the considerably lower effective Z compared to density of Al_2O_3 supports a greater relative stopping power and a slightly smaller beta correction. Figure 5.6 explores the variation of the correction for materials made of different compositions to quartz for K emissions. Once the density dependence is removed, the correction is relatively consistent across mineral types except aluminium oxide and, to a lesser extent, salt.

144
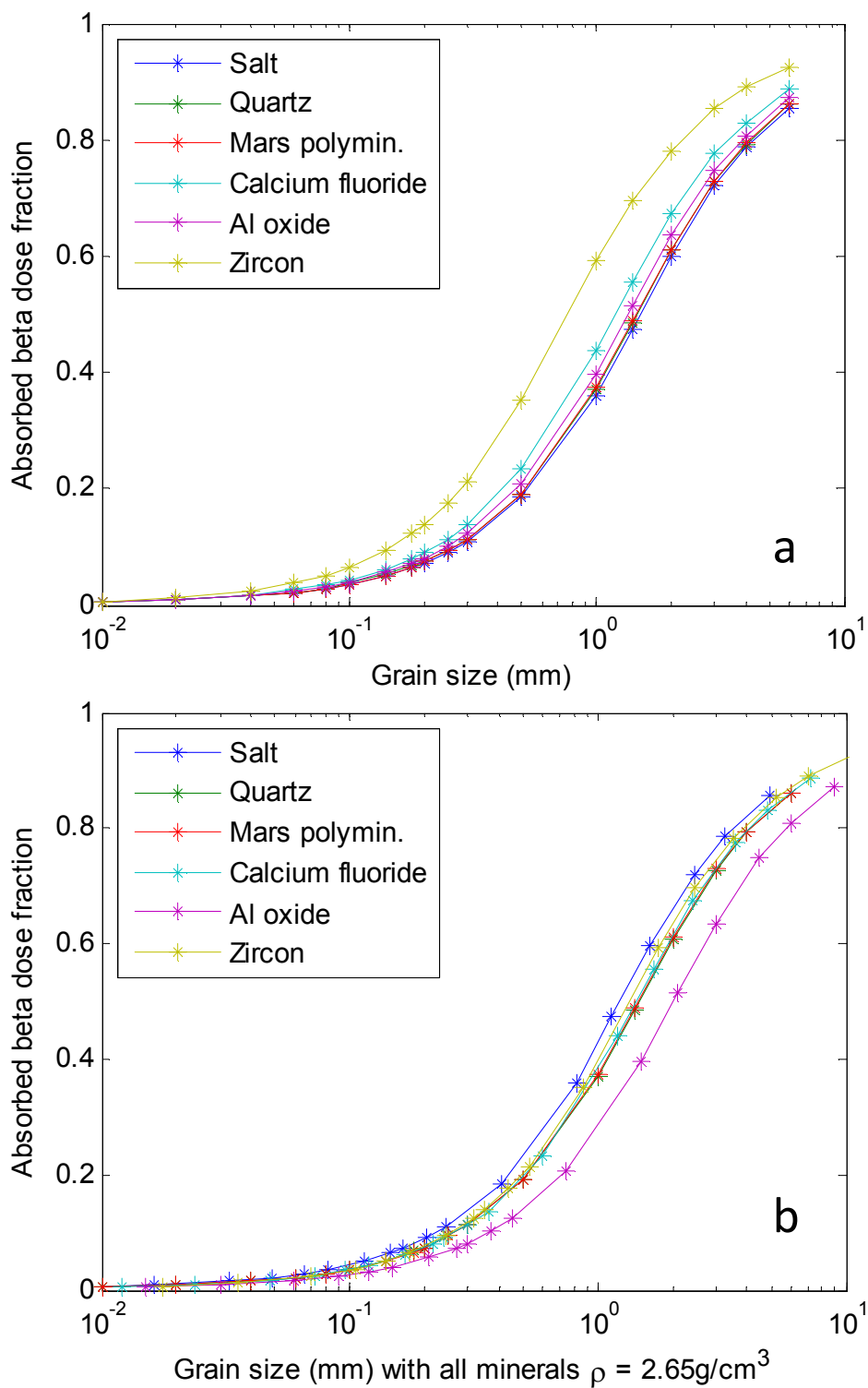
Figure 5.6. Dose point kernel evaluation of Ω for spherical grains from K emissions for different minerals: a) grain size dependence; and b) grain size scaled to remove density dependence.

.

145

	Salt	Orthocl. feldspar	Plagiocl. feldspar	Quartz	Average polymin.	Mars polymin.	Calcium fluoride	Al oxide	Zircon
Chemistry	NaCl	KAlSi$_3$O$_8$	NaAlSi$_3$O$_8$	SiO$_2$	Table 2.3	See text	CaF$_2$	Al$_2$O$_3$	ZrSiO$_4$
Density (g cm^{-3})	2.16	2.55	2.61	2.65	2.65	2.65	3.18	3.97	4.65
Effective Z	14.64	11.85	10.71	10.80	11.60	13.09	14.65	10.65	24.84
Grain size (mm)	Potassium beta emissions								
0.01	0.004	0.005	0.005	0.005	0.005	0.005	0.005	0.005	0.007
0.02	0.007	0.008	0.008	0.008	0.008	0.008	0.009	0.009	0.013
0.04	0.012	0.014	0.015	0.015	0.015	0.015	0.018	0.016	0.025
0.06	0.017	0.021	0.022	0.022	0.022	0.022	0.026	0.024	0.037
0.08	0.023	0.028	0.029	0.029	0.029	0.029	0.035	0.032	0.051
0.10	0.029	0.035	0.036	0.036	0.037	0.036	0.043	0.040	0.064
0.14	0.040	0.049	0.050	0.051	0.052	0.051	0.062	0.056	0.093
0.18	0.052	0.064	0.065	0.066	0.067	0.066	0.080	0.073	0.123
0.20	0.058	0.071	0.072	0.074	0.074	0.074	0.090	0.081	0.138
0.25	0.073	0.089	0.091	0.093	0.094	0.093	0.113	0.102	0.175
0.30	0.089	0.108	0.109	0.112	0.113	0.113	0.137	0.123	0.213
0.50	0.152	0.183	0.185	0.189	0.191	0.191	0.233	0.208	0.352
1.00	0.307	0.358	0.360	0.368	0.371	0.373	0.439	0.397	0.592
1.40	0.413	0.472	0.474	0.482	0.486	0.488	0.557	0.514	0.696
2.00	0.539	0.596	0.598	0.606	0.609	0.612	0.673	0.635	0.782
3.00	0.672	0.718	0.720	0.726	0.728	0.730	0.776	0.748	0.853
4.00	0.748	0.785	0.786	0.791	0.793	0.795	0.830	0.808	0.890
6.00	0.829	0.855	0.856	0.859	0.861	0.862	0.886	0.871	0.926
Grain size (mm)	Thorium beta emissions								
0.01	0.030	0.034	0.035	0.035	0.036	0.035	0.040	0.037	0.052
0.02	0.048	0.054	0.054	0.055	0.056	0.055	0.062	0.058	0.079
0.04	0.074	0.082	0.082	0.083	0.084	0.084	0.093	0.088	0.117
0.06	0.093	0.103	0.103	0.104	0.106	0.105	0.117	0.110	0.148
0.08	0.109	0.120	0.121	0.122	0.124	0.123	0.138	0.129	0.173
0.10	0.123	0.137	0.137	0.139	0.141	0.140	0.156	0.147	0.196
0.14	0.149	0.165	0.166	0.168	0.170	0.169	0.188	0.177	0.233
0.18	0.172	0.189	0.190	0.192	0.194	0.194	0.215	0.202	0.265
0.20	0.182	0.200	0.201	0.203	0.206	0.205	0.227	0.214	0.279
0.25	0.205	0.225	0.226	0.228	0.230	0.230	0.254	0.240	0.311
0.30	0.226	0.247	0.248	0.250	0.252	0.252	0.277	0.262	0.340
0.50	0.291	0.317	0.318	0.321	0.324	0.324	0.356	0.336	0.438
1.00	0.408	0.443	0.445	0.449	0.452	0.453	0.497	0.470	0.605
1.40	0.480	0.520	0.522	0.527	0.530	0.531	0.579	0.549	0.689
2.00	0.566	0.609	0.610	0.616	0.619	0.621	0.700	0.639	0.770
3.00	0.669	0.709	0.711	0.716	0.719	0.720	0.763	0.737	0.842
4.00	0.737	0.773	0.774	0.779	0.781	0.782	0.818	0.796	0.880
6.00	0.818	0.844	0.845	0.849	0.850	0.851	0.877	0.861	0.920
Grain size (mm)	Uranium beta emissions								
0.01	0.022	0.025	0.026	0.026	0.026	0.026	0.030	0.028	0.038
0.02	0.036	0.040	0.040	0.040	0.041	0.041	0.046	0.043	0.056
0.04	0.053	0.058	0.059	0.059	0.060	0.060	0.066	0.066	0.081
0.06	0.066	0.072	0.073	0.073	0.074	0.074	0.081	0.077	0.100
0.08	0.076	0.084	0.084	0.085	0.086	0.086	0.095	0.090	0.118
0.10	0.085	0.094	0.095	0.096	0.097	0.096	0.107	0.101	0.136
0.14	0.103	0.114	0.115	0.116	0.117	0.116	0.130	0.122	0.168
0.18	0.118	0.132	0.133	0.134	0.136	0.135	0.152	0.142	0.197
0.20	0.126	0.140	0.141	0.143	0.144	0.144	0.162	0.152	0.211
0.25	0.144	0.161	0.162	0.164	0.166	0.166	0.187	0.174	0.245
0.30	0.162	0.181	0.182	0.184	0.186	0.186	0.210	0.196	0.275
0.50	0.224	0.251	0.252	0.255	0.257	0.258	0.291	0.271	0.379
1.00	0.347	0.385	0.387	0.392	0.395	0.396	0.442	0.413	0.555
1.40	0.424	0.467	0.468	0.474	0.477	0.478	0.529	0.497	0.644
2.00	0.515	0.560	0.562	0.568	0.571	0.572	0.624	0.592	0.732
3.00	0.623	0.666	0.668	0.674	0.676	0.678	0.725	0.696	0.813
4.00	0.697	0.735	0.737	0.742	0.744	0.746	0.786	0.761	0.858
6.00	0.786	0.816	0.817	0.821	0.823	0.824	0.854	0.835	0.904

Table 5.3. Dose point kernel estimates of Ω for spherical grains of different sizes and composition.

5.4 Influence of grain shape

The correction for the beta dose rate is largely a function of dose-depth distribution of beta radiation and geometry. The previous sections have concentrated largely on accounting for changes in Ω for different materials and other dose-depth factors. However, the assumptions made about the symmetry of the grain (unetched and etched) in the preceding work require the dosimeter to be spherical. It is of interest to determine the sensitivity of the correction to irregular and elongated grain shapes and to examine the work of Fain et al. (1999) who studied this subject in some detail (Fain models spheres, 2:1 oblate spheroids, 2:1 prolate spheroids and a regular tetrahedron - in fact, the illustration would suggest that a regular octahedron was modeled - for different mesh sizes and obtains values of Ω for K, Th and U.). Fain et al. differentiated grain sizes by considering the smallest grains of a particular shape that can pass through a square mesh of uniform width. The method of calculation used a Monte Carlo approach to compute the integrated dose within arbitrary grain shapes from dose point kernel distributions. The technique is essentially a numerical solution of a geometrical problem and may be sensitive to the sampling of draws for low energy beta emissions. The authors attempt to correct for the omission of internal conversion electrons by making an allowance for a thin undosed layer beneath the surface of the grain.

In this work, the correction has been calculated over selected mesh sizes and various proportions of minor, intermediate and major axes for ellipsoids, including those chosen by Fain et al., using MCNP to compute dose from internal sources. Table 5.4 presents values of Ω for K, Th and U for quartz grains. The potassium correction agrees fairly well with the values proposed by Fain et al. with the maximum difference around 0.02. Although presumably a similar agreement exists for thorium and uranium, it appears that the correction factors from Fain et al. are presented from emissions with no contribution from internal conversion electrons and they are substantially lower. In this work, the following convention is followed for naming grain axes: a is shortest, b intermediate and c longest axis.

An examination of the change in the correction with grain shape leads to predictable behaviour that can be used if required. Firstly, for two examples of specified mesh size, the change in Ω with shape is illustrated in Figure 5.7. The zero contour describing the same correction as a sphere is asymmetrical across the Zingg diagram; the main features being 1) a considerable variation in the a/b ratio down to around 0.6 is found as long as the b/c ratio is near unity. This effect is explained by the modulation of the mesh size by the shorter and intermediate axes such that as a is reduced relative to b, the mesh size also decreases and offsets expected reduction in Ω for a given mesh size; and 2) a greater sensitivity to changes in the b/c ratio for a/b ratios less than around 0.6 due to the mesh size becoming less responsive with changing a/b and the increases in c/b offsetting further decreases in a/b. The largest difference in the correction factor for a sphere is associated with rod-shaped grains. Again, this is a geometrical artifact that arises due to the mesh filtering the short and intermediate axes whereas the long axis is not constrained from being substantially elongated. However, for a particular a/b ratio and mesh size, the correction will tend towards an asymptotic value for very elongated grains. For larger grains that have marked platy characteristics (ie a/b < 0.4 and b/c $\approx$ 1), the rapid reduction in Ω as the short axis decreases is notable and will tend to $\Omega \rightarrow 0$ as a $\rightarrow 0$. The changes in the distribution of Ω as a function of mesh size is principally in terms of magnitude with some small migration of the modal correction difference from a sphere towards coarser mesh for disc-like grains compared to rod-like grains.

Some consideration of Ω for ellipsoidal etched grains is required. It is fortuitous for ease of calculation that the response on the unetched correction for various grain shapes is not markedly different to the change in the correction from etching a spherical grain. For example for mesh sizes between 0.1-6mm and potassium emissions, the difference of Ω expected between unetched and a 30μm etched spherical grains is around the same difference of Ω (mostly within ±0.01) between an unetched and a 30μm etched grain for all the shapes analysed in Table 5.4. Therefore, it is suggested that the spherical etching correction difference is applied to the ellipsoidal shapes with an associated uncertainty included.

148

Grain type	Sphere		Rod (prolate spheroid)				Disc (oblate spheroid)				Blade (scalene ellipsoid)		
Axis length (relative)	a = 1 b = 1 c = 1		a = 2 b = 2 c = 3	a = 1 b = 1 c = 2		a = 1 b = 1 c = 4	a = 2 b = 3 c = 3	a = 1 b = 2 c = 2		a = 1 b = 4 c = 4	a = 2 b = 3 c = 4	a = 2 b = 3 c = 8	a = 1 b = 2 c = 4
Sphericity	1.00		0.97	0.93		0.78	0.97	0.91		0.70	0.94	0.80	0.79
Data	*Fain et al.*	MCNP	MCNP	*Fain et al.*	MCNP	MCNP	MCNP	*Fain et al.*	MCNP	MCNP	MCNP	MCNP	MCNP
Mesh (mm)	**Potassium beta emission (unetched)**												
0.1	*0.039*	0.037	0.042	*0.046*	0.045	0.051	0.037	*0.037*	0.036	0.027	0.041	0.047	0.042
0.2	*0.077*	0.076	0.086	*0.091*	0.093	0.105	0.077	*0.075*	0.073	0.055	0.084	0.097	0.086
0.3	*0.111*	0.116	0.131	*0.137*	0.141	0.159	0.117	*0.111*	0.111	0.084	0.127	0.147	0.131
0.5	*0.188*	0.196	0.221	*0.227*	0.237	0.260	0.198	*0.182*	0.187	0.141	0.214	0.244	0.218
1.0	*0.356*	0.378	0.416	*0.411*	0.436	0.463	0.380	*0.333*	0.361	0.276	0.402	0.440	0.403
2.0	*0.593*	0.615	0.650	*0.640*	0.666	0.683	0.616	*0.572*	0.591	0.475	0.636	0.662	0.625
6.0	*(0.846)*	0.864	0.876	*(0.857)*	0.883	0.889	0.863	*(0.846)*	0.850	0.778	0.870	0.882	0.864
Mesh (mm)	**Potassium beta emission (30µm etched)**												
0.1		0.003	0.005		0.006	0.013	0.002		0.001	0.008	0.003	0.005	0.005
0.2		0.031	0.039		0.045	0.054	0.031		0.026	0.005	0.036	0.047	0.036
0.3		0.067	0.082		0.090	0.106	0.068		0.061	0.029	0.077	0.094	0.077
0.5		0.146	0.170		0.186	0.209	0.147		0.136	0.084	0.163	0.191	0.164
1.0		0.331	0.370		0.391	0.420	0.333		0.312	0.221	0.356	0.395	0.356
2.0		0.580	0.618		0.635	0.654	0.581		0.554	0.430	0.602	0.631	0.591
6.0		0.849	0.863		0.872	0.878	0.848		0.834	0.764	0.857	0.869	0.850
Mesh (mm)	**Thorium beta emission (unetched)**												
0.1	*0.087*	0.133	0.143	*0.097*	0.147	0.157	0.134	*0.085*	0.130	0.108	0.140	0.151	0.141
0.2	*0.134*	0.198	0.211	*0.156*	0.217	0.230	0.199	*0.138*	0.193	0.161	0.207	0.221	0.208
0.3	*0.184*	0.245	0.260	*0.206*	0.267	0.283	0.246	*0.176*	0.239	0.201	0.256	0.272	0.256
0.5	*0.256*	0.317	0.336	*0.284*	0.345	0.364	0.318	*0.244*	0.309	0.263	0.331	0.350	0.331
1.0	*0.395*	0.444	0.472	*0.445*	0.483	0.506	0.447	*0.378*	0.435	0.372	0.464	0.489	0.462
2.0	*0.584*	0.611	0.638	*0.631*	0.650	0.669	0.611	*0.559*	0.595	0.514	0.631	0.652	0.623
6.0	*(0.823)*	0.837	0.851	*(0.845)*	0.857	0.866	0.834	*(0.820)*	0.825	0.755	0.846	0.855	0.838
Mesh (mm)	**Uranium beta emission (unetched)**												
0.1	*0.065*	0.094	0.101	*0.073*	0.105	0.112	0.095	*0.061*	0.092	0.077	0.099	0.107	0.100
0.2	*0.110*	0.142	0.153	*0.123*	0.159	0.172	0.143	*0.105*	0.138	0.115	0.151	0.164	0.152
0.3	*0.149*	0.184	0.199	*0.169*	0.207	0.223	0.185	*0.144*	0.179	0.148	0.196	0.212	0.197
0.5	*0.222*	0.257	0.277	*0.249*	0.287	0.307	0.258	*0.205*	0.248	0.204	0.272	0.293	0.272
1.0	*0.358*	0.393	0.422	*0.403*	0.435	0.459	0.396	*0.344*	0.381	0.315	0.414	0.441	0.413
2.0	*0.534*	0.569	0.599	*0.574*	0.612	0.633	0.570	*0.527*	0.553	0.466	0.590	0.614	0.583
6.0	*(0.809)*	0.817	0.835	*(0.803)*	0.841	0.851	0.817	*(0.790)*	0.803	0.726	0.828	0.841	0.822

Table 5.4 Evaluation of Ω for K, Th and U calculated by MCNP using internal sources for a variety of ellipsoid quartz grain shapes. The values of Fain et al. within brackets are estimated using linear interpolation of (log-10) mesh size.
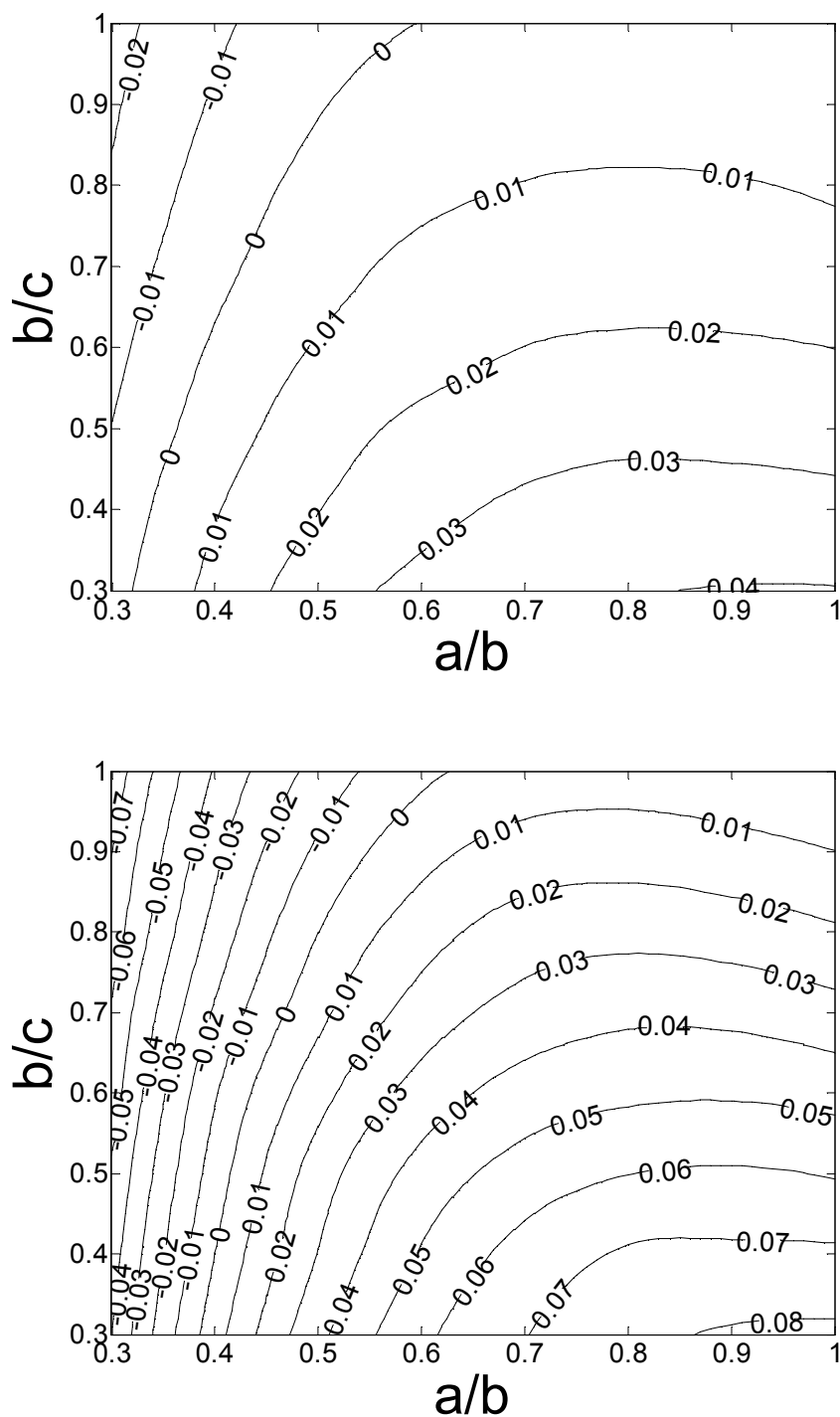
Figure 5.7. The difference of Ω for K emission for different quartz grain ellipsoidal shapes compared to a sphere. Two mesh sizes are illustrated, namely 0.3mm (top) and 1mm (bottom) widths. The short, intermediate and long axes of the ellispsoids are denoted as a, b, c respectively.

5.5 Heterogeneous environments

Commonly in sedimentary environments, the mineral composition is not uniform and Ω needs to be modified to reflect the changes in the charged particle fluence in the grain. There are two principle mechanisms that effect these changes: 1) the ratio in the effective stopping power of the external environment compared to the grain and 2) the change in backscattering characteristics of the external environment. There is not a simple solution for these issues, since the secondary electron flux is not in equilibrium to allow analytical analysis unless the grain size is small. The correction for internal beta emissions in grains that are positioned in heterogeneous environments is primarily affected by the changes in stopping powers and backscattering properties of the exterior. Since the change in backscattering is weakly dependent on Z and the backscattering provides a relatively minor contribution to the correction, the Ω for grains is expected to be largely insensitive to heterogeneous environments apart from strongly contrasting stopping power differences.

MCNP was used to investigate the changes in dose rate of quartz grains embedded in various types of soils. Spherical grains ranging in size from 0.1-6mm were inserted within a uniform material of four types; the fraction of quartz in this material was varied between 0 and 1 to examine the change of Ω along a compositional gradient with the grain treated as the beta radiation source (self-dosing). Table 5.5 presents the difference in the correction from quartz which was found to be largely insensitive (at most Ω changed < 0.02). The correction becomes larger for materials with a smaller effective Z to quartz such as peat and water and Ω decreases for greater effective Z surroundings but the effects were relatively insignificant.

Non-quartz material			Fraction of material in surrounding sediment				
			0	0.2	0.5	0.8	1
Water	Effective Z	10.80		10.09	9.01	7.93	7.22
Peat				9.95	8.67	7.39	6.54
Ave. sediment				10.96	11.20	11.44	11.60
Martian soil				11.26	11.95	12.63	13.09
Potassium beta emissions							
Water	Grain size (mm)	0.1	0.000	0.000	0.001	0.001	0.001
		0.5	0.000	0.003	0.005	0.007	0.008
		1.4	0.000	0.004	0.009	0.015	0.018
		6	0.000	0.001	0.003	0.006	0.008
Peat		0.1	0.000	0.000	0.001	0.001	0.001
		0.5	0.000	0.002	0.006	0.008	0.009
		1.4	0.000	0.004	0.010	0.016	0.019
		6	0.000	0.001	0.004	0.006	0.008
Average sediment		0.1	0.000	-0.001	-0.001	0.000	0.000
		0.5	0.000	0.000	-0.001	-0.001	-0.001
		1.4	0.000	-0.001	-0.001	-0.002	-0.003
		6	0.000	0.000	0.000	-0.001	-0.001
Martian soil		0.1	0.000	0.000	0.000	0.000	0.000
		0.5	0.000	0.000	-0.001	-0.002	-0.003
		1.4	0.000	-0.001	-0.003	-0.005	-0.006
		6	0.000	-0.001	-0.002	-0.002	-0.003
Thorium beta emissions							
Water	Grain size (mm)	0.1	0.000	0.001	0.003	0.003	0.004
		0.5	0.000	0.002	0.004	0.006	0.007
		1.4	0.000	0.002	0.006	0.009	0.011
		6	0.000	0.002	0.004	0.006	0.007
Peat		0.1	0.000	0.000	0.003	0.004	0.004
		0.5	0.000	0.001	0.004	0.006	0.007
		1.4	0.000	0.002	0.006	0.009	0.011
		6	0.000	0.002	0.005	0.007	0.008
Average sediment		0.1	0.000	-0.003	-0.003	-0.002	-0.002
		0.5	0.000	-0.001	-0.001	-0.002	-0.002
		1.4	0.000	-0.001	-0.002	-0.002	-0.002
		6	0.000	0.000	-0.001	-0.001	-0.001
Martian soil		0.1	0.000	0.000	-0.001	-0.001	-0.001
		0.5	0.000	0.000	-0.001	-0.002	-0.003
		1.4	0.000	-0.001	-0.002	-0.004	-0.004
		6	0.000	-0.001	-0.001	-0.002	-0.003
Uranium beta emissions							
Water	Grain size (mm)	0.1	0.000	0.001	0.002	0.002	0.002
		0.5	0.000	0.002	0.004	0.006	0.007
		1.4	0.000	0.002	0.006	0.010	0.012
		6	0.000	0.002	0.004	0.006	0.008
Peat		0.1	0.000	0.000	0.001	0.002	0.002
		0.5	0.000	0.002	0.005	0.007	0.008
		1.4	0.000	0.002	0.007	0.010	0.012
		6	0.000	0.001	0.004	0.007	0.009
Average sediment		0.1	0.000	-0.001	-0.001	-0.001	-0.001
		0.5	0.000	0.000	-0.001	-0.002	-0.001
		1.4	0.000	0.000	-0.001	-0.002	-0.002
		6	0.000	-0.001	-0.001	-0.001	-0.002
Martian soil		0.1	0.000	0.000	0.000	0.000	-0.001
		0.5	0.000	0.000	-0.001	-0.002	-0.002
		1.4	0.000	-0.001	-0.002	-0.003	-0.004
		6	0.000	0.000	-0.001	-0.002	-0.002

Table 5.5. Evaluation of the difference of the fraction of internal beta dose rate (Ω) for K, Th and U calculated by MCNP for spherical quartz grains using internal sources for four different types of sedimentary environments that vary in mass concentration from pure quartz to pure water, peat, "average" sediment or Martian soil respectively.

5.6 Further considerations

The correction to dose rate applies also to alpha and gamma radiation (cosmic radiation is sufficiently penetrating to not require a correction. In both cases, an accurate correction can proceed in a similar way to the beta correction. Brennan et al. (1991) provide a summary of the alpha correction for 0.001-1mm diameter grains by deriving absorbed dose through integration of the track length for spherical grains and their results are presented in Figure 5.8. For finer grains, say 5-11μm, the correction remains substantial (~0.8-0.9 for self-dose correction) and the associated uncertainties must be considered. However, alpha particles have a short range in relation to silt/sands sizes leading to a greater sensitivity to small-scale geometrical effects and consistent heterogeneities in the source distribution coupled with shape irregularities of the grain may lead to significant (and unknown) perturbations in the correction. Possibly even more importantly, impurities arising along track damage in the mineral may affect the alpha efficiency as well. A correction for these types of effect has not been examined in detail. These alpha correction issues are outside the scope of this study and have not been pursued here but software has been developed by the author to address these issues as well as anomalous grain shapes. The correction for gamma radiation is negligible for sandy grains (1mm quartz grains have a gamma self-dose correction of around 0.1-0.2%).
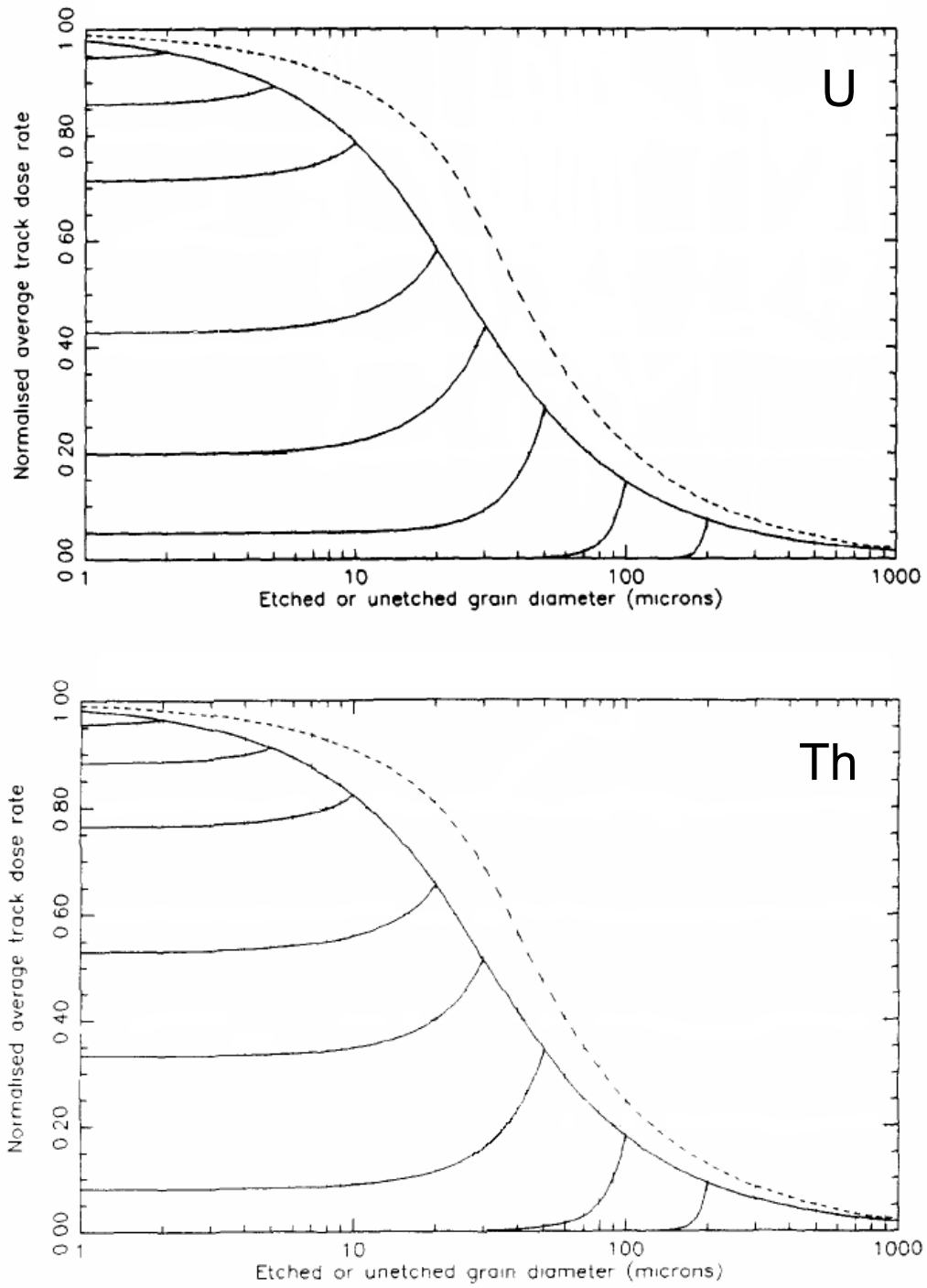
Figure 5.8. Evaluation of 1-Ω for alpha radiations. From Brennan et al. (1991) (solid) and including data from Bell (1980) (dotted).

154

Some mention should be made of issues of grain etching on the correction. During coarse grain pre-treatment, the etching of the outer shell of the grain, where most of the alpha contribution resides, may reduce the uncertainties of achieving a date due to these problems but introduce inaccuracies by the uneven distribution of the remaining material due to preferential etching along mineral defects such as those caused by track damage. Bell and Zimmerman (1978) studied the effects of HF etching of quartz grains and observed pitting and fissures across the grain surface after 40 minutes of 40% HF. Since the evaluation of correction factors assumes that etching is uniform, a small error should be incorporated into the correction to account for this. A *ad hoc* modelling of grains to reproduce etching effects, using software written to address arbitrary grain shapes, would suggest that the average diameter of the etched grain provides a robust starting point for Ω within several percent.

An exciting method of isochron trapped-charge dating using differences in Ω for the internal activity of K-feldspar grains and quartz has been examined by Zhao and Li (2002) following a proposal by Mejdahl (1983) and further examined in articles such as Li et al. (2011). If the internal activities of the mineral grains are sufficiently well-known and both the alpha dose rate and non-dosimetry effects are discounted, the authors propose a linear correlation can be made between absorbed dose and beta dose rate of quartz and feldspar grains of the same size, with the slope giving the OSL age. If several grain sizes are used, a date can be estimated by replacing the dependence on the external beta dose rate (assumed to be uniform) with a dependence on Ω. The strength of the method, therefore, is the ability to achieve a date solely by separating fractions in terms of grain size and mineralogy, measuring internal activities, computing equivalent doses for each fraction and forming an isochron. However, apart for non-dosimetry problems that are readily acknowledged within their paper and assumptions of uniform external dosimetry, they suggest that the internal beta dose is depenedent only on grain size and parent activity. An accurate estimate of the internal beta dose rate is not addressed by the authors. Additionally, even if the D_e changes linearly with grain size, there are indications but no underlying basis to support the view that dose rate also is changing linearly with grain size. For example, variation between grain shapes may occur for

155

different size fractions, leading to a systematic deviation for Ω from the assumption of a spherical grain shape. It is recommended that the uncertainties of the beta grain size correction need to be incorporated into the technique.

5.7 Summary

The beta dose rate correction, Ω, for grains of different sizes have been calculated for each decay group using both dose point kernel integration and direct MCNP computations. Values for Ω in spherical quartz grains compare favourably with previous studies to within ± 0.03. The dependence of the correction on the mineralogy of the grain was relatively minor ($<\pm 0.01$) for a wide variety of elemental compositions with the notable exception of zircon which had a values of Ω up to 0.04 higher than quartz. A more important effect on the grain size correction was the dependence on grain shape. Due to the mesh-based size separation techniques, the longest axis of the grain was the dominating parameter with a significant variation of Ω (>0.03 for 300μm diameter and >0.06 for 1mm diameter) for relatively minor changes from a sphere (Wadell sphericity of 0.8). The effect of the composition of the surrounding sediment on the values of Ω is unlikely to cause a difference of more than 0.02 on the correction.

Chapter 6: Dose rate modelling for hominin skull dating

6.1 Introduction

Reconstructing the evolution and dispersion of hominins remains a central endeavour in archaeology. The dating of hominin evidence aims to ascertain a sequence (or a point in a sequence) of chronological markers for environmental, cultural or physical development in human history. A variety of methods are used:

a) Chronometric including ESR (Grun et al., 2005), OSL (Jacobs and Roberts, 2009), radiocarbon dating (Higham et al., 2010); U-series dating (Pike et al., 2006), Ar/Ar dating (Scaillet et al., 2008), amino acid racemisation (de Torres et al., 2010);

b) Genetic (Endicott et al., 2010); and

c) Material assemblage and environmental proxies including faunal and floral markers (Stuart and Lister, 2001).

Each technique offers different advantages for forming chronologies in terms of time-scale, accuracy and ubiquity of application but direct dating of the fossil is favoured (Grun et al., 2006). Trapped charge dating can be applied to the fossil itself using ESR methods on teeth or OSL/TL methods can be applied indirectly by dating sediments deposited contemporaneously with the fossil (and preferably still attached *in situ*). Since the time range of OSL dating can span much of the presence of *Homo erectus* in Britain some 500ka (Rhodes and Nathan, 2000) up to modern times and suitable materials are ubiquitous, OSL dating offers a useful chronometric tool in resolving Palaeolithic issues. It should be emphasised that trapped charge dating both provides

ages beyond the range of radiocarbon and does not suffer from bias relating to the radiocarbon calibration curve. However, the presence of fossils in sediments is problematical for dose rate estimation for several reasons and this chapter provides approaches to address such issues.

Fossils may substantially affect the energy spectrum of radiation in the sediment due to differences in composition and activity. This may in turn lead to dose rate gradients near the fossil that must be modelled to achieve accurate dates. In this chapter, hominin fossil skulls have been modelled in detail from CT scans and the gamma (and beta) radiation field has been mapped using MCNP. A second problem is the post-depositional alteration of fossils, such as phosphate leaching, which may require time evolution modelling of the dose rate. In addition, the activity of the fossil may change significantly over its depositional history. The uranium content of living bone and teeth is negligible (Chen, 1995, Iyengar et al., 1978). However, the presence of significant concentrations of uranium in groundwater, in a soluble form (hexavalent state) as a uranyl complex (Langmuir, 1978), over the burial history of fossil bone and teeth may have significant consequences for dose rate exposure. Archaeological bone and teeth are particularly effective adsorbers of uranium (due to a number of factors, primarily the large microscopic surface area of bone and the high affinity of hydroxyapatite for uranyl ions (Millard and Hedges, 1996)). The partition coefficient - the ratio of adsorbed U per unit mass of bone/dentine to groundwater concentrations – may rise to an excess of 10^5 or more (Pike et al., 2002) and a "closed-system" assumption is often not applicable. Unfortunately, the uranium uptake history of the fossil is unknown and leaching of uranium due to changes in the redox conditions during burial can occur. Recent models predicting the diffusion of uranium into bone and/or U-series/ESR coupled dating (Pike et al., 2002, Grun et al., 2010) may reduce the uncertainty in the uranium contribution to dose rate in some circumstances. However, the dose rate arising from adsorbed uranium decay chain emissions is time dependent in terms of both in-growth of daughters and migration of uranium. Since the daughters within the uranium decay chains release

different energy spectra, the modelling of the fossils has been independently implemented for each decay group as a function of time. A third problem with skull dating is the difficultly in comprehensive sampling of the fossil due to curatorial concerns and we have been able to collect only limited material from unobtrusive locations.

In this chapter, the environmental dose rate of three archaeologically significant hominin fossil skulls is examined with a discussion of the trapped-charge dates achieved where possible. They are all museum specimens with two being poorly associated with contextual sediments. The calculation of an accurate dose rate for the fossil skulls remains case specific although the approach can be generalised to other studies. The case studies presented here were not selected primarily as illustrative examples of dose rate modelling but came about as collaborative work during the course of this D.Phil. owing to the important role that dose rate modelling represents in these complex scenarios.

6.2 Case studies
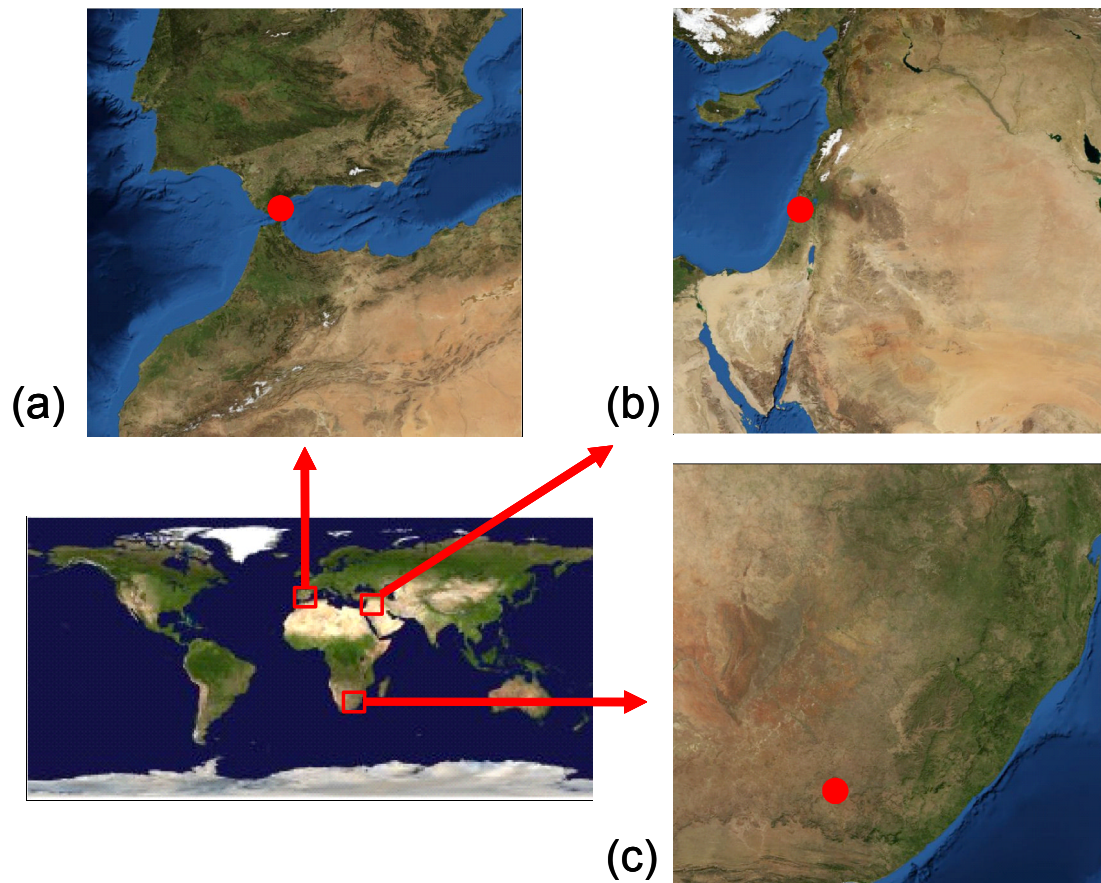
Figure 6.1. Locations of the three case studies: (a) Forbes' Quarry, Gibraltar; (b) Skhul Cave, Israel; and (c) Hofmeyr, South Africa. The three images are approximately 1100km length and breadth and were downloaded from the NASA image gallery (www.nasa.gov).

6.2.1   Skhul V skull

The caves on the slopes of Mount Carmel (see Figure 6.1), including Es Skhul (McCown and Keith, 1939), Tabun (Jelinek, 1982), Kebara (Rak, 1990) and Qafzeh (Vandermeersch, 1981)

contain a well-preserved and complex record of hominin occupation. The sites are placed along the so-called "Middle East Corridor" (Stringer and Gamble, 1993) which has been proposed as a major early human migration route between Africa, Europe and Asia. Of particular interest to the study of hominin development are the sequence of colonisation by both anatomically modern humans and Neanderthals in this area and the nature of the relationship between hominin societies. The key site of Mugharet Es Skhul (Garrod and Bate, 1937), containing a collection of about nine early *Homo sapien* individuals some of whom appear to have been intentionally buried, has been the subject of a considerable dating effort +(Stringer et al., 1989, McDermott et al., 1993, Mercier et al., 1993, Grun et al., 2005). The motivation for high-resolution analysis of the gamma dose rate associated with fossils in the Skhul cave was to inform the calculation of coupled ESR/U-series dates ranging from 100 to 135 ka for the site presented by Grun et al. (2005). The bulk of the analysis presented in this chapter is published by Nathan and Grun (2003) together with a discussion of the ESR dating implications of gamma dosing and shielding by a fossil skull of a tooth. The Skhul V skull was used as a proxy fossil for this work due to its remarkable preservation (see Figure 6.2) and the availability of CT data.

Figure 6.2. The Skhul V skull. (D.Brill, Peabody Museum)

6.2.2   Hofmeyr skull

Genetic studies of present-day humans suggest a migration of anatomically modern humans out of Africa some 25-65ka ago (Ingman et al., 2000, Forster, 2004, Kivisild et al., 2006) from sub-Saharan Africa. However, conflicting evidence points towards modern populations having some genetic ancestry from non-African sources (Eswaran et al., 2005, Garrigan et al., 2005). Changes in human fossil morphology, particularly craniometric approaches (Roseman and Weaver, 2004), may be used as an independent method to resolve interregional variability. This strategy has been applied to the Hofmeyr skull (Grine et al., 2007), which is anatomically modern but has some archaic features (see Figure 6.3), and demonstrated that the individual was most closely related to

Upper Palaeolithic Eurasians. This is significant because the Hofmeyr skull was found in South Africa (see Figure 6.1) and recently dated to 36±3ka (described below) which would be consistent with Upper Palaeolithic Eurasians migrating from sub-Saharan Africa. The skull was discovered in 1952 residing in a dry channel bed of Vlekpoort River near Hofmeyr. No contextual sediments were available as the site was flooded and buried soon after discovery. The skull cavities were filled with sand cemented by carbonate. The sand within the skull is likely to provide a good proxy for the age of death since a) the organic material would decay quickly and rapid infilling was probable; b) the good preservation of the skull would suggest little mobility after deposition as well as insignificant disturbance of the endocranial matrix; and c) several sub-samples provided similar dates (Grine et al., 2007). The dates for the Hofmeyr skull were obtained using OSL with a dose rate estimate that coupled U-series dating of carbonate to a time- and space-dependent model. Radiocarbon dating was not viable due to insufficient intact collagen content. Three samples (H_1, H_2 and H_3) were extracted by drilling in locations near the centre of the cranial cavity so that beta radiation may be assumed to be uniform. Part of each sample provided quartz grains that were separated for OSL measurement (75-150μm grain diameter) and part of the remaining fraction was used for dosimetry measurements. The D_e values were calculated for H_1, H_2 and H_3 to 50.3±4.0Gy, 49.5±1.8Gy and 51.1±2.8Gy respectively providing dates of 40.9±4.2ka, 33.0±2.5ka and 34.7±3.4ka respectively. The contribution to the project discussed here considers only the estimated dose rate and its influence on the final dates achieved.

Figure 6.3. The Hofmeyr skull (from Grine et. al., 2007)

6.2.3 Forbes' Quarry skull

The Southern Iberian peninsula supports a rich record of human occupation in the Late Pleistocene with over eighty Middle Palaeolithic and over sixty Upper Palaeolithic sites identified (Finlayson and Giles Pacheco, 2000), allowing an intensive view of human interaction with their

environment and environmental change. In 1848, a cranium (see Figure 6.4) was found during industrial excavations at Forbes' Quarry, Gibraltar (Busk, 1865) (see Figure 6.1), placing the remains as historically one of the earliest found Neanderthal fossil specimens (Stringer, 2000). Unfortunately, little of the *in situ* sedimentary material remains intact – at least not within the cave itself – with cemented, sandy sediments around the immediate vicinity of the quarry considered to be geomorphologically and chronologically disassociated with the cave (Rodríguez-Vidal, pers. comm.). Two U-series dates (Rodriguez-Vidal et al., 2004) of spleleothems have been obtained at Forbes' Quarry of 79.8±8.4ka and 19.9±1.1ka with the former achieved from a "dirty" calcite sample. Small quantities of sediment were removed from within the nasal cavity and these form the basis for an ongoing OSL dating project lead by Prof. E.J.Rhodes who found a collective D_e of 22.91 ± 1.34Gy for 180-220µm quartz grain diameters.

Figure 6.4. The Forbes Quarry skull (Natural History Museum, London)

6.3 MCNP modelling of the skull

6.3.1   Methodology

The geometrical basis for modelling fossil skulls was facilitated by computed tomography imaging (Hounsfield, 1973), so-called CT scans. Although there have been numerous examples of using CT images in MCNP modelling, primary for medical radiotherapy (DeMarco et al., 1999, Oliveira et al., 2004, Park et al., 2004, Solberg et al., 2001, Zemanhof et al., 1996), there has not been a widely distributed software utility available (now supplied by commercial firms e.g. van Riper (2005)) prior to the work presented in this chapter for automated CT to MCNP conversion. In order to undertake these projects, and allow spatial dose rate modelling, the CT scans were manipulated into a "standard" format through the following steps:

1) The image stack was converted to bitmap format using ETDIPS v2.0 (Mullick et al., 1998) and a three-dimensional matrix of voxels was created.

2) The matrix was resampled to the required resolution, usually around 3-4mm voxels for gamma dose rate applications.

3) Conversion of 8-bit greyscale into binary (i.e. bone or not bone). Fossil bone was selected for greyscales over 110. This criterion approximated a median value between conservative selections of either only non-black voxels (>0) or only white voxels (=255) in the greyscale.

4) Compute the density changes (to be later used as input into the radiation model) needed to be made for the skull and sediment in order to keep the corresponding number of voxels in the resampled matrix consistent with the original matrix. This guarantees a constant mass for the skull independent of resampling.

5) A maximal cropping (reducing) of the voxel matrix without loss of information.

Since this work progressed over an extended interval, the built-in functionality of the codes improved and was incorporated into models as it became available.

A so-called "boxed-cell" approach was used in the first instance, before the circulation of MCNPX lattice speedup routines (see below), for the input of the geometrical information of the skull into MCNP4C. The geometry was divided into 252 blocks plus several additional surrounding regions. Where skull heterogeneities occur within a block, the region is voxellated into constituent materials to accurately model the geometry. Computational considerations (speed and memory) required that both the number of cells and, more importantly, the complexity of the cells, that is the number of bounding surfaces per cell, were minimised. However, due to coding constraints, the maximum permitted number of source cells in MCNP4C was 1,999. The following protocol was used to build the geometrical inputs with a view to optimise the above considerations (see Figure 6.5):

1) The entire geometry was divided into a mesh of parallelepipeds that matched the voxel matrix of the skull plus a 100cm x 100cm x 100cm block region of sediment surrounding the skull.

2) Volumes around the teeth were retained as discreet, high resolution spatial regions in order to achieve flux tallies with a view for ESR dating applications.

3) The cells, their bounding surfaces and the sources were inserted into MCNP input format automatically using bespoke software. The energy deposition track-length tally (F6) was used for all defined cells.

4) The sequential axial slices of the input were checked using the internal MCNP geometry plotter to compare with the bitmap images. Up to 10,000 source points were simulated, using MCNP4C, to ensure that starting locations were consistent with either the skull or sediment acting as the gamma source with uniform activity.

A) For sedimentary sources

5) Two models were run with one placing sedimentary sources in the region around the skull and one with sources in the outer periphery. This enhanced the precision of the simulation.

6) A mesh of rectangular parallelepipeds was formed. All material within each box was grouped as either sediment or skull.

B) For skull sources

7) A collection of rectangular parallelepipeds was formed, where adjacent voxels along the first dimension (x-axis) of the matrix that had the same composition were combined.

8) If a region had a number of parallelepipeds with the same composition, these were combined. This allowed the number of cells to decrease but the number of boundary surfaces (six per parallelepiped) to remain constant.

9) The complex axial slices were stacked into the geometry input for the radiation model.
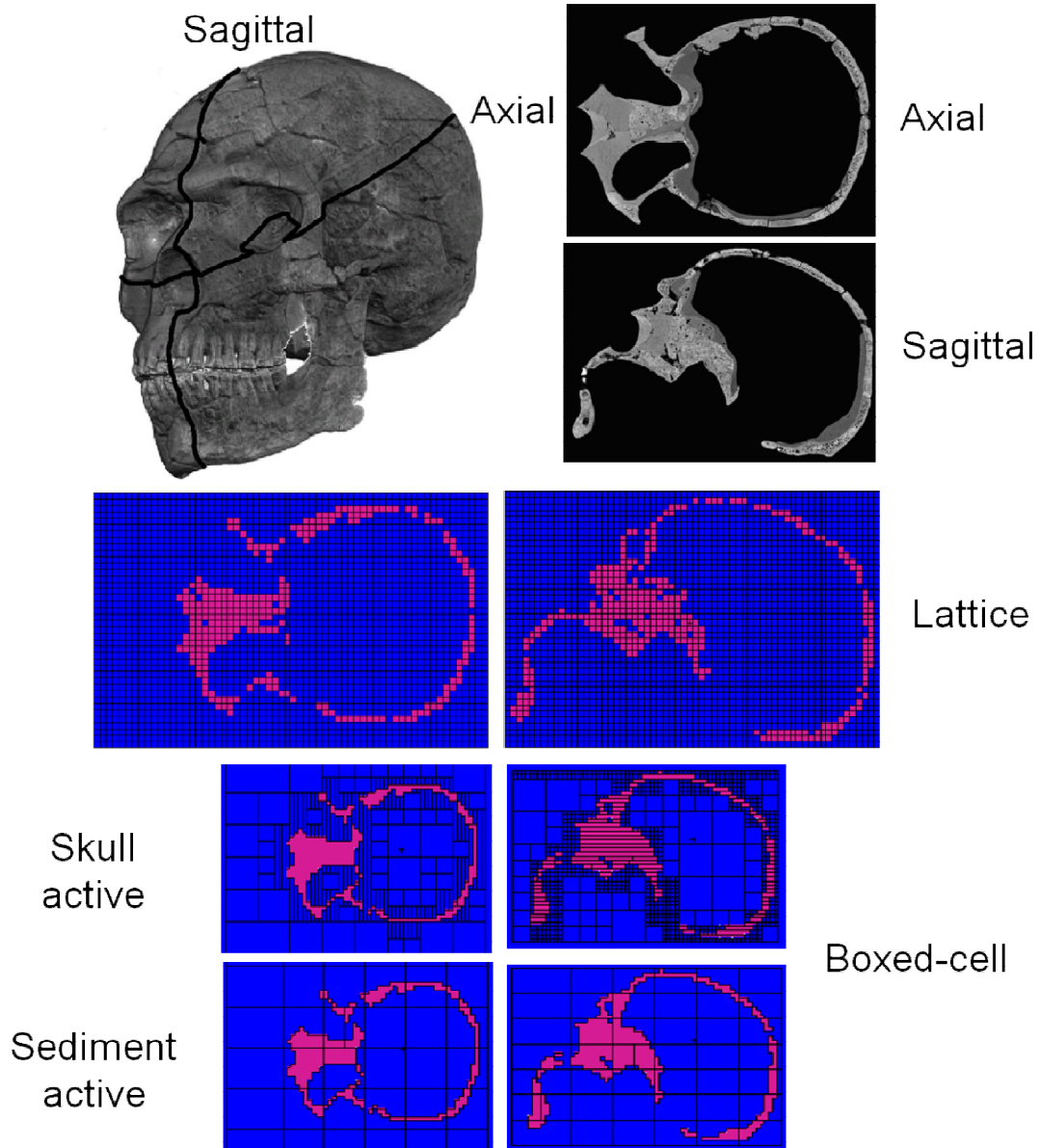
Figure 6.5. The construction of geometrical inputs for MCNP models from CT scan data. A rendered image of the Skhul V skull is marked with the position of axial and sagittal slices used in this example (seen at the top right). The lattice approach for MCNP modelling is built from isotropic voxels filled with the sediment (blue) or skull (red). By contrast, the "boxed-cell" approach takes two forms: either skull-based radioactive sources or sediment-based radioactive sources.

With the advent of the lattice tally "speedup" found in MCNPX2.5 and subsequently included in MCNP5, significant gains in calculation speed, by several orders of magnitude, became available for gamma transport modelling of voxellated geometries. A lattice in MCNP(X) consists of a three-dimensional grid template overlaying the volume within a specified region (see Figure 6.5). Within each grid space, the user may specify certain characteristic geometries. As the CT voxel matrix is essentially a three-dimensional rectilinear grid, it is a relatively trivial task (compared to the previous "boxed-cell" method) to insert the geometry and associated sources into a MCNP lattice input, with fossil, sediments and the modelled region identified by different "universes". The speedup gains computational efficiencies by essentially swapping memory for speed (G. W. McKinney, pers. com.). A few simple cells are replicated throughout the geometry. In these circumstances, the code only requires the position of the current particle location for sourcing, tracking and tallying instead of investigating the entire model geometry at each step using computationally expensive search algorithms. Since exactly the same geometry is modelled as with the boxed-cell approach, an equivalent dose deposition is tallied. A check for correspondence between results from the two methods was made and found identical within precisional uncertainties. Additional benefits of the lattice input includes: an enormous simplification of the geometry, source and tallies to facilitate checking and interpretation (since an x,y,z index of all the voxels is commented in the lattice cards); no limits on the number of voxels used as sources; and allows a finer resolution for equivalent computing resources. The building of input files for MCNP was automated.

6.3.2   Physical parameters

Fossil bone was assumed to consist entirely of the predominate mineral phase, hydroxyapatite ($Ca_5(PO_4)_3(OH)$), with differences in bone density becoming a simple proxy in the model for either post-depositional leaching of calcium phosphate and/or degradation of collagen or further

mineralisation (Hedges, 2002). The average density of dense human bone, over the life time of an individual is approximately $1.9g/cm^3$ (Cameron et al., 1999). Hydroxyapatite is treated as the key component of fossil bone since "in general, for a constant environment, the older the fossil bone the less organic matrix it contains" (Hare, 1980). However, it is a concern that the changes in composition of the bone may not be treated adequately, with remaining collagen-based organic matter in specimen fossils incurring systematic errors in the dose rate calculation. Table 7.1 presents the standardised energy-integrated mass-absorption coefficients for infinite-matrix gamma radiation transversing different compositional mixtures of infinitesimally thin fossil bone encased within "typical" sediment (Garrels and Mackenzie, 1971) with 25% water content (by mass). This is the measure of the efficiency of the material to absorb gamma radiation. In addition, an estimate of the dose rate fluctuations within a 4mm isotropic voxel comprising inert bone is made, with a density of $2 g/cm^3$. Bone collagen was taken to be composed of 7% H, 51% C, 18% N, 24% O, by mass (L. Reynard, pers. com.; after Eastoe (1955)). For the sensitivity testing presented in Table 6.1, collagen appears to be an adequate surrogate for the organic matrix of modern bone, as it accounts for about 90% of organic dry mass, and modern bone is comprised of no more collagen than 25% of total dry mass (Hare, 1980). Despite the potentially large variation of alterations that fossil bone may have undergone, the effect on gamma radiation dose deposition is shown to be minimal. Surrounding sediments, including material within the cranial cavity, for lack of additional information was assumed to be consistent with an infinite, uniform 'average' sediment. Sediments were extended to a spherical radius of at least 55cm, which effectively provides an infinite-matrix. The effect of carbonate (or other minerallic interstitial material) is treated, with little loss of validity, with a post-modelling dose rate correction, to allow the modelling results themselves to be of more general applicability.

	Radiation source	'Effective' mass-absorption coefficient	Absorbed dose (Gy/Gy)
0% collagen	U	1.00	1.00 ± 0.03
	Th	1.00	1.00 ± 0.03
	K	1.00	1.00 ± 0.02
10% collagen	U	0.98	0.98 ± 0.03
	Th	0.99	0.99 ± 0.03
	K	1.00	1.00 ± 0.02
25% collagen	U	0.96	0.96 ± 0.03
	Th	0.98	0.97 ± 0.03
	K	1.01	0.99 ± 0.02

Table 6.1. Effective mass-absorption coefficients of IMD gamma radiation traversing bone and dose deposited in 4mm isotropic voxel of inert bone, for varying amounts of preserved collagen in bone. Results are presented as standardised against the inorganic bone fraction.

Due to possible cases of secular disequilibrium of the uranium decay chains, the uranium contributions to dose rate, from both sediment and bone, were divided into simple decay groups: $^{238}U \rightarrow ^{234}Pa$; ^{234}U; $^{230}Th \rightarrow ^{206}Pb$; $^{235}U \rightarrow ^{231}Th$; and $^{231}Pa \rightarrow ^{207}Pb$.

All models were run for approximately 20 million particle histories, except those where outer sediments were used as sources, which were continued to approximately 80 million particle histories. This provided a relative uncertainty in absorbed dose of less than 5% in voxels near the skull. All results were assessed as the ratio of energy deposited in the tally detector to the infinite-matrix dose.

6.3.3 Skhul V skull modelling

Skhul V has been intensively studied and fortuitously the CT scans of the skull were publicly available (courtesy of the Peabody Museum, Harvard University; at

172

http://www.peabody.harvard.edu/skhul.html). The images of the Skhul V skull comprised a stacked deck of 256 noheader files with isotropic voxel dimensions of 0.488mm presented as axial slices. Due to some reconstruction of the skull using plaster and the paucity of available sediments that surrounded the Skhul fossils, any dose rate modelling work of the skull in its burial context can only be considered to be representative. The "boxed-cell" approach initially was used to represent the skull and sediment geometry. However, the modelling of the skull was repeated using MCNP5 with the lattice speedup approach when available. For the Skhul V specimen, the environment was modelled in both dry and wet (25% water by mass (Aitken, 1985a)) conditions, with bulk densities of 1.755g cm^{-3} and 2.0g/cm^3 respectively. Bone densities of 1.6g/cm3 and 2.7g/cm3 were used for modelling of the Skhul V specimen to account for a wide range of, though not necessarily extreme, diagenetic changes to fossil bone.

	Sediment type	$^{238}U \rightarrow {}^{234}Pa$	$^{230}Th \rightarrow {}^{206}Pb$	$^{235}U \rightarrow {}^{231}Th$	$^{231}Pa \rightarrow {}^{207}Pb$	U	Th	K
IMD (μGy/a per ppm U, Th; %K)		2.0	109.0	0.5	1.4	113	48	243
Lower incisor	Dry	0.166 ± 0.002	0.070 ± 0.001	0.254 ± 0.001	0.150 ± 0.001	0.073 ± 0.001	0.069 ± 0.001	0.061 ± 0.001
	Wet	0.169 ± 0.002	0.070 ± 0.001	0.256 ± 0.001	0.153 ± 0.001	0.074 ± 0.001	0.069 ± 0.001	0.061 ± 0.001
Upper incisor	Dry	0.165 ± 0.002	0.070 ± 0.001	0.252 ± 0.002	0.149 ± 0.001	0.073 ± 0.001	0.066 ± 0.002	0.061 ± 0.001
	Wet	0.167 ± 0.002	0.070 ± 0.001	0.257 ± 0.002	0.154 ± 0.001	0.074 ± 0.001	0.066 ± 0.001	0.061 ± 0.001
Lower molar	Dry	0.192 ± 0.001	0.086 ± 0.001	0.282 ± 0.001	0.179 ± 0.001	0.090 ± 0.001	0.084 ± 0.001	0.074 ± 0.001
	Wet	0.195 ± 0.001	0.086 ± 0.001	0.285 ± 0.001	0.183 ± 0.001	0.090 ± 0.001	0.084 ± 0.001	0.074 ± 0.001
Upper molar	Dry	0.191 ± 0.001	0.086 ± 0.001	0.280 ± 0.001	0.178 ± 0.001	0.090 ± 0.001	0.083 ± 0.001	0.075 ± 0.001
	Wet	0.195 ± 0.001	0.087 ± 0.001	0.285 ± 0.001	0.183 ± 0.001	0.091 ± 0.001	0.084 ± 0.002	0.076 ± 0.001

Table 6.2(a). Gamma dose contributions (columns 3–6) and gamma shielding (columns 7-9, U and Th chains in equilibrium) for the whole skull as a fraction of the infinite matrix dose, IMD (skull density 1.6g/cm³). Uncertainties are precision contributions only.

	Sediment type	$^{238}U \rightarrow {}^{234}Pa$	$^{230}Th \rightarrow {}^{206}Pb$	$^{235}U \rightarrow {}^{231}Th$	$^{231}Pa \rightarrow {}^{207}Pb$	U	Th	K
Upper incisor	Dry	0.146 ± 0.002	0.059 ± 0.001	0.233 ± 0.002	0.129 ± 0.001	0.062 ± 0.001	0.057 ± 0.002	0.049 ± 0.001
Upper molar	Dry	0.162 ± 0.001	0.068 ± 0.001	0.251 ± 0.001	0.147 ± 0.001	0.071 ± 0.001	0.065 ± 0.001	0.058 ± 0.001

Table 6.2(b). Same as Table 6.2a for the skull cap.

	Sediment type	$^{238}U \rightarrow {}^{234}Pa$	$^{230}Th \rightarrow {}^{206}Pb$	$^{235}U \rightarrow {}^{231}Th$	$^{231}Pa \rightarrow {}^{207}Pb$	U	Th	K
Lower incisor	Dry	0.131 ± 0.000	0.044 ± 0.000	0.216 ± 0.000	0.112 ± 0.000	0.048 ± 0.000	0.043 ± 0.000	0.037 ± 0.000
Lower molar	Dry	0.145 ± 0.000	0.052 ± 0.000	0.230 ± 0.000	0.126 ± 0.000	0.055 ± 0.000	0.050 ± 0.000	0.044 ± 0.000

Table 6.2(c). Same as Table 6.2a for the mandible.

	Sediment type	$^{238}U \rightarrow ^{234}Pa$	$^{230}Th \rightarrow ^{206}Pb$	$^{235}U \rightarrow ^{231}Th$	$^{231}Pa \rightarrow ^{207}Pb$	U	Th	K
IMD (µGy/a per ppm U, Th; %K)		2.0	109.0	0.5	1.4	113	48	243
Lower incisor	Dry	0.221 ± 0.002	0.110 ± 0.001	0.311 ± 0.002	0.211 ± 0.001	0.114 ± 0.001	0.108 ± 0.001	0.095 ± 0.001
Upper incisor	Dry	0.216 ± 0.003	0.110 ± 0.001	0.307 ± 0.002	0.205 ± 0.002	0.115 ± 0.001	0.104 ± 0.002	0.095 ± 0.001
Lower molar	Dry	0.259 ± 0.001	0.135 ± 0.001	0.350 ± 0.001	0.251 ± 0.001	0.139 ± 0.001	0.131 ± 0.001	0.116 ± 0.001
Upper molar	Dry	0.257 ± 0.001	0.136 ± 0.001	0.348 ± 0.001	0.248 ± 0.001	0.141 ± 0.001	0.131 ± 0.001	0.118 ± 0.001

Table 6.2(d). Gamma dose contributions (columns 3-6) and gamma shielding (columns 7-9, U and Th chains in equilibrium) for the whole skull as a fraction of the infinite matrix dose, IMD (skull density 2.7g/cm³). Uncertainties are precision contributions only.

	Sediment type	$^{238}U \rightarrow ^{234}Pa$	$^{230}Th \rightarrow ^{206}Pb$	$^{235}U \rightarrow ^{231}Th$	$^{231}Pa \rightarrow ^{207}Pb$	U	Th	K
Upper incisor	Dry	0.190 ± 0.002	0.091 ± 0.001	0.279 ± 0.002	0.177 ± 0.001	0.095 ± 0.001	0.089 ± 0.002	0.076 ± 0.002
Upper molar	Dry	0.215 ± 0.001	0.107 ± 0.001	0.304 ± 0.001	0.200 ± 0.001	0.111 ± 0.001	0.099 ± 0.001	0.090 ± 0.001

Table 6.2(e). Same as Table 6.3a for the skull cap.

	Sediment type	$^{238}U \rightarrow ^{234}Pa$	$^{230}Th \rightarrow ^{206}Pb$	$^{235}U \rightarrow ^{231}Th$	$^{231}Pa \rightarrow ^{207}Pb$	U	Th	K
Lower incisor	Dry	0.173 ± 0.001	0.071 ± 0.000	0.258 ± 0.000	0.154 ± 0.000	0.074 ± 0.000	0.069 ± 0.000	0.059 ± 0.000
Lower molar	Dry	0.195 ± 0.000	0.083 ± 0.000	0.278 ± 0.000	0.176 ± 0.000	0.087 ± 0.000	0.080 ± 0.000	0.070 ± 0.000

Table 6.2(f). Same as Table 6.3a for the mandible.

The fraction of the sediment-sourced infinite-matrix gamma dose rate within the teeth that is shielded by the skull was computed using the boxed-cell approach. The calculations for the upper and lower teeth of the incisor and molar regions are presented in Tables 6.2(a)-(c) for bone density of 1.6g cm^{-3} and Table 6.2(d)-(f) for bone densities of 2.7g cm^{-3}. To within several percent variation, the reciprocal relationship between source and shielded infinite-matrix dose rates of the skull and sediment is maintained so that Table 6.2 can be used to describe behaviour either as a source of radiation (giving Ω) or as a shield (giving 1-Ω). The shielding from the whole skull to specific teeth is not additive for comparing shielding to other parts of the skull; the geometrical relationship between different locations of the skull leads to asymmetrical shielding (eg. distance of skull cap to teeth; dose rate rising in skull cap to lower teeth shielded by upper teeth; etc.). It is clear that the density of the bone has a marked influence on the shielding (uranium IM dose rate shielding on lower incisor is 0.0731 for ρ = 1.6g cm^{-3} and 0.1137 for ρ = 2.7g cm^{-3}) and the magnitude of shielding is approximately proportional to the density. Molars were found to have a substantially higher shielding than incisors for two main reasons: 1) they have greater self-shielding due to their larger mass and 2) they have a closer proximity to the centre of mass of the skull. In Table 6.2(a), the effect of wet sediment IM dose rate were directly compared with dry sediment IM dose rate with no significant change in shielding (<2%) despite the increased proportion of lower energy photons in the energy flux spectrum entering the skull from wet sediments.

The application of obtained values to three archaeological dating programs using ESR/U-series methods was made by Grün[1] and presented in Nathan and Grün (2003). In the analysis of the Skhul II burial remains (Grun et al., 2005), which consists of a partial skull and partial mandible, two models can be evaluated: 1) U 60ppm dentine from Skhul II where the net effect of the skull

---

[1] The results presented in this paragraph was research performed by Grün and not explicitly work achieved during this D.Phil.

would alter the age by 1.6% and 2) U 9ppm bone surface from Skhul IX where a correction of less than 0.8% is obtained. The Mungo 3 mandible and skull cap (Thorne et al., 1999) had a somewhat higher sensitivity to the fossil correction with a net reduction in the early-uptake age of 63ka by some 3ka. The Border Cave 5 mandible date (Grun et al., 2003) due to low internal activity, was revised from 74ka to 77ka due to the shielding of the dose rate.

6.3.4   Hofmeyr skull modelling

MCNP5 was used to calculate the dose absorbed within the skull and an "average" sediment through the lattice speedup approach. The emission sources were either from the sediment or uranium (+ daughters) within the skull. The geometry for the skull was developed from a CT stack for the Hofmeyr skull comprised of 342 DICOM format files with isotropic voxel dimensions of 0.5mm (F. Grine, pers. com.). The average bone density value of 1.9g cm^{-3} was used for the Hofmeyr specimen, in the absence of a direct measurement. The bulk density of the sediment was estimated as 2.0g cm^{-3}.

The distributions of dose rate as a fraction of the IM dose rate within the cranial cavity for potassium are illustrated in Figure 6.6, with the radioactive source either the sediment (left) or the fossil skull (right). The spotty nature of the sediment-source dose rate results arise from precisional uncertainties in the MCNP tallies but increasing the number of histories does not significantly affect the accuracy of the dates derived from the modelling. The different decay groups have significantly different dose rate gradients near the skull depending on the weighting of the higher energies in the flux spectrum. For example, potassium sources from the sediment demonstrate a gradual convergence to maximal values from the bone to near the centre of the

skull whereas the photon emission of ^{234}U is a 13keV x-ray and the dose rate retains an IM dose rate throughout the skull with a precipitous drop-off near the bone (in this case, the dose rate will be near half IM on the bone surface).
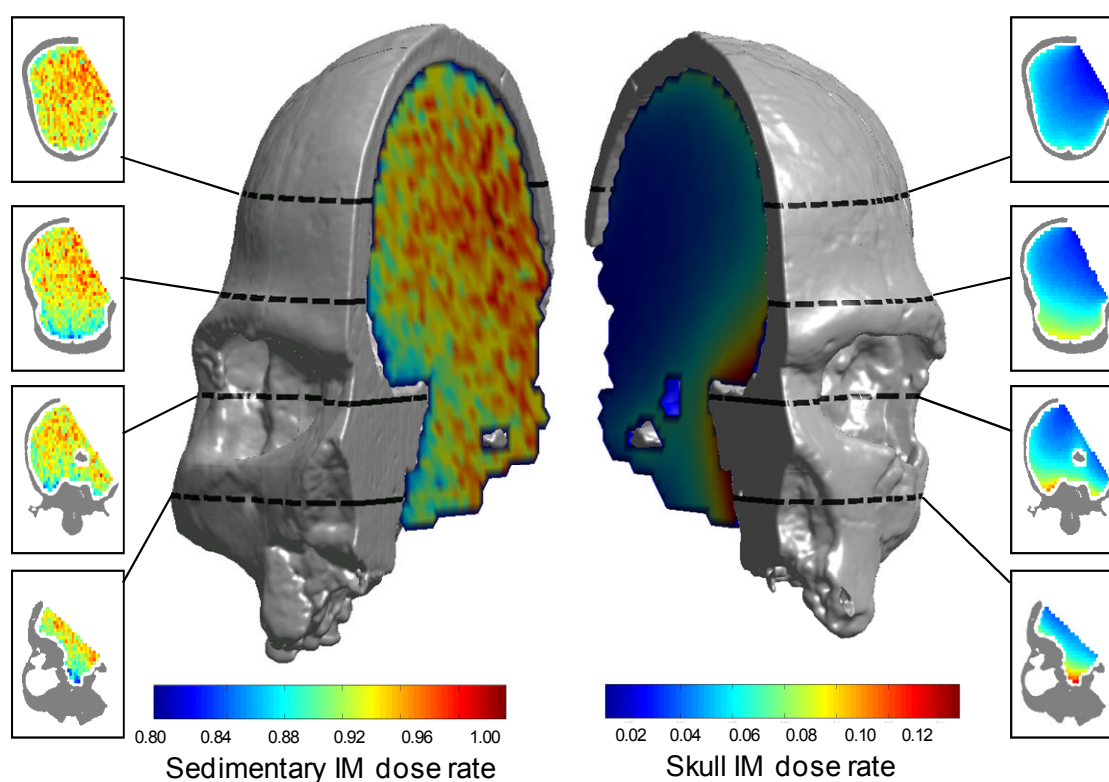
Figure 6.6. The infinite-matrix dose rate of uranium in sediments inside the Hofmeyr skull from sedimentary sources (left) and skull-based sources (right).

Figure 6.7 shows the extent of the shielding of the U, Th and K infinite-matrix gamma dose rate due to the skull. Three samples (H1, H2 and H3) were extracted near the centre of the cranial cavity, although the exact locations are unknown, though they resided within the innermost 2cm diameter of the cavity. The dose rate does not vary more than several percent systematically

across this region and an average gamma dose rate value was applied for all three samples. This includes the small effect of the skull shielding and the dose rate begins to converge to an IM shielding ratio of approximately 0.94±0.02(1σ) K, 0.93±0.02(1σ) Th, 0.94±0.03(1σ) U for sedimentary sources despite large precisional variation (arising due to sizeable number of voxels (>10^6) considered).
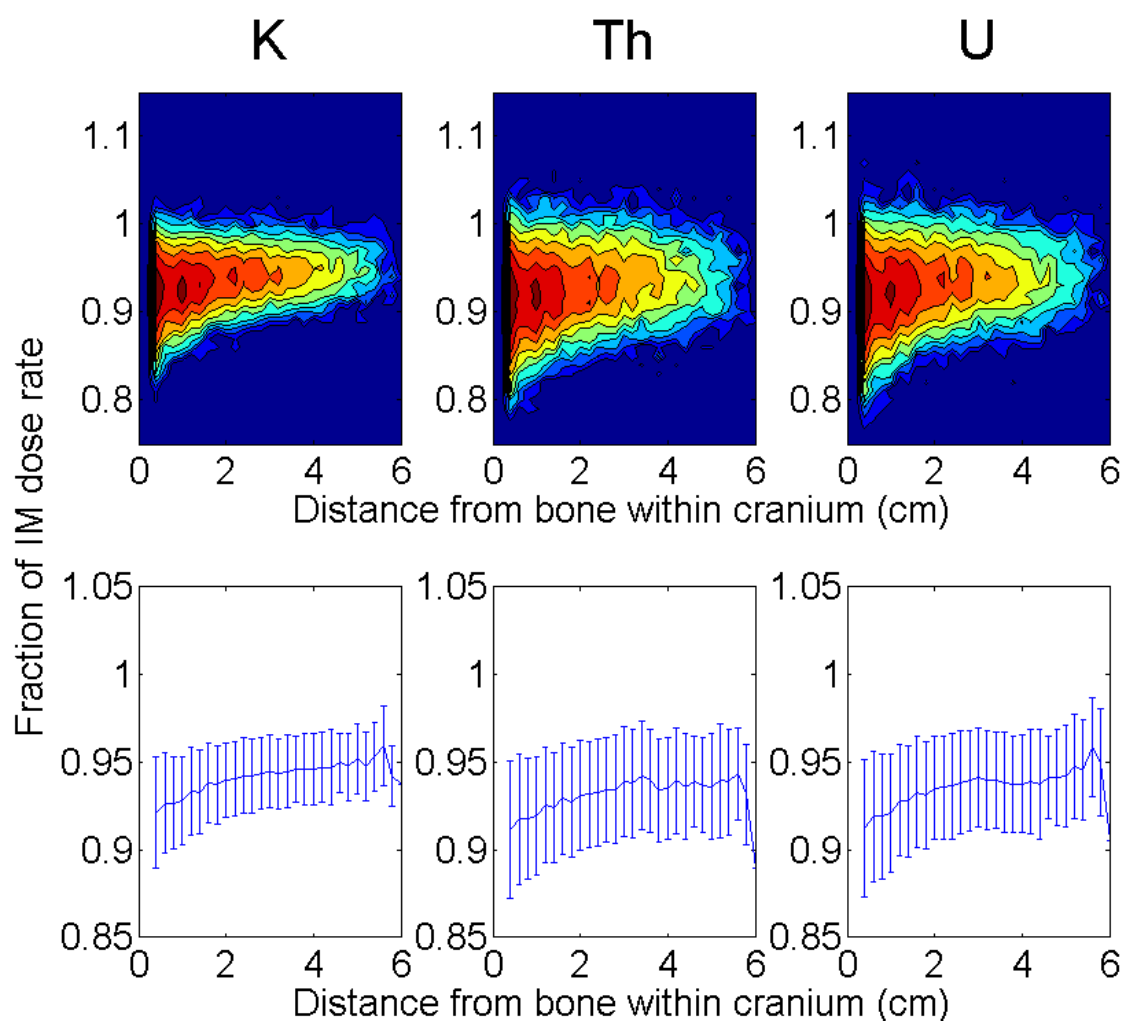
Figure 6.7. The fraction of the infinite-matrix dose rate from sediment sources of U, Th and K at different distances from fossil bone of the Hofmeyr skull. No data are given for distances within beta range of the bone. Top graphs are contour plots of the probability density of the shielding factor with distance (contours are approximately log-scale) and the bottom graphs are average values per distance interval with 1σ uncertainty. (Note: the maximum distance of a voxel from fossil bone, not illustrated, is approximately 6.04cm)

Figure 6.3 illustrates the deterioration of the skull after discovery and it is likely that the skull was in considerably better condition during burial. Since the CT scans were performed recently, they almost certainly have led to an underestimation of the effects of the skull on shielding of dose rate. However, no further correction has been made within this study owing to a lack of detailed supporting information.

6.3.5 Forbes' Quarry skull modelling

A CT image stack of the Forbes' Quarry skull was obtained (Prof. C.B.Stringer, Dr. M. Bastir, pers. com.) comprising of 167 axial slices with 1mm resolution. Although the location of the sampling within the nasal cavity of the skull could be accurately determined over the gamma scale, uncertainties remain as to proximal location of the sediments to the skull over the beta scale. To some extent, the beta dose rate from sedimentary sources is shielded by the skull, and reciprocally, the beta dose rate arising from uranium in the skull will partially contribute to the sample. Furthermore, the coarse quartz grains (180-220μm) used for dating were exposed to a brief HF etching resulting in the removal of approximately 5μm (Prof. E.J.Rhodes, pers. comm.), leading to incomplete removal of external alpha dose rate contributions. However, it is assumed the alpha dose rate is an IM calculation and was not required to be spatially modelled here.

The gamma IM modelling used the same parameters and methods as the Hofmeyr skull, since no intact contextual information was associated with the skull, giving values of 0.91±0.02(1σ)% K, 0.89±0.03(1σ)ppm Th, 0.89±0.03(1σ)ppm U for sedimentary sources. The beta IM modelling assumed the skull and sediment were semi-infinite slabs, since an insignificant contribution to beta dose rate is expected to arise from the sediment matrix beyond the fossil mass (ie. exterior to the nasal cavity), and tallied across the predicted region of sampling. The extraction was estimated from a layer between 1-3mm distant from the fossil bone (Dr. E.J.Rhodes, pers. com.)

giving beta IM ratios of 0.99±0.01(1σ)% K, 0.97±0.02(1σ)ppm Th, 0.97±0.02(1σ)ppm U across this region for sedimentary sources.

6.4 Dose rate modelling

The preservation of hominin remains in caves and other typical environments frequently encounter an evolution of burial conditions over time. Two main, often correlated, changes calculated here are the migration of uranium leading to secular disequilibrium of the decay chains and the diluting effect of carbonate formation on activity. Trapped-charge studies have included time evolution calculations (using Equation 1.2) for archaeological dating (Olley et al., 1997).

Only the Hofmeyr and Forbes Quarry skulls were explicitly dated in this research and the remaining sections pertain to these skulls only. It must be stressed, however, that both skulls involved a collaborative process with colleagues and results presented here are not the sole work of this author.

6.4.1   Elemental measurements

Dr Richard Bailey performed all chemistry and analytical methods on the Hofmeyr samples except Prof. Gideon Henderson and Dr. Alistair Pike who were responsible for U-Series measurements. Prior to dissolution, the three Hofmeyr skull samples were given ~10% HCl wash to separate the elemental composition of material associated with the carbonate fraction from the insoluble remains. The view was taken that the leach fraction would yield uranium and daughters in secular disequilibrium and the residue would reside in secular equilibrium. U-series data (^{238}U, ^{234}U, ^{232}Th and ^{230}Th) were collected for the samples by MC-ICP-MS and the secondary carbonate provided a 95% confidence date of 24.0±5.2ka for formation (Prof. G.Henderson, pers

com). These measurements, along with the insoluble fraction, were used to provide U and Th concentrations for the dose rate calculations. Potassium concentrations for the Hofmeyr skull sediments were measured independently using ICP-MS (Dr. R.M.Bailey, pers. comm.). The results are recorded in Table 6.3. Since the three subsamples were collected relatively close together over the gamma radiation scale, we combined the three concentrations of radioisotopes when calculating gamma dose rate in order to improve uncertainty estimation. This gave combined elemental concentrations of $0.46\pm0.07(1\sigma)\%$ K, $3.28\pm2.18(1\sigma)$ppm Th and $1.27\pm0.47(1\sigma)$ppm U.

Sample	Soluble U (ppm)	Insoluble U (ppm)	Th (ppm) (Sol.+Insol.)	K (%) (Sol.+Insol.)	$(^{232}Th/^{238}U)$	$(^{230}Th/^{238}U)$	$(^{234}U/^{238}U)$
H1	2.541 ± 0.003	0.799 ± 0.001	2.063 ± 0.007	0.410 ± 0.014	0.202 ± 0.003	0.225 ± 0.004	1.658 ± 0.001
H2	1.263 ± 0.001	1.744 ± 0.002	5.791 ± 0.122	0.550 ± 0.021	0.631 ± 0.022	0.408 ± 0.020	1.304 ± 0.001
H3	6.211 ± 0.070	1.253 ± 0.002	1.978 ± 0.007	0.435 ± 0.024	0.087 ± 0.002	0.354 ± 0.002	1.955 ± 0.001
Assumed detritus					1.2 ± 0.6	1.0 ± 0.1	1.0 ± 0.1

Table 6.3. Elemental concentrations of subsamples from the Hofmeyr skull. 'Sol.' and 'Insol.' refer to the acid soluble (leach) and acid insoluble (residue) fractions respectively. All errors shown are 2σ. The assumed detritus values are described in Ludwig and Paces (2002).

Small amount of sediment from the Forbes Quarry skull were analysed (Dr. T. Barrows, pers com.) using ICP-MS (U and Th) and ICP-AES (K and Ca) and found to contain $0.123\pm0.006(1\sigma)\%$ K, $0.583\pm0.029(1\sigma)$ppm Th and $0.255\pm0.013(1\sigma)$ppm U (see Table 6.4). However, it must be emphasised that the sample is very small and may not be representative of the dose rate over the gamma scale. This is problematical since no suitable bulk *in situ* sediment is available to be sampled directly. However, two unpublished OSL dating suites were measured for adjacent (and likely representative) relict coastal sand bank deposits overlooking Catalan Bay and the analysis of these sediments may offer some points of comparison. Rodriguez et al. (2004)

suggest that these sands originate from a marine beach before being deposited as wind-blown dunes on coastal plains. Prof. Edward Rhodes collected two samples in 2001 from the lower regions of the sand to achieve dates of IOS5. He recorded a calibrated NaI gamma spectrometer dose rate of 0.22±0.02mGy/a. Two samples (Roderiguez et al., 2007) were collected by the author in 2006 at ~31m and ~39m above mean sea level (corresponding to the bases of the lower and upper sand units respectively) and analysed using OSL (Dr. J-L. Schwenninger, pers com.) to achieve dates of 130±15ka and 95±9ka respectively. The μNomad NaI gamma spectrometer recorded a gamma dose rate of 0.24±0.01mGy/a and 0.23±0.01mGy/a for the lower and upper samples respectively. This compares favourably with the measurements made in 2001. Further ICP-MS of the two 2006 samples yielded values of 0.34±0.08(1σ)% K, 2.2±0.4(1σ)ppm Th and 0.7±0.1(1σ)ppm U and 0.34±0.08(1σ)% K, 2.1±0.4(1σ)ppm Th and 0.5±0.1(1σ)ppm U for the upper and lower samples respectively. The similarity of elemental concentrations between the two samples supports the geomorphological interpretation that the sands have a single source and the cave sediments buried with the skull are likely to have similar elemental concentrations to the sediments of the sand bank. Two scenarios are proposed for the Forbes Quarry skull: Scenario A) The *in situ* sediments in the nasal cavity of the skull has representative elemental concentrations of all the IM burial sediments; or Scenario B) The *in situ* sediments are only representative over the alpha and beta scale but the gamma dose rate is more likely to be common with the sediments found in the relict sand bank. A further gamma NaI spectrometry measurement at the foot of the cliff collapse at the quarry by Prof. Ed Rhodes in 2001 but this has not been used for further analysis.

		U (ppm)	Th (ppm)	K (%)
Skull sediments		0.255 ± 0.013	0.583 ± 0.029	0.123 ± 0.006
Catalan Bay	**Lower unit**	0.5 ± 0.1	2.1 ± 0.4	0.34 ± 0.08
sediments	**Upper unit**	0.7 ± 0.1	2.2 ± 0.4	0.34 ± 0.08
Skull		top of chain: $\quad 0.310 \pm 0.017$ bottom of chain: 0.159 ± 0.002	0.147 ± 0.015	0.014 ± 0.001

Table 6.4. Elemental concentrations of sediments and bone associated with the Forbes' Quarry skull.

6.4.2 Alpha dose rate

The IM alpha dose rate for the Forbes Quarry sediments, using the elemental concentrations of the nasal cavity and an a-value (Aitken and Bowman, 1975) for OSL of 0.04 ± 0.01 (Rees-Jones 1995, Mauz et al 2006, Lai et al. 2008) despite measuring finer grain sizes. The HF etch lead to an IM grain size correction of ~5%U and ~8%Th (Brennan et al., 1991). The external alpha dose rate for these sediments is evaluated as <0.003mGy/a for measured U and Th values. However, internal activity was found by Sutton and Zimmerman (1978) to be ~4% of beta/gamma dose rate and Vanderberghe (2008) found concentrations of 0.08 ± 0.02ppm U and 0.18 ± 0.03ppm Th in coarse grains which would suggest a total alpha dose rate of 0.013 ± 0.009mGy/a for modern *in situ* sediments. The dose rate was sufficiently small not to involve time evolution modelling and we used the modern dose rate across all burial time.

6.4.3 Cosmic dose rate

The cosmic dose rate was calculated using the data from Prescott and Hutton (1994) and estimated for average overburden. The cosmic dose rate for the Hofmeyr skull was estimated as

184

0.18±0.02mGy/a assuming an average burial depth of 1±0.1(1σ)m. The burial depth of the Forbes Quarry skull was substantially higher, but it is unresolved since much of the overburden for the cave either collapsed or was removed during quarrying. Radiocarbon dating of unweathered shells from the top of the aeolian dune at the foot of the shelter (which immediately underlies the avalanche event) provides a date of approximately 43-45calBP (J. Roderiguez-Vidal, pers. comm.). Prof. Roderiguez-Vidal suggests a modern average overburden of 22±5m with the overburden estimated to 17±5m prior to the cliff collapse; the cosmic dose rate of the Forbes Quarry skull is evaluated as 0.037±0.011(1σ)mGy/a and 0.027±0.006(1σ)mGy/a respectively.

6.4.4   Effect of carbonate formation

A time evolution model for the presence of water/carbonate in the environment must be constructed to account for changes of dose rate at the onset and conclusion of carbonate formation (Nathan and Mauz, 2007). The time evolution of the formation of calcretes in sediments is difficult to assess since it is expected to be site specific and dependent on the chemical properties of the groundwater (such as conditions of carbonate oversaturation), the nature of the soil, bacterial processes (Scoffin, 1987) and the climate. Furthermore, evidence of secondary recrystallisation may be found suggesting episodic formation (McClaren, 2004). However, a starting point for a calculation would be to suggest that the sediment contained no exogeneous carbonate initially ($c_{t(0) \to t(c1)}=0$) and a linear buildup of carbonate at $t=t(c_1)$ proceeds until a cessation of formation at $t=t(c_2)$ occurs at a modern measure of carbonate fraction ($c_{t(c2) \to t(present)}=c_p$), perhaps due to a lack of groundwater or complete pore infilling. An anti-correlation of dose rate is expected to accompany exogeneous carbonate formation due to dilution of activity (see Figure 6.8). Since the water/carbonate correction (see Chapter 4) is intended to apply to "dry" sediments (that is, "dry" having no exogeneous carbonate or interstitial water), the

185

activity of the sediments is enhanced to pre-diluted levels and the correction is applied at each time step for a given water and exogeneous carbonate content present.
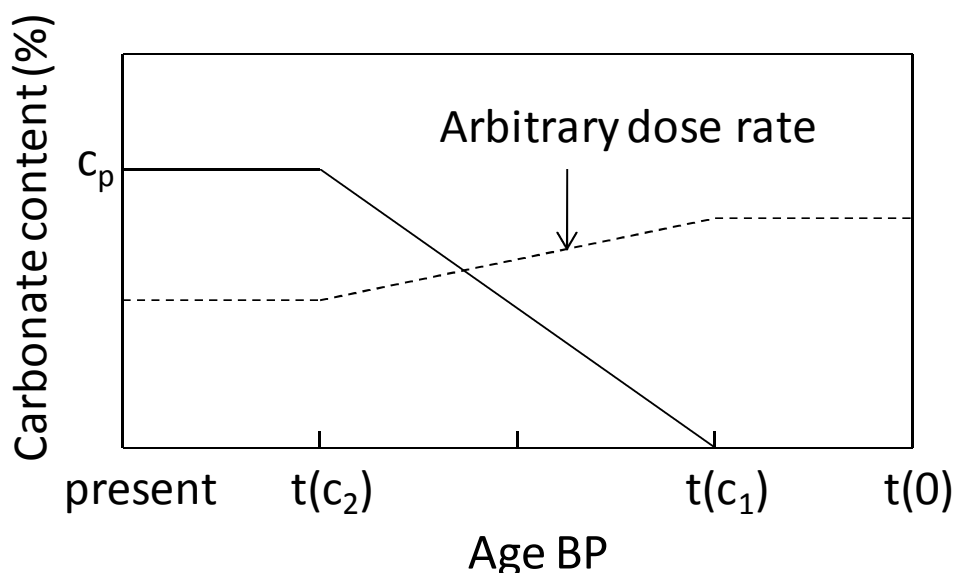
Figure 6.8. An illustration of the relationship between changes in carbonate and dose rate. As carbonate content increases, the activity of the sediment is diluted and dose rate decreases.

The Hofmeyr skull sediments were measured with a fractional carbonate content (c_p) of 31±3%. The Forbes Quarry skull carbonate infilling proved somewhat more difficult to model since a proportion of the measured carbonate was endogeneous arising from recrystallisation of the shell fraction of the original marine sediments and partially exogeneous from precipitation of the carbonate-rich groundwater. Unfortunately, micromorphological investigations of the sediments were not possible, as only a tiny quantity is preserved within the skull. Therefore, the possible carbonate scenarios are modelled to elucidate sensible values. Figure 6.9 attempts to elucidate the following reasoning. The late chemical phase of calcite cementation in the cave was dated between 36.2±4.5ka (alpha U/Th) and 26.85±0.67ka (cal. BP) (J.Rodriguez-Vidal, pers. comm.)

and we assume carbonate precipitation within the skull occurred at the same time. To determine the ratio of carbonate related to shell fragments in beach sediments and from exogeneous sources, Prof. Ed Rhodes and the author propose an argument based on preservation of the Th/U ratio content in the sediments. This assumes that the changes in carbonate content correlate with mobility of uranium and, most importantly, the elemental concentrations in Catalan Bay sediments provide a viable proxy for the skull sediments. The Th/U ratio of the skull sediments are ~2.3 whereas the Catalan Bay sediments contained a ratio of ~3.6 (Table 6.4). The increase in relative uranium concentration for the skull sediments is approximately 36%. The measured carbonate content of the in situ skull sediments was 0.858±0.005 (T. Barrows, pers. com.) based on ICP-AES. If we attribute all the elemental thorium and potassium to reside in the non-carbonate fraction (this material would have concentrations of 0.8% K and 3.9ppm Th) and apply the Catalan Bay Th/U ratio, we estimate the bulk uranium content of the skull sediments before exogeneous carbonate formation to be ~0.162ppm; therefore, ~0.093ppm U of bulk is adsorbed into the system during the late chemical stage of carbonate formation and it is in secular disequilibrium. The concentrations of thorium and potassium in the non-carbonate fraction of the skull compared with Catalan Bay concentrations (and assuming the uncemented Catalan Bay sediments only contain endogeneous carbonate) would indicate an endogeneous carbonate content of sediments in the skull of either ~45% using thorium or ~58% using potassium values. It follows that the exogeneous carbonate content in the skull is ~41% using Th or ~28% using K. However, visual inspection of the sediments (E.J.Rhodes, pers comm.) revealed slightly reddish colouration which may indicate less carbonate content (and possibly more silty material). Clearly there is a large uncertainty involved with the exogeneous carbonate content and we provide dose rate estimates for the carbonate value from the Th/U ratio and from the K/U ratio (henceforth denoted high carbonate and medium carbonate respectively) as well as a possible lower 15% exogeneous carbonate content (denoted as low carbonate) with an content uncertainty of ±5%(1σ) for each of the three possibilities.
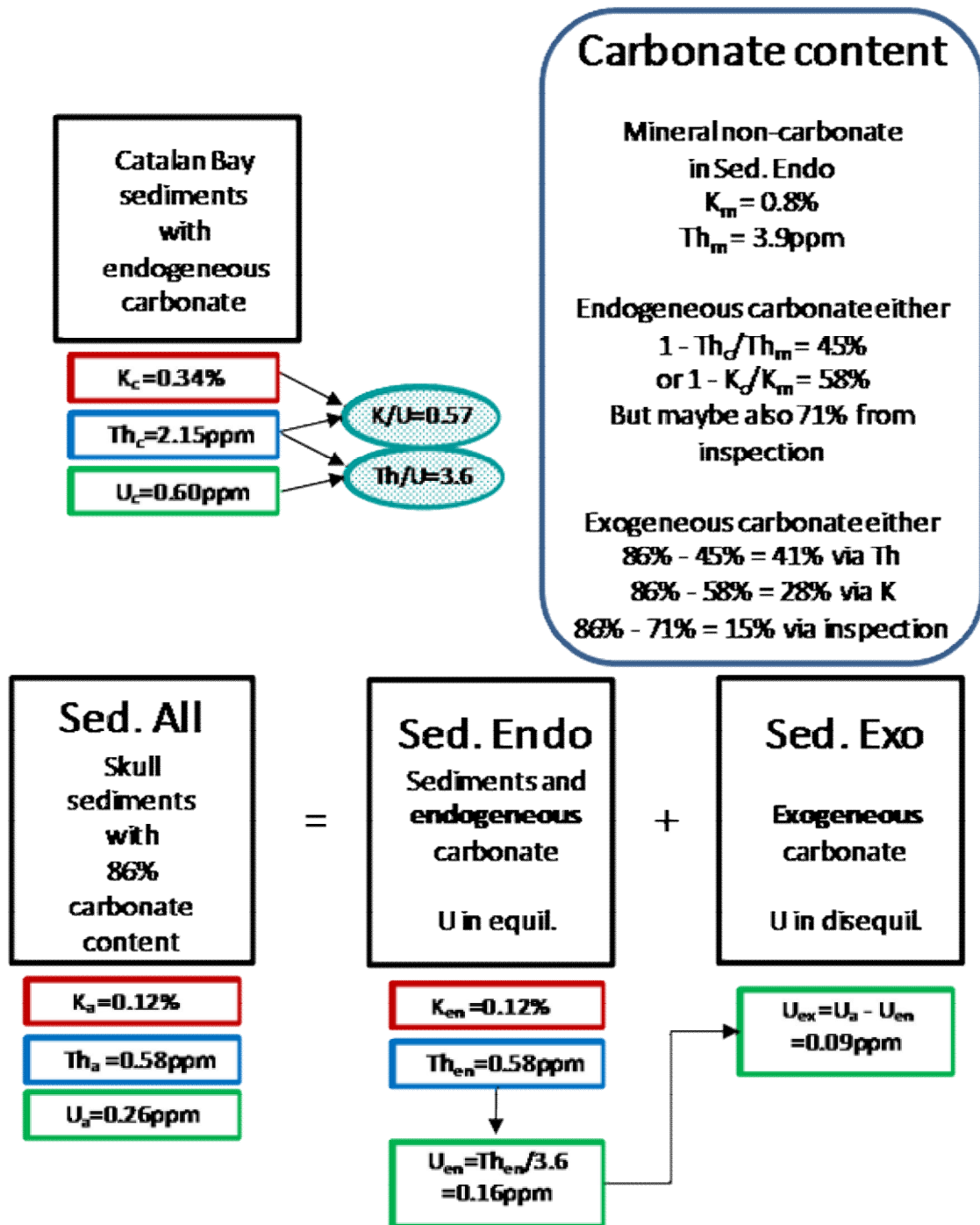
Figure 6.9. A diagramme elucidating the derivation of uranium concentrations and carbonate content for the Forbes Quarry dose rate calculation.

The Hofmeyr skull was assumed to reside in relatively dry conditions (5±2% water by mass), though substantial episodic fluctuations in water content may have existed. The Forbes Quarry site is attributed a time-independent water content of 0.075±0.025. It is assumed the water content was decoupled from carbonate content in the sediments of the Hofmeyr and Forbes Quarrry skulls. This is more contentious for the Hofmeyr skull intracranial sediment since it was found in a predominantly nonporous state thereby minimising modern water content; however, no supporting evidence was available to suggest that moisture levels were significantly elevated before cementation.

The water/carbonate correction for the Hofmeyr skull was applied before the updated corrections (Chapter 4) were calculated. In this case, dose rate is

$$\dot{D}_{\beta,\gamma} = \dot{D}_{\beta,\gamma(dry)} / (1 + \kappa_c f_c + \kappa_w f_w)$$

(6.1)

where $\dot{D}_{\beta,\gamma(dry)}$ is the "dry" beta and gamma dose rate, κ_c and κ_w are the mass stopping power ratios of carbonate and water to sediment respectively and f_c and f_w are the mass ratios of carbonate and water to "dry" sediment respectively. The values for κ_c and κ_w were calculated using MCNP4C following the methods of Aitken and Xie (1990) and provided in Table 6.5. The correction for the carbonate and water contents in the Forbes Quarry skull was handled using results from Nathan and Mauz (2007).

Nuclides	K_w	K_c
$^{238}U \rightarrow ^{234}Pa$	1.19	1.00
^{234}U	1.25	1.01
$^{230}Th \rightarrow ^{206}Pb$	1.19	1.00
$^{235}U \rightarrow ^{231}Th$	1.22	1.01
$^{231}Pa \rightarrow ^{207}Pb$	1.20	1.01
elemental U	1.19	1.00
elemental Th	1.20	1.01
elemental K	1.19	1.00

Table 6.5. Correction factors for water and carbonate used for the Hofmeyr skull sediments.

6.4.5 Secular disequilibrium of uranium

The Hofmeyr skull was not sampled for uranium content, however we include a value of 20±10ppm U as representative (A.W.G. Pike, pers. comm.). After modelling the presence of 0 to 100ppm U in the skull, we found the change in date to be less than ±2%. The elemental content of the Forbes Quarry skull was estimated (E.J. Rhodes, pers. comm.) using Ge gamma spectrometry by comparing the difference in response between the skull and a previously well characterised sediment sample. The skull was found to contain 0.014±0.001(1σ)% K, 0.147±0.015(1σ)ppm Th, 0.310±0.017(1σ)ppm U(top of chain: ^{234}Th, ^{235}U) and 0.159±0.002(1σ)ppm U(bottom of chain: ^{214}Pb, ^{214}Bi, ^{210}Pb).

Several parameters are required to provide a unique time-dependent dose rate model for a specific situation – some are known, and some approximated or bounded. These include: the timing of initial uptake of uranium at $t=t(u_1)$; the initial ratio of $^{234}U/^{238}U$ (assumed the same as in the groundwater from which precipitation took place); the rate of uptake of uranium as a function of time governed by the p-parameter (Grun et al., 1988) such that

$$U(t) = U \left[\frac{t}{T}\right]^{p+1} \qquad (6.2)$$

where U(t) is the uranium concentrationat time, t, U is the measured uranium concentration and *T* is the age of the sample. In cases where *t(u₁))*, the timing of the start of U uptake, is the age of the sample and p is not large (recent uptake), the uptake profile can only be found by iteratively calculating dates to find T at each cycle until a solution reaches convergence; and the timing that a closed system behaviour is achieved at *t=t(u₂)*, when no further movement in or out of isotopes can occur. It should be emphasised that this is not a complete list of significant variables, but rather the only ones considered in a general manner for treatment here. Significant omissions, due to lack of supporting data, include: mobility of several important daughter radioisotopes, particularly radium and radon; the diffusion gradient of uranium within the fossil bone; and the occurrence of multiple open system episodes. We incorporate the contribution of ^{235}U disequilibrium by assuming crustal abundance of ^{235}U at 0.72% to natural uranium (Steiger and Jäger, 1977).

Since the carbonate chemical phase is dated for the Hofmeyr skull, we use an early uranium uptake (EU) regime (p=-1). Using 24ka for the timing of unsupported uranium, the initial ^{234}U/^{238}U is 1.704, 1.325 and 2.022 for samples H1, H2 and H3 respectively. The Forbes Quarry skull was found to be in secular disequilibrium and the time evolution of the uranium uptake is unknown; for simplicity we have assumed linear uptake (LU, p=0±0.3) over the duration of the late chemical stage. Modern seawater ^{234}U/^{238}U activity ratios of 1.14±0.02 (Chen et al. 1986) are used. The secular disequilibrium in the marine sand fraction of the intra-skull sediment was not measured directly and elevated ^{234}U/^{238}U activity ratios in marine shells have been found in the eastern Mediterranean region (Jedoui et al. 2002, McLaren and Rowe, 1996). However, we suggest (perhaps controversially) that little uranium disequilibria exist in Gibraltan sands since the NaI/NAA uranium ratios measured for the two samples at Catalan Bay only showed several percent unsupported uranium. In addition, proxy data from 18 NaI/NAA sampled points in Gibraltar suggested the main gamma emissions (lower in decay series) compared to elemental U

have an activity ratio of 1.18±0.23 (E. J. Rhodes, pers. comm.) which is not consistent with uranium uptake assumptions of initial ^{230}Th/^{238}U << 1. The initial ^{234}U/^{238}U activity ratio for the Forbes Quarry fossil is assumed to be the same as sea water. Since there is significant Th and K observed in the Ge measurements of the skull, clearly some detrital material is present within or attached to the fossil which may contain some uranium that is in secular equilibrium at present. In the time-dependent model, supported U (in secular equilibrium) is introduced iteratively until the modern measured ^{230}Th/^{238}U ratio from Ge measurements is consistent with the date found. Usually, about 5-10 iterations of the date were required to achieve convergence within 100 years. Linear uptake of uranium is assumed in the skull over the duration of burial (p = 0±0.3).

The population of daughter radioisotopes was calculated analytically using standard exponential decay equations (Faure, 1986) with the p-parameter (Grun et al., 1988) included such that

$$N_{U234}(t) = \frac{\lambda_{238}}{\lambda_{234}} N_{U238}(t) \left[r - \lambda_{234}(r-1) \int_0^T (\theta/t)^{p+1} \exp\left(-\lambda_{234}(t-\theta)\right) d\theta \right]$$

and (6.4)

$$N_{Th230}(t) = \frac{\lambda_{238}}{\lambda_{230} - \lambda_{234}} N_{U238}(t) \left[(r\lambda_{230} - \lambda_{234}) \int_0^T \left(\frac{\theta}{t}\right)^{p+1} \exp\left(-\lambda_{230}(t-\theta)\right) d\theta \right.$$
$$\left. - \lambda_{234}(r-1) \int_0^T \left(\frac{\theta}{t}\right)^{p+1} \exp\left(-\lambda_{234}(t-\theta)\right) d\theta \right]$$

where N is the population of isotopes, λ is the decay constant, and r is the initial ^{234}U/^{238}U activity ratio and similarly for ^{231}Pa (substitute $N_{U238,\ U234}$ for $N_{U235,\ Pa231}$ and likewise for λ; $r = 0$). The algorithm is implemented so that $d\theta = 0.0001T$ to ensure acceptable precision.

6.4.6   Computational methods

A time vector was constructed with 100 year increments. At each time datum, the radioisotope concentrations and water/carbonate contents were evaluated and the effective dose rate calculated

by scaling the IM dose rate by the correction for the skull heterogeneity in the sediment matrix coupled with grain size and water/carbonate corrections such that

$$\dot{D}(t) = \dot{D}_\alpha + \dot{D}_\beta(t) + \dot{D}_\gamma(t) + \dot{D}_{cosmic}(t) \tag{6.5}$$

Overall uncertainty was calculated by Monte Carlo modelling of the dose rate, where all variables with uncertainties are perturbed (10,000 cycles to give uncertainty convergence to within ~1%), and the standard deviation for dose rate at each time step is established. The perturbed variables are sampled from normal distributions centred around the value and standard deviation as the uncertainty except for water content and grain size which are uniformly sampled from the span of uncertainty. It should be noted that the uncertainty of the grain size correction mistakenly was not applied for the Hofmeyr skull work published in Grine et al. (2007). The contribution to dose rate is summed between skull and sedimentary emission sources. The sampling may lead to negative values which have undefined meaning (e.g. cosmic dose rate < 0 Gy/a); in this case the value is set to near zero. Sensitivity testing is performed by perturbing one variable only and finding the variation in dose rate.

6.4.7   Hofmeyr skull

Figure 6.10 presents the time evolution of the dose rate for the samples from the Hofmeyr skull. The gamma dose rate involving the spatially resolved modelling was approximately a third of the total dose rate so that associated uncertainties are not predominant. Up to the carbonate formation, the dose rate is constant since no secular disequilibrium of uranium is assumed. Carbonate formation is modelled as an instantaneous episode; however, due to the uncertainty of its timing, Monte Carlo methods have acted to perturb the dose rate accordingly to smooth out the timing of formation. After carbonate formation, the growth of daughters from unsupported

uranium acted to increase dose rate. A curious feature for sample H3 was the lack of dilution of dose rate due to exogeneous carbonate. Elevated contributions from soluble U concentrations (>6ppm), in addition to a high initial $^{234}U/^{238}U$ ratio of 2.02, offset the dilution due to carbonate.
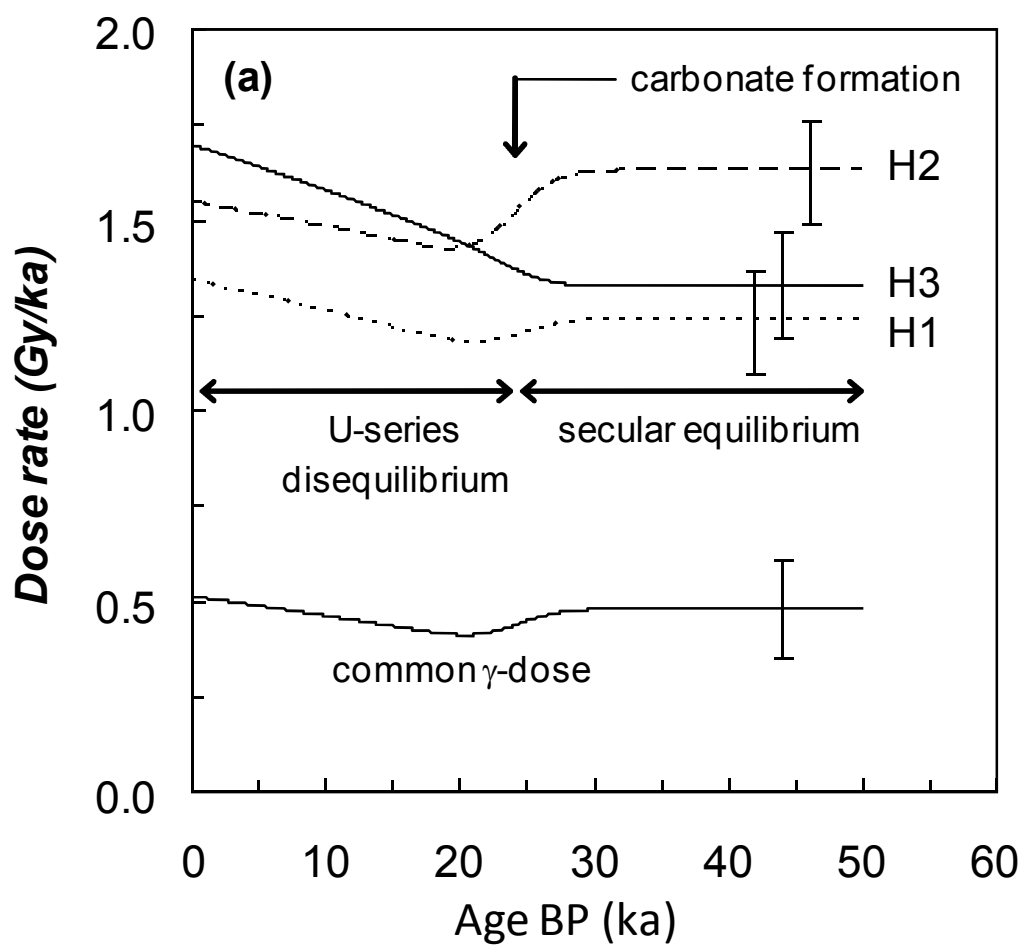
Figure 6.10. The time evolution of dose rate for samples from the Hofmeyr skull.

194

Sensitivity testing of the dose rate to each parameter grouping is presented in Figure 6.11. Clearly, the largest uncertainty in the dose rate arises from elemental concentration analysis. This is expected since the dose rate from U (in equilibrium), Th and K contributed approximately 60-85% of the total dose rate. Next in importance for the three samples was the variability of the concentration of uranium in disequilibrium including the uncertainty of the uranium concentration in the skull bone. Thirdly, the uncertainty of the cosmic dose rate was significant as well as parameters associated with the age of carbonate formation, carbonate content and water content.
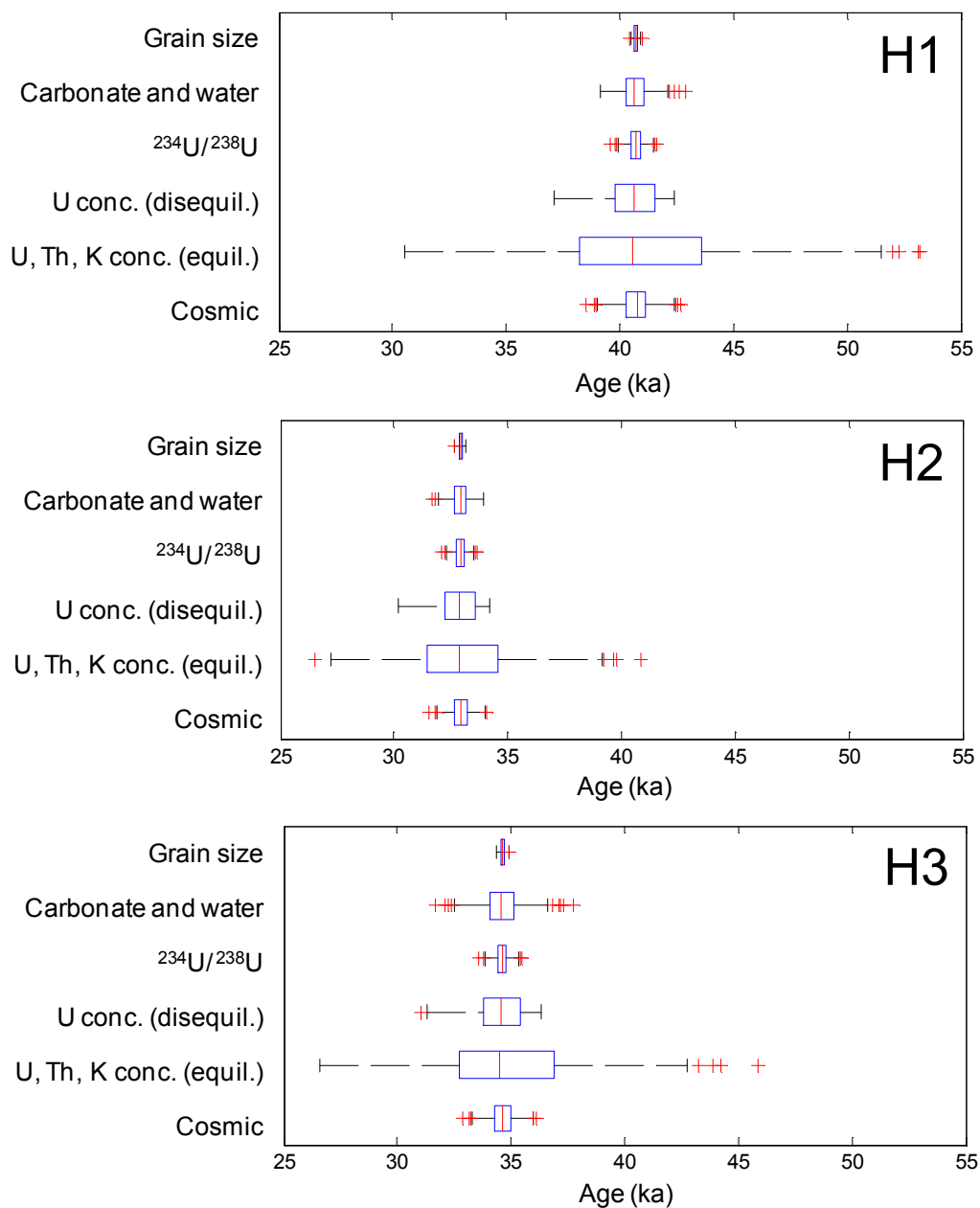
Figure 6.11. Sensitivity testing for different groups of Hofmeyr skull parameters presented as box and whisker diagrams showing mean, upper/lower quartiles, range and outliers. "Grain size" includes the uncertainty associated with beta grain size corrections for all decay groups and elemental U, Th and K emissions. "Carbonate and water" includes the uncertainty of timing of carbonate formation and carbonate and water contents. "$^{234}U/^{238}U$" includes the uncertainty of sample and collective activity ratios. "U conc. (disequil.)" include the uncertainty for all uranium concentrations associated with secular disequilibrium calculations. "U, Th, K conc. (equil.)" includes the uncertainty for all elemental concentrations. "Cosmic" refers to the uncertainty of the cosmic dose rate.

6.4.8 Forbes' Quarry skull

The time evolution of dose rates (for different scenarios) in samples from the Forbes' Quarry skull is presented in Figure 6.12. Before approximately 45ka, the dose rate increased insignificantly from U uptake in the skull. At approximately 45ka, the cliff collapse heralded an abrupt drop in cosmic dose rate, and this is followed by the formation of exogeneous carbonate until approximately 28ka ago. Due to Monte Carlo estimation of the average time-dependent dose rate, these timings have been smoothed. The carbonate event is clearly the most dramatic for dose rate evaluation, especially in situations where high carbonate content may arise. Interestingly, the greatest absolute uncertainty in dose rate occurred during the onset of carbonate formation. Modern values for dose rate are provided in Table 6.6. Apart from minor contributions to dose rate from alpha and cosmic radiations, the majority of dose rate arises from U, Th and K of sediments in secular equilibrium. Perhaps this is not surprising since the spatial modelling of the skull using MCNP would indicate that contributions from the skull are largely absent.

1σ uncertainty				Scenario A: Sedimentary gamma dose rate from skull sands			Scenario B: Sedimentary gamma dose rate from Catalan Bay sands		
Exogeneous carbonate content (%)				High: 0.41 ± 0.05	Medium: 0.28 ± 0.05	Low: 0.15 ± 0.05	High: 0.41 ± 0.05	Medium: 0.28 ± 0.05	Low: 0.15 ± 0.05
Modern dose rate to sample (mGy/a)	C. Bay sediments	γ	U_{eq}, Th, K				0.204 ± 0.023	0.205 ± 0.022	0.201 ± 0.024
	In situ skull sediments	β	U_{eq}, Th, K	**0.108 ± 0.004**	**0.110 ± 0.004**	**0.110 ± 0.005**	**0.109 ± 0.005**	**0.110 ± 0.005**	**0.111 ± 0.005**
			U_{diseq}	0.004 ± 0.000	0.005 ± 0.000	0.006 ± 0.000	0.005 ± 0.000	0.005 ± 0.000	0.006 ± 0.001
		γ	U_{eq}, Th, K	**0.060 ± 0.002**	**0.061 ± 0.002**	**0.061 ± 0.002**			
			U_{diseq}	0.002 ± 0.000	0.002 ± 0.000	0.002 ± 0.000			
	Skull	β	U_{eq}, Th, K	0.000 ± 0.000	0.000 ±0.000	0.000 ± 0.000	0.000 ± 0.000	0.000 ± 0.000	0.000 ± 0.000
			U_{diseq}	0.000 ± 0.000	0.000 ± 0.000	0.000 ± 0.000	0.000 ± 0.000	0.000 ± 0.000	0.000 ± 0.000
		γ	U_{eq}, Th, K	0.001 ± 0.000	0.002 ± 0.000	0.002 ± 0.000	0.002 ± 0.000	0.002 ± 0.000	0.002 ± 0.000
			U_{diseq}	0.001 ± 0.000	0.002 ± 0.000	0.002 ± 0.000	0.001 ± 0.000	0.001 ± 0.000	0.001 ± 0.000
	Total	Alpha		0.013 ± 0.009					
		Beta		0.113 ± 0.004	0.115 ± 0.004	0.117 ± 0.005	0.114 ± 0.005	0.116 ± 0.005	0.117 ± 0.005
		Gamma		0.065 ± 0.002	0.066 ± 0.002	0.067 ± 0.002	0.207 ± 0.023	0.208 ± 0.022	0.204 ± 0.024
		Cosmic		Before 44 ± 1ka: 0.037 ± 0.011; After 44 ± 1ka: 0.027 ± 0.006					
Date (ka)				**85.9 ± 6.0**	**90.1 ± 6.6**	**95.1 ± 7.4**	**55.2 ± 4.5**	**57.1 ± 4.9**	**59.3 ± 5.2**

Table 6.6. Calculated dose rate values for present (t = 0) and associated dates for the Forbes' Quarry skull samples for different gamma dose rate scenarios and carbonate contents.
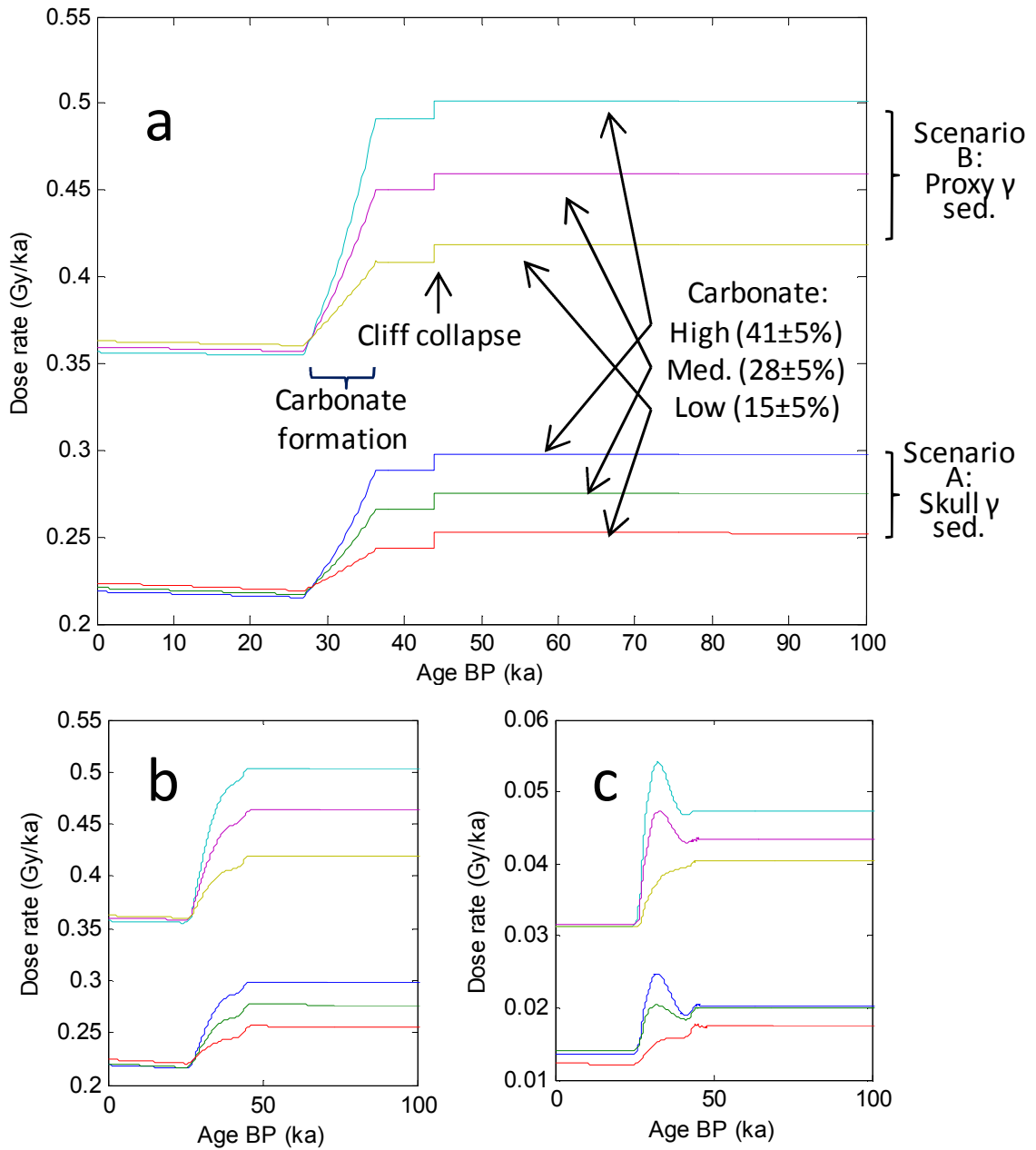
Figure 6.12. (a) the time evolution of dose rate for the Forbes' Quarry skull sample using the best estimate of all parameters; (b) a smoothing of the dose rate response due to Monte Carlo modelling of uncertainty (1000 trials); and (c) the uncertainty estimate (1σ) of dose rate at each time step. Different gamma dose rate scenarios and exogeneous carbonate contents are presented (see text for details).
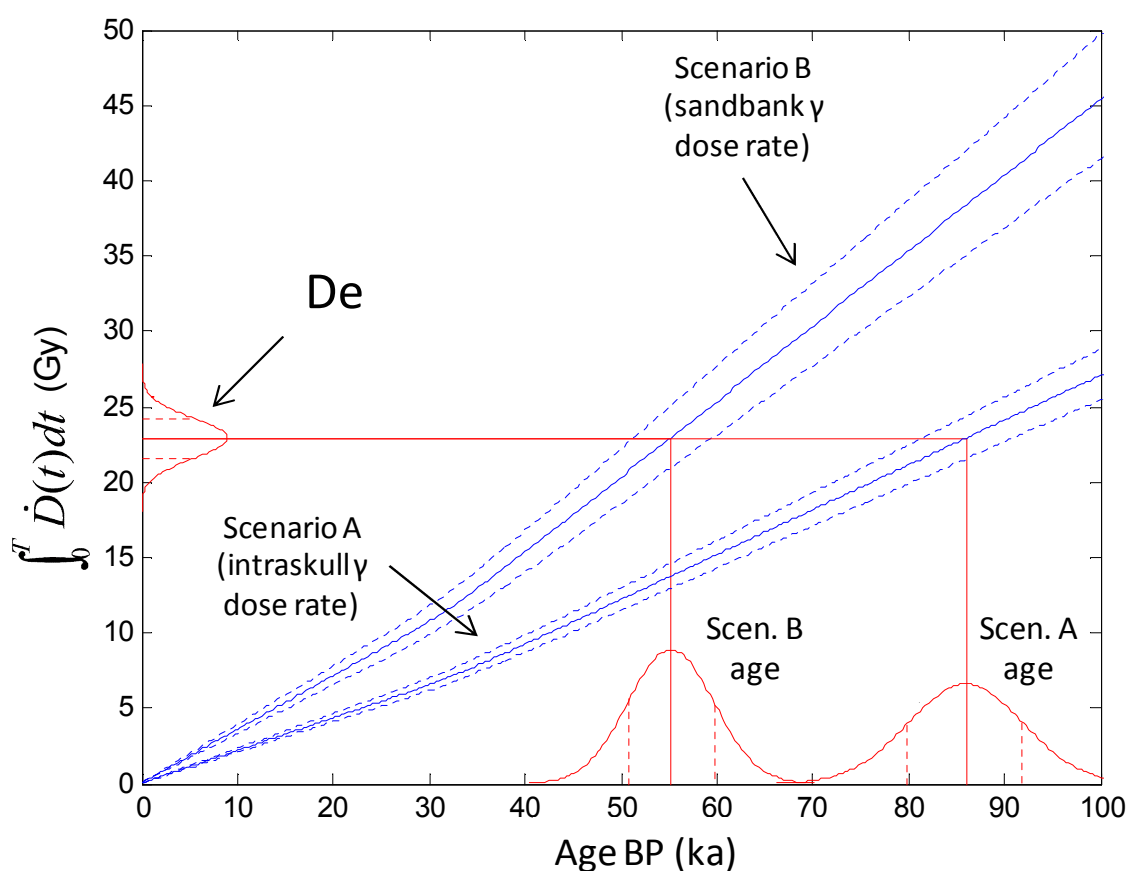
Figure 6.13. The relationship between the equivalent dose measurement (red, left normal curve, horizontal line), the cumulative dose rate (blue) and the age estimation (red, bottom normal curves, vertical lines). Dotted lines represent 1σ uncertainty. Two case studies from Forbes' Quarry are illustrated, both for the high carbonate evaluation (see text): Scenario A is where the sedimentary gamma dose rate is calculated from measurements from *in situ* sediments remaining in the skull; Scenario B is where the sedimentary gamma dose rate is calculated from proxy marine sediments from the adjacent sandbank.

Figure 6.13 illustrates the method for estimating dates from the equivalent dose and the cumulative dose rate. The equivalent dose and uncertainty was measured by Prof. Ed Rhodes (pers. comm.) using a central age model from a small (<100) cohort of single grain OSL measurements. With increasing the time from present, the absolute uncertainty also expands. The sensitivity testing of the parameters used in modelling dose rate for the Forbes' Quarry study is shown in Figure 6.14. As Scenario A has a lower dose rate, the uncertainty of the parameters

leads to a greater sensitivity to changes in the OSL date. Important parameters include D_e, radioisotope activities in sediment, carbonate content as well as alpha and cosmic dose rate uncertainty.
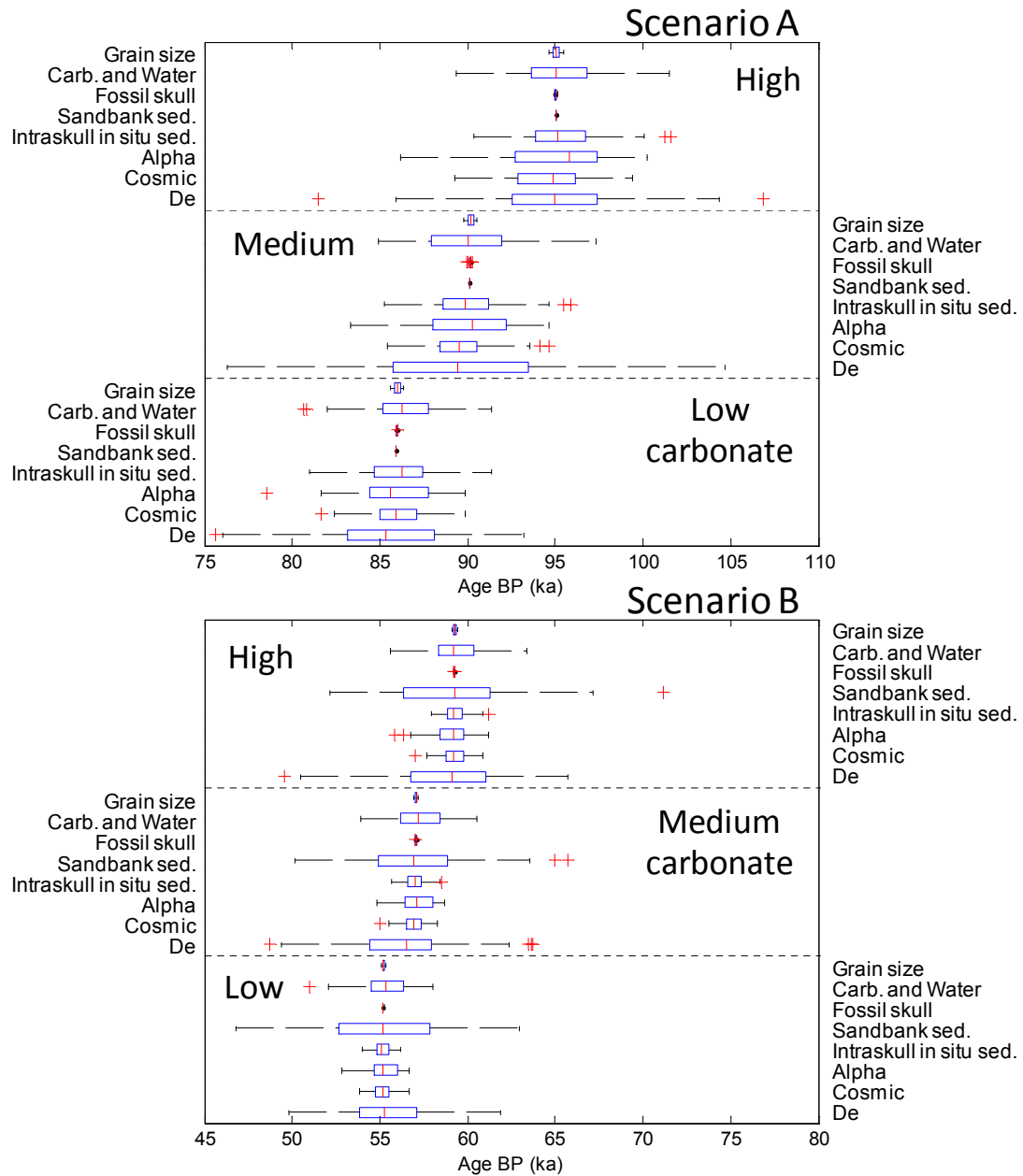
Figure 6.14. Sensitivity testing for different groups of Forbes' Quarry skull parameters presented as box and whisker diagrams showing mean, upper/lower quartiles, range and outliers. "Grain size" includes the uncertainty associated with beta grain size correction. "Carbonate and water" includes the uncertainty of timing of carbonate formation and carbonate and water contents. "Fossil skull", "Sandbank sediments" and "Intraskull *in*

200

situ sediments" include the total dose rate contribution from these respective active sources. "Alpha", "Cosmic" and "De" refers to the uncertainty of alpha and cosmic dose rates respectively and in the equivalent dose. See text for the description of Scenarios A and B and High, Medium and Low carbonate content.

The Forbes Quarry skull was dated to between 55.2±4.5ka (for high exogeneous carbonate content and the gamma sedimentary dose rate calculated from Catalan Bay sediments) and 95.1±7.4ka (for low exogeneous carbonate content and the gamma sedimentary dose rate calculated from *in situ* sediments sampled from the skull) (see Table 6.6 for all modelled situations). The older dates match the previous OSL dating of the Catalan Bay sand formation (95±9ka), however, the younger dates overlap well with other dating of the Catalan Sands (40-75ka) using geomorphological inferences (Rodriguez-Vidal et al., 2004). Given the larger differences in the dates between Scenarios A and B compared with the varying carbonate content estimates, it may be of some benefit to combine the carbonate uncertainty to achieve two dates only. The three possibilities for carbonate content are given equal weight and the uncertainty is calculated by Monte Carlo perturbation to give an OSL age of 90.2±7.7ka for Scenario A and 57.4±5.1ka for Scenario B.

6.5 Concluding remarks

The three case studies presented in this chapter have illustrated the use of Monte Carlo radiation transport modelling in fossil dose rate estimations. Although fossils by their nature are unique, the methodology described here can be extended to other case studies. One proviso is that the input to the models is robust. Dose rate evaluation associated with fossils is difficult. Not only do the spatial heterogeneities require assessment, but time-dependent chemical alteration of the site

requires an extensive modelling of ancillary considerations such as carbonate and uranium disequilibrium.

One avenue of endeavour, which may be particularly fruitful in future studies, is the ability to perform isochron dating of a skull by taking advantage of the differential dose rates in sediments within the skull. Since an accurate internal map of dose rate within the skull can be made for measured quantities, those parameters which are not measured (e.g. uranium in the fossil due to curatorial concerns) can be partially offset. The main requirement for isochron dating would be to collect samples at regular intervals from close to the fossil to further from the fossil and accurately record the radioisotope activity at these positions.

Chapter 7: Conclusions

7.1 Summary of results

The first part of this thesis has elucidated a detailed methodological approach for numerical modelling of dose rate. Monte Carlo codes, MCNP and PENELOPE, were chosen as state-of-the-art software with each having different algorithms to determine the behavior of the radiation. Inputs required for modelling were discussed with updated emission spectra, typical mineralogy and ancillary cards. Previous studies had identified a systematic error in the electron transport algorithms of MCNP when a large number of surfaces are crossed per primary particle although a relatively small difference was found compared to PENELOPE.

The geometrical inputs for sedimentary environments were trivial for infinite-matrix homogeneous materials. However, in granular contexts, where over the sub-millimeter scale charged particle equilibrium may not hold, several different types of structures were designed. A prerequisite for implementing geometries into the radiation model was that grains must not overlap otherwise the parts of the radiation model geometry would become undefined. Using the Lubachevsky-Stillinger algorithm, ellipsoidal grains were randomly packed to a range of densities. The system was flexible to allow arbitrary grain size and shape distributions. Pair correlation and chord length distributions were computed; the former for use in the analysis of beta/gamma source heterogeneity (not presented in this thesis) and the latter for the water content correction. Perhaps unsurprisingly, the more disperse the grain size and shape becomes, the less the two structural parameters resemble the random spherical packing.

The chord length distribution across the pore spaces became exponential for chords longer than the median grain size which agreed well with theoretical results.

Recalculation of the effects of water content was presented. Water in sediment affects the dose rate in two ways. Firstly, since dry sediment is used for estimations of activity in the sediment, the burial activity is diluted by the mass of water and the dose rate during burial is reduced. More subtly, and the focus in this thesis, is the relative efficiency of dose absorption in water compared to dry sediment (in other words, the competition between water and sediment for scavenging radiation energy) and denoted x. The standard evaluation of x is 1.25 for beta radiations and 1.14 for gamma radiations (Aitken, 1985a). An enhanced theoretical basis for this calculation was constructed which has not been satisfactorily elucidated in the trapped-charge dating literature. It was shown that an appropriate estimation of secondary electron behaviour is required as the correction will change depending on the grain size and the dimensions of the water residing in the pore space ranging from 1.22 for very small cavities to near unity for very large structures. Additional concerns that have not been fully appreciated by the trapped-charge dating community include the variation in the correction due to the sediment structure. A brief analysis of the combined water and carbonate content is presented and it was shown that intermediate values can be found using a linear interpolation method.

The activity of the sedimentary matrix and the grains used for dating will be dissimilar in general. Therefore, the beta dose rate estimation can be partitioned into dose rate from either internal or external sources. The beta dose rate correction is used to allocate the weighting of this partition and it is dependent on the size of the grain. The standard treatment is to evaluate the correction for spherical grains (Aitken, 1985). The corrections have been updated with differences found of up to several percent compared to previous findings. However, the application of the corrections has been extended to include consideration of material type, grain shape, and dissimilar grain and matrix materials. The correction for zircon was most markedly different from quartz. The effects of grain shape were modelled for ellipsoids and the correction was found to be sensitive to the departure of the grain from spherical shapes. However, more

significant variation occurred for changes in the ratio of the longest axis of the grain. The effect of quartz grains embedded in peaty or water saturated environments was found to be significant due to changes in the stopping power and backscattering cross-sections but insignificant for other material types.

This thesis also presented three case studies of dose rate estimation associated with hominin fossil skull dating: the Skhul V skull from Israel with both modern and archaic human features; the Hofmeyr skull from South Africa with both modern and archaic human features; and the Forbes' Quarry Neanderthal skull. An important feature of this work is the presentation of a robust methodology to deal with spatial and temporal variation of dose rate. Three-dimensional images (CT scans) of the skulls were inserted into MCNP and the absorbed dose in intra-cranial sediments (and teeth for Skhul V) was modelled. The quantity of data required automation for almost all of the stages of simulation. It was found that the skull may shield the samples from an infinite-matrix sedimentary dose rate up to about 10% but more likely "rule of thumb" values are 4-7% when the samples are some distance from the bone. Dose rate was modelled for the Hofmeyr and Forbes' Quarry case studies to achieve OSL dates. The time evolution of dose rate included consideration of the formation of exogeneous carbonate, secular disequilibrium of uranium in the skull and sediments and other events such as overburden changes during burial. The gamma dose rate of samples from the Hofmeyr skull was combined between the three samples whereas beta dose was assessed individually. The Hofmeyr skull was dated using OSL to 36±3ka and this provided a robust date for the first early modern human fossil found in sub-Saharan Africa. The estimation of dose rate for the Forbes' Quarry skull study was hindered by the lack of material available for elemental analysis or contextual analysis. These raised concerns that the collected sample was unrepresentative over the scale of gamma radiations as well as uncertainty about the amount of infilling carbonate. Therefore, different scenarios were posed leading to two alternative OSL dates of 57±3ka or 90±8ka. Accurate dating of the Forbes' Quarry skull also is of some historical interest as was found before the Neander Valley type specimen.

7.2 Future directions

An important absence in this thesis is the validation of the numerical modelling with experimental data. A first step may be to use the uranium-doped concrete blocks sited in the Research Laboratory for Archaeology and the History of Art, Oxford for water content measurements and other gamma related areas. However, the numerical modelling is very well benchmarked for gamma dosimetry (within several percent); rather it is granular structures over the beta scale which is more problematical for codes such as MCNP. It is unfortunate that many naturally occurring uranium- and thorium-enriched sediments that were available to previous generations of trapped-charge dating researchers at Oxford are no longer acceptable for open bench-top experiments. Beamline experiments are perhaps the way forward but the energy spectra are no longer associated with naturally occurring radioisotopes and there may be problematical geometric issues involved. Like all numerical modelling, until experimental validation of specific results is performed, the modelling calculations remain as estimates rather than canonical.

The suite of water content and beta grain size corrections in Chapter 4 and Chapter 5 is not complete – nor will it ever be. The wide range of possible water contents, grain size and shape distributions, material types, etc. preclude exactly matching the situation for a particular dating sample. However, this thesis gives some illustration of a methodological path forward and also presents a view of potential issues and their importance. Similarly, the skull dating work can be lifted, whole or in part, into another study with the various parameters adjusted as needed.

A large body of unpublished work (as well as published work e.g. Nathan et al. (2003)) has been done – unfortunately not presented in this thesis – on the effects of beta heterogeneity on dose rate estimates. This is particularly relevant for singe grain (or small aliquot) dating using OSL since the shape of the De distribution will be modulated by the dose rate variation leading to potentially inaccurate interpretations the distribution. Heterogeneities take two main types: 1) dispersed active grains that lead to skewed De

distributions with long, thin De tails; and 2) inert bodies in an active matrix that shield dose rate to adjacent grains leading to a slightly longer leading edge to the De distribution. Although it is relatively straightforward to address these issues for simple shapes and size distributions (using pair-correlation functions when considering active grains!), it is difficult to generalize the results. Presumably the optimal approach is to model a wide variety of contexts and use these to inform (magnitude of possible effects) about situations which may be of concern.

References

ADAMIEC, G. & AITKEN, M. J. 1998. Dose-rate conversion factors: update. *Ancient TL,* 16**,** 37-50.

AITKEN, M. J. 1985a. *Thermoluminescence Dating,* New York, Academic Press.

AITKEN, M. J. 1985b. Alpha particle effectiveness: numerical relationship between systems. *Ancient TL,* 3**,** 22-25.

AITKEN, M. J. 1987. Alpha dose to a thin layer. *Ancient TL,* 5**,** 1-3.

AITKEN, M. J. & BOWMAN, S. G. E. 1975. Thermoluminescent dating: assessment of alpha particle contribution. *Archaeometry,* 17**,** 132-138.

AITKEN, M. J. & XIE, J. 1990. Moisture correction for annual gamma dose. *Ancient TL,* 8**,** 6-9.

ATTIX, F. H. 1986. *Introduction to radiological physics and radiation dosimetry*, John Wiley.

AZNAR, M. C., NATHAN, R., MURRAY, A. S. & BOTTER-JENSEN, L. 2003. Determination of differential dose rates in a mixed beta and gamma field using shielded Al2O3 : C: results of Monte Carlo modelling. *Radiation Measurements,* 37**,** 329-334.

BAILEY, R. M., SMITH, B. W. & RHODES, E. J. 1997. Partial bleaching and the decay form characteristics of quartz OSL. *Radiation Measurements,* 27**,** 123-136.

BARRETT, P. J. 1980. The shape of rock particles, a critical review. *Sedimentology,* 27**,** 291-303.

BEHRENS, H. & SZYBISZ, L. 1976. Shapes of Beta Spectra, Physics *Physics Data 6-1.* Germany: Zentralstelle für Atomkernenergie-Dokumentation (ZAED).

BELL, W. T. 1979. Attenuation factors for the absorbed radiation dose in quartz grains for thermoluminescence dating. *Ancient TL,* 8**,** 2-13.

BELL, W. T. & ZIMMERMAN, D. W. 1978. The effect of HF acid etching on the morphology of quartz inclusions for thermoluminescence dating. *Archaeometry,* 20**,** 63-65.

BENEDITO, E., FERNÁNDEZ-VAREA, J. M. & SALVAT, F. 2001. Mixed simulation of the multiple elastic scattering of electrons and positrons using partial-wave differential cross-sections. *Nuclear Instruments and Methods in Physics Research B,* 174**,** 91-110.

BERGER, M. J. 1963. Monte Carlo calculation of the penetration and diffusion of fast charged particles. *In:* ALDER, B., FERNBACH, S. & ROTENBERG, M. (eds.) *Methods in computational Physics Vol. 1.* New York: Academic Press.

BERGER, M. J. 1971. Distribution of absorbed dose around point sources of electrons and beta particles in water and other media. (MIRD/Pamphlet No. 7) *Journal of Nuclear Medicine,* 5 (Suppl.) 5-23.

BERGER, M. J. 1973. *Improved point kernels for electron and beta-ray dosimetry. NBSIR 73-107,* Washington DC, National Bureau of Standards.

BERGER, M. J., COURSEY, J. S., ZUCKER, M. A. & CHANG, J. 2000. ESTAR, PSTAR, and ASTAR: Computer Programs for Calculating Stopping-Power and Range Tables for Electrons, Protons, and Helium Ions (Version 1.2.2). . Gaithersburg, MD: National Institute of Standards and Technology.

BERGER, M. J. & HUBBELL, J. H. 1987. XCOM: Photon cross sections on a personal computer. Report NBSIR 87-3597. Gaithersburg, MD: National Bureau of Standards.

BERGER, M. J. & SELTZER, S. M. 1964. Tables of energy losses and ranges of electrons and positrons. *Studies in penetration of charged particles in matter.* Washington D.C.: National Academy of Sciences-National Research Council Publication 1133.

BERGER, M. J. & WANG, R. 1988. Multiple-scatterung angular deflections and energy loss straggling. *In:* JENKINS, T. M., NELSON, W. & RINDI, A. (eds.) *Monte Carlo Transport of Electrons and Photons.* New York and London: Plenum Press.

BERNAL, J. D. 1964. Bakerian Lecture 1962 - Structure of Liquids. *Proceedings of the Royal Society of London Series a-Mathematical and Physical Sciences,* 280**,** 299-+.

BLATT, H., MIDDLETON, G. V. & MURRAY, R. C. 1972. *Origin of sedimentary rocks,* Englewood Cliffs, N.J.,, Prentice-Hall.

BLUNCK, O. & LEISEGANG, S. 1950. Zum Energieverlust schneller Elektronen in dünnen Schichten. *Zeitschrift fur Physik,* 128**,** 500-509.

BOOTH, F. 2005. Fundamentals of Monte Carlo particle transport (Lecture notes). LA-UR-05-4983. Los Alamos: Los Alamos National Laboratory.

BOTTER-JENSEN, L., ANDERSEN, C. E., DULLER, G. A. T. & MURRAY, A. S. 2003. Developments in radiation, stimulation and observation facilities in luminescence measurements. *Radiation Measurements,* 37**,** 535-541.

BOURDON, B., TURNER, S. P., HENDERSON, G. M. & LUNDSTROM, C. C. 2003. Introduction to U-series geochemistry. *In:* BOURDON, B., HENDERSON, G. M., LUNDSTROM, C. C. & TURNER, S. P. (eds.) *Uranium-Series Geochemistry.* Washington D.C.: Mineralogical Society of America.

BOURDON, S., LAGGOUN-DÉFARGE, F., DISNAR, J.-R., MAMANA, O., GUILLET, B., DERENNE, S. & LARGEAU, C. 2000. Organic matter sources and early diagenetic degradation in a tropical peaty marsh (Tritrivakely, Madagascar). Implications for environmental reconstruction during the Sub-Atlantic. *Organic Geochemistry,* 31**,** 421-438.

BOWMAN, S. G. E. & HUNTLEY, D. J. 1984. A new proposal for the expression of alpha efficiency in TL dating. *Ancient TL,* 2.

BRAGG, W. H. 1912. *Studies in Radioactivity,* New York, Macmillan.

BRENNAN, B. J. 2003. Beta doses to spherical grains. *Radiation Measurements,* 37**,** 299-303.

BRENNAN, B. J., LYONS, R. G. & PHILLIPS, S. W. 1991. Attenuation of alpha particle track dose for spherical grains. *Nuclear Tracks and Radiation Measurements,* 18**,** 249-253.

BRENNAN, B. J., SCHWARCZ, H. P. & RINK, W. J. 1997. Simulation of the gamma radiation field in lumpy environments. *Radiation Measurements,* 27**,** 299-305.

BRIESMEISTER, J. F. 2000. MCNP - A General Monte Carlo N-Particle Transport Code Version 4C. Report LA-13709-M. USA: Los Alamos National Laboratory.

BURCH, P. R. J. 1955. Cavity ion chamber theory. *Radiation Research,* 3**,** 361-378.

BURLIN, T. E. 1968. Cavity-chamber theory. *In:* ATTIX, F. H. & ROESCH, W. C. (eds.) *Radiation dosimetry, Volume I: Fundamentals.* New York and London: Academic Press.

BUSK, G. 1865. On a very ancient human cranium from Gibraltar. *Report of the 34th meeting of the British Association for the Advancement of Science, Bath 1864***,** 91-92.

CAMERON, J. R., SKOFRONICK, J. G. & GRANT, R. M. 1999. *Physics of the Body,* Madison, WI, Medical Physics Publishing.

CHEFETZ, B., DESHMUKH, A. P., HATCHER, P. G. & GUTHRIE, E. A. 2000. Pyrene sorption by natural organic matter. *Environmental science and technology,* 34**,** 2925-2930.

CHEN, X.-A. 1995. Body content of various naturally occurring radionuclides of Chinese people. *Journal of Radiological Protection,* 15**,** 77-84.

CHIBANI, O. & LI, X. A. 2002. Monte Carlo dose calculations in homogeneous media and at interfaces: A comparison bewteen GEPTS, EGSnrc, MCNP, and measurements. *Medical Physics,* 29**,** 835-847.

COBUT, V., CIRIONI, L. & PATAU, J. P. 2004. Accurate transport simulation of electron tracks in the energy range 1 keV - 4 MeV. *Nuclear Instruments and Methods in Physics Research B,* 215**,** 57-68.

COUSIN, I., LEVITZ, P. & BRUAND, A. 1996. Three-dimensional analysis of a loamy-clay soil using pore and solid chord distributions. *European Journal of Soil Science,* 47**,** 439-452.

CROSS, W. G. 1968. Variation of beta dose attenuation in different media. *Physics in Medicine and Biology,* 13**,** 611-618.

CROSS, W. G., FREEDMAN, N. O. & WONG, P. Y. 1992. Beta-Ray Dose Distributions from Point Sources in an Infinite Water Medium. *Health Physics,* 63**,** 160-171.

CULLEN, D. E., HUBBELL, J. H. & KISSEL, L. 1997. EPDL97 The evaluated data library, '97 version. Report UCRL-50400 vol.6, rev.5. Livermore, CA: Lawrence Livermore National Laboratory.

CURRAY, J. R. & GRIFFITHS, J. C. 1955. Sphericity and roundness of quartz grains in sediments. *Bulletin of the Geological Society of America,* 66**,** 1075-096.

DAS, I. J., MOSKVIN, V. P., KASSAEE, A., TABATA, T. & VERHAEGEN, F. 2002. Dose purturbations at high-Z interfaces in kilovoltage photon beams: comparison with Monte Carlo simulations and measurements. *Radiation Physics and Chemistry,* 64**,** 173-179.

DE TORRES, T., ORTIZ, J. E., GRUN, R., EGGINS, S., VALLADAS, H., MERCIER, N., TISNERAT-LABORDE, N., JULIA, R., SOLER, V., MARTINEZ, E., SANCHEZ-MORAL, S., CANAVERAS, J. C., LARIO, J., BADAL, E., LALUEZA-FOX, C., ROSAS, A., SANTAMARIA, D., DE LA RASILLA, M. & FORTEA, J. 2010. Dating of the Hominid (Homo Neanderthalensis) Remains Accumulation from El Sidron Cave (Pilona, Asturias, North Spain): An Example of a Multi-Methodological Approach to the Dating of Upper Pleistocene Sites. *Archaeometry,* 52**,** 680-705.

DEMARCO, J. J., SMATHERS, J. B., BURNISON, C. M., NCUBE, Q. K. & SOLBERG, T. D. 1999. CT-based dosimetry calculations for I-125 prostate implants. *International Journal of Radiation Oncology Biology Physics,* 45**,** 1347-1353.

DEMARCO, J. J., WALLACE, R. E. & BOEDEKER, K. 2002. An analysis of MCNP cross-sections and tally methods for low-energy photon emitters. *Physics in Medicine and Biology,* 47**,** 1321-1332.

DIEPENBROEK, M., BARTHOLOMA, A. & IBBEKEN, H. 1992. How Round Is Round - a New Approach to the Topic Roundness by Fourier Grain Shape-Analysis. *Sedimentology,* 39**,** 411-422.

DONEV, A., CISSE, I., SACHS, D., VARIANO, E., STILLINGER, F. H., CONNELLY, R., TORQUATO, S. & CHAIKIN, P. M. 2004. Improving the density of jammed disordered packings using ellipsoids. *Science,* 303**,** 990-993.

DONEV, A., TORQUATO, S. & STILLINGER, F. H. 2005. Neighbor list collision-driven molecular dynamics simulation for nonspherical hard particles. II. Applications to ellipses and ellipsoids. *Journal of Computational Physics,* 202**,** 765-793.

EASTOE, J. E. 1955. The amino acid composition of mammalian collagen and gelatin. *Biochemical Journal,* 61**,** 589-600.

ENDICOTT, P., HO, S. Y. W. & STRINGER, C. 2010. Using genetic evidence to evaluate four palaeoanthropological hypotheses for the timing of Neanderthal and modern human origins. *Journal of Human Evolution,* 59**,** 87-95.

ESWARAN, V., HARPENDING, H. & ROGERS, A. R. 2005. Genomics refutes an exclusively African origin of humans. *Journal of Human Evolution,* 49**,** 1-18.

EVANS, M. L., CLOSE, D. A. & JAIN, M. 1982. Transport of Gamma-Rays through an Infinite Homogeneous Ore Medium. *Nuclear Instruments & Methods in Physics Research,* 192**,** 583-593.

EVANS, R. D. 1955. *The atomic nucleus,* New York, McGraw-Hill.

FAIN, J., SOUMANA, S., MONTRET, M., MAILLIER, D., PILLEYRE, T. & SANZELLE, S. 1999. Luminescence and ESR dating: Beta-dose attenuation for various grain shapes calculated by a Monte-Carlo method. *Quaternary Geochronology,* 18**,** 231-234.

FANO, U. 1952. *Tables for the Analysis of Beta Spectra. Applied Mathematics Series No. 13,* Washington, DC, National Bureau of Standards.

FANO, U. 1954. A note on the Bragg-Gray cavity principlefor measuring energy dissipation. *Radiation Research,* 1**,** 237-240.

FANO, U., SPENCER, L. V. & BERGER, M. J. 1959. Penetration and diffusion of X-rays. *In:* S., F. (ed.) *Handbuch der Physik.* Berlin: Springer.

FERMI, E. 1934. Versuch einer Theorie der beta-Strahlen. *Zeitschrift fur Physik A,* 88**,** 161-177.

FERNÁNDEZ-VAREA, J. M., MAYOL, R., BARÓ, J. & SALVAT, F. 1993. On the theory and simulation of multiple elastic scattering of electrons. *Nuclear Instruments and Methods in Physics Research B,* 73**,** 447-473.

FINLAYSON, J. C. & GILES PACHECO, F. (eds.) 2000. *The Southern Iberian peninsula in the Late Pleistocene,* Oxford: Oxbow.

FINNEY, J. L. 1970. Random Packings and Structure of Simple Liquids .1. Geometry of Random Close Packing. *Proceedings of the Royal Society of London Series a-Mathematical and Physical Sciences,* 319**,** 479-&.

FITZGERALD, J. J., BROWNELL, G. L. & MAHONEY, F. J. 1967. *Mathematical Theory of Radiation Dosimetry,* New York, Gordon and Breach.

FLEMING, S. J. & STONEHAM, D. 1973. Thermoluminescent Authenticity Study and Dating of Renaissance Terracottas. *Archaeometry,* 15**,** 239-&.

FOLK, R. L. & WARD, W. C. 1957. Brazos River Bar: a study in the significance in grain size analysis. *Journal of Sedimentary Petrology,* 27**,** 3-26.

FORSTER, P. 2004. Ice Ages and the mitochondrial DNA chronology of human dispersals: a review. *Philosophical Transactions of the Royal Society of London Series B-Biological Sciences,* 359**,** 255-264.

GARRELS, R. M. & MACKENZIE, F. T. 1971. *Evolution of Sedimentary Rocks.,* New York, Norton.

GARRIGAN, D., MOBASHER, Z., SEVERSON, T., WILDER, J. A. & HAMMER, M. F. 2005. Evidence for archaic Asian ancestry on the human X chromosome. *Molecular Biology and Evolution,* 22**,** 189-192.

GARROD, D. & BATE, D. 1937. *The Stone Age of Mount Carmel I: Excavations at the Wady El-Mughara,* Oxford, Clarendon Press.

GILLESPIE, R. & ROBERTS, R. G. 2000. On the reliability of age estimates for human remains at Lake Mungo. *Journal of Human Evolution,* 38**,** 727-732.

GILMORE, J. & HEMINGWAY, J. 1995. *Practical gamma-ray spectrometry,* Chichester, John Wiley and Sons.

GOKSU, H. Y., FREMLIN, J. H., IRWIN, H. T. & FRYXELL, R. 1974. Age-Determination of Burned Flint by a Thermoluminescent Method. *Science,* 183**,** 651-654.

GOLDSTEIN, H. 1959. *Fundamental aspects of reactor shielding,* Reading, MA. , Addison -Wesley.

GOUDSMIT, S. & SAUNDERSON, J. L. 1940. Multiple scattering of electrons. *Physical Review,* 57**,** 24-29.

GRAY, L. H. 1929. The absorption of penetrating radiation. *Proceedings of the Royal Society,* A122**,** 647-668

GRAY, L. H. 1936. An ionization method for the absolute measurement of gamma-ray energy. *Proceedings of the Royal Society,* A156**,** 578-596.

GREILICH, S., GLASMACHER, U. A. & WAGNER, G. A. 2005. Optical dating of granitic stone surfaces. *Archaeometry,* 47**,** 645-665.

GRINE, F. E., BAILEY, R. M., HARVATI, K., NATHAN, R. P., MORRIS, A. G., HENDERSON, G. M., RIBOT, I. & PIKE, A. W. G. 2007. Late Pleistocene human skull from Hofmeyr, South Africa, and modern human origins. *Science,* 315**,** 226-229.

GRUN, R., BEAUMONT, P., TOBIAS, P. V. & EGGINS, S. 2003. The age of the Border Cave 5 mandible. *Geochimica Et Cosmochimica Acta,* 67**,** A126-A126.

GRUN, R., EGGINS, S., AUBERT, M., SPOONER, N., PIKE, A. W. G. & MULLER, W. 2010. ESR and U-series analyses of faunal material from Cuddie Springs, NSW, Australia: implications for the timing of the extinction of the Australian megafauna. *Quaternary Science Reviews,* 29**,** 596-610.

GRUN, R., MAROTO, J., EGGINS, S., STRINGER, C., ROBERTSON, S., TAYLOR, L., MORTIMER, G. & MCCULLOCH, M. 2006. ESR and U-series analyses of enamel and dentine fragments of the Banyoles mandible. *Journal of Human Evolution,* 50**,** 347-358.

GRUN, R., SCHWARCZ, H. P. & CHADAM, J. 1988. ESR dating of tooth enamel: coupled correction for U-uptake and U-series disequilibrium. *Nuclear Tracks and Radiation Measurements,* 14**,** 237-241.

GRUN, R., STRINGER, C., MCDERMOTT, F., NATHAN, R., PORAT, N., ROBERTSON, S., TAYLOR, L., MORTIMER, G., EGGINS, S. & MCCULLOCH, M. 2005. U-series and ESR analyses of bones and teeth relating to the human burials from Skhul. *Journal of Human Evolution,* 49**,** 316-334.

GUERIN, G. & MERCIER, N. 2011. Determining gamma dose rates by field gamma spectroscopy in sedimentary media: Results of Monte Carlo simulations. *Radiation Measurements,* 46**,** 190-195.

HAJI-AKBARI, A., ENGEL, M., KEYS, A. S., ZHENG, X. Y., PETSCHEK, R. G., PALFFY-MUHORAY, P. & GLOTZER, S. C. 2009. Disordered, quasicrystalline and crystalline phases of densely packed tetrahedra. *Nature,* 462**,** 773-U91.

HARE, P. E. 1980. Organic geochemistry of bone and its relation to the survival of bone in the natural environment. *In:* BEHRENSMEYE, A. K. & HILL, A. P. (eds.) *Fossils in the Making: Vertebrate Taphonomy and Paleoecology.* Chicago: University of Chicago Press.

HEDGES, R. E. M. 2002. Bone diagenesis: An overview of processes. *Archaeometry,* 44**,** 319-328.

HENDRIKS, P. H. G. M., MAUCEC, M. & DE MEIJER, R. J. 2002. MCNP modelling of scintillation-detector gamma-ray spectra from natural radionuclides. *Applied Radiation and Isotopes,* 57**,** 449-457.

HIGHAM, T., JACOBI, R., JULIEN, M., DAVID, F., BASELL, L., WOOD, R., DAVIES, W. & RAMSEY, C. B. 2010. From the Cover: Chronology of the Grotte du Renne (France) and implications for the context of ornaments and human remains within the Chatelperronian. *Proc Natl Acad Sci U S A,* 107**,** 20234-9.

HILLAS, A. M. 1972. *Cosmic rays,* Oxford, Pergamon Press.

HOUNSFIELD, G. N. 1973. Computerized transverse axial scanning (tomography). 1. Description of system. *British Journal of Radiology,* 46**,** 1016-1022.

HUBBELL, J. H. & SELTZER, S. M. 2004. Tables of X-ray mass attenuation coefficients and mass energy-absorption coefficients (version 1.4). National Institute of Standards and Technology, Gaithersburg, MD.

HUNTLEY, D. J., GODFREY-SMITH, D. I. & THEWALT, M. L. W. 1985. Optical Dating of Sediments. *Nature,* 313**,** 105-107.

ICRU 1980. Radiation quantities and units. Bethesda, MD: Internation Commission on Radiation Units and Measurements.

IKEYA, M. 1975. Dating a Stalactite by Electron-Paramagnetic Resonance. *Nature,* 255**,** 48-50.

IKEYA, M. 2004. ESR dating, dosimetry and microscopy for terrestrial and planetary materials. *Electron Paramagnetic Resonance,* 19**,** 1-32.

INGMAN, M., KAESSMANN, H., PAABO, S. & GYLLENSTEN, U. 2000. Mitochondrial genome variation and the origin of modern humans. *Nature,* 408**,** 708-713.

IVANOVICH, M. & HARMON, R. S. 1992. *Uranium-series disequilibrium: applications to Earth, Marine, and Environmental Sciences,* Oxford, Clarendon Press.

IYENGAR, G. V., KOLLMER, W. E. & BOWEN, H. J. M. 1978. *The Elemental Composition of Human Tissue and Body Fluids.,* New York, Springer-Verlag.

JACOBS, Z., DULLER, G. A. T. & WINTLE, A. G. 2003. Optical dating of dune sand from Blombos Cave, South Africa: II - single grain data. *Journal of Human Evolution,* 44**,** 613-625.

JACOBS, Z. & ROBERTS, D. L. 2009. Last Interglacial Age for aeolian and marine deposits and the Nahoon fossil human footprints, Southeast Coast of South Africa. *Quaternary Geochronology,* 4**,** 160-169.

JACOBS, Z., WINTLE, A. G., ROBERTS, R. G. & DULLER, G. A. T. 2008. Equivalent dose distributions from single grains of quartz at Sibudu, South Africa: context, causes and consequences for optical dating of archaeological deposits. *Journal of Archaeological Science,* 35**,** 1808-1820.

JAEGER, H. M. & NAGEL, S. R. 1992. Physics of the granular state. *Science,* 255**,** 1523-1531.

JAIN, M., EVANS, M. L. & CLOSE, D. A. 1979. Nondestructive assay technology for uranium source evaluation: infinite medium calculations. Report LA-7713-MS/UC-51. Los Alamos: University of California.

JANSSENS, A. & EGGERMONT, G. 1974. Spectrum perturbation and energy deposition models for stopping power ratio calculations in general cavity theory. *Phys Med Biol,* 19**,** 619-30.

JELINEK, A. J. 1982. The Tabun Cave and Paleolithic Man in the Levant. *Science,* 216**,** 1369-1375.

JONEJA, O. P., NEGREANU, C., STEPANEK, J. & CHAWLA, R. 2003. Comparison of Monte Carlo simulations of photon/electron dosimetry in microscale applications. *Australasian Physical & Engineering Sciences in Medicine,* 26**,** 12-18.

JUN, I. 2003. Benchmark study for energy deposition by energetic electrons in thick elemental slabs: Monte Carlo results and experiments. *Ieee Transactions on Nuclear Science,* 50**,** 1732-1739.

KAWRAKOW, I. & ROGERS, D. W. O. 2001. *The EGSnrc code system: Monte Carlo simulation of electron and photon transport. Report PIRS-701,* Ottawa, National Research Council of Canada.

KIVISILD, T., SHEN, P. D., WALL, D. P., DO, B., SUNG, R., DAVIS, K., PASSARINO, G., UNDERHILL, P. A., SCHARFE, C., TORRONI, A., SCOZZARI, R., MODIANO, D., COPPA, A., DE KNIJFF, P., FELDMAN, M., CAVALLI-SFORZA, L. L. & OEFNER, P. J. 2006. The role of selection in the evolution of human mitochondrial genomes. *Genetics,* 172**,** 373-387.

LANDAU, L. 1944. On the energy loss of fast particles by ionization. *Journal of physics USSR,* 8**,** 201-205.

LANG, A. & WAGNER, G. A. 1996. Infrared stimulated luminescence dating of archaeosediments. *Archaeometry,* 38**,** 129-141.

LANGMUIR, D. 1978. Uranium Solution-Mineral Equilibria at Low-Temperatures with Applications to Sedimentary Ore-Deposits. *Geochimica Et Cosmochimica Acta,* 42**,** 547-569.

LAURENCE, G. C. 1937. The measurement of extra hard x-rays and gamma-rays in roentgens. *Canadian Journal of Research,* A15**,** 67-.

LI, B., LI, S.-H., DULLER, G. A. T. & WINTLE, A. G. 2011. Infrared stimulated luminescence measurements of single grains of K-rich feldspar for isochron dating *Quaternary Geochronology,* 6**,** 71-81

LOCKWOOD, G. J., RUGGLES, L. E., MILLER, G. H. & HALBLEIB, J. A. 1980. Calorimetric measurement of electron energy deposition in extended media - Theory vs. experiment. SAND79-0414: Sandia National Laboratory.

LOEVINGER, R. 1956. The Dosimetry of Beta Sources in Tissue - the Point-Source Function. *Radiology,* 66**,** 55-62.

LU, B. L. & TORQUATO, S. 1993. Chord-Length and Free-Path Distribution-Functions for Many-Body Systems. *Journal of Chemical Physics,* 98**,** 6472-6482.

LUBACHEVSKY, B. D. & STILLINGER, F. H. 1990. Geometric-Properties of Random Disk Packings. *Journal of Statistical Physics,* 60**,** 561-583.

LYONS, R. G. 1988. Determination of alpha effectiveness in ESR dating using linear accelerator techniques: methods and energy dependence. *Nuclear Tracks and Radiation Measurements,* 14**,** 275-288.

MASON, B. & MOORE, C. B. 1982. *Principles of geochemistry,* New York, John Wiley.

MATHESON, A. J. 1974. Computation of a Random Packing of Hard Spheres. *Journal of Physics C-Solid State Physics,* 7**,** 2569-2576.

MCCOWN, T. D. & KEITH, A. 1939. *The Stone Age of Mount Carmel II: The fossil human remains from the Levalloiso-Mousterian,* Oxford, Clarendon Press.

MCDERMOTT, F., GRUN, R., STRINGER, C. B. & HAWKESWORTH, C. J. 1993. Mass-Spectrometric U-Series Dates for Israeli Neanderthal Early-Modern Hominid Sites. *Nature,* 363**,** 252-255.

MCQUARRIE, D. A. 1975. *Statistical mechanics,* New York, Harper & Row.

MEJDAHL, V. 1979. Thermoluminesce dating: beta-dose attenuation in quartz grains. *Archaeometry,* 21**,** 61-72.

MEJDAHL, V. 1983. Feldspar inclusion dating of ceramics and burnt stones. *European PACT J. 9***,** 351-364.

MERCIER, N., VALLADAS, H., BARYOSEF, O., VANDERMEERSCH, B., STRINGER, C. & JORON, J. L. 1993. Thermoluminescence Date for the Mousterian Burial Site of Es-Skhul, Mt-Carmel. *Journal of Archaeological Science,* 20**,** 169-174.

MERCIER, N., VALLADAS, H., FROGET, L., JORON, J. L., REYSS, J. L., WEINER, S., GOLDBERG, P., MEIGNEN, L., BAR-YOSEF, O., BELFER-COHEN, A., CHECH, A., KUHN, S. L., STINER, M. C., TILLIER, A. M., ARENSBURG, B. & VANDERMEERSCH, B. 2007. Hayonim Cave: a TL-based chronology for this levantine mousterian sequence. *Journal of Archaeological Science,* 34**,** 1064-1077.

MILLARD, A. R. & HEDGES, R. E. M. 1996. A diffusion-adsorption model of uranium uptake by archaeological bone. *Geochimica Et Cosmochimica Acta,* 60**,** 2139-2152.

MULLICK, R., VENKATARAMAN, S., WARUSAVITHANA, S., NGUYEN, H. T. & RAGHAVAN, R. Year. eTDIPS: 2D/3D Image Processing System for Volume Rendering and Telemedicine. *In:* Annual Meeting of the Society for Computer Applications in Radiology (SCAR), 1998 Baltimore.

MURRAY, A. S. 1981. *Environmental radioactivity studies relevant to thermoluminescence dating.* University of Oxford.

MURRAY, A. S. & OLLEY, J. M. 2002. Precision and accuracy in the optically stimulated luminescence dating of sedimentary quartz: a status review. *Geochronometrica,* 21**,** 1-16.

MURRAY, A. S. & WINTLE, A. G. 2000. Luminescence dating of quartz using an improved single-aliquot regenerative-dose protocol. *Radiation Measurements,* 32**,** 57-73.

MURTHY, M. S. S. 1971. Shape and Average Energy of Beta-Particle Spectra. *International Journal of Applied Radiation and Isotopes,* 22**,** 111-&.

NAKAI, Y. 1963. Energy dissipation of electron beams in matter. *Japan Journal of Applied Physics,* 2**,** 743-756.

NATHAN, R. & GRUN, R. 2003. Gamma dosing and shielding of a human tooth by a mandible and skull cap. *Ancient TL,* 21**,** 79-84.

NATHAN, R. P., THOMAS, P. J., JAIN, M., MURRAY, A. S. & RHODES, E. J. 2003. Environmental dose rate heterogeneity of beta radiation and its implications for luminescence dating: Monte Carlo modelling and experimental validation. *Radiation Measurements,* 37**,** 305-313.

NATIONAL BUREAU OF STANDARDS 1951. *Monte Carlo Method,* Washington, US Department of Commerce.

NORMAN, L. D. & SKOLNICK, L. P. 1968. A Computer Simulation of Dense Random Packing of Spherical Particles. *Journal of Metals,* 20**,** A121-&.

OLIVEIRA, C., YORIYAZ, H., OLIVEIRA, M. C. & FERREIRA, L. M. 2004. Monte Carlo simulation for dose distribution calculations in a CT-based phantom at the Portuguese gamma irradiation facility. *Nuclear Instruments & Methods in Physics Research Section B-Beam Interactions with Materials and Atoms,* 213**,** 662-665.

OLLEY, J. M., MURRAY, A. & ROBERTS, R. G. 1996. The effects of disequilibria in the uranium and thorium decay chains on burial dose rates in fluvial sediments. *Quaternary Science Reviews,* 15**,** 751-760.

OLLEY, J. M., ROBERTS, R. G. & MURRAY, A. S. 1997. Disequilibria in the uranium decay series in sedimentary deposits at Allen's Cave, Nullarbor Plain, Australia: Implications for dose rate determinations. *Radiation Measurements,* 27**,** 433-443.

PARK, S. H., HAN, C. Y., KIM, S. Y. & KIM, J. K. 2004. Use of the CT images for BNCT calculation: Development of BNCT treatment planning system and its applications to dose calculation for voxel phantoms. *Radiation Protection Dosimetry,* 110**,** 661-667.

PAVLOVITCH, A., JULLIEN, R. & MEAKIN, P. 1991. Geometrical Properties of a Random Packing of Hard-Spheres. *Physica A,* 176**,** 206-219.

PIKE, A. W. G., FOSTER, G. L., STRINGER, C., EGGINS, S. M. & GRUN, R. 2006. Direct U-series dating of fossil human bone by laser ablation MC-ICPMS. *Geochimica Et Cosmochimica Acta,* 70**,** A494-A494.

PIKE, A. W. G., HEDGES, R. E. M. & VAN CALSTEREN, P. 2002. U-series dating of bone using the diffusion-adsorption model. *Geochimica Et Cosmochimica Acta,* 66**,** 4273-4286.

POLLARD, A. M. & HERON, C. 1996. *Archaeological chemistry,* Cambridge, Royal Society of Chemistry.

PORCELLI, D. & SWARZENSKI, P. W. 2003. The behaviour of U- and Th-series nuclides in groundwater. *In:* BOURDON, B., HENDERSON, G. M., LUNDSTROM, C. C. & TURNER, S. P. (eds.) *Uranium-Series Geochemistry.* Washington D.C.: Mineralogical Society of America.

PRESCOTT, J. R. & HUTTON, J. T. 1994. Cosmic-Ray Contributions to Dose-Rates for Luminescence and Esr Dating - Large Depths and Long-Term Time Variations. *Radiation Measurements,* 23**,** 497-500.

PRICE, R. 2000. The deterministic approach to radiation transport. *In:* TAGZIRIA, H. (ed.) *Review of Monte Carlo and deterministic codes in radiation protection and dosimetry.* UK: National Physicsal Laboratory.

RAK, Y. 1990. On the Differences between 2 Pelvises of Mousterian Context from the Qafzeh and Kebara Caves, Israel. *American Journal of Physical Anthropology,* 81**,** 323-332.

READHEAD, M. L. 1987. Thermoluminescence dose rate data and dating equations for the case of disequilibrium in the decay series. *Nuclear Tracks and Radiation Measurements,* 13**,** 197-207.

READHEAD, M. L. 2002. Absorbed dose fraction for 87Rb β particles. *Ancient TL,* 20**,** 25-28.

RESTER, D. H. & DERRICKSON, J. H. 1971. Electron transmission measurements for Al, Sn, and Au targets at electron bombarding energies of 1.0 and 2.5 MeV. *Journal of Applied Physics,* 42**,** 714-721.

RHODES, E. J. & NATHAN, R. P. 2000. OSL dating of quartz: New developments. *In:* ROBERTS, M. B. & PARFITT, S. A. (eds.) *Boxgrove: A Middle Pleistocene Hominid site at Eartham Quarry, Boxgrove, West Sussex.*: English Heritage Arch. Rep. .

RODERIGUEZ, J., CACERES, L. M., ABAD, M., RUIZ, F., NATHAN, R., SCHWENNINGER, J. L., FINLAYSON, J. C., FINLAYSON, G. & FA, D. Year. The Catalan Bay cliff-front dune, Gibraltar: A Late Pleistocene palaeoclimatic record in the Western Mediterranean. *In:* Resumenes XII Reunion Nacional de Cuaternario, 2007 Avila.

RODRIGUEZ-VIDAL, J., CACERES, L. M., FINLAYSON, J. C., GRACIA, F. J. & MARTINEZ-AGUIRRE, A. 2004. Neotectonics and shoreline history of the Rock of Gibraltar, southern Iberia. *Quaternary Science Reviews,* 23**,** 2017-2029.

RODRIGUEZ, J., CACERES, L. M., FINLAYSON, J. C., GRACIA, F. J. & MARTINEZ-AGUIRRE, A. 2004. Neotectonics and shoreline history of the Rock of Gibraltar, southern Iberia. *Quaternary Science Reviews,* 23**,** 2017-2029.

ROESCH, W. C. & ATTIX, F. H. 1968. Basic concepts of dosimetry. *In:* ATTIX, F. H. & ROESCH, W. C. (eds.) *Radiation dosimetry, Volume I: Fundamentals.* 2 ed. New York and London: Academic Press.

ROGERS, D. W. O. & BIELAJEW, A. F. 1986. Differences in electron depth dose curves calculated with EGS and ETRAN and improved energy-range relationships. *Medical Physics,* 13**,** 687-694.

RONOV, A. B. & YAROSHEVSKY, A. A. 1969. Chemical composition of the Earth's crust. *In:* HART, P. J. (ed.) *The Earth's Crust and Upper Mantle.* American Geophysical Union Monograph 13.

ROSEMAN, C. C. & WEAVER, T. D. 2004. Multivariate apportionment of global human craniometric diversity. *American Journal of Physical Anthropology,* 125**,** 257-263.

ROSHOLT, J. N. 1959. Natural radioactive disequilibrium of the uranium series. Washington D.C.: Geological Survey Bulletin 1084-A.

SALVAT, F., FERNÁNDEZ-VAREA, J. M. & SEMPAU, J. 2006. *Penelope-2006: A code system for Monte Carlo simulation of electron and photon transport,* Barcelona, NEA.

SANDERSON, D. C. W., BISHOP, P., STARK, M., ALEXANDER, S. & PENNY, D. 2007. Luminescence dating of canal sediments from Angkor borei, mekong delta, southern Cambodia. *Quaternary Geochronology,* 2**,** 322-329.

SCAILLET, S., VITA-SCAILLET, G. & GUILLOU, H. 2008. Oldest human footprints dated by Ar/Ar. *Earth and Planetary Science Letters,* 275**,** 320-325.

SCHAART, D. R., JANSEN, J. T. M., ZOETELIEF, J. & DE LEEGE, P. F. A. 2002. A comparison of MCNP4C electron transport with ITS 3.0 and experiment at incident energies between 100 keV and 20 MeV: influence of voxel size, substeps and energy indexing algorithm *Physics in Medicine and Biology,* 47**,** 1459-1484.

SEGRÈ, E. 1953. *Experimental nuclear physics,* New York,, Wiley.

SEIDLER, G. T., MARTINEZ, G., SEELEY, L. H., KIM, K. H., BEHNE, E. A., ZARANEK, S., CHAPMAN, B. D., HEALD, S. M. & BREWE, D. L. 2000. Granule-by-granule reconstruction of a sandpile from x-ray microtomography data. *Physical Review E,* 62**,** 8175-8181.

SELTZER, S. M. 1991. Electron-photon Monte Carlo calculations: The ETRAN code. *Applied Radiation Isotopes,* 42**,** 917-935.

SEMPAU, J., FERNÁNDEZ-VAREA, J. M., ACOSTA, E. & SALVAT, F. 2003. Experimental benchmarks of the Monte Carlo code PENELOPE. *Nuclear Instruments and Methods in Physics Research B,* 207**,** 107-123.

SIEBERT, B. 2000. The Monte Carlo method. *In:* TAGZIRIA, H. (ed.) *Review of Monte Carlo and deterministic codes in radiation protection and dosimetry.* UK: National Physicsal Laboratory.

SIMPKIN, D. J. & MACKIE, T. R. 1990. Egs4 Monte-Carlo Determination of the Beta-Dose Kernel in Water. *Medical Physics,* 17**,** 179-186.

SINGH, J. J. 1969. Transmission of 2.43 MeV electrons through thick silicon targets. NASA technical note D-5075. Langley, USA: NASA.

SOLBERG, T. D., DEMARCO, J. J., CHETTY, I. J., MESA, A. V., CAGNON, C. H., LI, A. N., MATHER, K. K., MEDIN, P. M., ARELLANO, A. R. & SMATHERS, J. B. 2001. A review of radiation dosimetry applications using the MCNP Monte Carlo code. *Radiochimica Acta,* 89**,** 337-355.

SPENCER, L. V. 1955. Theory of electron penetration. *Physical Review,* 98**,** 1597-1615.

SPENCER, L. V. 1959. *Energy dissipation by fast electrons. Monograph 1,* Washington DC, National Bureau of Standards.

SPENCER, L. V. & ATTIX, F. H. 1955. A theory of cavity ionization. *Radiation Research,* 3**,** 239-254.

SPENCER, L. V. & FANO, U. 1954. Electron spectrum resulting from electron slowing down. *Physical Review,* 93**,** 1172-1181.

STABIN, M. G. & DA LUZ, L. 2002. Decay data for internal and external dose assessment. *Health Physics,* 83**,** 471-475.

STORM, E. & SRAEL, H. I. 1970. Photon Cross Sections from 1 keV to 100 MeV for Elements Z=1 to Z=100. *Nuclear Data Tables A7***,** 565-681.

STRINGER, C. B. (ed.) 2000. *Gibraltar and the Neanderthals 1848-1998,* Oxford: Oxbow.

STRINGER, C. B. & GAMBLE, C. S. 1993. *In search of the Neanderthals,* London, Thames and Hudson.

STRINGER, C. B., GRUN, R., SCHWARCZ, H. P. & GOLDBERG, P. 1989. Esr Dates for the Hominid Burial Site of Es Skhul in Israel. *Nature,* 338**,** 756-758.

STUART, A. J. & LISTER, A. M. 2001. The mammalian faunas of Pakefield/Kessingland and Corton, Suffolk, UK: evidence for a new temperate episode in the British early Middle Pleistocene. *Quaternary Science Reviews,* 20**,** 1677-1692.

TABATA, T. 1967. Backscattering of electrons from 3.2 to 14MeV. *Physical Review,* 162**,** 336-347.

TABATA, T. 1997. Smoothing and interpolation by moving-window least squares polynomial fits: application to energy and charge-deposition distributions by electrons. *Bulletin of Osaka Prefecture University, Series A,* 46**,** 71-78.

TANNER, A. B. 1964. Radon migration on the ground: a review. *In:* ADAMS, J. A. S. & LOWDER, W. M. (eds.) *The Natural Radiation Environment III.* Chicago: University of Chicago Press.

THORNE, A., GRUN, R., MORTIMER, G., SPOONER, N. A., SIMPSON, J. J., MCCULLOCH, M., TAYLOR, L. & CURNOE, D. 1999. Australia's oldest human remains: age of the Lake Mungo 3 skeleton. *Journal of Human Evolution,* 36**,** 591-612.

TORQUATO, S. 2002. *Random Heterogeneous Materials: Microstructure and Macroscopic Properties*, Springer.

TORQUATO, S. & JIAO, Y. 2009. Dense packings of the Platonic and Archimedean solids (vol 460, pg 876, 2009). *Nature,* 461**,** 828-828.

TORQUATO, S., TRUSKETT, T. M. & DEBENEDETTI, P. G. 2000. Is random close packing of spheres well defined? *Physical Review Letters,* 84**,** 2064-2067.

TRUMP, J. G., WRIGHT, K. A. & CLARKE, A. M. 1950. Distribution of ionization in materials irradiated by two and three million-volt cathode rays. *Journal of Applied Physics,* 21**,** 345-348.

TUREKIAN, K. K. & WEDEPOHL, K. H. 1961. Distribution of the elements in some major units of the Earth's crust. *Geological Society of America Bulletin,* 72**,** 175-192.

VALLADAS, H. & VALLADAS, G. 1982. Effet de l'irradiation alpha sur des grains de quartz. *PACT,* 6**,** 171-178.

VALLADAS, H. & VALLADAS, G. 1987. Thermo-Luminescence Dating of Burnt Flint and Quartz - Comparative Results. *Archaeometry,* 29**,** 214-220.

VAN RIPER, K. A. 2005. A CT and MRI scan to MCNP input conversion program. *Radiation Protection Dosimetry* 115**,** 513-516.

VANDERMEERSCH, B. 1981. *Les Hommes Fossiles de Qafzeh, Israel,* Paris, CNRS.

VISSCHER, W. M. & BOLSTERLI, M. 1972. Random Packing of Equal and Unequal Spheres in 2 and 3 Dimensions. *Nature,* 239**,** 504-&.

WADELL, H. 1935. Volume, shape and roundness of quartz particles. *Journal of Geology,* 43**,** 250-280.

WALL, J. & BURKE, E. A. 1974. Dose distributions at and near the inetrface of different materials exposed to Cobalt-60 gamma radiation. Report AFCRL-TR-0004. Albuquerque, NM.: Sandia Laboratories.

WINTLE, A. G. 2008. Fifty years of luminescence dating. *Archaeometry,* 50**,** 276-312.

WÜST, R. A. J., WARD, C. R., BUSTIN, R. M. & HAWKE, M. I. 2002. Characterization and quantification of inorganic constituents of tropical peats and organic-rich deposits from Tasek Bera (Peninsular Malaysia): implications for coals. *International Journal of Coal Geology,* 49**,** 215– 249.

X-5 MONTE CARLO TEAM 2003. *MCNP - A general Monte Carlo N-particle transport code, Version 5,* Los Alamos, Los Alamos National Laboratory.

YE, S. J., BREZOVICH, I. A., PAREEK, P. & NAQVI, S. A. 2004. Benchmark of PENELOPE code for low-energy photon transport: dose comparisons with MCNP4 and EGS4. *Physics in Medicine and Biology,* 49**,** 387-397.

ZAIDI, H. 2000. Comparative evaluation of photon cross-section libraries for materials of interest in PET Monte Carlo simulation. *IEEE Transactions on Nuclear Science,* 47**,** 2722-2735.

ZEMANHOF, R., REDMOND, E., SOLARES, G., KATZ, D., RILEY, K., KIGER, S. & HARLING, O. 1996. Monte Carlo-based treatment planning for boron neutron capture therapy using custom designed models automatically generated from CT data. *International Journal of Radiation Oncology Biology Physics,* 35**,** 383-397.

ZHAO, H. & LI, S. H. 2002. Luminescence isochron dating: A new approach using different grain sizes. *Radiation Protection Dosimetry,* 101**,** 333-338.

ZIMMERMAN, D. W. 1971. Thermoluminescent dating using fine grains from pottery. *Archaeometry,* 13**,** 29-52.

ZIMMERMAN, D. W. & HUXTABLE, J. 1971. Thermoluminescent Dating of Upper Palaeolithic Fired Clay from Dolni Vestonice. *Archaeometry,* 13**,** 53-57.

ZINGG, T. 1935. Beitrage zur schotteranlyse. *Schweizerische Mineralogische und Petrologische Mitteilungen,* 15**,** 39-140.